

UNCLASSIFIED

AD NUMBER
AD818887
NEW LIMITATION CHANGE
TO Approved for public release, distribution unlimited
FROM Distribution authorized to U.S. Gov't. agencies and private individuals or enterprises eligible to obtain export-controlled technical data in accordance with DoDD 5230.25. Controlling DoD office is Air Force Aero Propulsion Lab., Wright-Patterson AFB, OH 45433.
AUTHORITY
AFAPL ltr, 12 Apr 1972

THIS PAGE IS UNCLASSIFIED

20

FILE COPY

Charles N. McKinnon, Jr.
University of Missouri

TECHNICAL REPORT AFAPL-TR-67-64

August 1967

Air Force Aero Propulsion Laboratory
Directorate of Laboratories
Air Force Systems Command
Wright-Patterson Air Force Base, Ohio

Reproduced by
NATIONAL TECHNICAL
INFORMATION SERVICE
Springfield, Va. 22151

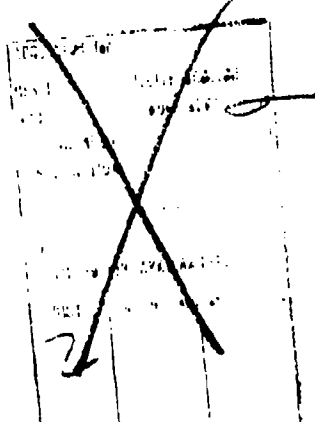
NOTICES

When Government drawings, specifications, or other data are used for any purpose other than in connection with a definitely related Government procurement operation, the United States Government thereby incurs no responsibility nor any obligation whatsoever; and the fact that the Government may have formulated, furnished, or in any way supplied the said drawings, specifications, or other data, is not to be regarded by implication or otherwise as in any manner licensing the holder or any other person or corporation, or conveying any rights or permission to manufacture, use, or sell any patented invention that may in any way be related thereto.

This document is subject to special export controls and each transmittal to foreign governments or foreign nations may be made only with the prior approval of the Aerospace Power Division of the Air Force Aero Propulsion Laboratory.

Foreign announcement and dissemination of this report by DDC is not authorized.

Copies of this report should not be returned to the Directorate of Laboratories unless return is required by security considerations, contractual obligations, or notice on a specific document.



② EXPLOSIVE MAGNETOHYDRODYNAMICS

⑨ Final technical rept. Apr 66-Apr 67, 1

⑩ Malcolm S. Jones, Jr., Clinton D. Bangerter, Albert H. Peterson,
Charles N. McKinnon, Jr.

⑪ Aug 67

⑫ 1857

⑬ AF 35 (615)-3233

⑭ AF 5560

⑮ 555004

⑯ MHD-700

⑰ HFAPL

⑱ TR-67-64

This document has been approved
for public release and notes its
distribution is unlimited

m/21

(227950)

1473
021


FOREWORD

This report was prepared by MHD Research, Incorporated, of Newport Beach, California under contract AF33(615)-3233. The contract was initiated under Project 5350 and Task 535004. This effort was administered under the direction of the Air Force Aero Propulsion Laboratory, Directorate of Laboratories, Air Force Systems Command. Lt. Richard D. Chronister, Jr. was the Air Force engineer for this work.

The work reported herein was conducted from April 1966 to April 1967 and was the joint effort of MHD Research, Incorporated; the Hercules, Incorporated MHD Group at the Bacchus Works, Magna, Utah; and the Mechanical Engineering Department of the University of Missouri, Columbia, Missouri. This report was submitted to the Air Force for review and approval in May 1967. Prior to the Air Force review, this report was identified as MHD Report 700.

The valuable technical contributions made by Paul W. Webster and Guenter Guthoff at MHD Research, Incorporated and by J. W. Lindsey, L. J. Davis, T. K. Baechler, and D. U. Bannion at Hercules, Incorporated are gratefully acknowledged.

This technical report has been reviewed and is approved.


PAUL E. PEKO, Captain, USAF
Chief
Propulsion & Power Branch
Aerospace Power Division

ABSTRACT

The objective of this program was to investigate the feasibility of using explosively driven MHD generators to produce pulses of various time durations and to investigate the feasibility of producing alternating currents. Four principal approaches were investigated with the following achievements:

- (1) Power densities of 5×10^7 w/m² were achieved in Composition C-4 explosive with copper and iron powder dopants. Detonation zone conductance was increased by three orders of magnitude, with magnetic Reynolds numbers approaching unity.
- (2) Sixty kilohertz alternating current was generated using segmented electrodes to commutate the current in an explosive-driven MHD channel and the output was transformer-coupled to various loads.
- (3) One millisecond pulses with maximum power outputs of 277 kw were achieved with 50 grams of seeded propellant. These fuels were successfully ignited using standard 20-mm electrically fired cartridges.
- (4) A series of pulses was generated in the explosive-driven MHD channel using a multiple-charge transport mechanism. Channel pumping-down times were found to limit this technique to the 10 to 20 pulse/sec pulse repetition frequency.

The report also covers analysis of the physical characteristics and sizes of potential systems utilizing each of these approaches to fill existing requirements.

TABLE OF CONTENTS

<u>Section</u>		<u>Page</u>
I	INTRODUCTION AND SUMMARY	
	A. Alternating Current Explosive MHD Power Generation	2
	B. Magnetically Loaded MHD Explosives	3
	C. Millisecond-Duration Pulsed MHD Power Generation .	3
	D. Conclusions and Recommendations	3
II	ALTERNATING CURRENT EXPLOSIVE MHD POWER GENERATION	
	A. High-Frequency Alternating Current Power Generation	6
	1. Background	6
	2. Experimental Work	7
	3. Transformer Tests	23
	4. Conclusions	26
	B. Low-Frequency Alternating Current Power Generation	28
	1. Background	28
	2. Apparatus	29
	3. Experimental Work	36
	4. Conclusions	52
III	MAGNETICALLY LOADED MHD EXPLOSIVES	
	A. Introduction and Summary	53
	1. Summary of Conductance Measurements - Phase I .	53
	2. Summary of Power Generation Experiments - Phase II	54
	B. Theory	55
	1. General Principles	55
	2. Magnetic Materials	63
	3. Conductivity	67
	C. Conductance Measurements	84
	1. Experimental Apparatus	84
	2. Procedure	91
	3. Discussion of Conductance Measurement Data . .	97
	D. Power Generation Experiments	108
	1. Experimental Apparatus	108
	2. Results of Power Generation Experiments	112
	3. Magnetic Reynolds Number	122
	E. Conclusions	125
IV	MILLISECOND-DURATION PULSED MHD POWER GENERATION	
	A. Introduction	127
	B. Fuel Characteristics	127
	C. Theory and Method	128
	D. Fuels Used in the Study	129
	E. Experimental Equipment	129
	F. Experimental Results	141
	G. Data Analysis	143
	H. System Design	152
	I. Conclusions and Recommendations	158

LIST OF FIGURES

<u>Number</u>		<u>Page</u>
1(a)	Electrode connections - alternating current output, both electrodes segmented	8
1(b)	Electrode connections - one electrode segmented, showing probable distribution of conductive, seeded detonation products	8
2	Details of explosive-driven, linear MHD channel	9
3	Arrangement of probes and electrodes used in segmented electrode experiments	11
4	Circuit diagram showing power supply and capacitor connected to electrostatic probe in channel electrode	12
5	Oscilloscope traces for electrostatic probes 1 through 4 installed in electrode (compare to Figure 6 in which the probes were biased to -100 volts)	13
6	Oscilloscope traces for electrostatic probes 1 through 4 when biased to -100 volts with respect to the electrode	14
7	X-t plot showing traces from Figure 5 arranged at their respective distances from the trigger electrodes.	15
8	Oscilloscope trace showing open circuit voltage of segmented electrode generator (50 mg of cesium picrate)	19
9	Oscilloscope trace showing open circuit voltage of segmented electrode generator (200 mg of cesium picrate)	19
10	Exploded view of output transformer showing single-turn primary coil and closely coupled secondary	20
11	Oscilloscope traces from segmented electrode experiment with one-turn primary.	21
12	Oscilloscope traces from segmented electrode generator experiment.	22

LIST OF FIGURES (Cont)

<u>Number</u>	<u>Title</u>	<u>Page</u>
27	Pressure as a function of time when charge is fired in multiple-charge apparatus	43
28	Time after firing first pulse for second and third pulses as a function of P_1 , with P_2 at atmospheric pressure	44
29	Plot showing recovery of generator output as a function of delay time after previous shot	45
30	Output voltage as the function of initial pressure in the channel for 100, 0.25, and 0.012 ohms	47
31	Experimental current-voltage characteristics for the channel	48
32	Estimated maximum power output generated with a given initial pressure in the channel	49
33	Summary of pressure effect results (based on Figures 26 and 27)	50
34(a)	Plot of voltage output for three initial pressures (3, 6, and 30 torr); load for upper curve was 100 ohms; lower two curves, 0.250 ohms	51
34(b)	Plot of magnetic induction as a function of axial position along the channel	51
35	Schematic view of pulsed explosive generator undergoing detonation	56
36	Simplified cross section of one-dimensional detonation process	57
37	Equivalent electrical circuit for direct coupling	58
38	Load current versus time for the circuit of Figure 36	61
39	Typical magnet material demagnetization curve	64
40(a)	Cube model for conductivity enhancement - unit cell	72
40(b)	Cube model for conductivity enhancement - breakdown of unit cell	73

LIST OF FIGURES (Cont)

<u>Number</u>	<u>Title</u>	<u>Page</u>
40(c)	Cube model for conductivity enhancement - equivalent network	73
41	Conductivity ratio versus volume fraction of inclusion for simple cube model, Rayleigh's sphere model, and Keller's improvement near simple cubic limit	75
42(a)	Simple spherical model for conductivity enhancement	76
42(b)	Multiple-size conductivity model	77
43	Theoretical conductance ratio G_T/G_0 as a function of the copper fraction by weight, Q	81
44	Particle size distributions	82
45	Theoretical conductance ratio G_T/G_0 as a function of the weight fraction of Type 316 stainless-steel powder, Q	83
46	Schematic of blast facility	85
47	Photo of blast tank and associated equipment indicated in Figure 22	86
48	Conductance measurement firing control and safety circuit	87
49	Schematic of test charge assembly	88
50	Cutaway view of charge assembly (test charge darkened for contrast)	90
51	Instrumentation circuit	92
52	Typical test record, Shot 57, 20.8% copper by weight (upper trace, 5v/div vertical and 2 microsec/ div horizontal; lower trace, 10v/div vertical and 5 microsec/div horizontal)	94
53	Conductance ratio G_T/G_0 versus Q , copper fraction by weight.	99
54	Conductance ratio G_T/G_0 versus Q , Type 316 stainless-steel fraction by weight	101

LIST OF FIGURES (Cont)

<u>Number</u>	<u>Title</u>	<u>Page</u>
55	Conductance ratio for sponge iron and spherical iron in Detasheet versus Q (solid lines are averaged experimental values from nominal 3-cm charges of spherical copper and 316 stainless-steel, from Figures 53 and 54)	103
56	Average detonation velocity \bar{D} vs Q, metal fraction by weight for both copper and Type 316 stainless-steel	104
57	Rationalized magnetic Reynolds number versus Q, metal fraction by weight for copper and Type 316 stainless-steel	107
58	Phase II power generation equipment: magnet is behind metal cabinet and test section is hanging on I-beam withdrawn from magnet gap; oscilloscopes are in lower right-hand corner	109
59	Test charge mounted on sting: blasting cap is on right end, then wave shaper and test charge; electrodes protrude from charge case for load and signal lead connection	110
60	Charge configuration, electrical schematic, and typical test record	111
61	Generator characteristics curve, 71.5% copper in Detasheet, 1/8-in.-thick charges	113
62	Summary of normalized generator characteristics for Type 316 stainless-steel in Composition C-4; reciprocal of load lines slope is the plasma conductance ($B \approx 0.5$ tesla; charge thickness is 1/4 in.)	115
63	Summary of normalized generator characteristics for sponge iron in Composition C-4 ($B \approx 5$ -K gauss; charge thickness is 1/4 in.)	117
64	Photograph of the sponge iron additive showing definite angular shape and size distribution (distance between superimposed vertical lines is 0.0005 in.)	119

LIST OF FIGURES (Cont)

<u>Number</u>	<u>Title</u>	<u>Page</u>
65(a)	Measured average detonation velocity as a function of calculated total charge density for sponge (Allen-Wood) iron and spherical stainless-steel	120
65(b)	Data in Figure 65(a) reduced to show average detonation velocity as a function of Q, metal weight fraction	120
66	Normalized generator characteristics for 65% spherical copper in Composition C-4 (B field is about 8-K gauss; charge thickness, 1/4 in.)	121
67	Summary of absolute magnetic Reynolds number, based on μ_0 , for various explosive-metal combinations as a function of the metal weight fraction	123
68	Magnet.	130
69	Magnet calibration curve.	132
70	Pulse motor cross section (2/3 scale)	133
71	One-pound-charge combustion chamber	134
72	20-mm combustor system.	135
73	Segmented-mode channel design	136
74	Cross sections of channel at exit end of electrode and at entrance to channel.	138
75	Toroid and integrator schematic	139
76	Typical load.	140
77	Plot of voltage versus current for 40-cm channel	145
78	Plot of voltage versus current for 60-cm channel	146
79	Discharge curve	148
80	Burning rate versus pressure - VJM fuel	149
81	Ratio of fuel surface area to nozzle area	150
82	Instantaneous mass flow rate with VJM fuel, throat diameter = 3.05 cm gm/ms.	151

LIST OF FIGURES (Cont)

<u>Number</u>	<u>Title</u>	<u>Page</u>
83	Voltage, current, and chamber pressure plots; test 403.	153
84	10^3 joule channel with aspect ratio of unity.	155
85	10^4 joule channel with aspect ratio of unity.	156
86	Weights of fuel and cartridge for 10^3 joule and 10^4 joule	157
87	Plot of mass flow rate versus burning time for hollow and solid cylinders	159
88	Experimental burning rates of several double-base type sporting powders up to 20,000 psi.	161

LIST OF TABLES

<u>Number</u>		<u>Page</u>
I	Charge and Seeding Configurations	17
II	Properties of Detasheet A	89
III	Calculated Parameters of Three MHD Fuels in Constant Mach Number Channel for Variation of Area Ratio (Magnetic Field Strength (B) Equals 2.8 Tesla).	137
IV	Experimental Data with OPC Combustor.	142
V	Experimental Data with 20-mm Combustor.	144

LIST OF ABBREVIATIONS AND SYMBOLS

<u>Item</u>	<u>Definition</u>
ac	alternating current
amp	ampere
BSS	Brown and Sharp sieve
cm	centimeter
dc	direct current
EMF	electromotive force
gm	gram
HMX	a solid explosive
in.	inch
j	joule
°K	degrees Kelvin
ka	kiloamp
kg	kilogram
kHz	kilohertz (1 hertz = 1 cycle per second)
kilobar	1 bar = 1.019 atmospheres
kj	kilojoule
km	kilometer
kv	kilovolt
kw	kilowatt
m	meter
mm	millimeter
mg	milligram
MHD	magnetohydrodynamic(s)
mho	reciprocal ohm

LIST OF ABBREVIATIONS AND SYMBOLS (Cont)

<u>Item</u>	<u>Definition</u>
min	minute
ms	millisecond
mw	milliwatt
OD	outside diameter
OPC	one-pound charge
PETN	a solid explosive
PRF	pulse repetition frequency
psi	pounds per square inch
psia	pounds per square inch, absolute
psig	pounds per square inch, gage
Q	metal fraction for copper and Type 316 stainless-steel
R.C.	resistor capacitance decay time constant
RDX	a solid explosive
R_m	magnetic Reynolds number
SCR	silicon-controlled rectifier
sec	second
tesla	1 tesla = 10,000 gauss
torr	1 torr = 1 millimeter of mercury
v	volt
VGM, VJM, VJP	solid-fuel formulations
w	watt
yr	year
σ_o	electrical conductivity, mho/m

LIST OF ABBREVIATIONS AND SYMBOLS (Cont)

<u>Item</u>	<u>Definition</u>
γ	specific heat ratio
$<$	less than
$>$	greater than
Ω	ohm

SECTION I

INTRODUCTION AND SUMMARY

The objective of this program has been to investigate the feasibility of using explosive-powered magnetohydrodynamic (MHD) generators to produce pulses of electrical power over a wide range of pulse durations and pulse repetition frequencies. Explosive-powered MHD systems have a number of advantages when compared with other systems for the production of pulses of electrical power for certain applications. Explosive MHD systems have a very high power density (1)* and, therefore, can reach almost any energy requirement within their pulse length regime in a much smaller volume than any potentially competitive system. In addition, the natural advantages of explosive MHD may include such factors as low initial cost, low weight per unit of power output, high reliability, and short response time.

Because of the relatively high cost per unit of thermal energy in explosives or rocket propellants compared to commercial electrical power or to the energy contained in conventional fuels, explosive-powered MHD units will become more competitive in areas where commercial power is not available or feasible. In addition to military applications this would include circumstances in which the total number of pulses to be produced is relatively small or they are produced infrequently so that it is difficult to justify installation of conventional generating and/or distribution facilities to meet the peak pulse load requirements.

The basic principles of explosive (1) (2) (3) and rocket-motor powered (4) (5) MHD have been explored in a number of previous programs and are relatively well understood. Most of the important parameters relating to power production or energy conversion have been identified and, although there is not a complete understanding of all of the physical and chemical principles involved, particularly with regard to the level of ionization of the seeded detonation products, sufficient experience and background exist to allow the design of units to cover a broad spectrum of power-time conditions with some degree of confidence.

It therefore seemed appropriate to investigate various explosive MHD techniques which could lead to useful applications of this technology. Several potential applications require pulse lengths which are either shorter or longer than the 50- to 200-microsec pulses produced in previous explosive-driven, linear MHD generator experiments. In addition these applications generally require that a series of pulses be produced in rapid order. Scaling the previous experiments up or down in power level is not difficult. However, to change the pulse length by an order of magnitude, to both longer and shorter pulses, new approaches were required. Because the electrical power may be required at higher or lower voltage levels than can be efficiently generated in an explosive-driven channel because of geometry limitations (1), it appeared necessary to generate alternating current so that transformers could be used to change voltage level. For this reason the generation of alternating current at high power

*Refer to List of References for this and subsequent numbers in ()

levels was of interest. An indirect objective of this program was to demonstrate a wider range of capabilities for explosive MHD systems. It was believed that the successful demonstration of the techniques would broaden the application area for explosive-driven MHD generators.

The work reported herein was the joint effort of MHD Research, Incorporated; the Hercules Incorporated MHD Group at Bacchus Works, Magna, Utah; and the Mechanical Engineering Department of the University of Missouri, Columbia, Missouri. The program is divided into three separate phases.

The first phase, conducted at MHD Research, Incorporated under the direction of Malcolm S. Jones, Jr., was related to the production of alternating current pulses. The program objectives of this phase were the production of 50-kHz alternating current with a pulse duration of 100 microsec, and the development of a rapid-pulsed explosive MHD device capable of pulse repetition frequencies of 90 pulses/sec. Work accomplished under this phase is reported in Section II of this report.

The second phase, conducted at the University of Missouri by Dr. Charles N. McKinnon, Jr., was concerned with the generation of short pulses of electrical energy through the use of a magnetically loaded explosive as an MHD generator. The objective of this phase of the program was a 20-microsec, 50-joule explosive pulse. This phase is presented in Section III.

The third phase was conducted by the MHD Group of Bacchus Works under the direction of Mr. Albert H. Peterson, with Clinton D. Bangerter as the Principal Investigator. The objective of this phase was the achievement of a 1-ms, 10^3 -joule output pulse from an MHD channel driven with a deflagrating energy source. This phase is reported in Section IV. Included in this section is a discussion of possible systems which might be developed using this technology. Charge-feeding mechanisms, channel cooling techniques, and channel geometry are considered. Estimates are made of system weights for various output pulse levels and pulse repetition rates for a 5-min operating period.

Technical progress has been made in all areas during the program. This progress is summarized in the subparagraphs that follow.

A. ALTERNATING CURRENT EXPLOSIVE MHD POWER GENERATION

It was found feasible to generate short bursts of 56-kHz power by using segmented electrodes which mechanically commutated the current path through the seeded detonation product plasma slug. Because of changes in the slug dimensions with time, nonuniform electrode spacing will be required if spectral purity is desired. The alternating current output was transformed to various impedance or voltage levels, illustrating the advantages of alternating-current power generation for a number of high-voltage applications.

Through the use of pneumatically operated cylinders, specially designed reusable explosive charge holders were driven past the entrance to the MHD channel at the velocities required to obtain a pulse repetition rate of 90 pulses/sec. It was found that the first pulse in a series would be satisfactory, but that the power output of subsequent explosive charges was seriously degraded. Subsequent tests showed that carbon soot buildup on the walls was but a small factor in the power output degradation. Measurements of the power output as a function of the pressure originally in the channel, coupled with pressure transducer measurements made during the rapid pulsing experiments, showed that the probable cause of the power output degradation was that when the next charge was fired, 11 ms after a preceding pulse, sufficient residual detonation product gases remained in the channel to reduce the generator output. Although this effect could be alleviated somewhat by improved mechanical design so as to produce a shorter channel, consideration of the natural pumping-down time of the channel forms an upper bound on the pulse repetition frequencies which can be achieved. Pulse repetition rates of 10 to 20 pulses/sec seem more appropriate for this technology.

B. MAGNETICALLY LOADED MHD EXPLOSIVES

It was shown that metal dopants could be used to increase the conductance of the detonation zone in condensed explosives. It was found that the conductance increased exponentially with the square of the dopant concentration. It was also determined that particle shape had an effect on the generated voltage. Explosives loaded with spherical particles have an effective velocity 0.1 times the detonation velocity; whereas, for angular particles, the effective velocity is 0.3. Power densities of 5×10^7 watts per square meter of explosive cross section were obtained. It was also shown that the magnetic Reynolds number could be increased by three orders of magnitude for the conditions studied and could be made to approach unity.

C. MILLISECOND-DURATION PULSED MHD POWER GENERATION

It was demonstrated that standard MHD solid fuels can be ignited with standard military primers and can be burned in millisecond periods to produce short pulses of power. The peak power produced from 50 grams of fuel was 277 kw with a pulse length of 1 ms. Incomplete combustion and large electrode drops were found to be the major problems. It is anticipated that these problems can be rather easily overcome with simple mechanical modifications to produce a more efficient device.

D. CONCLUSIONS AND RECOMMENDATIONS

It was shown that all three approaches followed were capable of generating power in the prescribed time and frequency ranges, although the power output levels were slightly below the original expectations for reasons which became clear as the experimental work proceeded. It is now possible to make more accurate predictions of the performance of

explosive-driven MHD channels or generators, and to predict accurately the performance of systems which might incorporate such devices.

On the basis of the studies presented in Section IV, it is clear that high-efficiency, millisecond-duration power generators can be constructed with additional development work.

In the case of the magnetically loaded explosives (Section III), the work is of a more basic nature and the development problems are not as clearly defined. Further work is needed to refine the theoretical models so as to account for the large magnetic Reynolds numbers, and additional experimental work is needed to both measure the parameters in the high magnetic Reynolds number regime and to incorporate finely divided permanent magnet materials into the explosive. Further experimentation would be aided if the size of the experimental apparatus could be scaled up so that edge effects in the explosive charges do not dominate the experiments.

SECTION II

ALTERNATING CURRENT EXPLOSIVE MHD POWER GENERATION

The objective of this phase of the program was to investigate the feasibility of generating alternating current in a linear, explosive-driven MHD channel. Two different approaches were followed to generate both high-frequency electrical power (50-kHz range) and low-frequency power (100-hertz range). Some degree of success was achieved in each of these approaches. The following paragraphs describe both of the approaches which were followed, the design of the apparatus, and the experimental results.

The experiments were conducted in a 1 x 4 x 48-in. explosive-driven, linear MHD channel which has been previously described (1). In the previous experiments conducted in this size channel (2), peak powers of the order of 23 mw were generated, with energy outputs of the order of 750 joules per pulse when feeding an optimum load. For those experiments, the magnetic induction was 2.3 tesla, and 15 grams of explosive contained in two 7.5-gram charges was used. However, for the present set of experiments, a different set of initial conditions and explosive geometry was used, so that the power output levels were below those previously achieved.

The high-frequency (56 kHz) power was generated by using a segmented electrode configuration which resulted in mechanical commutation of the generator output. These experiments are described in paragraph A. When using segmented electrodes, inductive effects become important and limit the rate at which energy can be delivered to the load for short pulse durations, because of the low internal resistance of the generator. Therefore, in an inductively limited system, the maximum power output, which goes as I^2R , should vary roughly as the square of the pulse length, since dI/dt is constant. For the high-frequency (50 kHz) power generation experiments, where the pulse rise time is 10 microsec, as compared to the 30-microsec rise time of the 23-mw pulses cited from the previous work, the peak power output should be about an order of magnitude lower, in the range of 2 mw. A peak power of 2.7 mw was observed. Through the use of a multiturn transformer, the generator output was boosted to 20 kv.

The low-frequency (90 hertz) power generation experiments were conducted by developing a charge-feeding mechanism which detonated a series of 7.5-gram charges opposite the channel entrance with the prescribed pulse repetition frequency. To avoid voltage breakdown problems between the electrodes and the ends of the channel, these experiments, described in paragraph B., were conducted with a magnetic induction of 1.0 tesla instead of 2.3 tesla. Because of the difference in magnetic induction, it is expected that the maximum power produced will vary by the ratio of the square of the magnetic fields, so that 5-mw output would be expected with 1.0 tesla. Peak power generation of 5.3 mw was observed in these experiments for the first pulse of the series. Because of insufficient time for

the channel to "pumpdown" during the 11 ms between detonations at a 90-pulse/sec repetition frequency, subsequent pulses in the series were greatly reduced in output. However, pulse repetition frequencies of 10 or 20/sec do appear to be feasible using these techniques.

On the basis of the present experiments, it is possible to describe a number of important factors which must be considered in the design of explosive-driven MHD channels for alternating current output.

A. HIGH-FREQUENCY ALTERNATING CURRENT POWER GENERATION

The feasibility of generating high-frequency electrical power in a linear, explosive-driven MHD channel was investigated in this phase of the program. If short bursts of high-frequency power can be generated directly from the detonation products, such an advance would greatly simplify the adaptation of explosive MHD technology to those applications where high-power alternating current is used; for example, in emergency communications and signaling systems. A device which generates high-voltage alternating current directly should be preferred to a system where direct current is generated and must then be transformed to an alternating current for utilization.

1. Background

One of the simplest ways to produce an alternating current output from a direct current generator is to introduce some form of commutation into the electrical output. There are many different ways that this can be accomplished electrically and mechanically. While the techniques for electrical commutation are well known (through the use of a resonant circuit and silicon-controlled rectifiers or by direct semiconductor control), it appeared appropriate to investigate the feasibility of using the inherent physical properties of the explosive-driven plasma to perform a mechanical commutation within the generator. In previous measurements in a small-scale (1 x 1 in.), explosive-driven generator (2), it was shown that most of the power is generated by a relatively thin layer of conductive plasma which is driven in front of the detonation products. These measurements showed that at the upstream end of the channel the thickness of the highly conductive region is of the order of a few centimeters. This was determined by measuring the duration of power-producing pulses as a function of electrode length for various electrodes centered at the same location. Extrapolating the pulse length to zero electrode length gave a residual time of 2 or 3 microsec which would correspond to a 0.02-m layer of plasma moving past the electrode at 10^4 m/sec. While such measurements had never been made at an appreciable distance from the charge, the fact that the power was being generated in a relatively small volume suggested that it would be appropriate to try mechanical commutation of the generator output by segmenting the electrodes and connecting them in such a fashion that alternating current could be generated.

Such a configuration is shown in Figure 1(a). The important design criterion is that the separation between electrode segments, b , should be greater than the width of the conductive region, S , shown schematically in Figure 1(b). Figure 1(b) shows an alternate approach to the problem wherein one of the electrodes is segmented and the other electrode is continuous. In this type of generator the output is a series of unidirectional pulses generated during the time the plasma is in contact with an electrode segment, with the output falling to zero when the plasma is in contact with the insulator between the electrodes. The result is an output that looks like a biased sine wave. If, however, a transformer is put into the output circuit, then an alternating current can be produced at the load, R_L . Through the use of a transformer with a turns ratio of N , the output can be transformed to a higher or lower voltage. However, when a transformer is used the generator internal impedance transforms as N^2 . Fortunately, the MHD generator has a relatively low internal impedance at low frequencies. The internal resistance of a typical generator is of the order of 10 milliohms, and the inductance is of the order of 1 microhenry (1).

One of the fundamental elements to determine in designing an alternating current experiment is the dimension of the conductive region, S , so that the proper electrode segmentation can be chosen. If the electrodes are too close together, circulating currents may be generated or commutation may not occur. Therefore a series of measurements was made to determine the effective size of the conductive region and to determine how the size of this region changed as the plasma moved down the channel. Once this information had been obtained, it was possible to design an effective electrode system.

We have at this point tacitly assumed that the conductive region had a dimension, S , which is to be determined experimentally, and that the detonation products would move at a constant velocity. In actual practice it is found that the front and rear of the detonation products have different velocities so that the plasma slug not only grows in the dimension S , but also slows down. This means that the electrode spacing must be non-linear to drive a fixed frequency, f_0 , and that the power generated in each succeeding pulse will be degraded by circulating currents when the slug is in the downstream section of the channel.

2. Experimental Work

To examine the various physical parameters involved in generating alternating current pulses, a series of experiments was conducted in an existing 1 x 4 x 48-in. linear MHD channel which had been used in previous experiments and has been described elsewhere (1) (3). The details of this channel are shown in Figure 2. The experimental program consisted of essentially three phases: (1) Measurement of the physical dimensions of the conductive slug of plasma, so the apparatus could be modified for high-frequency pulsed output; (2) a series of measurements to determine the

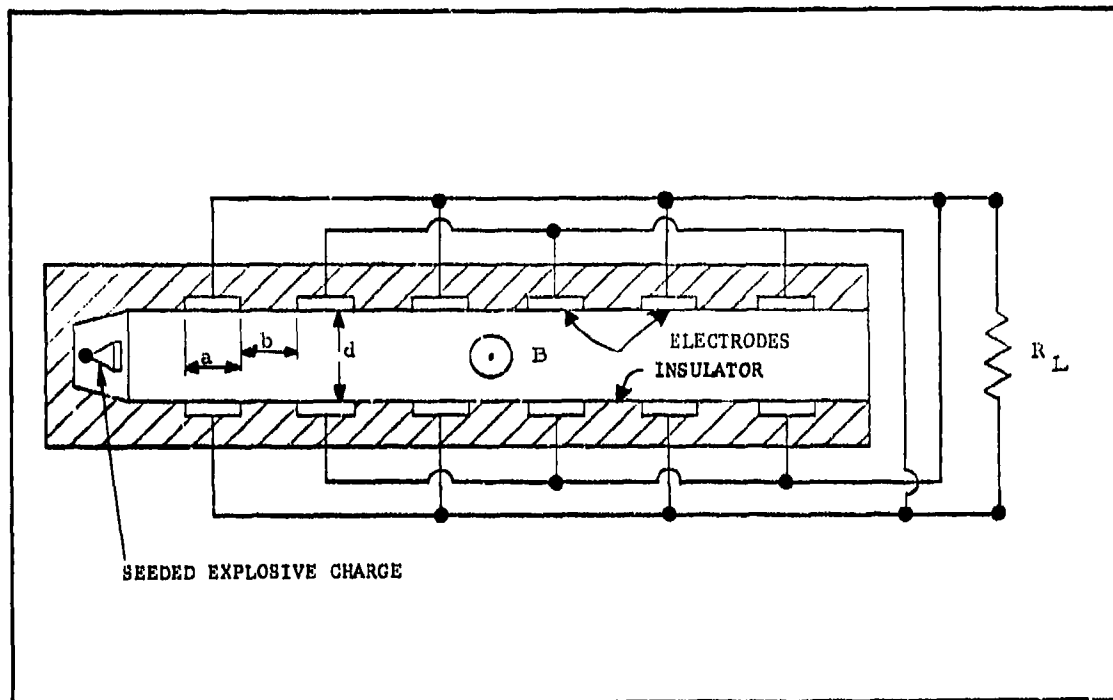


Figure 1(a). Electrode connections - alternating current output, both electrodes segmented

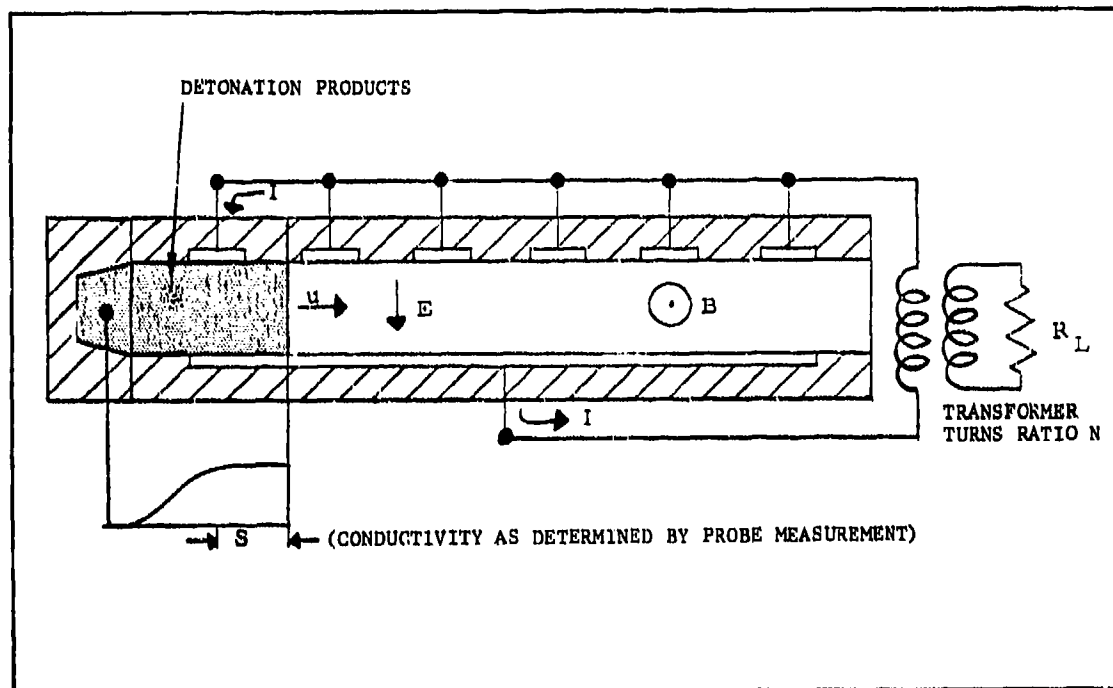


Figure 1(b). Electrode connections - one electrode segmented, showing probable distribution of conductive, seeded detonation products

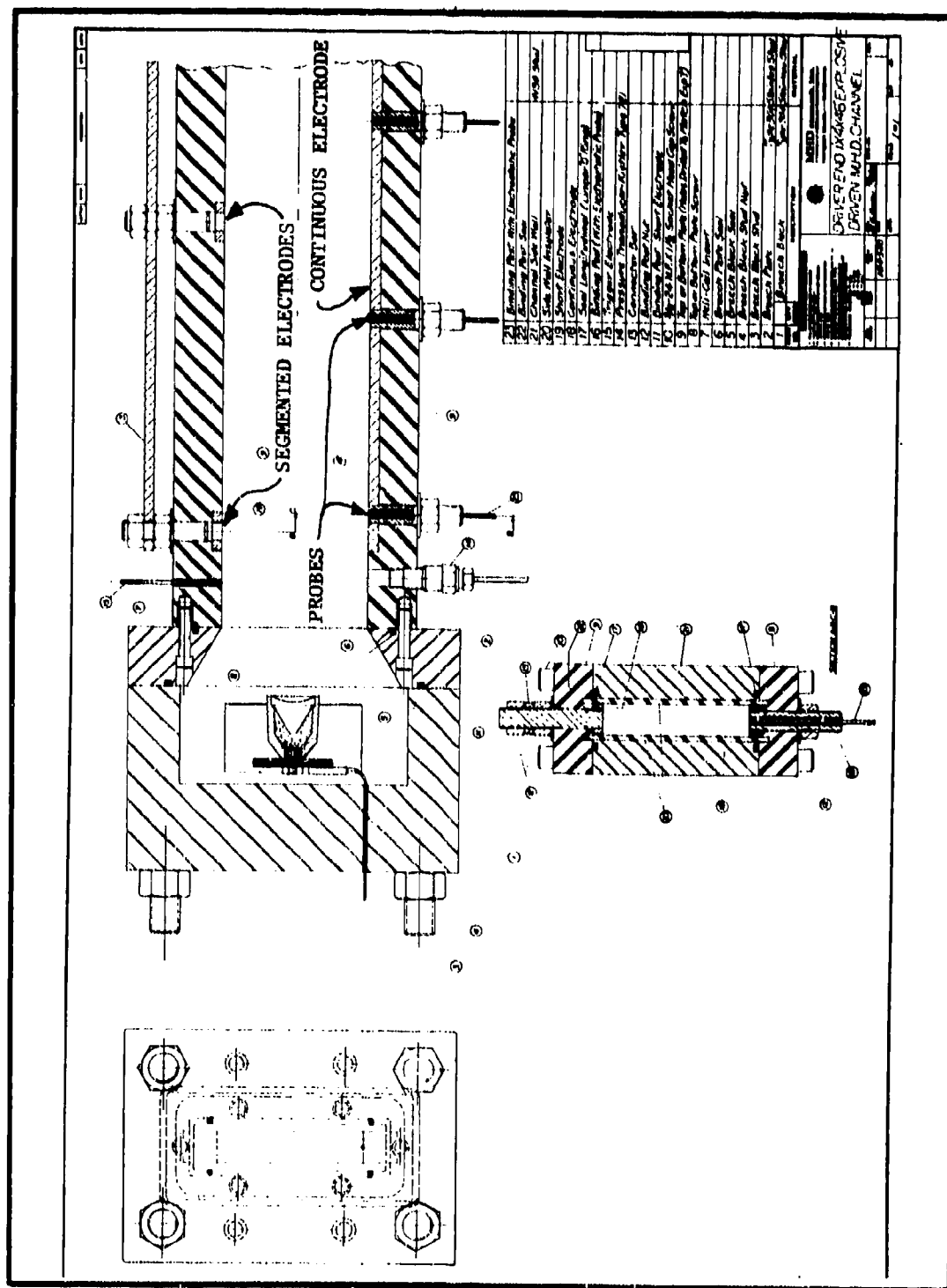


Figure 2. Details of explosive-driven, linear MHD channel

characteristics of a generator with a set of uniformly segmented electrodes having a small ratio of electrode length to insulator spacing; and (3) experiments in which alternating current output was connected to various output networks so as to provide high-voltage, high-frequency pulses. The following subparagraphs describe each set of experiments.

a. Probe Experiments

The probe experiments were conducted in the 1 x 4 x 48-in. channel using continuous electrodes. The probes were 1.5×10^{-3} m diameter copper wires mounted in 4×10^{-3} m diameter holes drilled in the center of the electrode. Figure 2 shows the details of the continuous electrode and the electrostatic probes. The probe wires were held in place by epoxy which filled the space between the electrode and the wire and provided electrical insulation. The probes were mounted 0.127-m apart along the electrode as shown in Figure 3 which gives the dimensions of the probes and electrodes in metric units. Two types of probe experiments were performed. For the first set of measurements the probes were connected to the recording oscilloscope by means of coaxial cables which were terminated with the characteristic impedance of 50 ohms. For the later experiments the probes were connected to a 100-volt power supply. The power supply included a 5-microfarad condenser placed across the probe so as to provide a relatively constant current during the period of the pulse. This circuit is shown in Figure 4. The current was measured by reading the voltage drop across the two 50-ohm resistors connected from the probe to the electrode. These experiments were performed without an applied magnetic field since the objective was to make a measurement of the conductivity independent of the induced electric field.

Figure 5 shows probe traces taken in the first set of experiments with a magnetic field of 1.3 tesla. Traces are shown for four probe positions on the top electrode, which is the anode or negative terminal of the generator. The first probe is 0.045 m from the trigger electrode while the other probes are 0.127-m apart as shown in Figure 3. The times of arrival of the ionizing front at each location can be used to construct an X-t diagram if desired. In this case, with an initial pressure of 1 torr of helium, the velocity of the front is 12.5 km/sec. The vertical gain on each channel is 200 v/cm. With the generator connected to a 0.25-ohm load, the probe signal is only a fraction of the generator output voltage which is about 800 volts. Figure 6 shows comparable data taken as part of the second set of probe measurements in the absence of an externally applied magnetic field. There was a small amount of residual magnetism in the channel side walls, less than 0.015 tesla. The output signal shown in Figure 5 is due primarily to the flow of current from the probe to the electrode through the plasma surrounding the electrode. While it is difficult to deduce an absolute value for the conductivity for these measurements, they do indicate the relative conductivity of the various portions of the conducting plasma as it passes the probe position. Some measure of the conductivity of the plasma in close proximity to the electrode can be deduced from a calculation of an equivalent cell constant

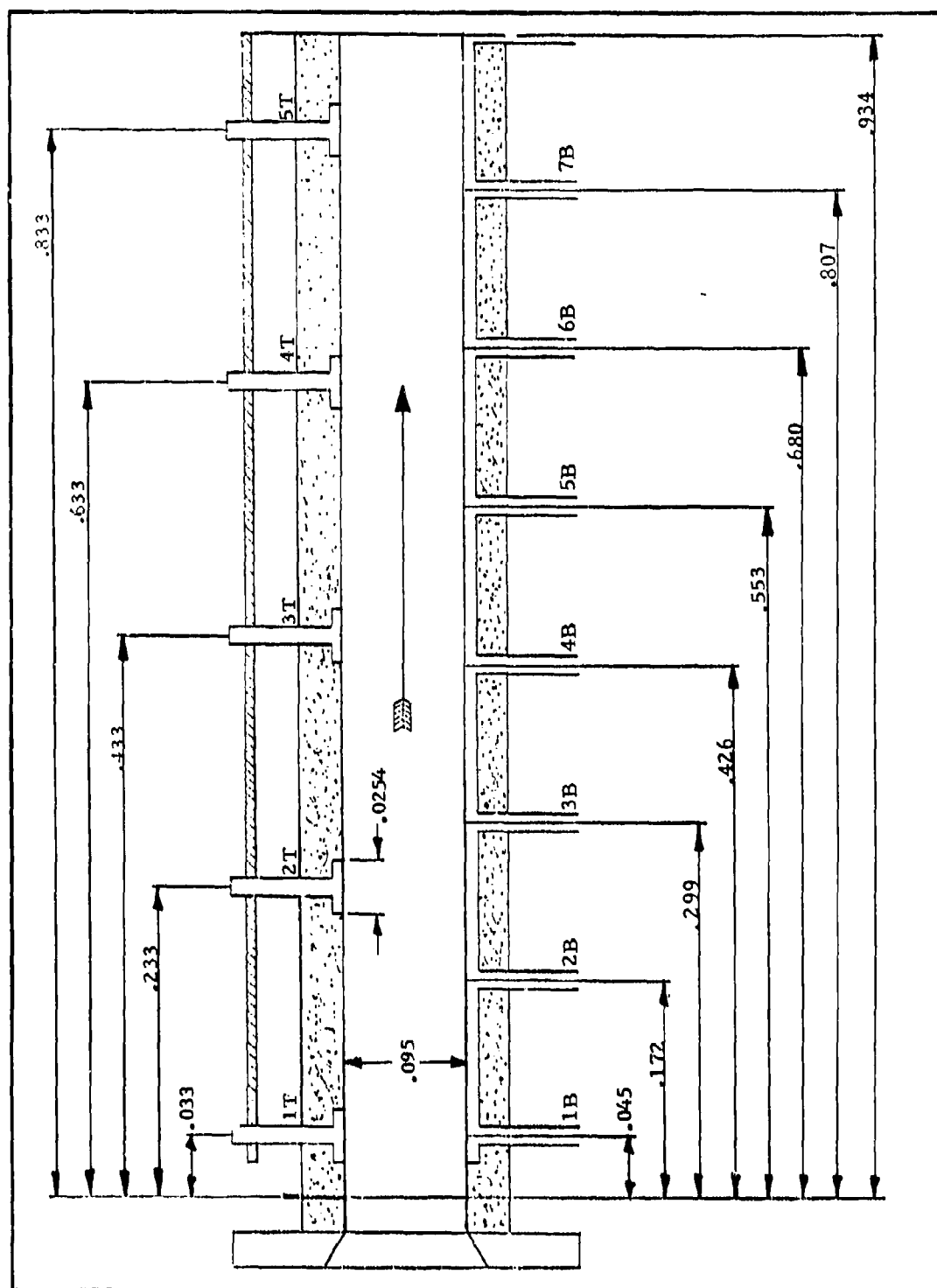


Figure 3. Arrangement of probes and electrodes used in segmented electrode experiments

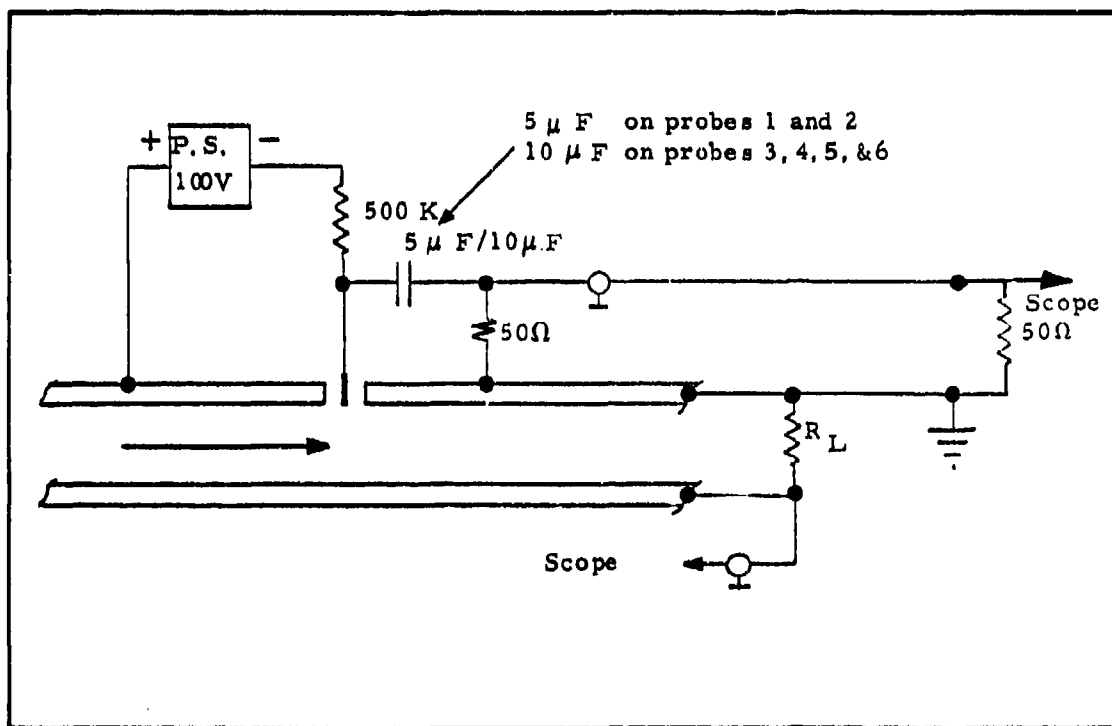


Figure 4. Circuit diagram showing power supply and capacitor connected to electrostatic probe in channel electrode

for the electrode-insulator-electrode geometry and from the measured conductance of the plasma circuit. The conductance can be calculated from the traces in Figure 6 and the known circuit parameters which are shown in Figure 4. If the plasma were infinitely conductive, the trace would be 100 volts in amplitude, which corresponds to the power supply voltage. A plasma resistance of 25 ohms would reduce the output to 50 volts. These traces show that the conductive slug has, for these levels of current density, a relatively uniform conductivity. Experiments which were taken with the segmented electrode channel (described later) show that when the generator is feeding a very low-resistance load, essentially short-circuited, the conductive region is much smaller. Figure 7 is an X-t plot showing the traces from Figure 6 arranged appropriate distances apart so that velocities of the front and rear of the conductive region can be determined. The velocity of the front determined by this method is the same at 12.5 km/sec as that by the other method. If we are somewhat arbitrary and choose the end of the "plateau" as the rear of the conductive region, we can deduce a velocity of 6 km/sec for that region. The data can be fitted with a linear relation to predict the size of the conductive region as:

PROBE 1

200 v/cm

PROBE 2

200 v/cm

5 μ sec/cm

PROBE 3

200 v/cm

PROBE 4

200 v/cm

10 μ sec/cm

Figure 5. Oscilloscope traces for electrostatic probes 1 through 4 installed in electrode (compare to Figure 6 in which the probes were biased to -100 volts)

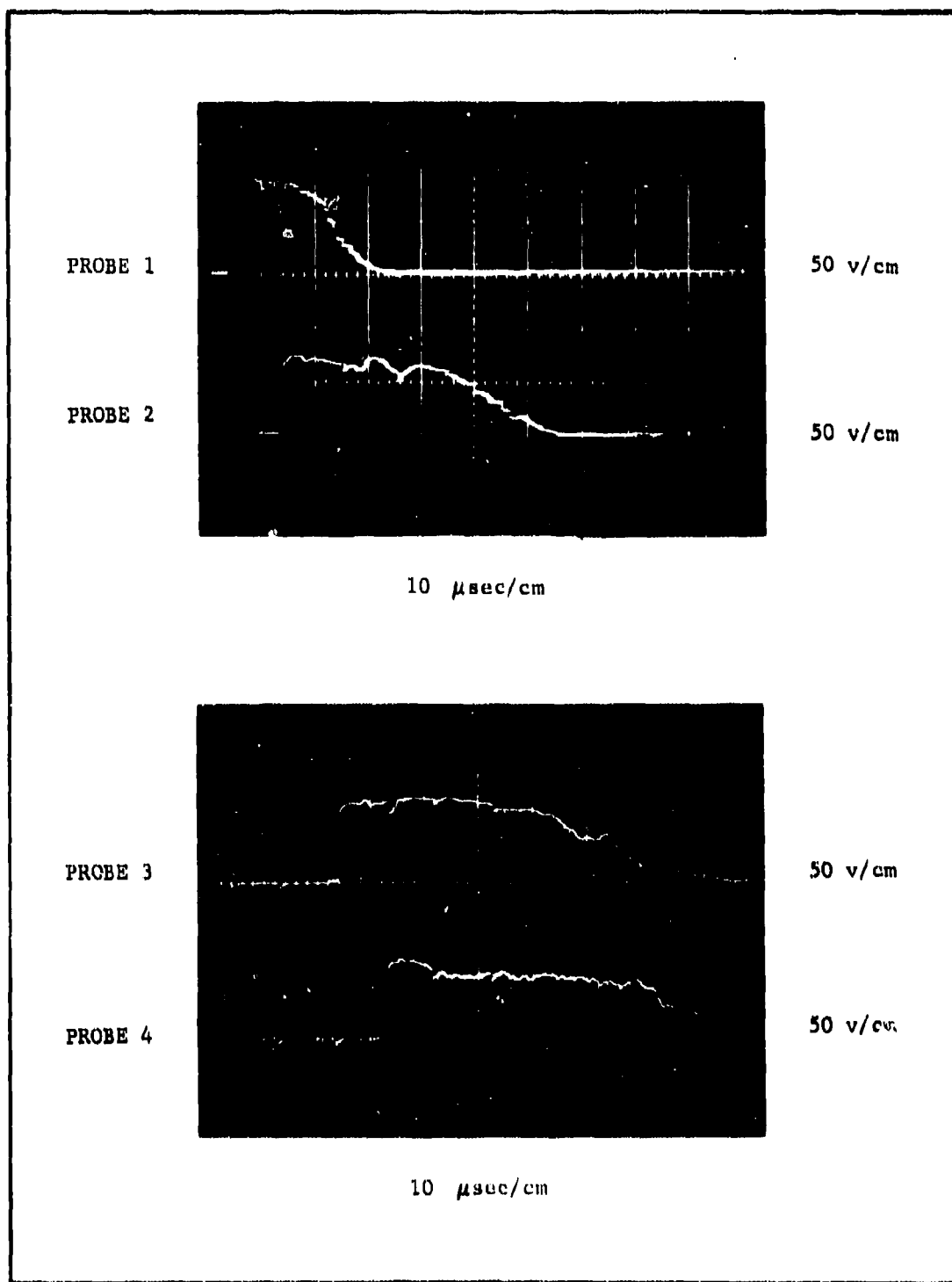


Figure 6. Oscilloscope traces for electrostatic probes 1 through 4 when biased to -100 volts with respect to the electrode

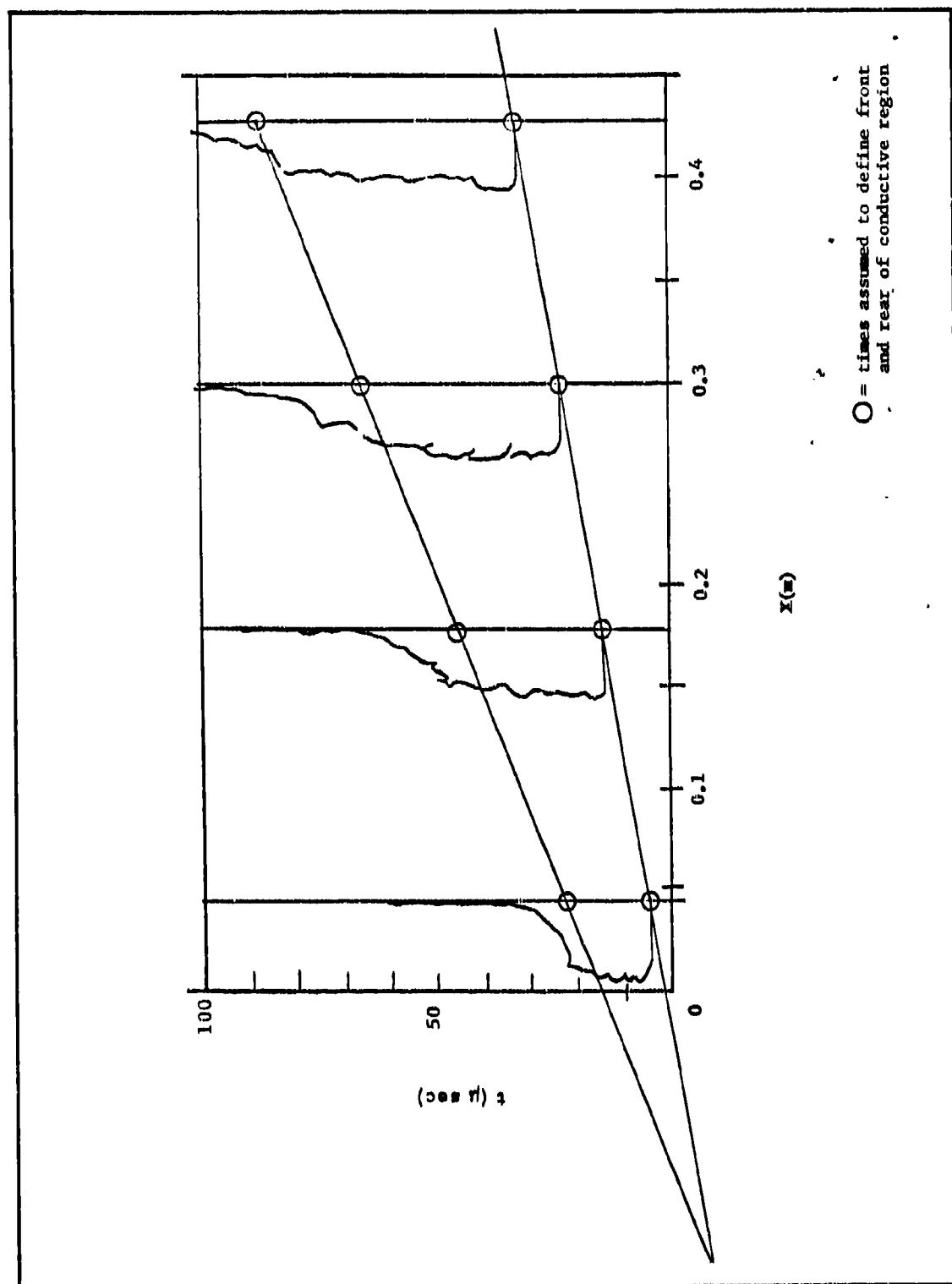


Figure 7. X-t plot showing traces from Figure 5 arranged at their respective distances from the trigger electrodes

$$s = \frac{(V_f - V_r)}{V_f} (X + X_0) \quad 1$$

where

V_f = velocity of the front of the conductivity region

V_r = velocity of the rear of the conductivity region

X = distance down the channel

X_0 = empirically determined constant which closely approximates the explosive charge to channel separation distance

For the traces shown in Figure 6, V_r is about one-half of V_f , and X_0 is about 0.14 m. Because of the complicated conical geometry of the charge, it is not known a priori where the plasma is generated. The value of X_0 cited above places the origin of the plasma within the conical section of the charge.

Having determined the size of the conducting region, several experiments were conducted to determine whether its size could be modified by changes in the geometry, the charge seed level, or the placement of the seeding within the charge; so that shorter pulses could be produced. Table I lists the various charge and seeding configurations and the length of the pulses seen at the six probe stations along the channel. The standard charge and seeding configurations used in the power generation experiments are two 7.5-gram pressed RDX conical charges seeded with 200 mg of cesium picrate seed per charge. These charges are designated as Type 20B. It is seen from Table I that if the amount of seed per charge is reduced (Cases 1, 2, and 3) that the length of the conductive region can be reduced. By firing only one charge it is seen that the width of the conductive region is smaller with the same quantity of seed (compare Cases 3 and 4). The shortest pulse lengths occurred when using a flat-front charge of HMX explosive seeded with 50 mg of cesium picrate (Case 7). It should be noted that the 20B charges are manufactured with a 60-degree conical internal cavity.

In the majority of the experiments the cesium picrate was distributed uniformly around the inner surface of the cone. Experiments were conducted wherein 50 mg of cesium picrate were placed at the apex of the cone, and in another set of experiments the cesium picrate was suspended on acetate film in front of the charge. Squeezing the cesium picrate into the apex of the cone was not satisfactory in that the probe signals were very small and the output voltage trace was unusual, not reaching the peak value of 600 volts until 20 microsec after the start. With the flat-front charge, a peak voltage of 800 volts was achieved in about 8 microsec. The magnetic field was the same for both shots.

TABLE I
CHARGE AND SEEDING CONFIGURATIONS

Case No.	Charge Configuration	Seed Level (mg)	Pulse Lengths (microsec)					
			1	2	3	4	5	6
1	2-20B	20	20	44	56	65	83	104
2	2-20B	100	18	35	53	53	70	88
3	2-20B	50	16	36	54	54	72	96
4	1-20B	50	13	15	26	26	38	64
5	1-20B	25	14	20	no trace	24	32	48
6	1-20B	0	20	24	12	10	no trace	24
7	1-HMX FF	50	14	18	28	32	40	48
8	1-20B	50 in apex	11	10	no trace	18	36	56
9	1-20B	50 on film	30	31	26	20	36	64

When the seed was held on the acetate film, the pulse length was much longer; however, at the third and fourth probe stations the pulse length had shortened to values appropriate for the number of charges and quantities of seed used. The pictures of the signal from the probes downstream from that point are undistinguishable from those associated with a normal shot.

For alternating current power generation, we may conclude from the measurements conducted that, (1) The flat-front charge geometry offers the shortest pulses, (2) single charges should be used, and (3) the seed levels should be held reasonably low. The feasibility of using bulk seeded charges in the explosive-driven MHD channel has also been investigated in a company-funded program. It was found that surface seeding is preferred for most applications.

b. Segmented-Electrode Experiments

Figure 3 shows the arrangement of the electrodes used in these experiments. The upper electrode is segmented into six separate parts, each 0.025-m (1 in.) long. The electrodes are spaced on 0.2-m centers. The bottom electrode was continuous and retained the probes reported in paragraph 2. The electrodes were connected to a bus bar which was connected to the external load. Provision was made for installing a current pickup loop around each of the connections to the electrode segments so that the current in each segment could be measured independently of the total current flowing in the system. The basic calibration of the current pickup loop integrator combinations, which were almost identical, was 9.3 kiloamp/volt of output signal. Passive R. C. integrator networks with a 1-ms time constant were used on all channels. With the external bus bar arrangement it was possible to place the load at a number of points up and down the channel.

The first set of experiments involved measurements of the generator open circuit voltage with the segmented electrode configuration. The magnetic induction was 1.3 tesla. Shots were made with single 20B charges seeded with 50 mg of cesium picrate (See Figure 8) and 200 mg of cesium picrate (See Figure 9). In Figures 8 and 9 it is seen that the first and second electrodes generated pulses approximately 800 volts in amplitude. The open circuit voltage pulse from the third electrode is somewhat reduced, presumably due to a drop in the magnetic field which ends at the position of the fourth probe, close to third electrode (See Figure 3). The results obtained with the 50-mg seed level show much cleaner pulses than those obtained with the 200-mg experiment. These measurements validate the conclusions drawn on the basis of probe measurements that the effective size of the conductive region is smaller for the lower seed levels. It may be noted that for this set of experiments the channel was filled to 1-mm initial pressure with sulfur hexafluoride. Experiments during the probe measurements had shown that voltage breakdown could occur in the channel ahead of the conductive region and that internal circulating currents could bypass the external load. To get reproducible data, it was necessary to reduce the magnetic field from its normal value of 2.3 tesla to 1.3 tesla and to introduce sulfur hexafluoride, which, as an electronegative gas, proved to be an effective insulator. Previous measurements had shown that the presence of the sulfur hexafluoride initially in the channel did not markedly affect the power generation capability.

For the second set of experiments the channel was connected to a low-inductance, one-turn primary coil which had a five-turn secondary (Figure 10). Typical oscilloscope traces from this experiment are shown in Figure 11. The top trace (Figure 11(a)) is the voltage across the primary of the transformer. Figures 11(c) and 11(d) show the currents through the various electrode segments (See Figure 7). Figure 11(b) shows the current through the transformer primary as the upper trace. It can be seen that the currents from the individual electrodes add with very little circulating current. Figure 12 shows traces from an identical experiment,

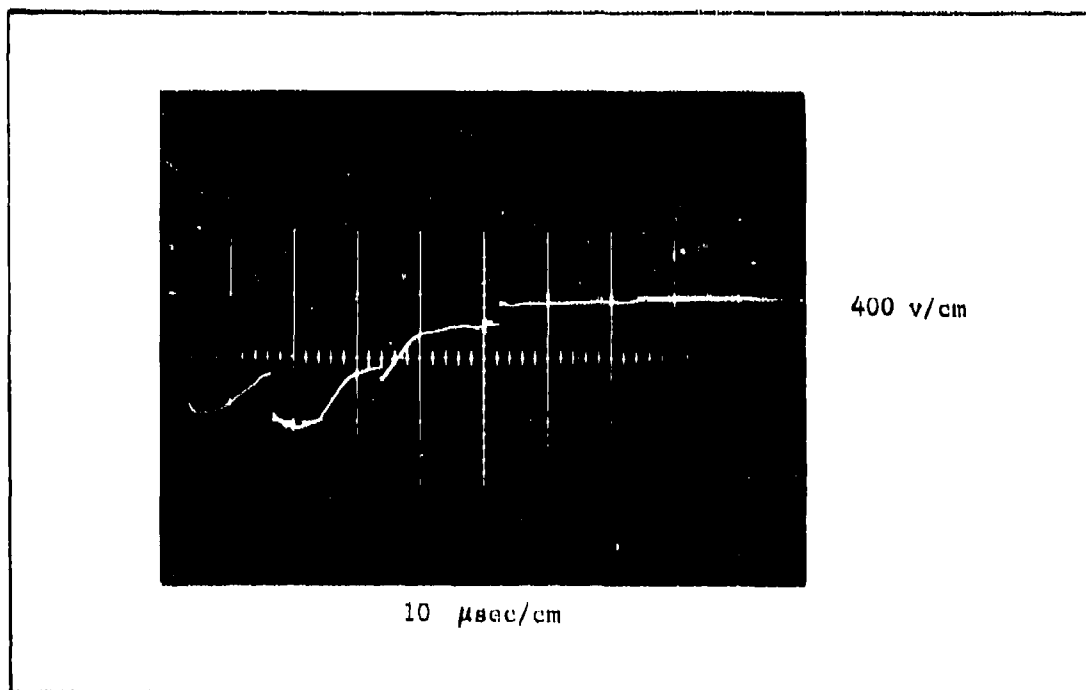


Figure 8. Oscilloscope trace showing open circuit voltage of segmented electrode generator (50 mg of cesium picrate)

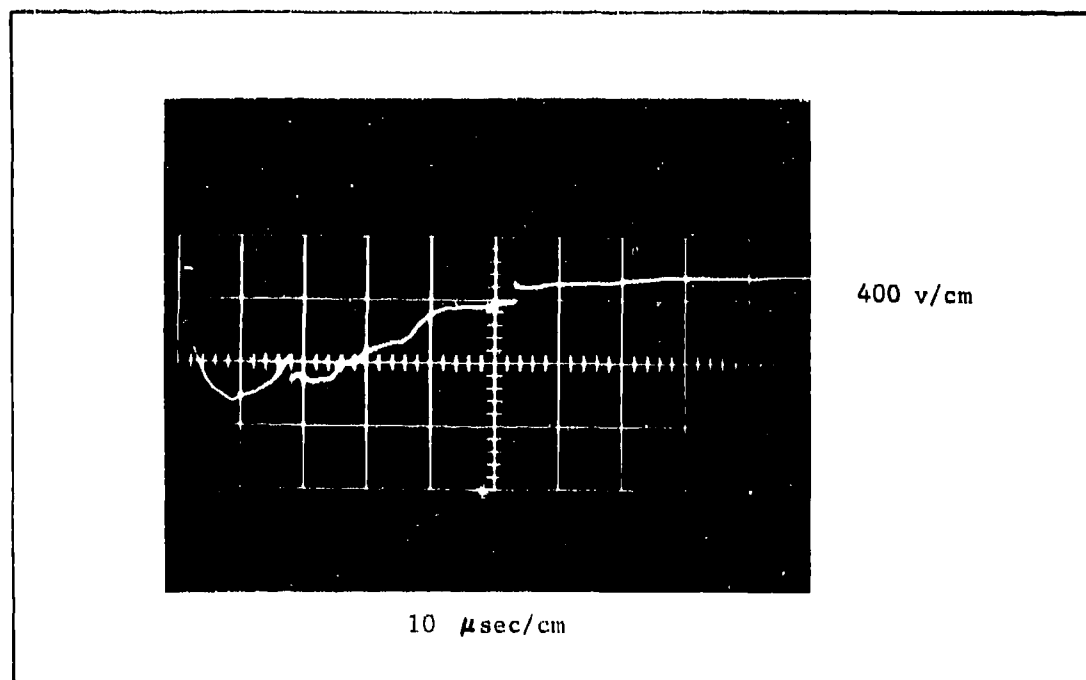


Figure 9. Oscilloscope trace showing open circuit voltage of segmented electrode generator (200 mg of cesium picrate)

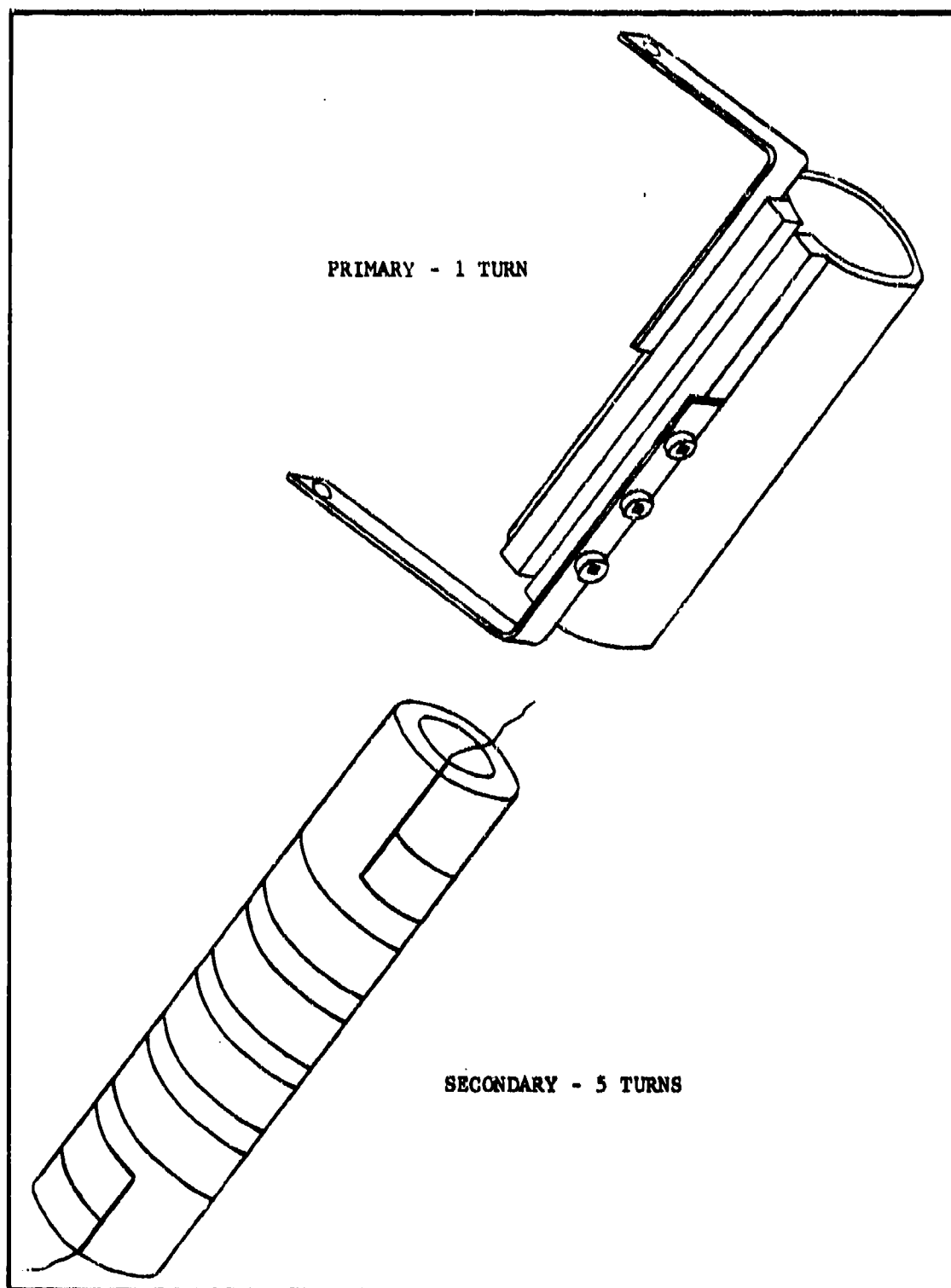


Figure 10. Exploded view of output transformer showing single-turn primary coil and closely coupled secondary

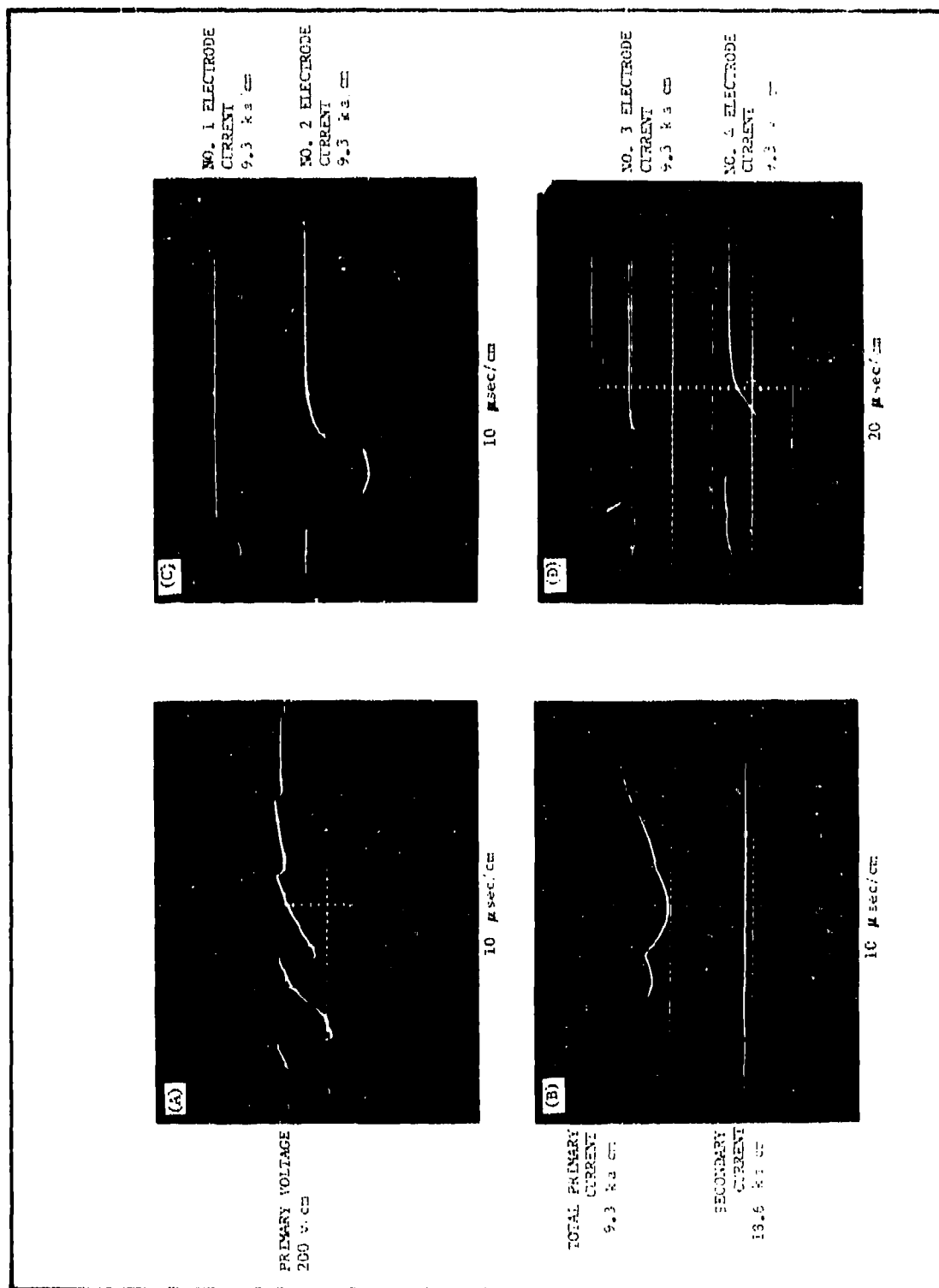


Figure 11. Oscilloscope traces from segmented electrode experiment with one-turn primary

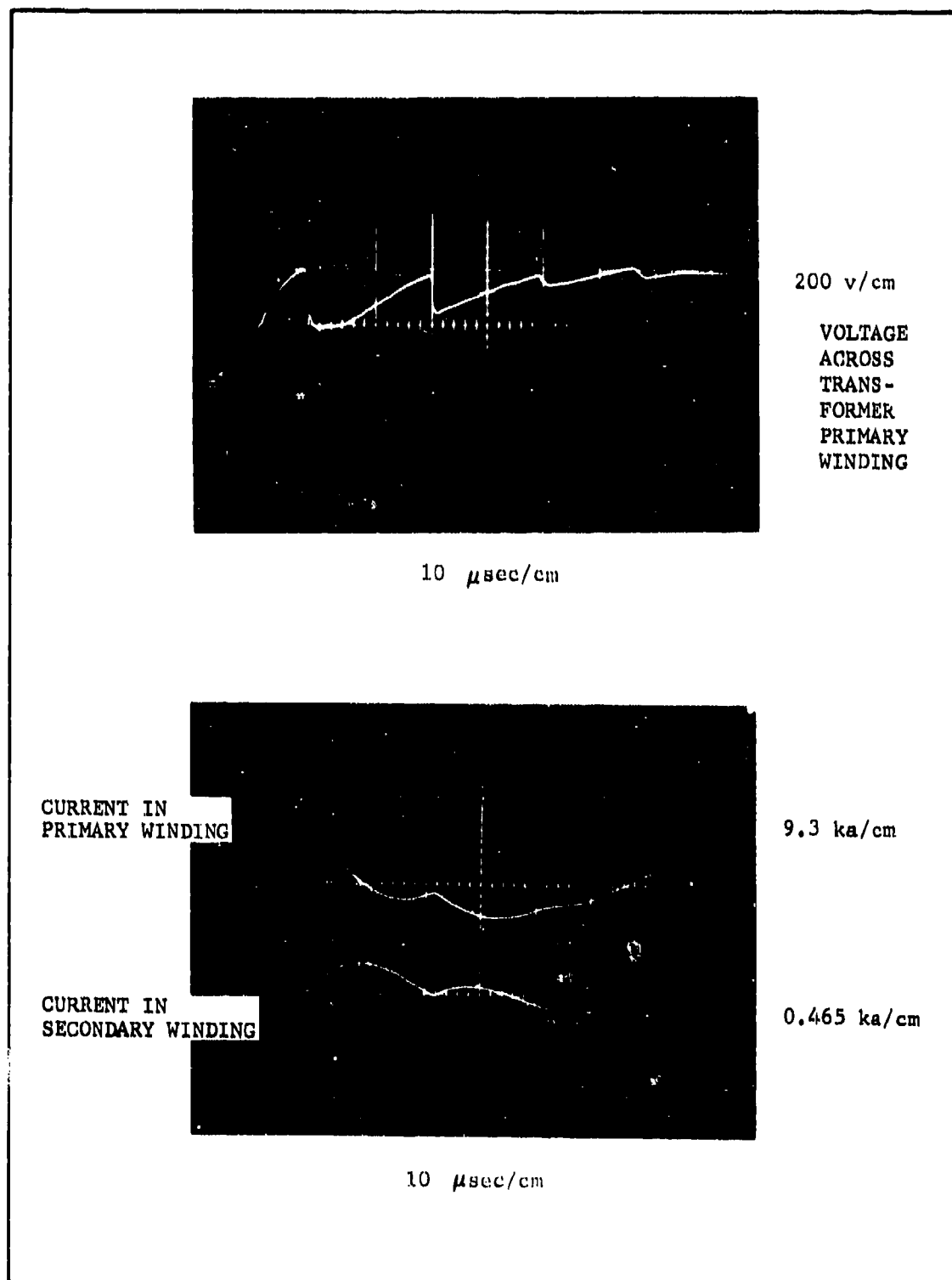


Figure 12. Oscilloscope traces from segmented electrode generator experiment

with the exception that the gain on the secondary current measurement was 0.05 v/cm, which would correspond to 465 amp/cm, instead of 2.0 v/cm as in the lower trace of Figure 11(b). It is seen that the coupling in this transformer is not exceptionally good.

3. Transformer Tests

To investigate the feasibility of generating high-voltage pulses, another transformer was constructed with a variable number of turns or taps on the primary. This transformer is shown in Figure 13. The secondary of the transformer was fixed at 50 turns which produced a secondary inductance of 126 microhenry and a resistance of 0.42 ohms. By connecting the channel to various taps on the primary, the turns ratio, N , could be varied over a wide range. The following tabulation gives the number of turns in the primary when the generator was connected to the terminals indicated, the turns ratio, and the inductance of the primary:

<u>Terminals</u>	<u>Primary Turns</u>	<u>Turns Ratio</u>	<u>Primary Inductance (microhenry)</u>
1-2	4	12.5	2.55
1-3	7	7.14	5.3
1-4	14	3.57	14.0
1-5	22	2.28	25.8

The transformer tests were of three general types: turns ratio experiments, resonance experiments, and loading experiments. The turns ratio experiments demonstrated that the output voltage increased with the turns ratio up to outputs of a 4 kv, and remained constant thereafter suggesting that breakdown was occurring. The primary current increased with the turns ratio, indicating that the current was being limited by the load resistance in the secondary as would be expected.

For the resonance experiment, the 12.5 to 1 turns ratio configuration was used and the secondary of the transformer was tuned with a capacitor to resonate at the generator fundamental frequency of about 55 kHz. When driving the resonant circuit, outputs up to 20 kv were observed; however, there was some evidence for breakdown in the secondary circuit which would terminate the pulse after a few cycles. If the resonant frequency was not exactly matched to the mechanical commutation frequency, it was possible to drive negative currents in the generator for part of a cycle. Because of the fact that the size of the detonation product slug changes with distance along the channel, it was not always possible to keep the mechanical commutation in phase with the electrical oscillations which were determined by a fixed inductance and capacitor. Electrical oscillation frequencies below the initial mechanical commutation frequency seem to be preferred.

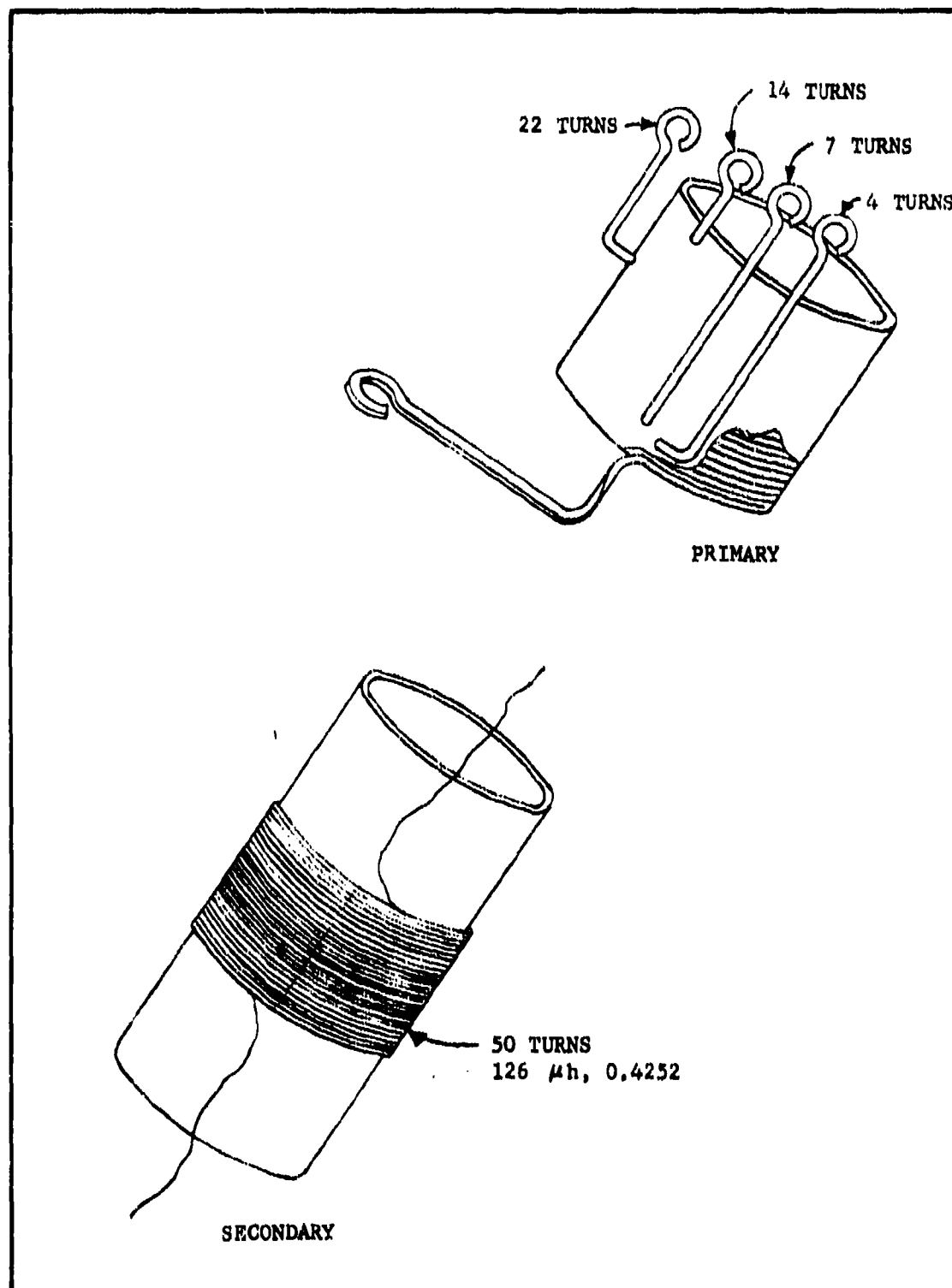


Figure 13. Exploded view of multiple-turn transformer

A series of tests was conducted wherein the secondary was loaded with various resistances. These measurements, which are summarized in Figure 14, show that loading of the secondary did not appreciably load the primary. However, it may be seen that loading the secondary with 50 ohms would have reduced the output by about 1/a. For a turns ratio of 12.5, this is equivalent to a load of about 0.330 ohms in the primary. From other experiments we know that when the generator is feeding a load of 0.250 ohms, its output voltage is reduced by about 12 percent, which is consistent with the 10-percent reduction in primary voltage we would observe in this experiment if we had used 50 ohms in the secondary. We have thus confirmed the predicted result, that the generator impedance transforms as the square of the turns ratio. Techniques exist for achieving much lower generator internal impedances than were observed in this experiment (1).

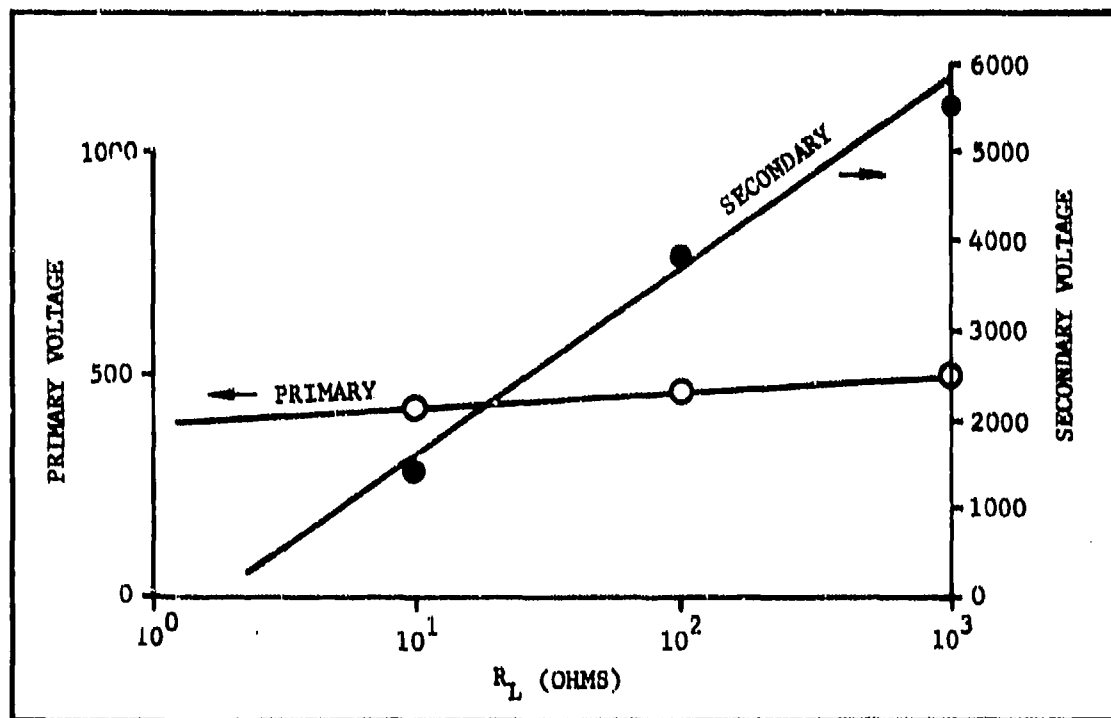


Figure 14. Plot of transformer primary and secondary peak voltages as a function of the load in the secondary circuit

We can use the individual electrode current traces to make an independent estimate of size of the conductive region. Figure 15 shows an X-t diagram constructed from the traces shown in Figure 11. The front of the conductive region is designated as the time when the current starts to rise at a given electrode. The end of the highly conductive region is identified with the time of peak current which is the time when the current starts to drop. Presumably this would occur when the rear of the highly conductive region reaches the downstream side of the electrode. From these data, two X-t diagrams can be drawn: one for the front of the conductive region, and the other for the rear as shown in Figure 15. The velocity of the front is about the same as determined by the probe methods (11.8 km/sec). However, the velocity of the rear is much higher when determined by this method--approximately 9.3 km/sec. The origin of the plasma appears to be the same in both cases. These measurements suggest that the size of the conductive region is sensitive to the current density and that for very high current densities, the highly conductive region is much shorter than would be suggested by the probe measurements.

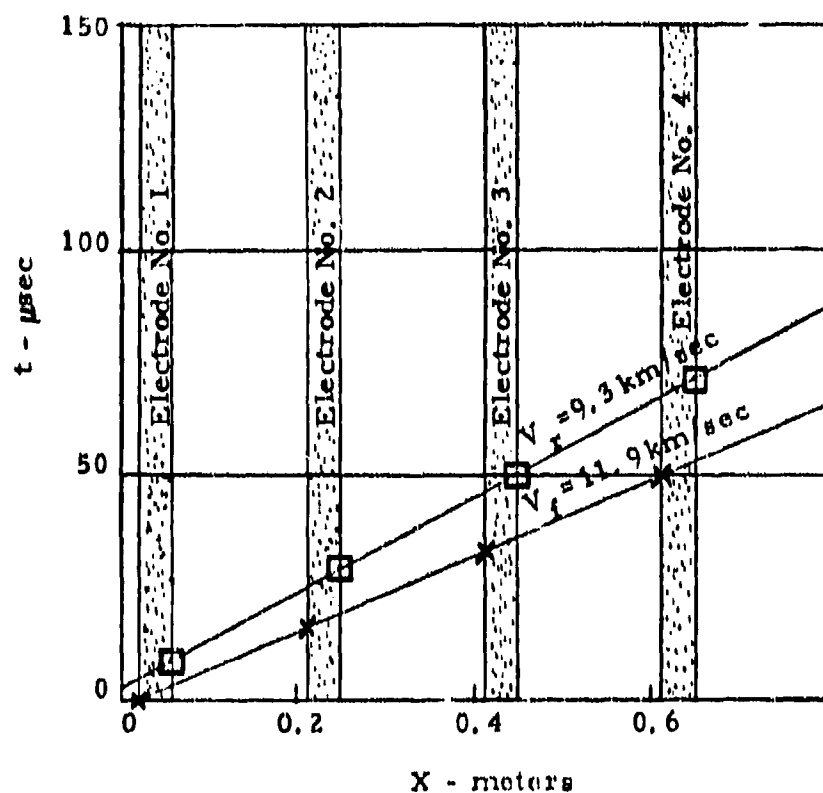
The model suggested by Equation 1 is still applicable, with the major difference that the velocity of the rear of the conductive region, V_r , is an apparent function of the current density. Presumably this is due to an axial distribution of conductivity within the seeded detonation product slug, suggesting that the current is concentrated in the front portion.

4. Conclusions

We have demonstrated that it is feasible to use mechanical commutation of the detonation products to produce high-frequency, alternating current pulses with an explosive-driven MHD channel. Alternating current has been generated in the frequency band between 55 and 60 kHz. While the system does have some limitations as far as frequencies which can be covered and spectral purity, it does represent an extremely simple and rugged device for generating megawatt or gigawatt pulses in this frequency range.

These studies have given added insight into the generation of plasmas with condensed explosives with the practical result that optimized seeding conditions for seeding charges for the generation of alternating current have been determined. These studies suggest that the plasma is formed from the seed material located in the middle-to-front portions of the conical charge, and that the flat-front charges produce a plasma region having a relatively narrow velocity distribution.

The probe measurements have suggested that the use of electrostatic probes along the electrode surface can yield some information about the structure of the detonation product conductivity at some distance from the point of detonation. This information can be supplemented by data showing the ability of the plasma to pass appreciable currents, which is a measure of the plasma conductivity in the flow channel proper. These probe measurements show that the plasma volume grows as the plasma moves



LEGEND

x = TIME OF CURRENT START

□ = TIME OF PEAK CURRENT

(VELOCITIES OF THE FRONT AND REAR OF THE HIGHLY CONDUCTIVE REGIONS ARE DETERMINED FROM THE SLOPE OF THE LINES)

Figure 15. X-t diagram time of current start and time of peak current in various electrode segments

away from the detonation point. It is expected that the increase in plasma volume is the element which allows the plasma conductance to remain fairly high for appreciable times after the explosion, even though the pressure and temperature are decreasing.

B. LOW-FREQUENCY ALTERNATING CURRENT POWER GENERATION

The objective of this phase of the program was to investigate the feasibility of generating a series of pulses at a rate of approximately 90/sec in the linear, explosive-driven MHD channel.

1. Background

Some of the interesting potential application areas for the explosive-driven MHD generator are in the production of a series of short, high-power pulses with a reasonably high-pulse repetition frequency. Typical examples would be in providing a pulse of electrical power to the output stage of a radar transmitter or to some sort of pulsed optical device or light source. If the total operating period during which the pulse train is required is of the order of 10^2 or 10^3 sec, so that the requirement is for 10^4 or 10^5 pulses between reloading operations, it may be advantageous to use the explosive-driven MHD generator in place of conventional energy generation and storage systems. It appeared desirable, therefore, to determine if there was any fundamental limitation on the use of a repetitively pulsed linear channel for such applications.

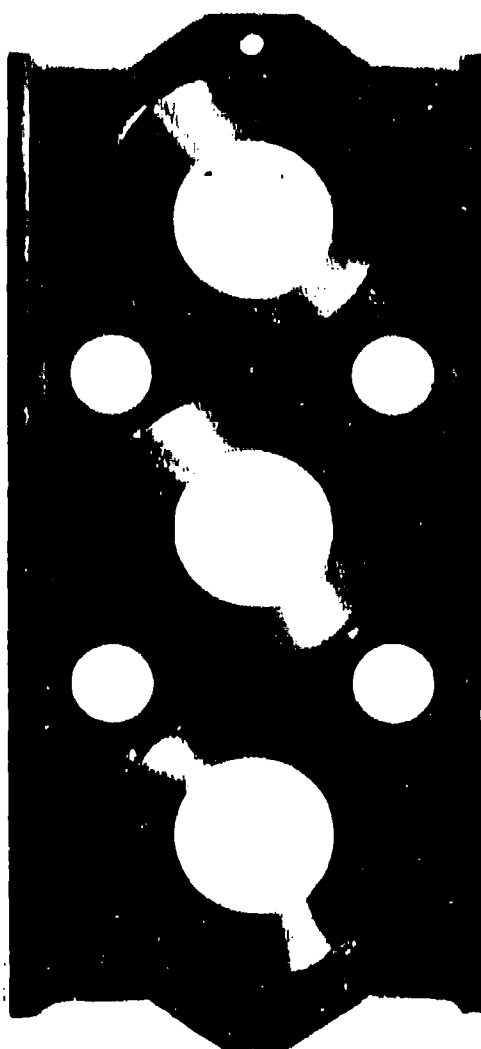
The objectives established for this investigation were that the system should be capable of providing a series of pulses at the rate of 90 pulses/sec with the output in the range of 1 kilojoule per pulse. Three pulses were selected as the minimum number which would adequately demonstrate that the quasi-steady-state operation could be established. It would have been desirable to demonstrate a longer series of pulses; however, the problem of feeding three explosive charges was formidable enough without having to develop, proof test, and qualify a cartridge and a continuous-feed mechanism. While high-feed-rate mechanisms have been developed for electrically fired aircraft cannon, these cartridges contain a deflagrating material such as smokeless powder or a seeded propellant. For these gun-type systems the breech pressure is limited to a few kilobars (45,000 psi) where the pressures can be contained by conventional high-strength materials. With a detonating explosive the pressures are of the order of 200 kilobars (3 million psi), and all materials suffer plastic deformation at these levels. Therefore, conventional breech and cartridge procedures are not suitable for use with detonating explosives, especially in a system designed for repetitious operation. Consequently, some exploratory work was required in the development of a new type multiple-charge feeding mechanism. Several intermediate approaches could be suggested (a series of static ports each containing a charge, a rotating wheel, etc); however, it was desired to develop a multiple-charge feeding mechanism which had growth potential. The paragraphs that follow describe the multiple-charge feeding mechanism which was finally developed and the multiple-pulse experiments which were conducted in the linear channel.

2. Apparatus

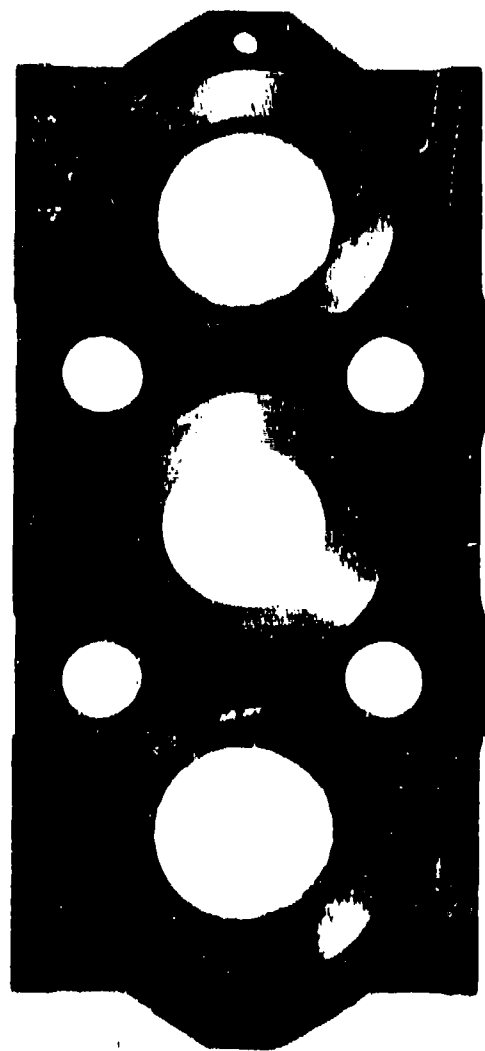
There were two major design problems which had to be solved: Development of a suitable charge holder which would transport the undetonated charges past the channel opening with the required frequency, and development of a mechanism which would provide some measure of safety to protect the undetonated charges. The two problems were somewhat interconnected, since the power required to drive the feeding mechanism and its complexity are related to the weight and size of the charge holder.

Previous experience in firing the explosive-driven MHD channel had shown that if the charge were given sufficient standoff from rigid metallic surfaces the charge could be contained with only minor surface damage to the containing vessel. The detonation products have a specific heat ratio, γ , which is approximately 3.0 in the detonated condensed state so that the pressure drops rapidly as the detonation products expand. As the detonation products expand, γ decreases toward unity, but the important factor is that the pressures are drastically reduced when the detonation products have expanded to several times their original volume. This fact was exploited in the design of a carrier for the explosive charge which is shown in Figure 16. The charge carrier on the left is shown in the "as manufactured" condition while the charge carrier at right, which is covered with soot, has had charges fired in each of its end positions. Some slight enlargement of the hole may be seen when compared to the unfired center position. The charge carriers were used for up to five shots before replacement. The charge was spaced away from the sides of the holder by means of a low-density polyurethane foam, as shown in Figure 17. A procedure was developed wherein the charge was held in place in a jig and the polyurethane was cast in the space between the charge and the holder. The elements of the explosive train (blasting cap and the primacord) were also embedded in polyurethane for protection. The internal details of the charge carrier and charge are shown in Figure 18. The front of the charge, which was protected by the holding fixture jig during assembly, was accessible after casting for placement of the cesium picrate seed.

One of the first problems to be faced was the matter of how close together the charges could be placed on any transport mechanism. If the charges are placed too close together, they may either be detonated sympathetically or damaged physically. To some extent, the mounting of the charges in the polyurethane foam insulates the adjacent charges from the shock transmitted through the charge carrier holder. In addition, the RDX explosive is rather insensitive; however, some of the elements in the explosive train may not be as insensitive. Another problem to be faced was that blast from one charge might force the adjacent charge out of position so that when it was fired it would not be pointing down the channel, or the blast might disrupt the initiation system. To test the several charge holder designs which had been developed, a series of tests was conducted in a large vacuum tank. The charges were mounted in the charge carrier as shown in Figure 17 and were suspended in the tank while



"AS MANUFACTURED"
CHARGE CARRIER



CHARGE CARRIER THAT HAS HAD
CHARGES FIRED IN EACH OF ITS
END POSITIONS

Figure 16. Explosive charge carriers

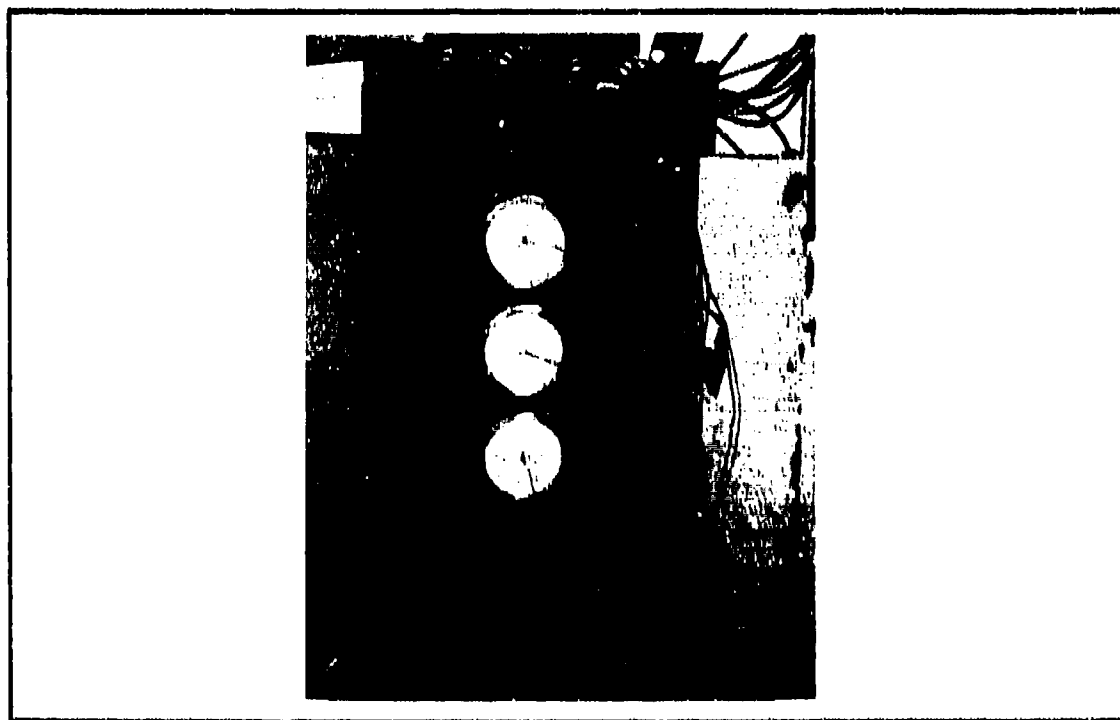


Figure 17. Charges in carrier with polyurethane foam

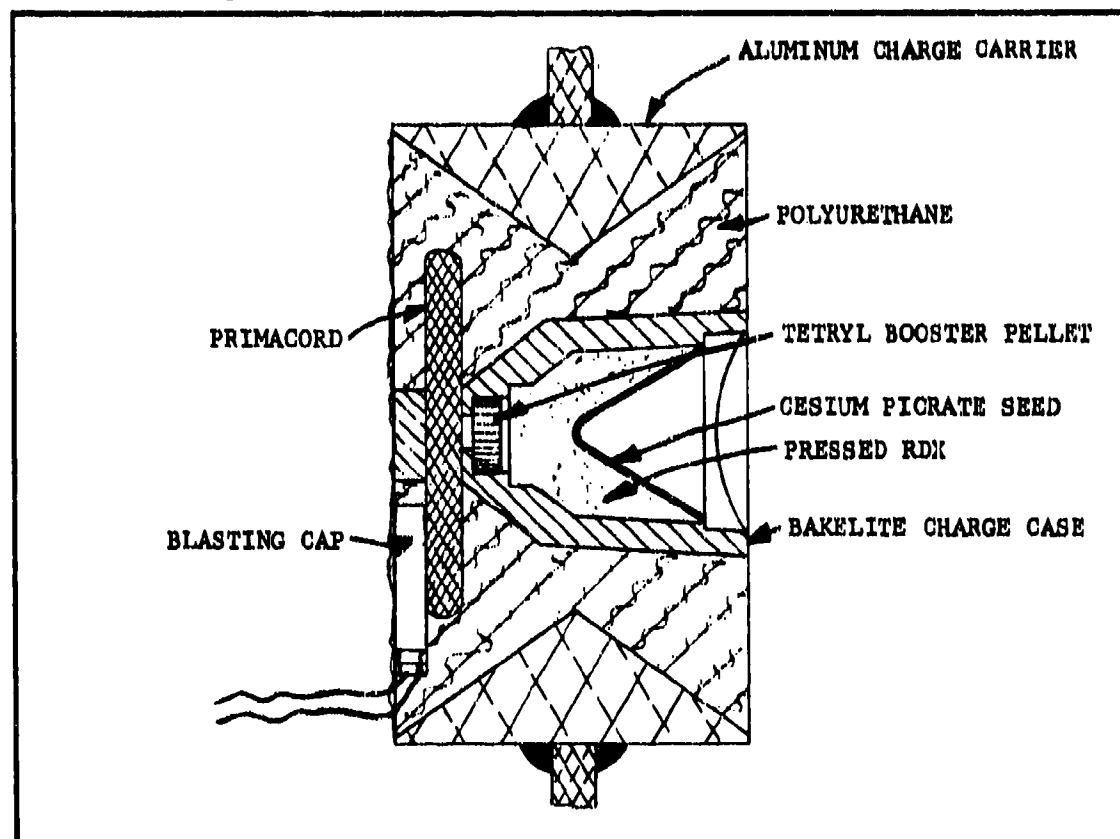


Figure 18. Charge carrier and explosive train

the tank was pumped down to a few millimeters of pressure. By firing at a reduced pressure, it is possible to avoid the air blast effects and to determine if sympathetic detonation would occur. At pressures of the order of a few torr, the charges could be detonated one after another, which indicated that the charges were still intact and that the blast had not torn off the wires leading to the blasting cap of the adjacent charge. The pressure was then increased to approximately one-half atmosphere and repeated in a satisfactory manner. Tests at higher initial pressure resulted in some physical damage to the adjacent charge.

Having fixed the charge separation at 4 in., a mechanism was then designed which was capable of moving one charge past the firing position every 11 ms, which would correspond to a 90 pulse/sec, pulse repetition frequency (PRF). Several basic mechanisms were considered, both linear and rotary. The rotary mechanisms were discarded because of the high angular velocity that would have to be obtained and because of the fact that there was little growth potential in developing a mechanism capable of firing a large number of pulses without stopping to reload. In principle, with a linear mechanism, the charge holders could be connected together in a fashion somewhat analogous to the way cartridges are now linked together and fed. With such a mechanism a very large number of cartridges could be fed continuously from a magazine to the entrance of the MHD channel at the prescribed feed rate.

For simplicity, a pneumatic piston was selected to drive the aluminum charge carrier shown in Figures 16 and 17 past the channel entrance. The principal details of this piston mechanism are shown in Figure 19. The mechanism selected was an air-driven actuator with a shaft out of each end of the cylinder from the piston. In operation the shaft is restrained by the release mechanism, and the chamber on the upper side of the piston is pressurized to pressure P_1 which may be 10 or 20 atmospheres. The lower chamber pressure, P_2 , can either be above or below atmospheric. When the top of the shaft is released, the piston forces the shaft downward moving the charges past the entrance of the channel. A cam on the upper shaft actuates microswitches which are used to trigger capacitor discharge firing circuits for each of the blasting caps as that particular charge passes the center of the channel. During the 100 microsec or less taken for the circuits to fire the blasting cap, the charge moves approximately 1 mm at maximum velocity. The air in the bottom part of the piston is compressed during the downward motion and forms a cushion which stops the motion of the piston and the charge carrier before the bottom of the cylinder is reached. By adjustment of the initial pressures, P_1 and P_2 , it is possible to drive the charge holder with an approximate sinusoidal motion. Figure 20(a) shows a theoretical plot of pressures P_1 and P_2 and their difference (which is the driving pressure) as a function of the piston displacement. Figure 20(b) shows a plot of the system velocity as a function of displacement for a typical condition. The firing points are indicated by circles.

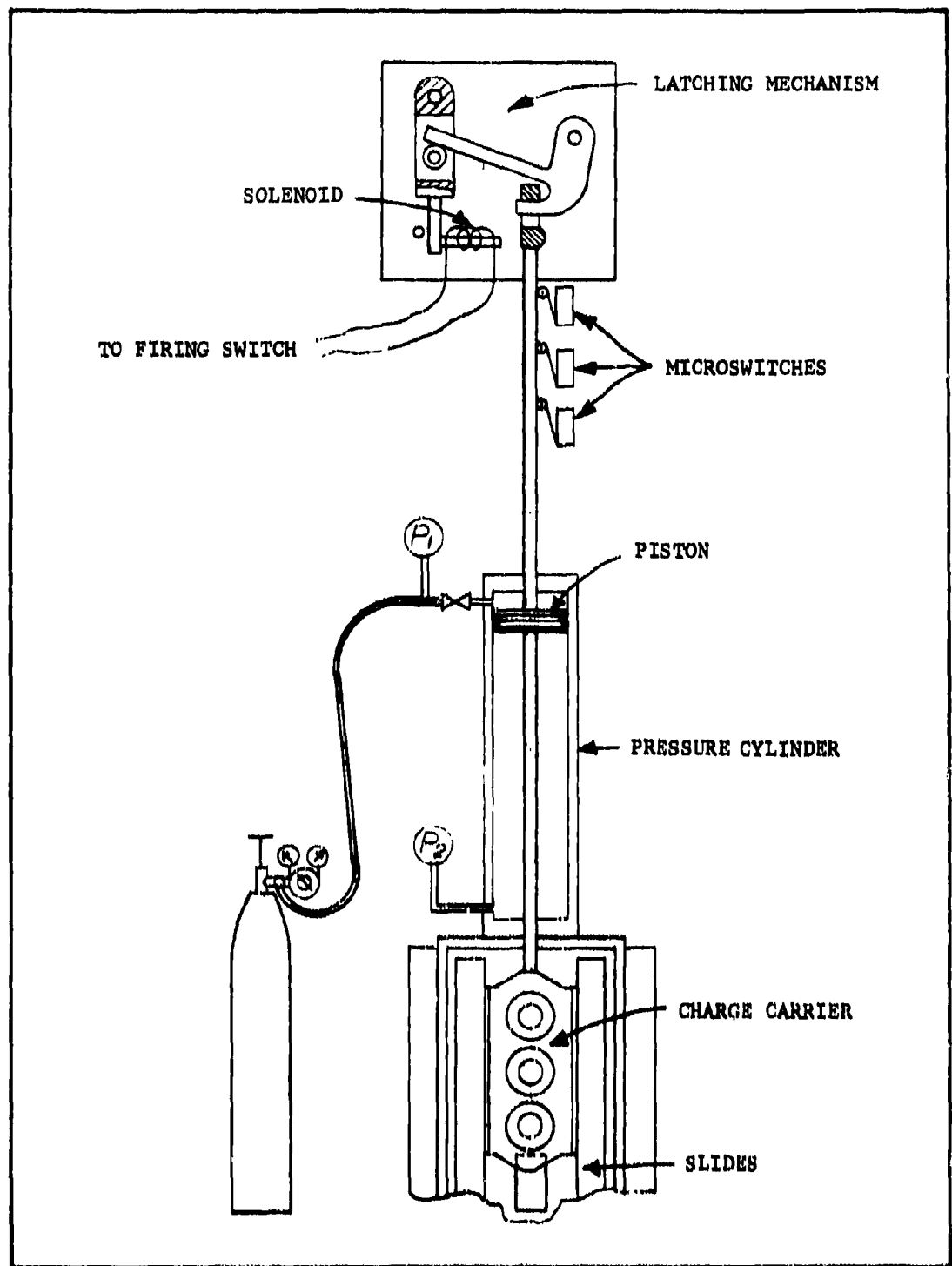


Figure 19. Pneumatic piston mechanism

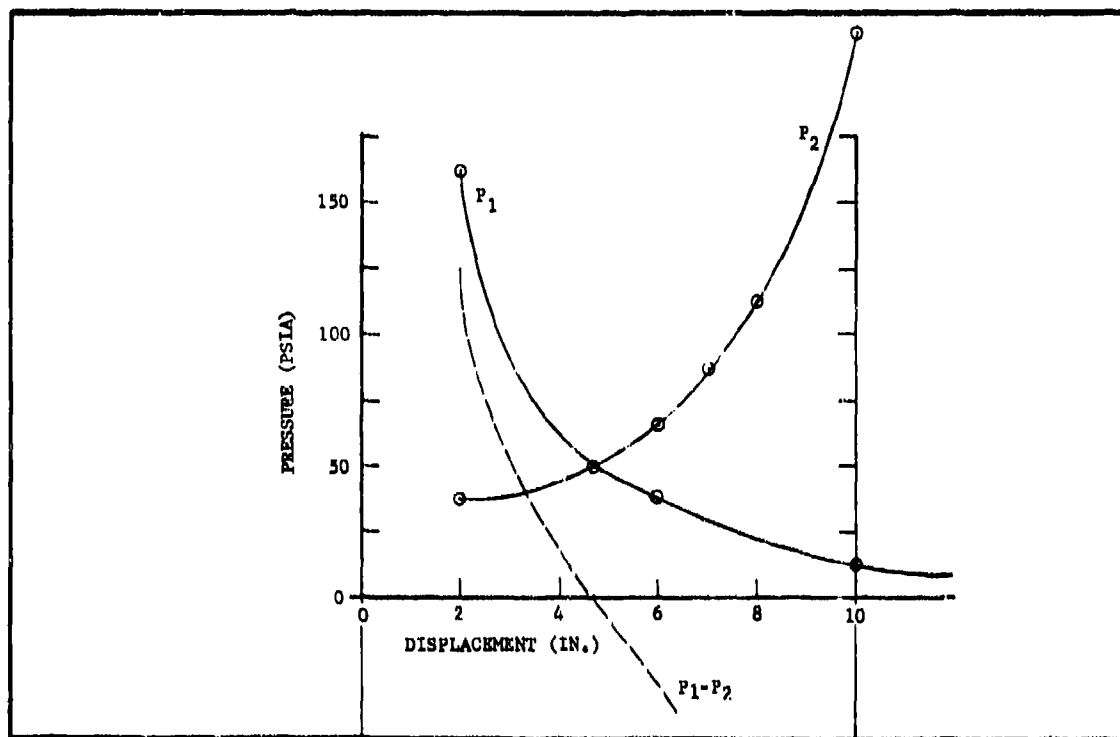


Figure 20(a). Theoretical plot of pressures P_1 and P_2 as a function of piston displacement (dotted line)

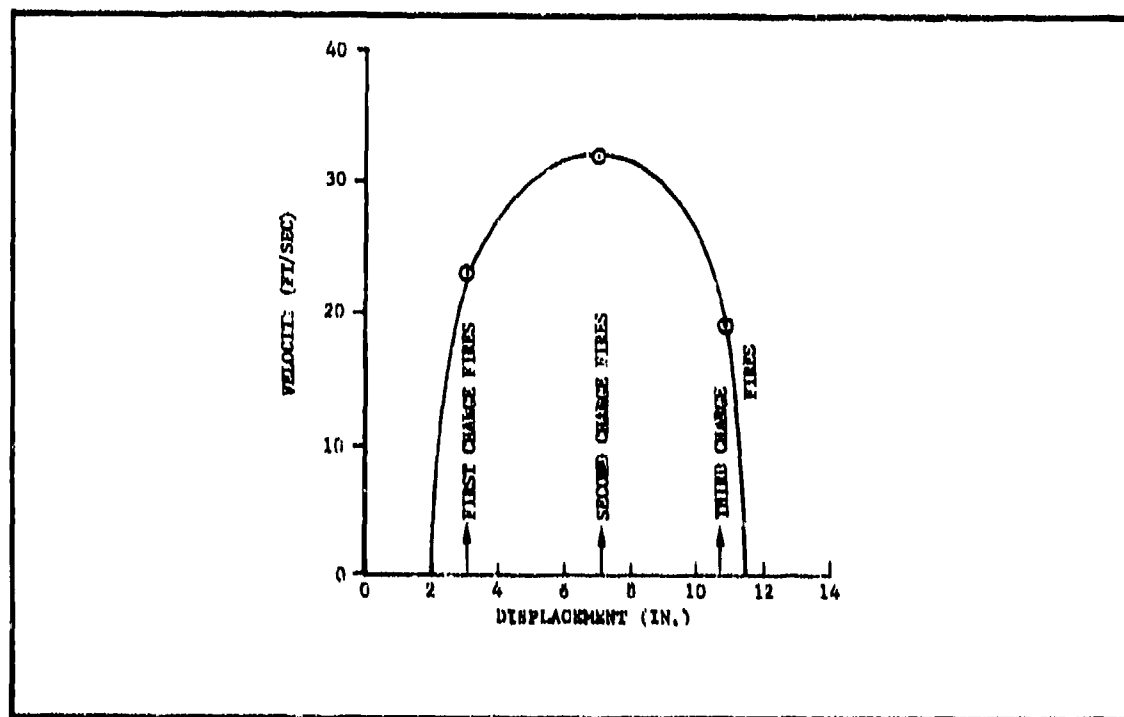


Figure 20(b). Plot of system velocity as a function of displacement (firing points indicated by circles)

One of the key elements for the design of the piston system was the latching mechanism which would allow a load of several thousand pounds to be released in a reproducible, reliable manner by a small solenoid. The elements of this mechanism are shown in Figure 19.

As cited above the object of the piston system was to accelerate the charge carrier rapidly so as to transverse the charge separation distance within the prescribed time and yet bring the mechanism to a stop before it strikes the bottom. Figure 21 is an oscilloscope trace which shows output of a photodiode used to sense when the charge holder was in one of the firing positions. The signal was obtained by placing strips of tape across the charge holders in such a manner that light from a source inside the channel would only pass at the time that each respective charge carrier passed through the firing positions. The light pulses are approximately 11-ms apart which indicates that the displacements and velocities required for the 90 pulse/sec repetition rate had been achieved. As shown in Figure 20(b) the first pulse occurs shortly after the charge holder has started its motion. The second pulse occurs at the time of maximum velocity, and the third pulse occurs close to the end of the stroke. The bottom trace in Figure 21 is the combined output from the three firing circuits. As shown in Figure 19, the firing signals are derived from cam-actuated microswitches which are deflected by the head of the piston rod as the assembly moves downward. Actuation of the microswitch fires a silicon-controlled rectifier (SCR) which discharges a capacitor charged to 300 volts through the blasting cap. The light pulses shown in Figure 21 after the first three firing pulses are due to oscillations of the charge carrier about the bottom firing position as its motion is damped out and it approaches an equilibrium position where the pressures are balanced.

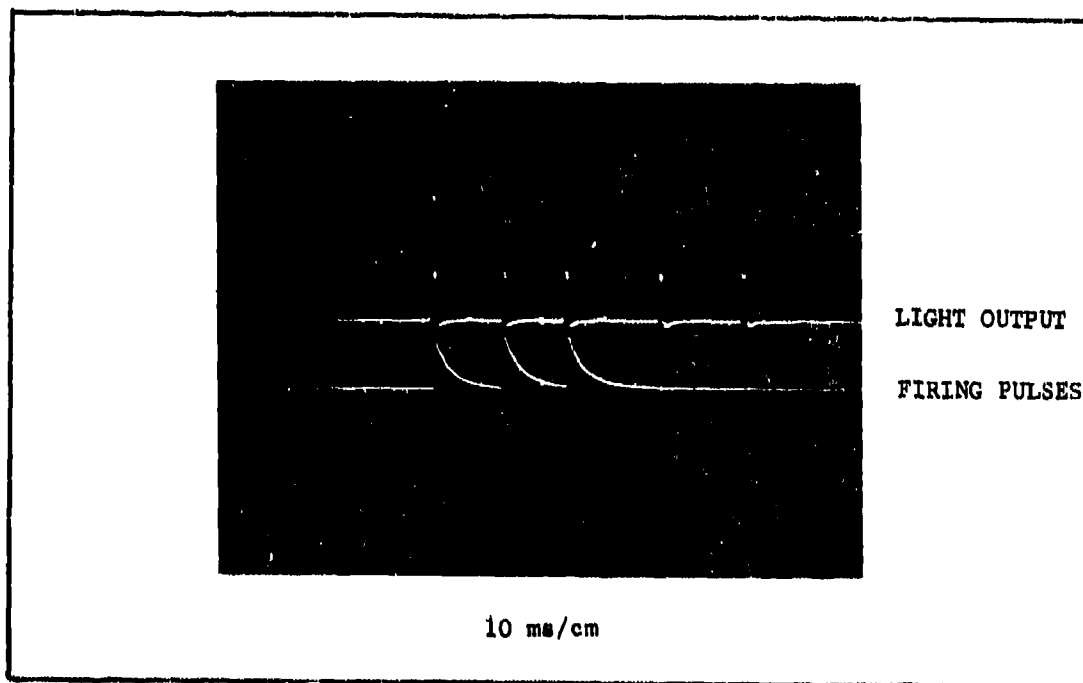


Figure 21. Oscilloscope traces showing photodiode output indicating charge carrier locations

3. Experimental Work

The apparatus was tested first by firing single charges in the various ports of the charge carrier to test the triggering mechanism. The charges were fired at the approximate center of the channel and produced pulses of the magnitude expected for the 1.0-tesla magnetic field. The charge carrier was then tested with two and three charges in place with only minor mechanical damage to the charge holders. The first electrical test firing of the three charges into the channel was somewhat disappointing, both because of triggering problems and because it was not possible to record anything more than a slight voltage disturbance (5 to 10 volt output in place of the 800 volts expected at the times the second and third charges detonated).

It was necessary to change the oscilloscope trigger circuit to the blasting cap firing signal because the trigger electrode which is normally used in this type of experiment was now outside of the region containing the magnetic field. This occurred because it was necessary to move the channel entrance outside of the magnetic coil system to accommodate the firing mechanism and blast tank which would not fit into the magnet gap. This detail is shown in Figure 22.

The oscilloscope trace for a typical first pulse is shown in Figures 23(a) and 23(b). The delay at the beginning of the sweep is because of the time taken for the blasting cap to detonate after the SCR is fired and for the detonation products to travel from the explosive charge to the beginning of the electrode. A low magnetic field at about 0.3 tesla is present in the region upstream from the magnet pole faces because of the presence of an iron support structure outside of the channel which was used to position the multiple-charge apparatus. This causes a low voltage output signal prior to the main pulse. The bottom trace in Figure 23(a) is the voltage to ground of one of the electrodes. This trace suggests breakdown of one of the electrodes to ground about 30 microsec after the start of the main pulse. The magnetic field for the shot was 1.0 tesla and the load resistance was 0.250 ohms. The lower trace in Figure 23(b) shows the voltage output of a typical second pulse.

To investigate the reason why the second and third pulses were greatly reduced in amplitude, several series of tests were conducted. Physical examination of the face plates and pressure transducer measurements disclosed that the charges were being fired at the proper time. This ruled out the possibility that the blast wave created by the first charge was being reflected from the face plate and was destroying or disturbing the other charges. Tests made with the second and third charges disconnected from the firing circuit showed that the charges were capable of withstanding the impulse loading and were neither damaged nor forced backward out of the charge holder by the previous detonation even though measurements with the pressure transducer showed that the pressure on the face opposite the unexploded charges was about 1000 psi. With damage to the charge carrier ruled out, several other possible reasons for the low performance were investigated.

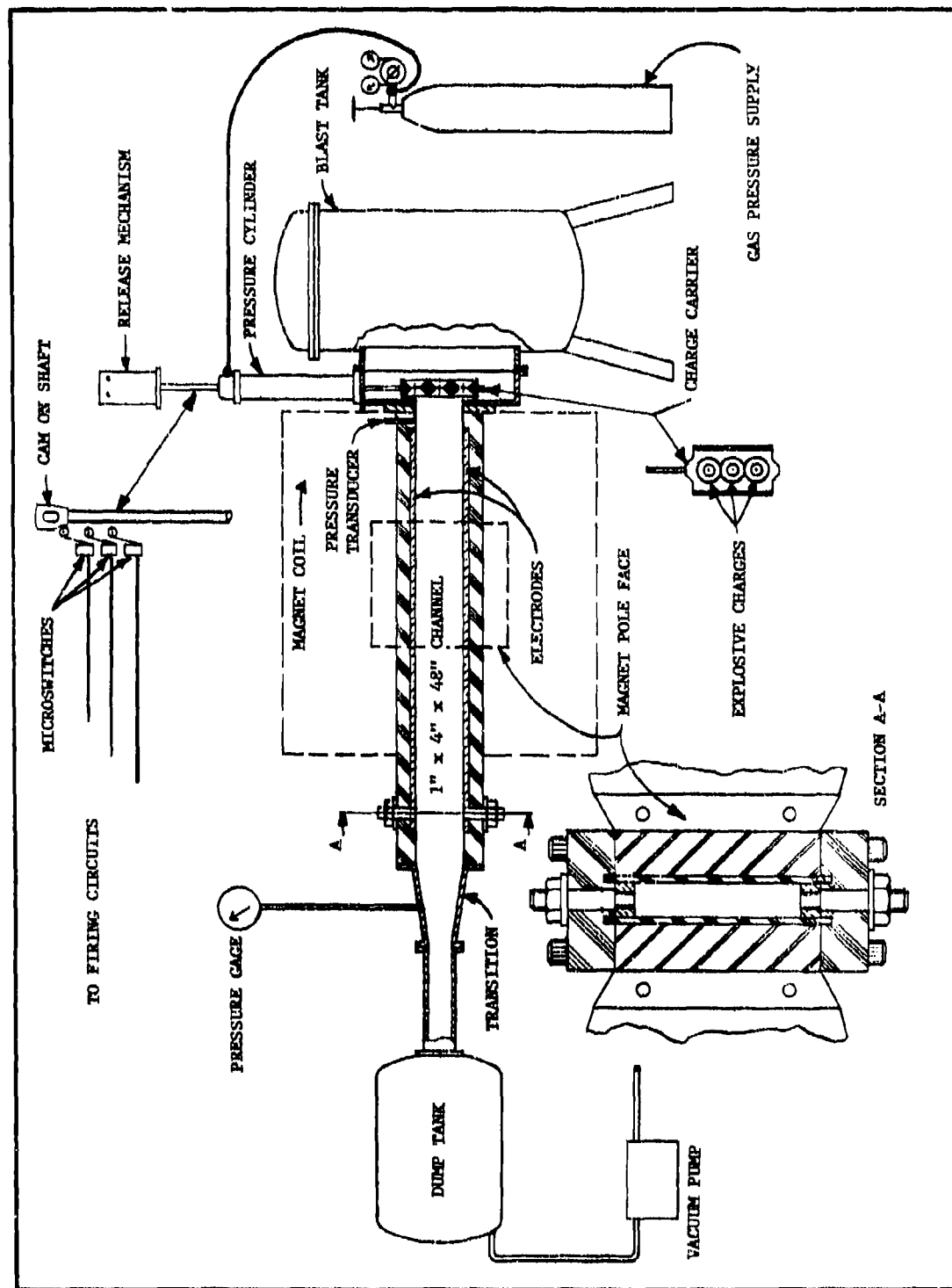


Figure 22. Multipulse apparatus showing placement of firing mechanism and blast tank

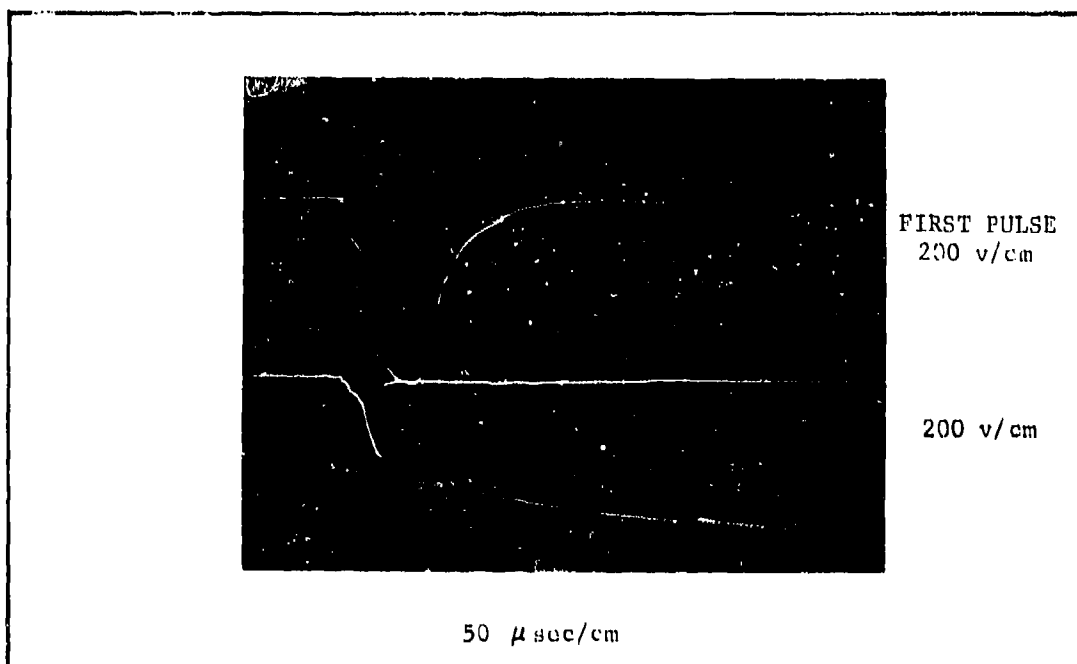


Figure 23(a). Voltage output for a typical first pulse (lower trace gives voltage to ground of bottom electrode and shows breakdown)

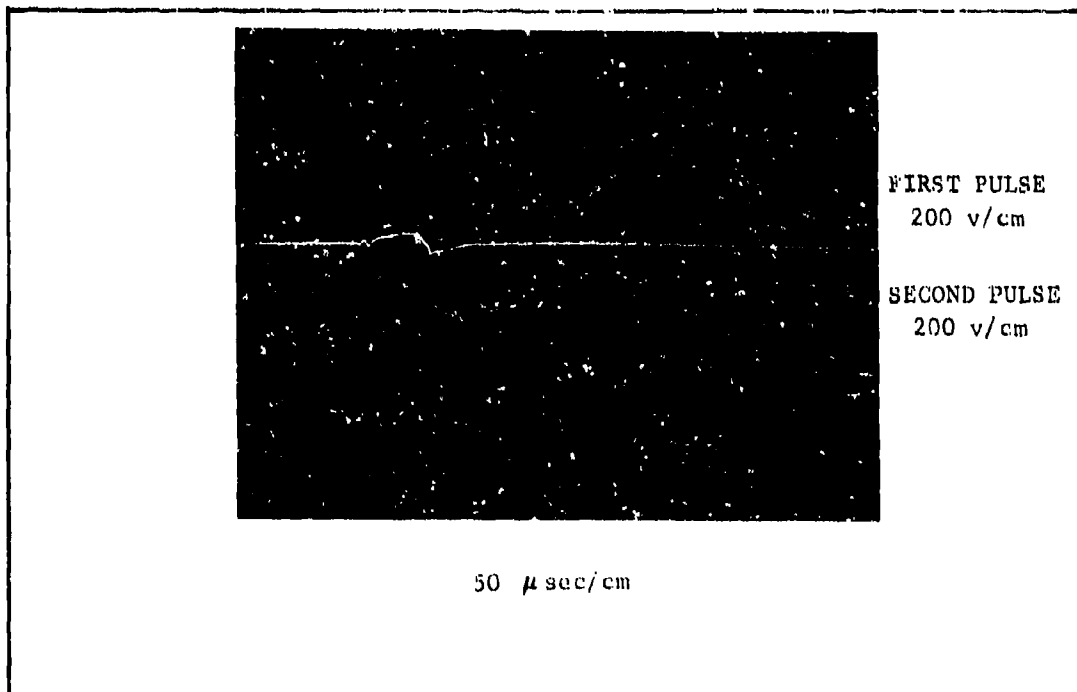


Figure 23(b). Voltage output for typical first and second pulses showing degradation of output for second pulse

At first it was thought that the sidewalls of the channel might become covered by soot from the first charge and thus set up a discharge circuit in parallel with the external load. This would allow a large current to circulate inside the generator instead of going through the load and reduce the power output. In previous experiments, the channel had always been cleaned by swabbing it out with an acetone-soaked rag to remove the carbon deposit between shots. For this reason tests were made with a "dirty" channel on a single-shot basis using the old breech block. Figure 24 is an oscilloscope trace showing the output from the "dirty" channel. This may be compared directly with the trace shown in Figure 23(a) which is for the "clean" channel under the same conditions. It is seen that there is some reduction in output if the channel is not cleaned between shots. Figure 25 shows the results of a number of tests made in this series plotted in the form of a current-voltage plot. It is seen that the effect of not cleaning the channel was the greatest in the region of maximum power output but that for the open circuit and short circuit condition, cleaning of the channel did not materially change the characteristics. In fact, for one shot with the 12-milliohm load, the highest current was measured using the "dirty" channel. While this is indeed an interesting effect and something that must be considered in the design of a repetitiously pulsed channel, it was not the cause of the great discrepancy in output which was observed when the second and third shots were fired.

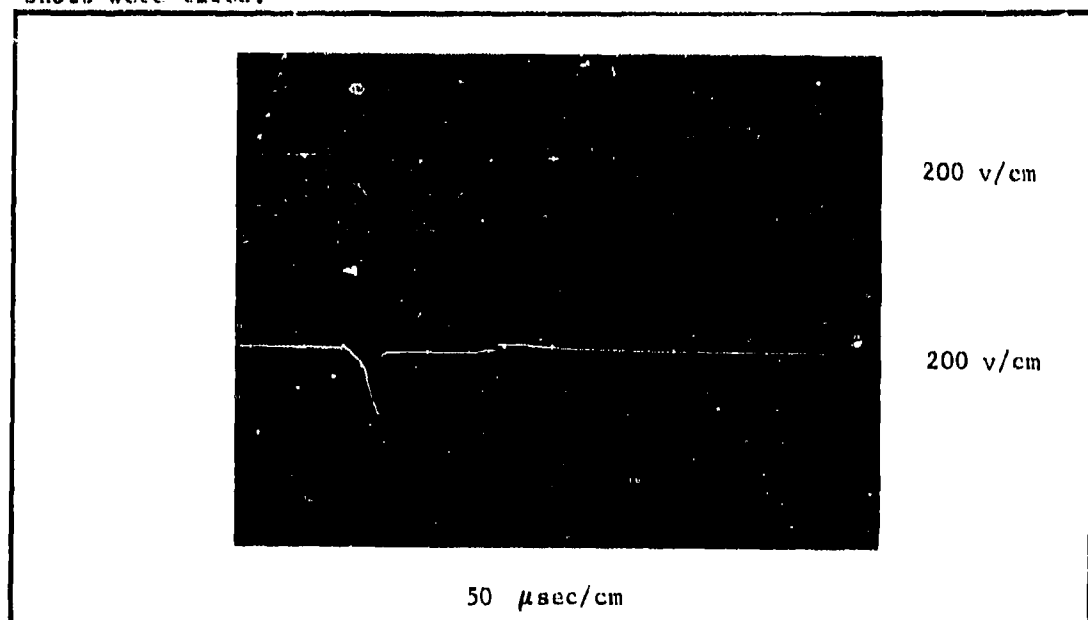


Figure 24. Output from "dirty" channel

It was found that if the time between pulses was markedly increased (if the charges were fired several minutes apart), the second and third charges were capable of producing the output voltages expected

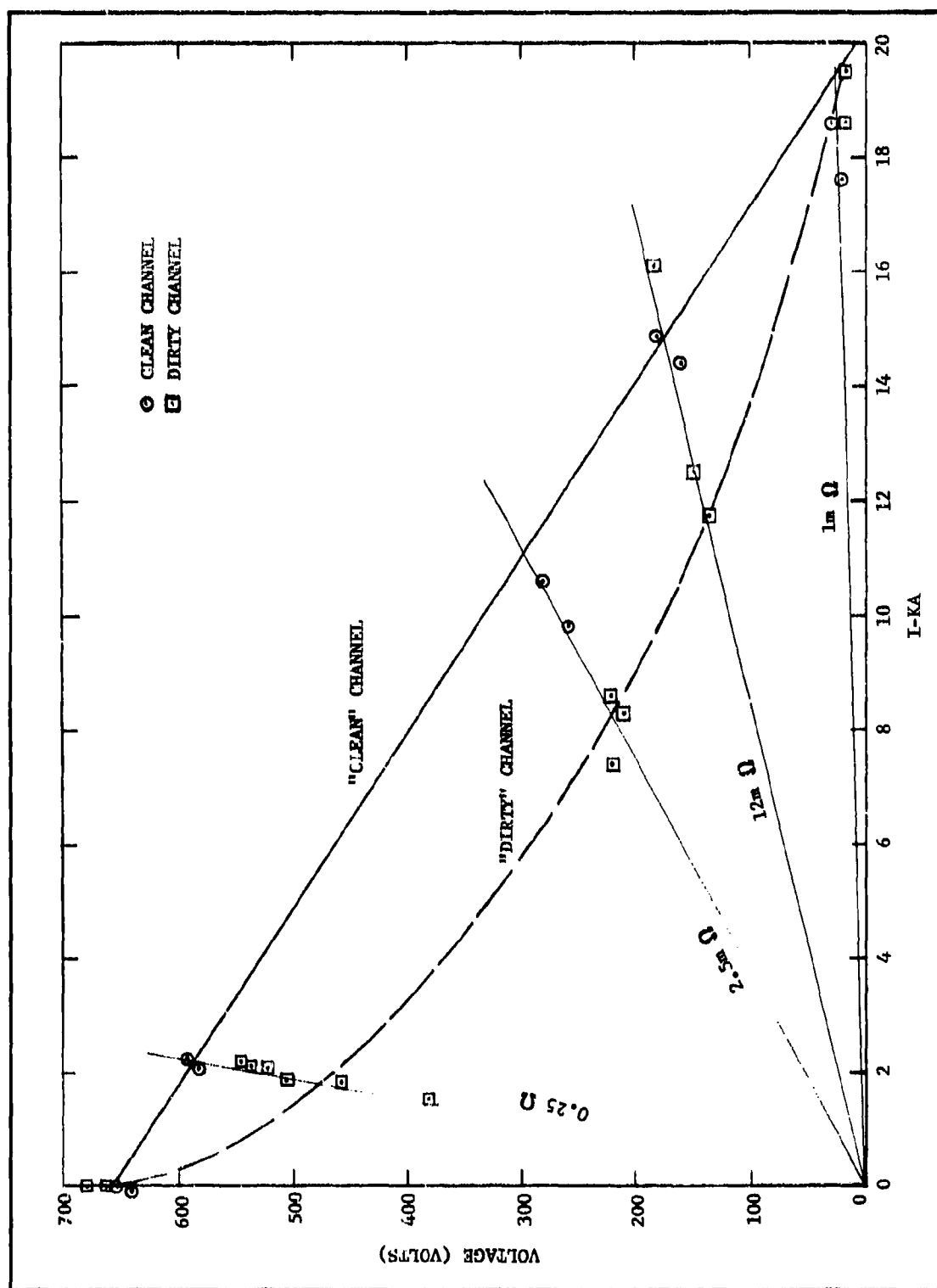


Figure 25. Current-voltage plot of test results obtained when channel was not cleaned after each shot, compared to normal cleaning

for a channel being fired at the pressure then existing in the channel. Measurements showed that the pressure in the system would come to equilibrium at a pressure about 12 torr higher after each charge was fired. This meant that the quantity of gas generated by the detonation of the charge was sufficient to fill the vacuum chamber which had a volume of 0.65 m^3 to pressure of 12 torr. In a typical run, firing the first charge with a static pressure of 2 torr produced a 700-volt output into a 0.25-ohm load. The second charge fired at 15 torr produced 400 volts and the third charge fired at 27 torr produced 130 volts. These results suggested that a high transient pressure in the channel at the time of firing the second and third charges was the reason for the decreased output.

To estimate the pressure in the channel at the time of the firing of a second pulse, measurements were made with the pressure transducer installed at the upstream end of the channel. Figure 26 shows the pressure as a function of time in the channel when fired with the charge in the solid breech block. The peak pressure is approximately 3×10^5 torr and the pressure decays with an initial time constant of several milliseconds which increases with time, suggesting that the gases are being cooled down and the speed of sound in the channel is changing. A complex system of pressure and rarefaction waves within the channel is suggested. Figure 27 is a similar plot showing the pressure transducer data when the charge is fired in the multiple-charge apparatus. Because of the fact that the gases can flow out both ends of the channel rather than being confined at one end as is the case when the breech block is used, the average pressure decay rate is much greater, approximating 700 microsec.

To test the residual pressure hypothesis, a series of tests was performed wherein the period of time between the firing of the charges was varied by changing the pressure in the driving mechanism reservoir (See P_1 in Figure 18). Figure 28 is a plot showing the time after firing the first pulse for the second and third pulses as a function of reservoir pressure, P_1 , with P_2 at atmospheric pressure. Figure 28 shows that the third pulse can be delayed for times of up to 500 ms by the proper choice of P_1 . These data, shown by circles and squares, were taken in dry runs. When the apparatus was operated with explosive charges, the times were changed slightly as shown by the crosses. This suggests that a slight widening of the charge carrier occurs when the charges are fired, which increases the friction on the side rails and slows down the charge carrier slightly. Using the time delays generated in this fashion, the data shown in Figure 29 were obtained. We have plotted the magnitude of the third pulse as a function of delay time. It is possible to fit this data with an exponential function which suggests a pressure equilibration time constant of roughly 12 ms.

To determine the effect of the static pressure on the output characteristics, a series of tests was conducted with the charge carrier being moved by hand between shots. The pressure in the channel was measured and recorded after each shot when the pressure had equalized throughout the

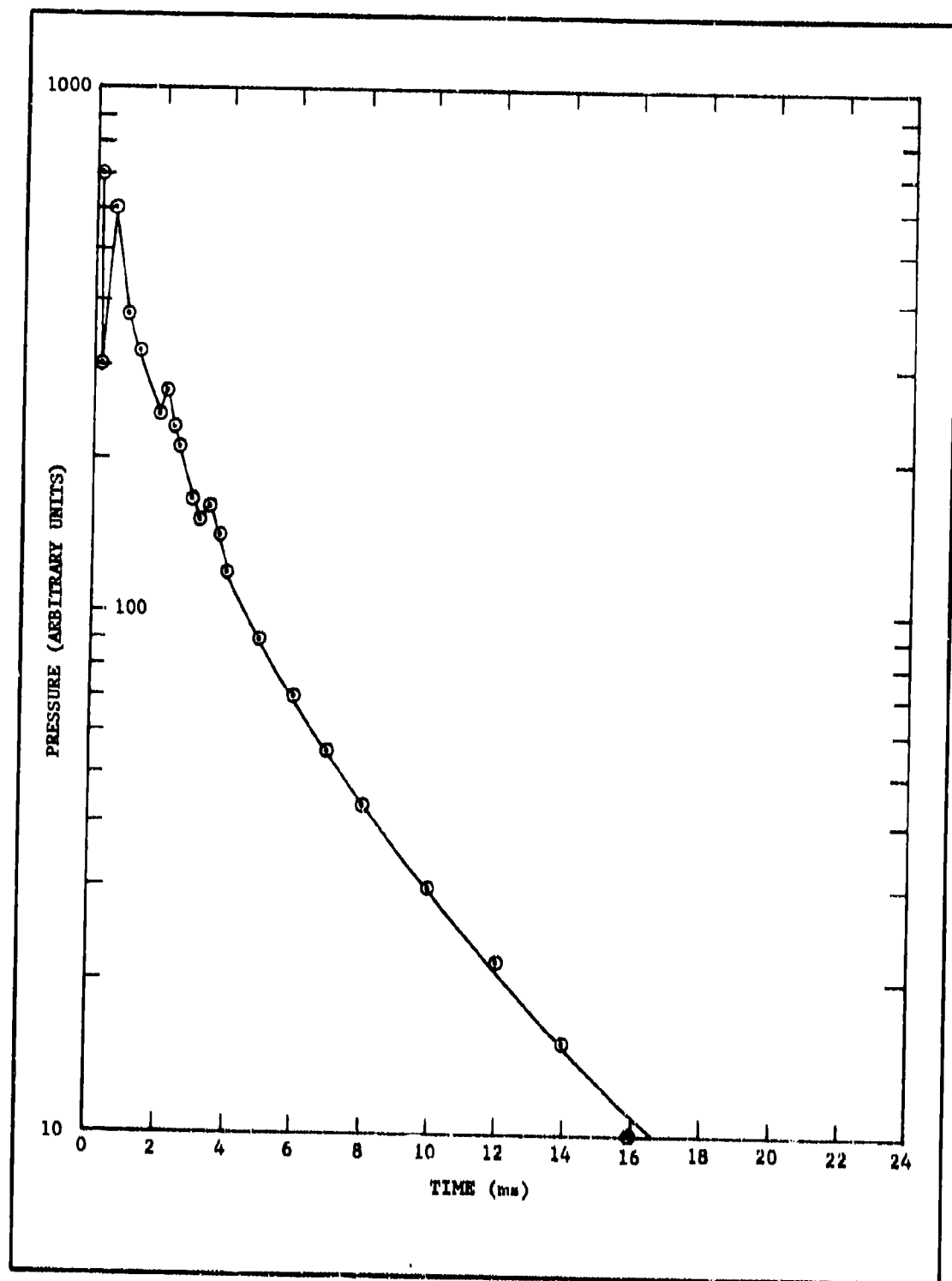


Figure 26. Pressure as a function of time in the channel when charge is fired in solid breech block

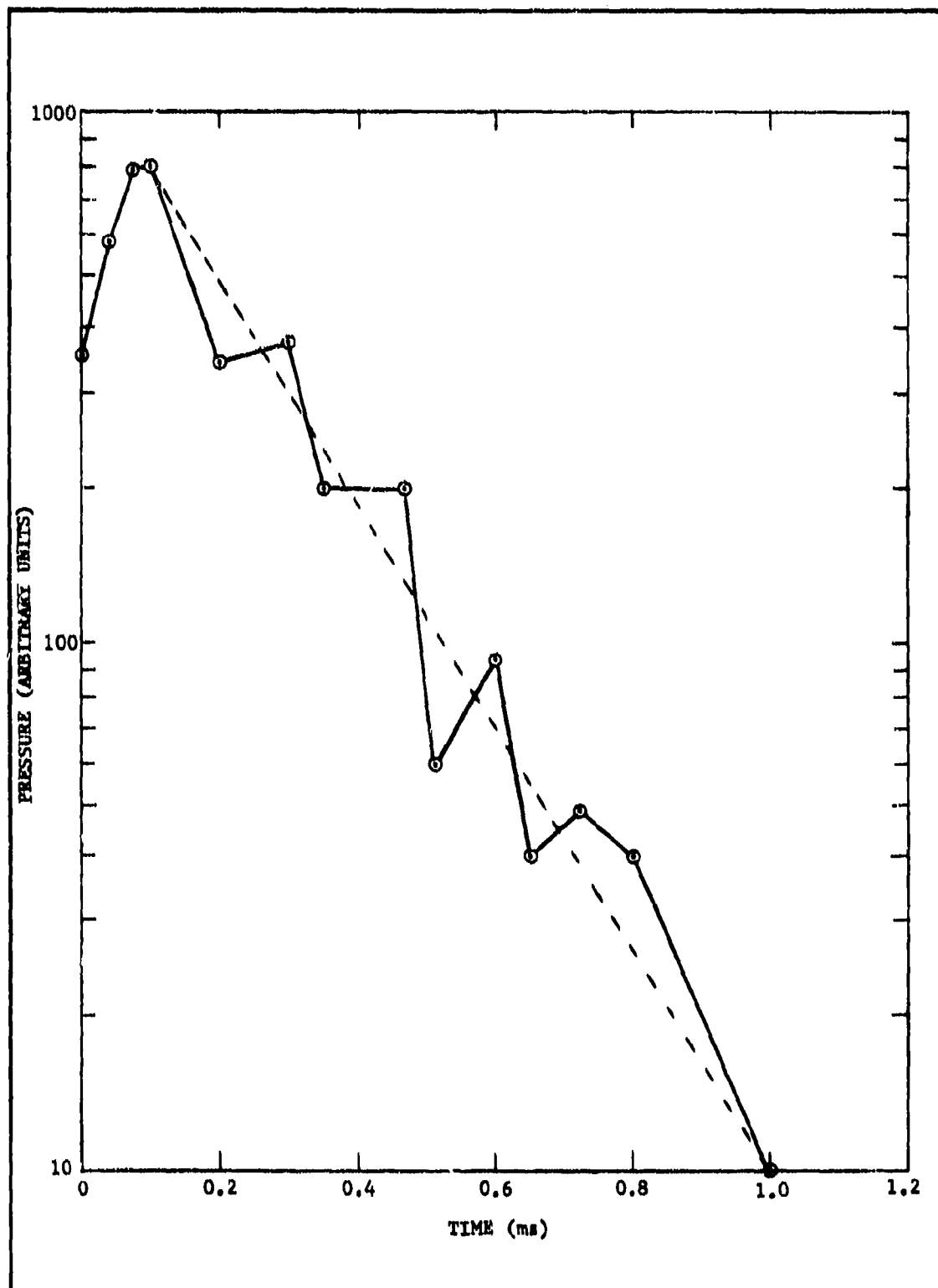


Figure 27. Pressure as a function of time when charge is fired in multiple-charge apparatus

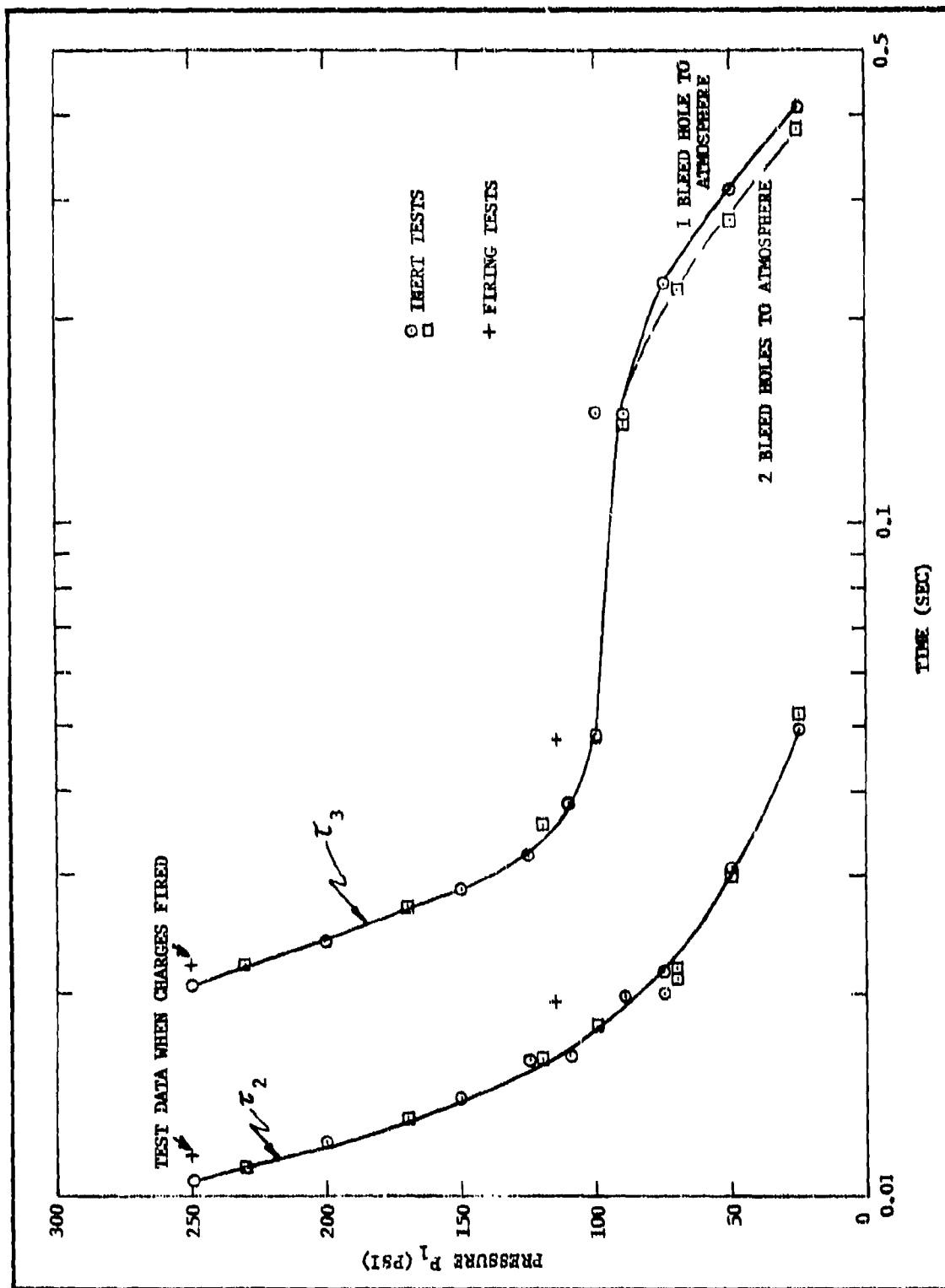


Figure 28. Time after firing first pulse for second and third pulses as a function of P_1 , with P_2 at atmospheric pressure

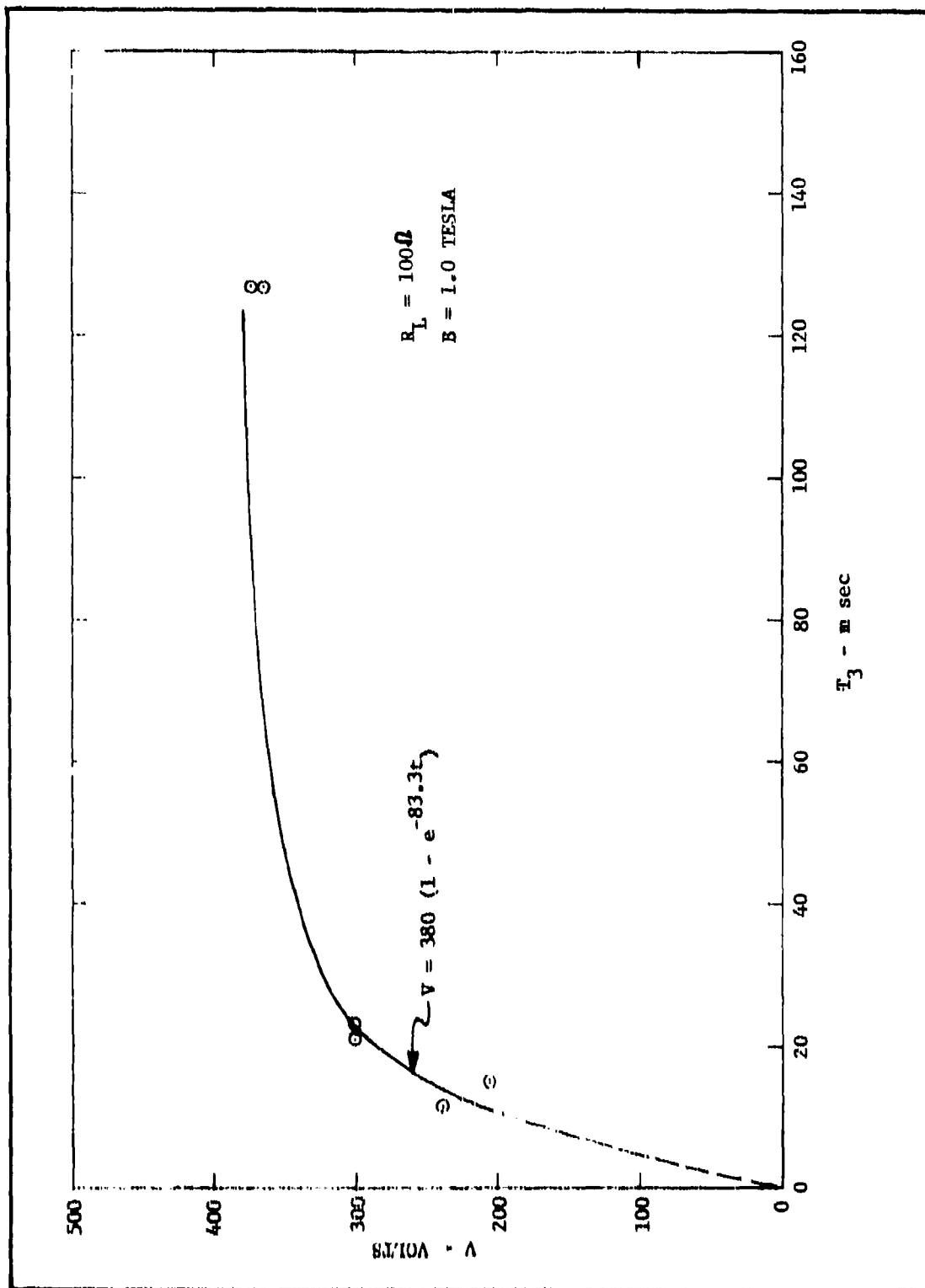


Figure 29. Plot showing recovery of generator output as a function of delay time after previous shot

system. Figure 30 shows the output voltage as the function of the initial pressure in the channel for loads of 1000 ohms, 0.25 ohms, and 0.012 ohms. For the 0.012-ohm experiment, the channel pressure had to be adjusted by pumping between pulses so as to obtain the data.

It is seen that the degradation of output with pressure is largest for the low-resistance loads and that the output is reduced in an exponential fashion with initial pressure. Using the exponential relations shown in Figure 30, it is possible to construct a theoretical current-voltage characteristic for the channel with various initial pressures. Such a characteristic is shown in Figure 31. Experimental data taken at 3, 10, and 30 torr seem to match the model quite well. The significance of this plot is that in this configuration, where the charge is fired some distance away from the magnetic field-containing region, there is a marked decrease in power output as a function of initial pressure. From the theoretical voltage-current curves, it is possible to estimate the maximum power output which could be generated with a given initial pressure in the channel. Such a curve is shown in Figure 32. This indicates that 30-torr initial pressure would reduce the maximum power output by several orders of magnitude, which is in agreement with the experimental observation. It should be noted that Figure 32 is based on matching the generator to the load to achieve maximum power output.

To summarize the pressure effect results, we have plotted the pressure transducer data shown in Figures 26 and 27 as Figure 33. The data taken with the multiple-pulse apparatus, which is open at the upstream end, shows a rapid decrease in the pressure. The data taken with the upstream closed by the breech block is the curve labeled "single confined charge". We may use the factor of two reduction in output for the 100-ohm case shown in Figure 29 to estimate that the pressure of the residual gases in the channel 10 ms after firing the previous charge is 50 torr. This point, which is plotted in Figure 33 at the 10-ms time, is consistent with the pumping speeds expected during the transition period as the gases are cooling down. It should be noted that the data in Figure 27 was taken with the charge carrier slide stationary so that the gases could be vented through the open hole, whereas in actual operation the slide carrier would be moving during this period and would offer some restriction to the flow of gases through the upstream end of the channel. Therefore, we should expect the pressure profile to be somewhere intermediate between the two statically fired cases. The data point taken from the reduction in output with the 100-ohm load is consistent with this hypothesis.

The effect of the residual channel pressure on the generator performance is shown in Figure 34(a) which is a plot of the voltage output for three initial pressures (3, 6, and 30 torr). The load for the upper curve was 100 ohms, while for the lower two curves the load was 0.250 ohms. Figure 34(b) is a plot of the magnetic induction as a function of axial position along the channel. The voltage data was derived by making an approximate transform from the time frame to the distance frame by

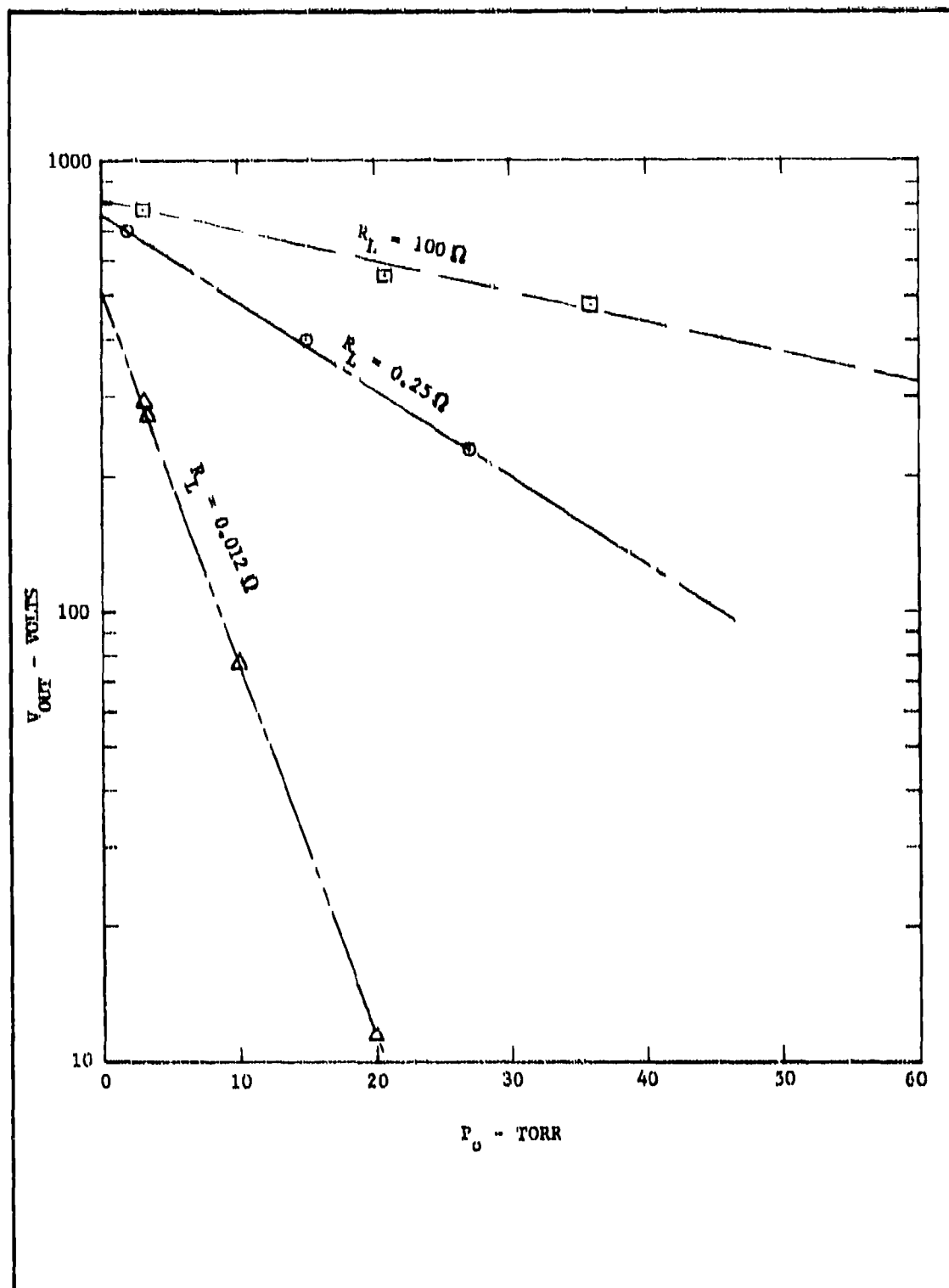


Figure 30. Output voltage as the function of initial pressure in the channel for 100, 0.25, and 0.012 ohms

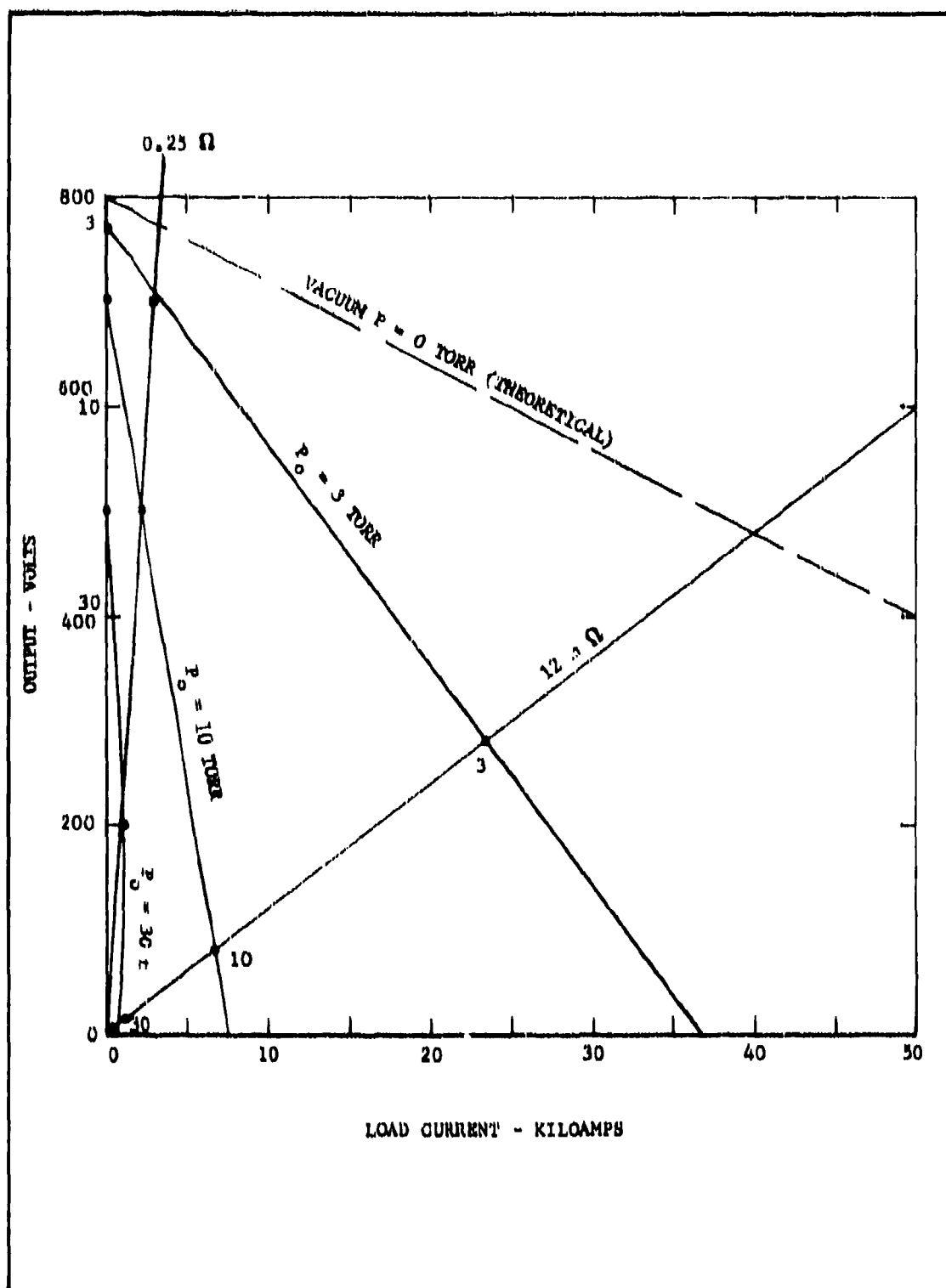


Figure 31. Experimental current-voltage characteristics for the channel (dotted line is based on exponential relation of Figure 30)

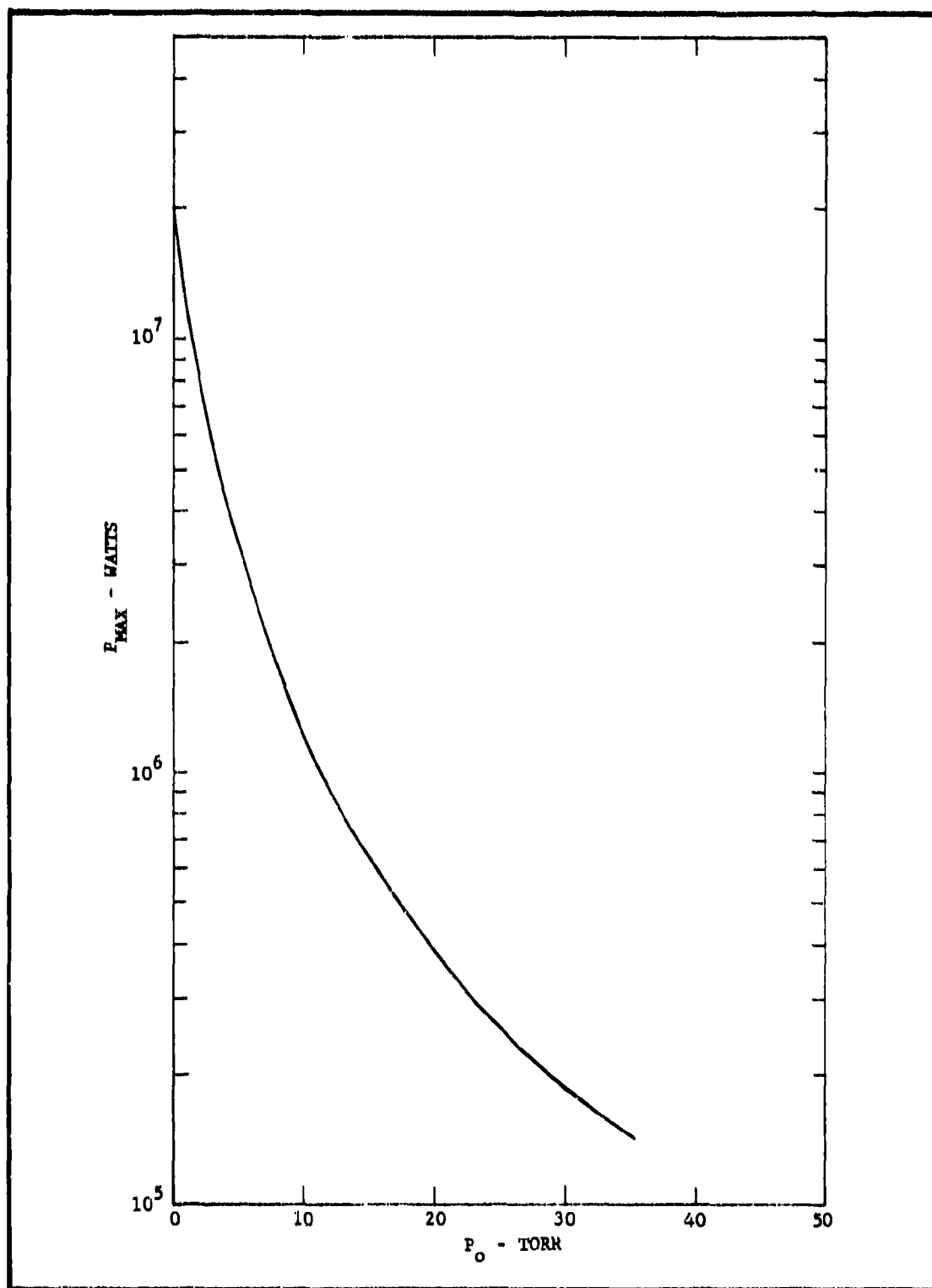


Figure 32. Estimated maximum power output generated with a given initial pressure in the channel

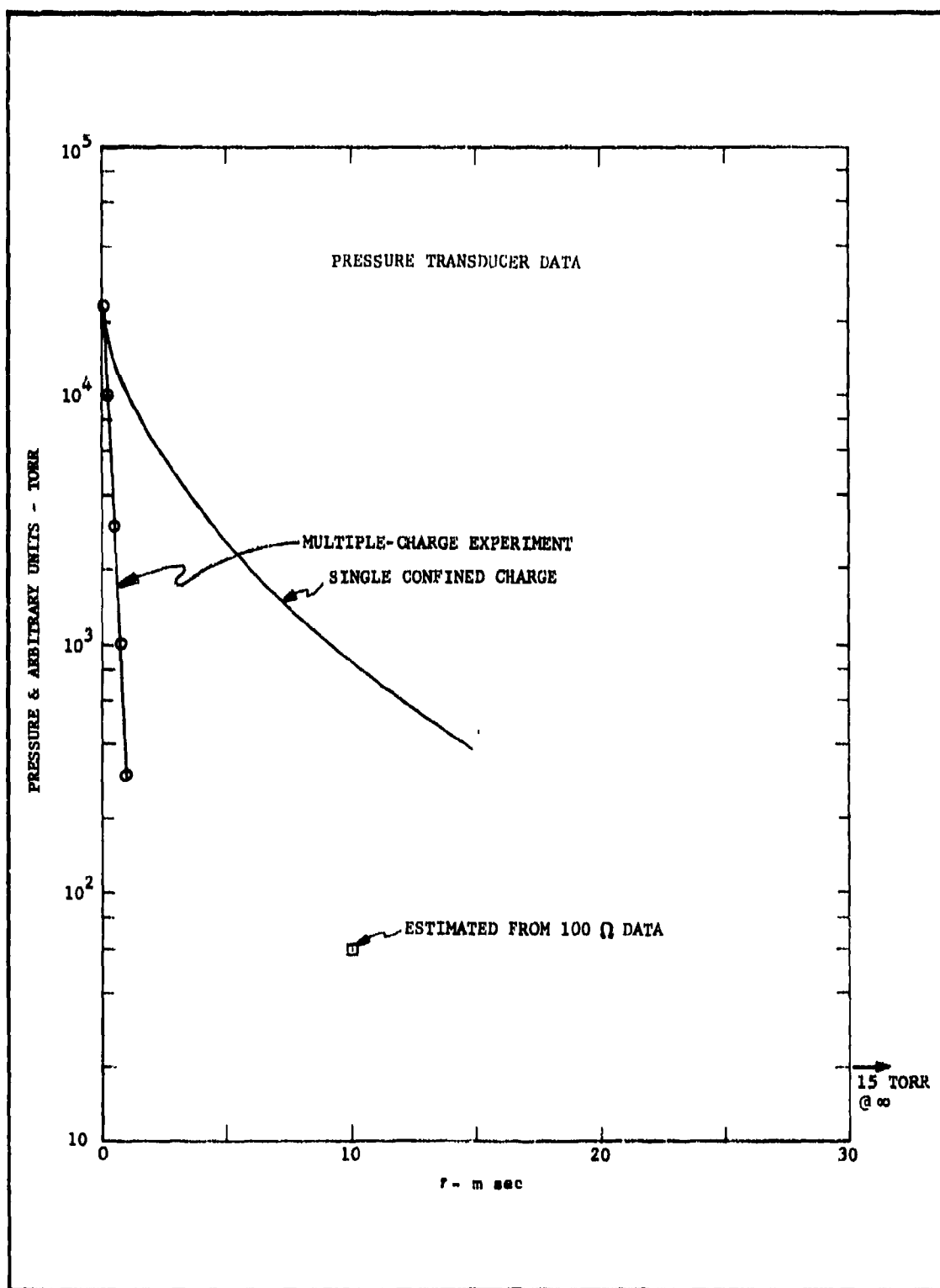


Figure 33. Summary of pressure effect results (based on Figures 26 and 27)

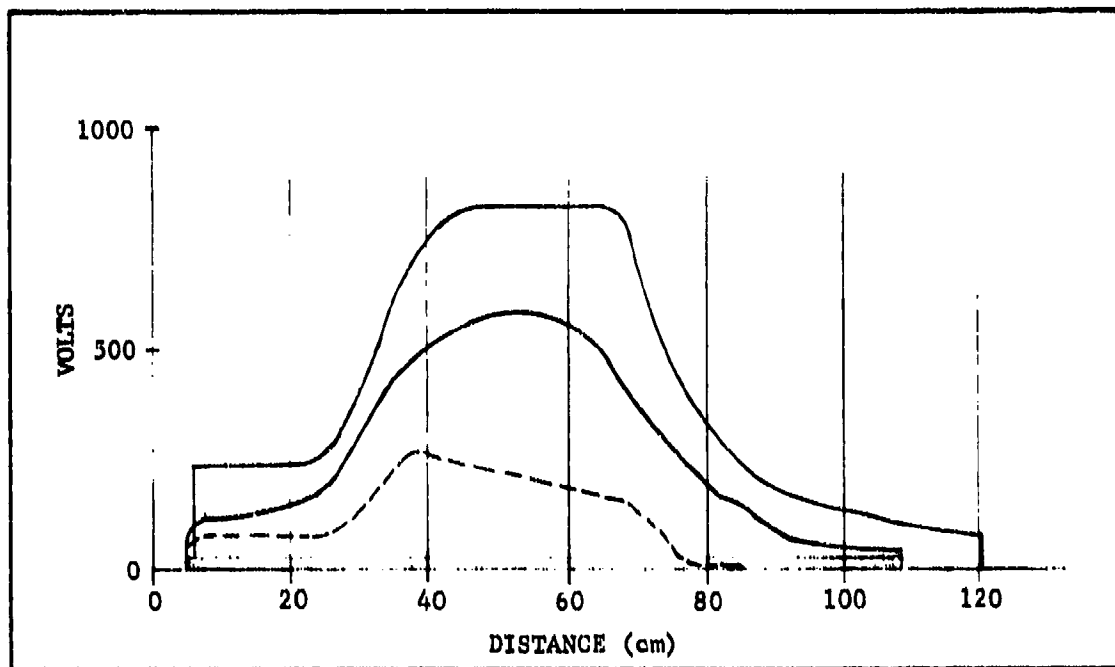


Figure 34(a). Plot of voltage output for three initial pressures (3, 6, and 30 torr); load for upper curve was 100 ohms; lower two curves, 0.250 ohms

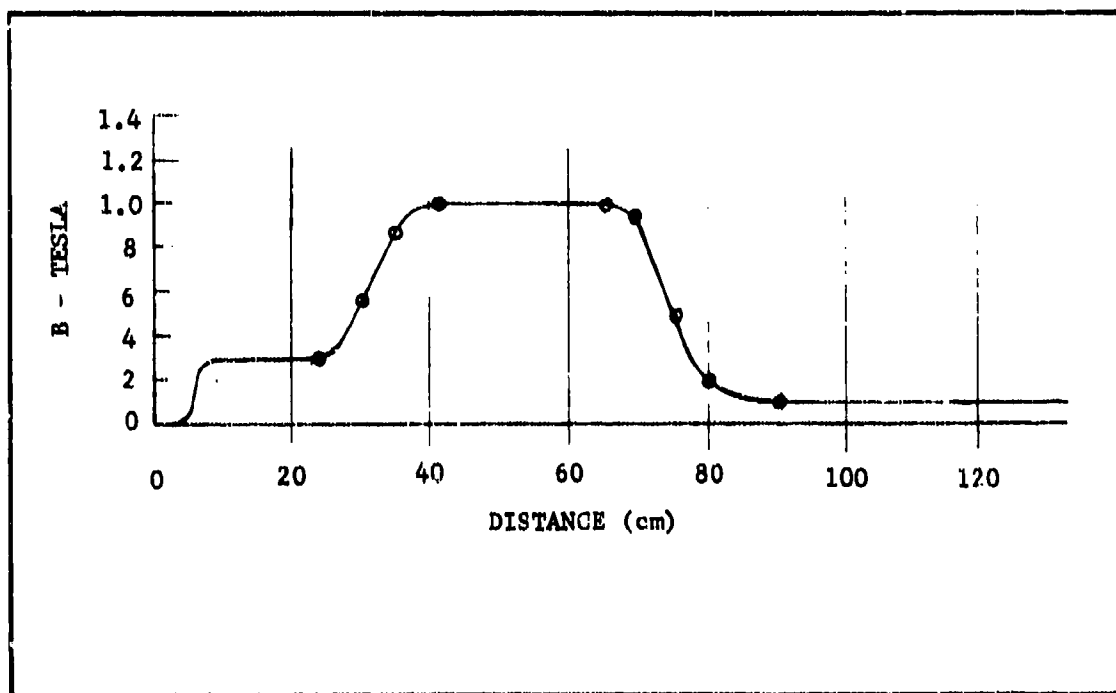


Figure 34(b). Plot of magnetic induction as a function of axial position along the channel

determining the velocity of the conductive plasma region as a function of distance along the channel. Since the load resistance is high, the voltage output of the channel is roughly proportional to the plasma velocity. The upper curve for 100 ohms at 3-torr initial pressure could be considered as close to theoretical performance. Figure 34(b) illustrates the relative distance of the explosive charge from the magnetic field region and the effect of the iron plates which were used to support the multiple-charge apparatus. As the initial pressure is increased, the voltage output decreases. In particular, the 30-torr initial pressure curve (Figure 34(a)) shows the plasma velocity decreasing as the detonation products move down the channel, presumably because of the mass of gas which must be accelerated in front of the detonation products thus increasing the entropy of the system.

4. Conclusions

The development of a multiple-charge feeding apparatus using high explosives as the energy source was shown to be feasible. The mechanical objectives of the program which called for the attainment of a pulse repetition rate of 90 pulses/sec were achieved. The electrical output of the first pulse of the series was of the magnitude expected; however, there was a severe degradation of output if the apparatus were operated at the design pulse repetition frequency. It was found that the reason for the degradation of electrical output was that after 10 ms an excessive quantity of residual gases remained in the channel from the previous pulses. Because the explosive feeding mechanism had to be located at some distance from the magnetic field region, this effect was accentuated. While the performance of the system might be improved slightly by operating with better vacuum at the upstream and downstream ends of the channel, it is primarily the thermodynamic properties of the gases within the channel that determine the speed at which they will flow out the open ends. Since the gases cool rapidly and the speed of sound decreases, it is estimated that times of the order of 30 to 50 ms between pulses would be needed to allow the channel pressure to return to a level that would not seriously degrade the power output. This would suggest that a rate of 10 or 20 pulses/sec would be more appropriate for a repetitively pulsed, explosive-driven MHD generator system.

It was also determined that the residual carbon left by the under-oxidized explosives built a deposit in the channel which resulted in a reduction of power output. However, because of the high velocity of the detonation products, it is expected that this buildup would stabilize at a small thickness after several shots and that this effect could be compensated for in the design of an apparatus by proper choice of dimensions and increase in magnetic field.

Aside from the pressure effects cited above, which place an upper limit on pulse repetition frequency, and the carbon deposit problem, there appear to be no major obstacles to the construction of repetitively pulsed, explosive-driven generator systems to operate over a wide range of energy outputs.

SECTION III

MAGNETICALLY LOADED MHD EXPLOSIVES

A. INTRODUCTION AND SUMMARY

The goal of this phase of the program was to investigate the concept of generation of pulsed electrical power which occurs when a moving, conductive detonation head of a condensed high-explosive interacts with a crossed magnetic field. This field may be provided by polarized permanent magnet particles dispersed in the explosive to form a magnetically loaded explosive. The results obtained to date using various metallic dopants to improve the conductance of the moving detonation zone indicate that the basic idea is technically feasible at the present state-of-the-art. An inexpensive, reliable generator can be constructed of presently available materials with known techniques. The most efficient device will result from an optimization considering basic explosive conductivity, magnetic material fraction, and magnetic energy density for the application under study.

1. Summary of Conductance Measurements - Phase I

Construction of the test facility was initiated during April 1966 and the first series of experiments, which were measurements of the electrical conductance of the detonation zone, was started in June 1966. These tests used commercial Detasheet explosive, which is primarily PETN in an organic binder, doped with various percentages of spherical copper powder. These were followed by a similar series using spherical Type 316 stainless-steel powder. Conductance ratios (pure Detasheet versus doped Detasheet) and velocity decrease due to doping were measured. Very significant increases in conductance (roughly two orders of magnitude maximum) were obtained depending on the conductivity of the dopant. When the velocity data and conductance data are combined to form a magnetic Reynolds number, the maximum magnetic Reynolds number apparently occurs near 80 percent metal fraction by weight. On the basis of these experiments, it was estimated that a magnetic Reynolds number of about 10 could be attained.

After completing the conductance experiments with copper and Type 316 stainless-steel, iron powder was tried. The first series used sponge iron, which is essentially finely ground, rolling mill scale reduced by hydrogen. The particles are angular, not spherical. The results indicated a conductance increase almost identical to copper-doped charges. Spherical iron powder from another supplier was also tried. The results were disappointing with this material. The conductance increase was similar to that of Type 316 stainless-steel. It was suspected that the difference in results when using two different types of iron was due to the fact that the spherical iron had a size distribution heavy in fine particles. Screening tests on both the sponge and spherical iron powders confirmed the fact that the spherical powder had half of its

weight in particles less than 325 mesh. A mixture was made of spherical particle sizes that duplicated the distribution of the sponge iron; several shots were fired, but still no improvement in conductance was noted. Physical examination of both iron powders under a high-power microscope indicated that both types of particles were equally bright and free of oxide, but differed only in particle shape, which would indicate that electrically insulating oxide layers were not a factor in the difference in conductance. We must tentatively conclude that particle shape is an important factor in the overall conduction process.

Having demonstrated that marked improvements could be made in the conductance of the detonation zone in Detasheet by the addition of metal dopants, a series of power generation experiments was then scheduled and conducted.

2. Summary of Power Generation Experiments - Phase II

The power generation experiments were begun in September 1966. The first series of charges were composed of 1/8-in.-thick Detasheet doped with 71.5-percent spherical copper. A steady magnetic field of about 0.7 tesla was applied transverse to detonation direction. The scatter in the data indicated thicker charges should be fabricated and that the data should be normalized to account for variation in geometry, magnetic field, and detonation velocity.

The next series used Type 316 stainless-steel in Composition C-4 explosive which is RDX mixed with mineral oil. The results of these and subsequent power generation experiments definitely confirmed the Phase I conductance experiments, showing stainless-steel inferior as an additive compared to copper.

Sponge iron dopant in Composition C-4 showed the highest power-producing ability, with open circuit potentials three times greater than when using spherical additives, and with load currents an order of magnitude greater. The increased voltage can possibly be explained on the basis of a higher particle drag coefficient (shape factor) of the sponge iron, as discussed in connection with the conductance measurements. The superior currents may be due to internal electrical field changes also associated with the angular shape.

Plasma magnetic Reynolds numbers (R_m) deduced from the Phase II experiments show that the addition of metal dopants has increased the magnetic Reynolds numbers of the detonation zone by up to three orders of magnitude into the range of 1 to 10, and could conceivably be even higher for optimum conditions of parent explosive, additive, and fabrication technique.

Calculations indicating the size of a device for generating 50 joules for 20 microsec are also included.

B. THEORY

1. General Principles

Although the present concept of pulse chemical-to-electrical conversion could assume numerous physical configurations (2) the general features of all embodiments are adequately described by the one-dimensional, direct-coupled device discussed below. To understand the principle involved, an equivalent circuit is developed and analyzed. This analysis leads to the conclusion that one of the most important parameters is the magnetic Reynolds number. The effect of R_m on power output is examined in some detail.

a. Operating Description

The general principle of operation can be understood by reference to Figure 35. It has been assumed in the figure that an initiation train has produced a plane wave which is shown advancing at rate "D" into the magnetically loaded explosive. For simplicity this composite material can be visualized as a regular array of spherical magnetic dipoles which provide a magnetic field in the explosive-filled gaps between spheres. This is similar to the more common case of a massive permanent magnet providing a magnetic field over a single gap, but now the gap is distributed throughout the volume of the magnet. The ionized-zone products possess a forward velocity, which interacts with the magnetic field to generate the Faraday Electromotive Force (EMF). Electrodes in contact with the composite apply the EMF to an electrical load. The current flows in the direction of the arrows through the load and returns through the electrodes and the ionized detonation zone. This is an example of direct coupling. Figure 35 is schematic, in that a practical device would not terminate in the "B" direction as shown. The maximum magnetic field in the distributed gap will result when "B" is large and the ends are joined to form a two-dimensional "Rowland Ring". In this embodiment of the concept into a device, the electrodes would be concentric cylinders with magnetic material in between, polarized in the azimuthal direction.

Figure 36 indicates the general nature of the reaction process. It is assumed that the detonation pressures are high enough to shock-heat the magnetic dipoles above the Curie temperature, which is depressed because of the high pressure. The magnetic field then decays approximately at an exponential rate (6) with a time constant given by:

$$\tau = \sigma_c \mu d^2.$$

2

The conductivity, σ_c , for contemplated magnetic materials is around 10^7 mho/m; particle size, d , could be anywhere between microns and a millimeter. Multiplying τ by the detonation rate, D , yields a length which is the characteristic distance behind the detonation front for the decay of the magnetic field. For the anticipated values of D this distance is around 10 cm, much longer than the expected detonation zone

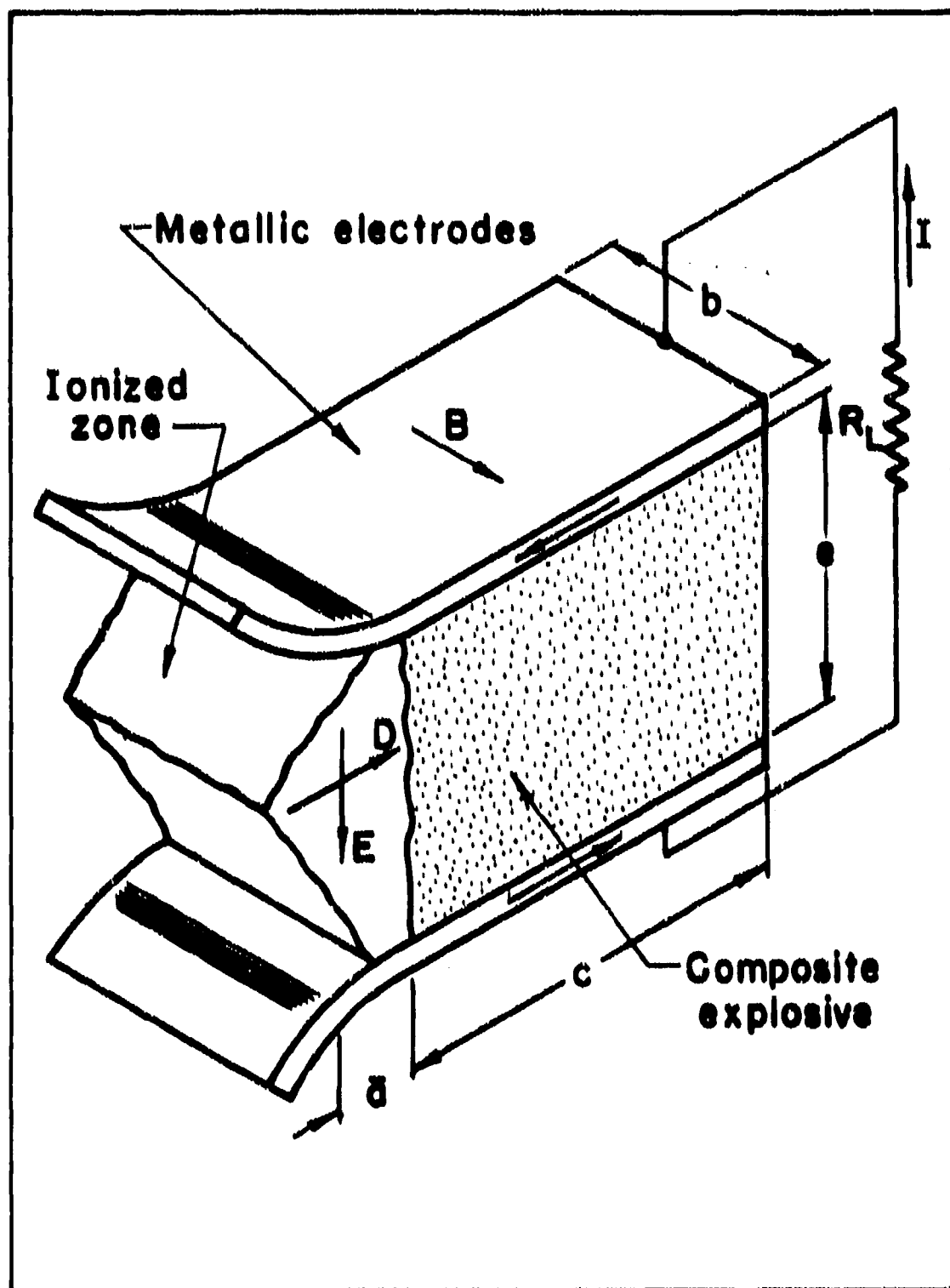


Figure 35. Schematic view of pulsed explosive generator undergoing detonation

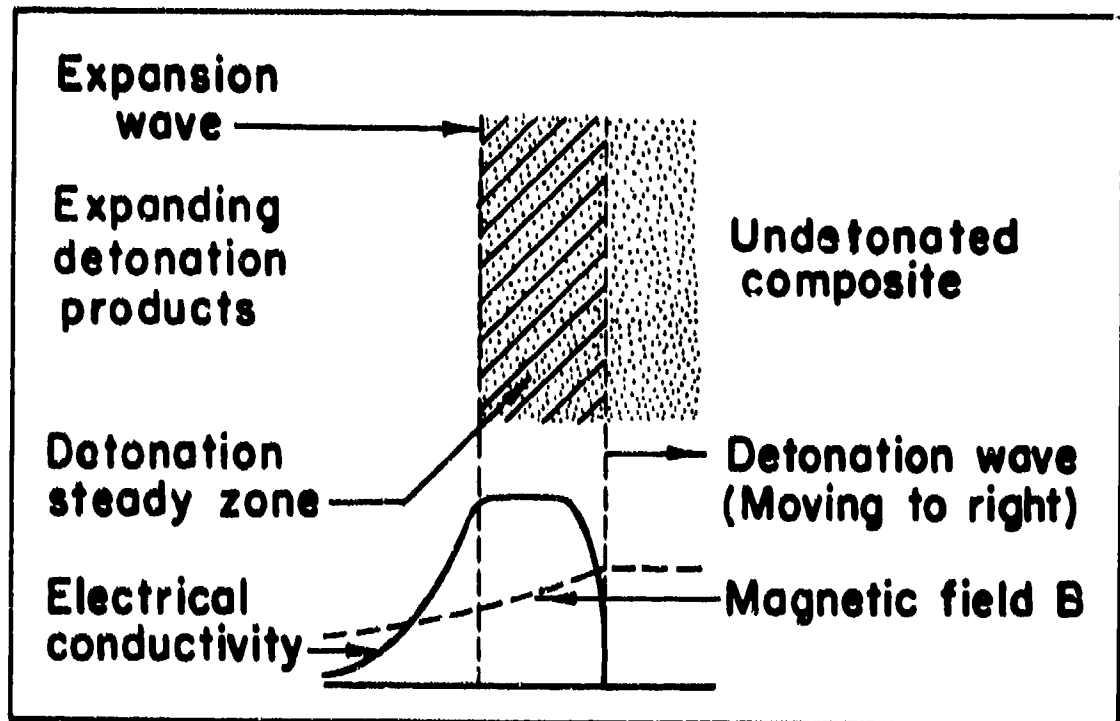


Figure 36. Simplified cross section of one-dimensional detonation process

width \bar{a} . Hence, for large particles, one can visualize that the conducting detonation products are in an approximately constant magnetic field. With very fine particles the situation is not so clear. If the individual particles were in free space, the magnetic field would decay at a very fast rate because of the dependence on d^2 . However, they are closely packed in a weakly conductive medium so the decay rate is influenced by the presence of the other particles or the effective size is larger than the individual particle size. What is important is the volume fraction of magnetic material.

The detonation wave proceeds into the composite, changing the explosive to a hot, high-density gas which has an electrical conductivity many orders of magnitude less than that of the included metal particles. The conductivity of the gas increases rapidly with passage of the detonation wave and maintains a fairly steady value in the detonation zone, then decays rapidly as the gas expands and cools. Due to the presence of the metallic particles, the conductivity of the whole mixture could be higher than that of the gas phase alone.

b. Equivalent Circuit and Power Output

Instead of deducing the output of such a device as shown in Figure 35 based on the microscopic processes of Figure 36, an overall microscopic circuit approach proves expedient and accurate provided several "averaging" parameters are included. Figure 37 shows the equivalent electrical circuit for the direct-coupled device of Figure 35 and illustrates the salient features of any contemplated configuration: that is, a voltage is generated by the $U \times B$ interaction and by changes in the geometry of the magnetic material.

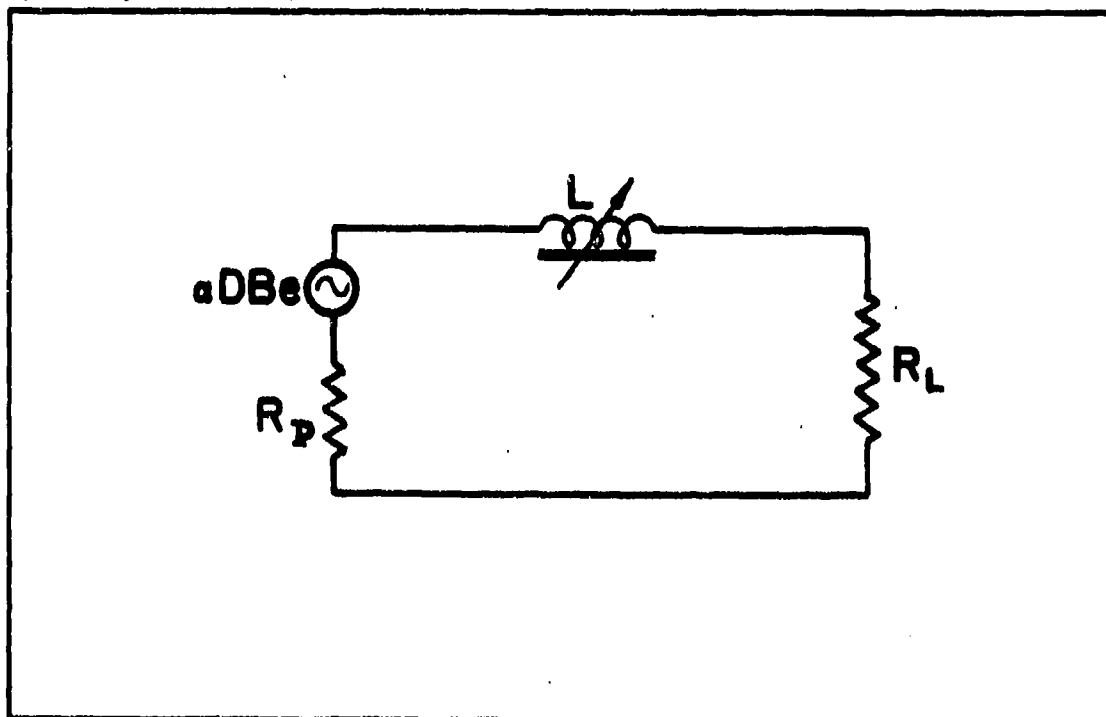


Figure 37. Equivalent electrical circuit for direct coupling

In conventional pulsed-MHD generator action, most of the voltage is generated as the slug of plasma interacts with the initial magnetic field, B . Usually, induced magnetic fields are negligible (magnetic Reynolds number, R_m , is much less than unity). On the other hand, existing explosive-electric transducers, such as the ferromagnetic and flux trapping (7) (8) (9) (10) and (11), generate power solely by the change in inductance and generally depend on high R_m . It is expected that this device will fall somewhere between the two extremes, with power coming both from $U \times B$ and rate of change of inductance; however, from a preliminary knowledge of the dynamics of detonation, it is assumed that R_m will be low. Since R_m controls the coupling between the hydrodynamic and electrical aspects of the process, no coupling is assumed, at least initially. This allows solving the electrical-circuit equations using a

steady-state detonation velocity and detonation-zone properties that are not functions of the electrical current.

The characteristics of the detonation process result from combining the hydrodynamic conservation equations and an equation of state as discussed quite well by Zeldovich and Kompaneets (12). This problem will not be discussed further. Rather, the detonation steady zone is assumed to have a given pressure, temperature, composition, electrical conductivity, and shape. This zone moves into the undetonated composite at a fixed velocity, D , with actual particle velocities, U , of magnitude $D/4$. Any deviations of velocity can be absorbed into the adjustment parameter, α .

The Kirchhoff voltage equation for the circuit of Figure 37 is:

$$\alpha D B e - I \dot{L} = I R + L \dot{I} \quad 3$$

where α = effective particle velocity/detonation velocity $\approx 1/4$

D = detonation velocity

B = magnetic field intensity

I = circuit current

L = circuit inductance

R = circuit resistance = plasma resistance plus

load resistance = $R_p + R_L$.

It is assumed that the load is resistive only since any complex reactance (mainly inductive) can be lumped with the inductance, L . By necessity of the configuration, the inductance of the circuit is decreasing with time and L is negative; thus, both terms on the left are sources of voltage equivalent to the voltage losses on the right.

Equation 3 can be integrated, but the general solution is cumbersome for the present purpose. A simplification can be made by comparing the L reactance with the resistance, R . For the configuration of Figure 35, the inductance is approximately given by:

$$L \approx \frac{\mu_0 c}{b} = \frac{\mu_0 c}{b} \left[1 - \frac{tD}{c_0} \right] = L_0 \left[1 - \frac{t}{t_0} \right] \quad 4$$

where the dimensions are as in Figure 36. We have neglected end effects in the "B" direction ($b \rightarrow \infty$; c_0 is the value of c at $t = 0$). Differentiating Equation 4 gives:

$$\dot{L} = \mu (e/b) \dot{c} = -\mu (e/b) D \quad 5$$

The resistance, R , is:

$$R = R_L + \frac{e}{\sigma \bar{a} b} \quad 6$$

where any geometrical fringing is lumped into the "effective" conduction zone width, \bar{a} . The ratio of reactance to resistance yields:

$$\frac{|\dot{L}|}{R} = \frac{\mu \frac{e}{b} D}{R_L + \frac{e}{\sigma \bar{a} b}} \quad 7$$

which for the short-circuit condition yielding minimum total resistance ($R_L = 0$), Equation 7 becomes:

$$\frac{|\dot{L}|}{R} = \mu \sigma \bar{a} D = R_m \quad 8$$

which is the magnetic Reynolds number of the interaction.

It is expected that basic electrical conductivity, σ_0 , will be about 10^3 mho/m (Refer to paragraph 3.); the effective detonation zone thickness, \bar{a} , is on the order of a centimeter, or 10^{-2} m. For maximum magnetic field in the distributed gap, the magnetic material will initially be at $(BH)_{max}$, and μ along the minor hysteresis loop should be about $5 \mu_0$ for any contemplated material (Refer to subparagraph 2.). D will be on the order of 5 km/sec. Thus, R_m is on the order of 1/3 and will be less for a finite load resistance or a magnetic material having a μ less than $5 \mu_0$. A value for R_m of 0.1 is reasonable for the present analysis.

Thus neglecting $I \dot{L}$ compared to $\sigma B D e$ in Equation 3 is justified. By omitting it, Equation 3 becomes:

$$\dot{I} + \frac{R}{L} I = \frac{\sigma B D e}{L} \quad (R_m \ll 1) \quad 9$$

This is recognized as a first-order linear differential equation. An integrating factor is:

$$\exp \int \frac{R}{L} dt \quad 10$$

where R is assumed constant and L is given by Equation 4; α , B , D , and e are also constant. Solving Equation 9 for I is accomplished by standard techniques; therefore, the final result only is given (13). With the initial condition that $I = 0$ at $t = 0$, there results:

$$I = \frac{\alpha B D e}{R} \left[1 - \left(1 - \frac{tD}{c_0} \right)^{\frac{1}{R_m}} \right] \quad (R_m < 1) \quad 11$$

This expression is drawn in Figure 38 for $R_m = 0.1$. For R_m small compared to 1, the second term in brackets goes to zero in a small fraction of total event time, $t_0 = c_0/D$. This leaves a steady-state current:

$$I_0 = \alpha B D e / R. \quad 12$$

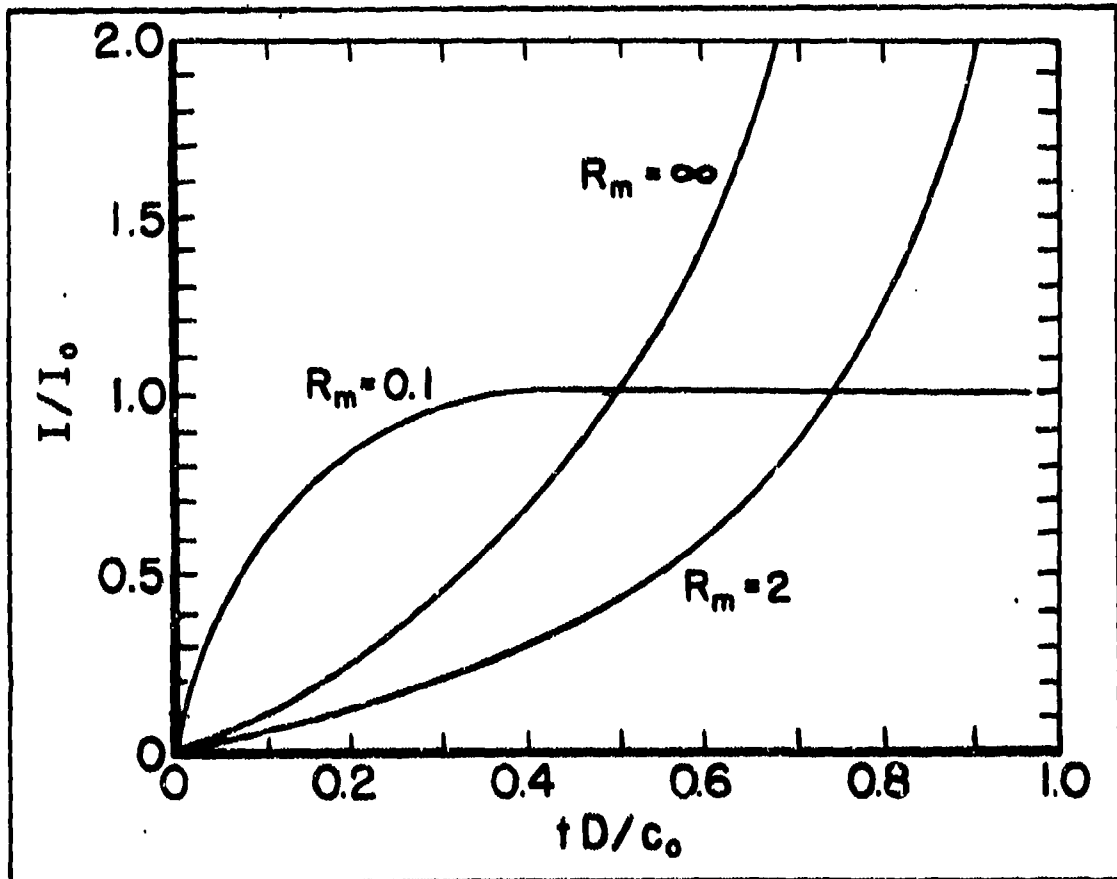


Figure 38. Load current versus time for the circuit of Figure 36

If the inductive term, IL , is included in Equation 3, then the exponent in Equation 11 becomes $1/R_m - 1$ instead of $1/R$. The character of current versus time changes as R_m increases past 1. The current will rise continuously as the inductance decreases. For very large values of R_m , essentially all the initial magnetic flux, BA , is trapped; or in the words defining R_m , the magnetic flux is transported ahead of the advancing conductive detonation wave instead of diffusing through it (14). Figure 38 also shows the current for $R_m = 2$ and $R_m = \infty$. In this case, I_0 is the initial equivalent surface current, $H_0 b$, due to the permanent magnetization.

1) Power and Efficiency, $R_m \ll 1$

Consider the electrical power output of the circuit in Figure 37 in the low R_m case after the steady-state current, I_0 , is attained. It is known from elementary circuit theory that for maximum power transfer to the load:

$$R_p = R_L = e/\sigma \bar{a} b. \quad 13$$

The power, K , delivered to the load is $I_0^2 R_L$, which for this matching condition reduces to:

$$K = \frac{\sigma \bar{a}^2 B^2 D^2}{4} (\bar{a} b e) \quad 14$$

where $\bar{a} b e$ is the effective volume of the conducting detonation products. A useful figure of merit is the power per unit cross section undergoing detonation, or K/be . Putting the following expected values of the parameters into Equation 14 results in:

$$K/be \approx 10^7 \text{ w/m}^2 \quad 15$$

where $\sigma = 10^3 \text{ mho/m}$

$B = 1.5 \text{ tesla}$

$D = 5 \text{ km/sec}$

$\bar{a} = 10^{-2} \text{ m}$

For example, a device 0.1 m on a side should produce 100 kw. To obtain an idea of the efficiency of this power conversion, consider the rate at which magnetic energy stored in the undetonated material, M , is decreased by virtue of the detonation process. The rate per unit area, M/be , equals $(BH)D$; $(BH)_0$ is of the order of 0.1 joule/cm, and, again $D = 5 \text{ km/sec}$. Thus $M/be \approx 5 \times 10^6 \text{ w/m}^2$.

The ratio of electrical power generated to magnetic energy destroyed is then K/\dot{M} , which can be considered an efficiency, call it η_1 .

$$\eta_1 = K/\dot{M} = \frac{\sigma a^2 B^2 D \bar{a}}{4 (BH)}$$

16

η_1 is on the order of one or two percent.

Another comparison can be made with the rate of chemical energy liberated. Even with a composite that is 20 percent by volume explosive, the chemical energy density is over 1 kJ/cm³. Comparing this with the K of Equation 14 shows an efficiency based on rate of liberation of chemical energy is so low as to be meaningless.

2) Power and Efficiency, $R_m > 1$

Since power delivered to the load is proportional to I^2 , it is seen from Figure 38 that greater power is produced when the magnetic Reynolds number is increased. The energy conversion efficiency, η_1 , can be 1 or more as R_m increases past 1. In Reference (10) the device of Besançon, et al., showed magnetic-energy recovery factors of 1000. Magnetic flux is not passed over but gathered up and compressed by the current sheet in the ionized zone. As the flux is transported forward and contained in a smaller area, B increases, offering a higher magnetic pressure for the detonation products to work against; but the detonation pressures are still orders of magnitude higher than any realistic magnetic pressure even with $R_m > 1$. Hence, the hydrodynamics of the process should remain unchanged; that is, the detonation rate, D, should not slow down. For this same reason, the amount of electrical energy obtained will still be a small fraction of the initial chemical energy.

It now appears that the best way to obtain the maximum output from this technique is to make the composite mostly magnetic material with just sufficient explosive present to maintain a steady rate of detonation. The restriction, of course, being that the conductivity and velocity of the detonation area are sufficient to make $R_m > 1$.

No matter which limit of magnetic Reynolds number is assumed, electrical power and energy will be produced. Because the high R_m case offers such tremendous increases in power, the process should be examined with the thought of achieving operation in this regime.

2. Magnetic Materials

The microscopic reaction zone process is admittedly complex. Microscopic difficulties were circumvented by taking the larger macroscopic view; averaged quantities were assumed. It is the main purpose of this presentation to establish the averaged magnetic material properties, such as the value of μ to use in determining R_m in Equation 8. The use of

magnetic materials dispersed in a nonmagnetic matrix is an established practice, so the following is intended as a brief review of proven concepts applicable to the present problem.

a. Permanent Magnetism

The origins of the magnetic properties of metals reside with the intrinsic spin of the electrons orbiting the individual atom. Each atom has a magnetic moment depending on the arrangement of electron spins in certain electron shells. In the metals iron, nickel, and cobalt, and their alloys, a mechanism called "exchange interaction" allows a large number of neighboring atoms to keep their magnetic moments aligned against the thermal agitation to randomize them. The result is a large number of such "domains", each having its magnetic moment in a different direction, so there is no net macroscopic moment in the material. This is called the demagnetized state. When a specimen is put into a magnetizing field, the domains begin to line up, producing a net magnetization. When the magnetizing field is slowly decreased to zero, a large majority of the domains remains aligned, producing a permanent magnetic field in the material; this is the basis for the hysteresis curve of iron and other similar metals. (See Figure 39.)

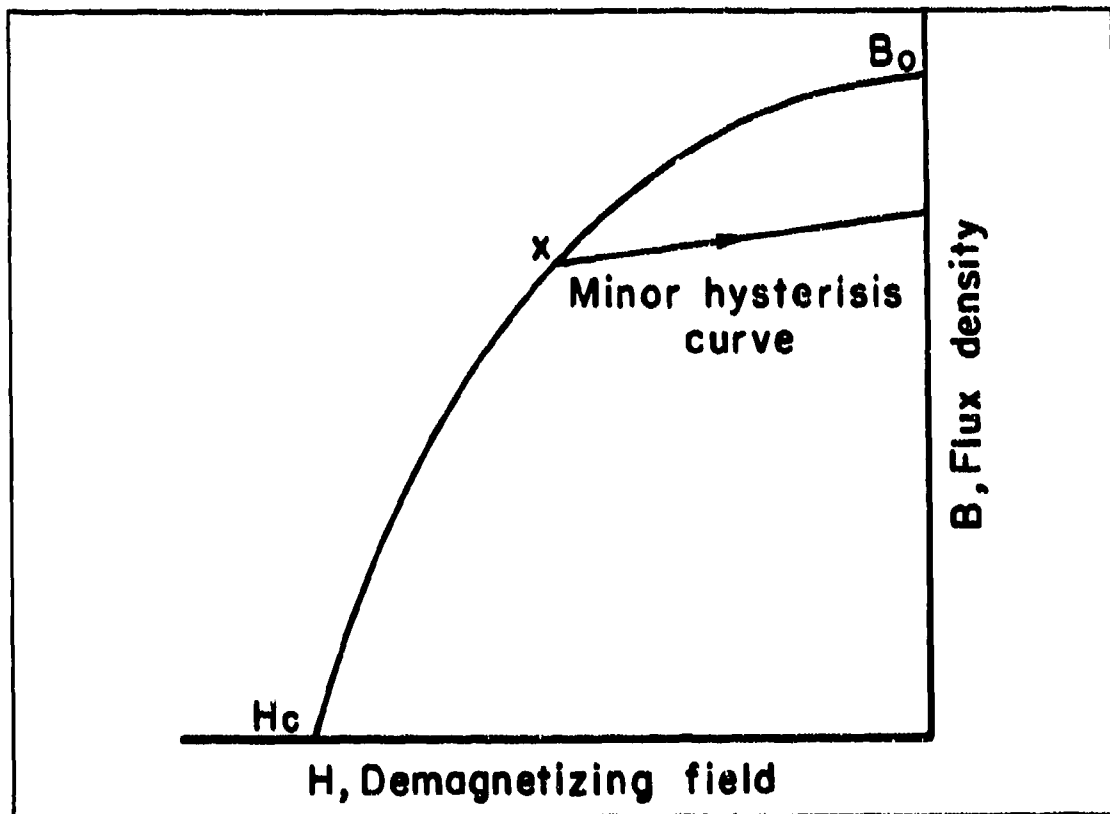


Figure 39. Typical magnet material demagnetization curve

The curve drawn is the upper left quadrant of a typical major hysteresis curve. During magnetization the state of the material moves from the origin to the upper right in a nonlinear fashion, not shown on Figure 39. When the field is brought to zero, the state of the material is B_0 . If demagnetizing fields are applied, the state of the material will follow the curve down to H_c , called the "coercive force". So far, the shape of the sample has not been specified. It is customary to assume a toroidal sample of material with the H-field supplied by a closely wound current-carrying coil. In addition to negative currents, there is another way of providing for a demagnetizing effect on the material; the toroid is cut to form an air gap. When the gap is small, the state in the material moves down the curve to some point, x, depending on the length of the gap and other factors of geometry. This is a stable condition of the magnet unless some other H-field, plus or minus, is applied to the material. A magnetic field is produced in the gap.

The magnetic field intensity in the gap is easily shown to be proportional to the volume of magnetic material relative to the gap volume and the BH product of the magnetic material. A minimum volume of magnetic material is necessary when the magnetic material state is at maximum BH product; for the curve of Figure 39, x is approximately at the maximum value.

In the present case, instead of a single gap in a magnet, a distributed gap is utilized and the effect is qualitatively the same. Fringing, which reduces the desired magnetic field in a single gap, is negligible with a distributed gap. If some positive magnetizing influence is applied, the state of the material will not move back up the curve toward B_0 , but will instead move along a minor hysteresis loop as indicated by the arrowed line. Since permeability is defined as B/H , then the slope of this line is the effective permeability of the gapped core. For most magnetic materials the slope of the minor hysteresis line equals the slope of the major hysteresis curve at B_0 . Actual values of μ are about five times μ_0 , the free space permeability, for the more common permanent magnet materials (Alnico V) (15). The actual magnetizing current of interest is that which flows through the detonation zone and electrode structure.

b. Composite Material

The above conclusions regarding the similarity of a distributed gap can be confirmed by reference to the information available concerning "dust cores", developed mainly for high-frequency electronics applications. Because the highly permeable materials most often used are also highly conductive of electricity, eddy current losses become prohibitive as the frequency is increased ($\sim f^2$). Laminating is one successful way to reduce these losses, but practical and economic limits are reached. A very fine powder of magnetic material suspended in an insulating binder successfully reduces eddy currents, giving excellent high-frequency results. Of interest in this study is the permeability of such a composite. Because of the distributed air gap, one can simply deduce the composite permeability by considering the particle length in series with an air gap length, then

applying Ohm's law to the magnetic circuit for reluctances in series (16).

As expected, the composite permeability is much reduced over that of the magnetic material. But the criteria of a gap length and particle length are difficult to formalize for arbitrary particle geometries and percentage of materials present. A better expression due to Howe gives composite permeability as a function of the volume fraction of magnetic material, P (17).

$$\frac{\mu_T}{\mu_o} = \frac{\frac{\mu_c}{\mu_o} - \frac{2}{3} (1 - P) \left(\frac{\mu_c}{\mu_o - 1} \right)}{1 + \frac{(1 - P)}{\left(\frac{\mu_c}{\mu_o - 1} \right)}} \quad 17$$

Where μ_c = particle permeability (incremental)
 μ_o = free space permeability
 μ_T = composite permeability

For instance, a material permeability of 200, with $P = 0.9$, yields a composite permeability of 23. Again, practical values of incremental permeability of permanent magnet materials are around 20, so for $P = 0.9$, values of composite permeability of about ten result.

c. Effect of Permeability on R_m

The range of μ in Equation 8 can be between one and ten from the foregoing discussion, depending on the volume fraction of magnetic material in the composite. It can also be stated that if R_m is low, then the present concept is very inefficient as an energy conversion device. The only purpose of the magnetic material will be to provide a weak field between particles for a $U \times B$ generator action. The stronger the gap field becomes by adding more magnetic material, the less gap volume there is for the interaction. On the other hand, with R_m large, the magnetic energy, BH , is swept up by the conduction wave; the more magnetic material present, the more energy recovered in the load.

Present magnetic materials have a storage energy density at BH_{max} of about 0.1 joule/cm³. There is every reason to believe that higher energy densities will be attainable in the future (18). For example, single-domain, elongated iron particles have a maximum energy product of 0.3 joule/cm³, and attain this value when the packing fraction, P, is 2/3. Adding cobalt can even increase that value to 0.4 joule/cm³. These materials owe their high-energy product to shape anisotropy.

If high R_m operation is assumed, then as magnetic energy is swept up by the detonation-produced current sheet, the magnetic field, B, necessarily increases in the undetonated material. This will be resisted by the eddy currents in the magnetic particles. Because their

conductivity is needed in the detonation zone to increase the overall conductivity, it should not be reduced as is done in ferrite cores. Keeping the particles small will alleviate this somewhat as an alternative to decreasing particle conductivity.

3. Conductivity

Often in the development of new devices, the main parameter on which success or failure hinges is the one about which least is known. In this particular study the electrical conductivity of the detonation products results from a regime of physical conditions that has been theoretically intractable.

To understand the nature of the present problem, it is necessary to review briefly the basic law of electrical conductivity applicable to any medium. In addition to the review of conductivity theory, past experimental work relating to the present problem is reviewed. The basic electrical conductivity of most condensed explosives is found to be low, and detonation velocity is decreased when inert additives are present. A simple theory is developed which shows that conductivity can be increased substantially by the presence of the magnetic additive or dopant.

Consider an isotropic medium in the absence of magnetic fields and the one-dimensional conduction of electricity through the medium by one species of charge carrier, for instance, electrons.

By definition (Ohm's Law):

$$J = \sigma E \quad 18$$

Where J is the current density resulting from the conductivity, σ , of the medium, on application of an electric field, E . On a microscopic scale the current density results from a density of charge carriers, N , each carrying charge, q , moving through the medium at some velocity, $\langle u \rangle$, or:

$$J = N q \langle u \rangle \quad 19$$

where $\langle u \rangle$, the drift velocity, is an averaged quantity resulting from acceleration of the carriers by the electric field ($a = qE/m$), balanced by "frictional" collision processes. The drift velocity thus becomes proportional to E :

$$\langle u \rangle = \theta E \quad 20$$

where θ is called the mobility. Combining Equations 18, 19, and 20 yields:

$$\sigma = Nq\theta \quad 21$$

If more than one specie of charge carrier is present, then the total conductivity is the sum of the individual conductivities over "i" species:

$$\sigma = \sum_i N_i q_i \theta_i \quad 22$$

From Equation 22, it is seen that the requirements for high conductivity are either a high carrier density or a high mobility, or both.

The mobility can also be written in terms of the mean free time, τ , between random encounters with other particles as:

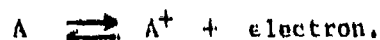
$$\theta = \frac{q \tau}{m} \quad 23$$

where m is the mass of the charge carrier (19). This explains why electrons with their much smaller mass have such high mobilities compared to ions.

The detonation products are a high-density fluid of molecules, atoms, ions, and electrons with temperatures on the order of 5000° K and pressures of about 100 kilobars. The density of this fluid can be as high as the density of the lighter metals (magnesium). Thus conductivity of the fluid can be thought of as a special case of conduction in a crystalline metal. Metals owe their high electrical conductivity to the regular array of atoms in a lattice and consequent long mean free time, τ , of the conduction-band electrons.

As the temperature of a metal increases, the atomic vibrations perturb the lattice and interfere with the electron motion; that is, τ decreases, resulting in decreased mobility of the electrons (Equation 23). In general, the conductivity of a metal is explained by band theory which has a quantum mechanical foundation. The essential feature is that the stationary lattice of the atoms forms a periodic potential for the electron wave functions. Extrapolation to the temperature of a high-density plasma fails as the lattice structure is destroyed. The atoms interact more violently, and the electrons encounter perturbing forces more often, decreasing τ ; hence, decreasing the mobility of the electrons further. Although there is no lattice, the atoms are still tightly packed and conduction is by transfer of conduction-state (bound) electrons.

Contrast this oversimplified picture with the classical notion of electrical conduction in a hot, partially-ionized, dilute gas. A velocity distribution of the particles represents the temperature of the gas ($1/2 m \bar{u}^2 = 3/2 kT$). At a sufficiently high temperature, particles in the tail of the distribution will have enough energy to liberate electrons upon collision with other heavy particles. Thus, by collision, some bound electrons achieve energy equalling the ionization potential. Free electrons are created having a mobility which depends on the time between scattering collisions with the heavier particles. The number of free electrons can be calculated from the Saha equation, which is essentially an equilibrium constant for the chemical reaction:



For small degrees of ionization, the number of electrons, N_e , is exponentially dependent on temperature and inversely dependent on $p^{1/2}$, where p is the total pressure. For some arbitrary degree of ionization, at constant temperature, two things happen as the pressure and density are increased toward the conditions of interest. First, because of high density, the time between collisions decreases, which tends to depress mobility. But charged electrons are now so numerous that they begin to cluster around ions and screen the coulombic potential, the net effect of which is to reduce the effective ionization potential of the plasma; hence, N_e increases. Also, the electrons can no longer be considered completely free. Because the lower ionization potential increases the electron density in an exponential manner while the decrease in mobility is essentially inversely proportional to total particle density, it is expected that overall conductivity increases at high pressure or density.

A theory that accounts for these effects in an attempt to explain electrolytes and stellar plasmas is known as the Debye-Hückel shielding theory (20). This theory has a rigorous theoretical basis, but it fails on extrapolation to cover the nonideal gas at high densities. For instance, in evaluating corrections to the ionization potential, the correction turns out to be larger than the original potential.

It is thus seen that an explosive plasma is in a "no-man's land". On one hand, it is like a metal but lacks a lattice; and on the other hand, it is such a dense gas that corrections to the classical kinetic theory of gases become meaningless. No matter which viewpoint is adopted, it is clear that the density is high enough for quantum effects to be significant. The virial theorem yields an equation of state which naturally accounts for the interparticle, quantum mechanical forces. Classically, the theorem states that for central forces, bound motion, the average kinetic energy equals $-1/2$ the average potential energy.

Cook has discussed the virial formulation to account for electrons in the detonation zone of high explosives and derived what is called the pulsating orbital model (21). One prediction of the theory is the strong cohesive property of explosive plasma which has been observed (22).

More recently, Robinson (23) compared the virial formulation for internal energy of a water-derived plasma at 100-kilobar pressure with experimental data. Qualitative agreement was shown, using a simple interparticle force law and simplified two-step energy levels in the two-species plasma. The weakness of the virial theorem is that all of the interparticle relations must be known or assumed; for a complex molecular gas with "many-body" collisions this is formidable. For even a simple two-component plasma, the computational effort is prodigious. Investigators are only now beginning to attack this problem.

a. Review of Related Experimental Work

In spite of theoretical difficulties that are just beginning to be contemplated, experimental results have been accumulating, especially in the last decade, which have given very definite insight into detonation-product electrical conductivity. Several pertinent facts related to electrical conductivity conditions are repeated here.

The ionization and consequent electrical conductivity in a condensed high explosive is limited to the detonation-head zone and does not extend into the colder expanding products. The detonation-head zone refers to that space between the end of the reaction zone and the beginning of the rarefaction wave. The reaction-zone thickness is typically less than 100 microns while the detonation-head zone can be from a millimeter to several centimeters, depending on charge size, geometry, and degree of confinement. As the rarefaction wave progresses into the conducting steady zone, it reduces the pressure and temperature of the fluid, thus producing increased velocity of the products. The degree of ionization which is strongly temperature-dependent decreases drastically in the colder products; previously free electrons quickly recombine. Any lattice-type conduction effects disappear because of the reduction of pressure. The rarefaction wave effectively cuts off any further electrical conductance.

The detonation-zone conductivity varies with the explosive composition but is generally in the range of 10 to 100 mho/m. A very accurate measurement has been made for Composition B and Pentolite at normal density by Jameson, et al. (24) with values of 330 and 110 mho/m respectively.

Experiments by Blish, et al. (25) have confirmed that as the density of the products increases, the conductivity increases. An exponential dependence was found such that at the pressure of 650 kilobars, a conductivity of 10^4 mho/m was determined in TNT. They also allude to experiments in which the conductivity of the detonation products is related to the free carbon content in the products. Lead azide also had a high conductivity, presumably due to free lead.

More recently, Hayes (26), as a result of a new technique for spatially resolving conductivity phenomena up to the very front edge of the reaction zone, found a definite relation between conductivity and the free carbon content in the reacting gas. The amount of free carbon shifts continuously throughout the detonation head because of shifting equilibrium constants for the components of the products formed. The maximum conductivity measured is tabulated against the free carbon content existing at the same position in the products, as follows:

<u>Explosive</u>	<u>Max σ (mho/m)</u>	<u>Product Carbon Content (gm/cm³)</u>
PETN	60	0.08
Nitromethane	160	0.19
Composition B	1,200	0.34
Liquid TNT	11,000	0.52

Hayes also pointed out the inverse dependence of conductivity on temperature. If thermal ionization were the controlling factor, then the conductivity would increase substantially at higher temperatures. But calculations by Mader showed that in PETN, as the initial explosive density changed from 1 gm/cm³ to 1.7 gm/cm³, the temperature dropped from 4000° K to 3000° K, while the conductivity increased roughly a factor of ten (27). The conductivity increase more closely resembled the rise in pressure from 100 to 300 kilobars.

This certainly confirms the experiments by Brish. The conclusion is that temperature of the plasma can only play a secondary role in the conduction process. Electrons generated by thermal ionization contribute to conductivity, but perhaps the largest contribution is from the bound conduction-state electrons in the quasi-metallic lattice.

As will be shown later, to obtain a high conductivity the conductivity of the magnetic particles is utilized. However, this increase is not without penalty, for the magnetic particles are effectively a diluent in the explosive and tend to suppress the detonation velocity. Since all other properties can be related to velocity, it may well be that the conductivity is decreased also.

By far the most extensive documentation to this effect is that by Taylor (28). Results of his experiments point out several factors which were used to guide the present experiments. In tests using NaCl as a diluent for nitroglycerin at 1.35 gm/cm³ and PETN at 1.00 gm/cm³, there is an almost linear decrease in the detonation velocity; in the case of PETN, a drop from 5.5 km/sec for 100-percent PETN to 3 km/sec for 40 percent by weight PETN was observed. A similar drop occurs for nitroglycerin. The data fit a theory that assumes complete entrainment of the diluent and some heat transfer from the gas to the diluent. The depression of the detonation velocity occurs primarily because of the translational energy lost by the gas phase in accelerating the diluent, and secondarily because of energy lost by heat transfer. The energy spent by the gas in compressing the diluent is found to be negligible by comparison with the above effects and would only change the detonation velocity on the order of 1 percent. Also of interest is the fact that diluent particle size is relatively unimportant in determining detonation velocity through the range of 30 to 72 Brown and Sharp sieve fineness.

What could actually happen is the exact opposite of the desired enhancement. The heat transfer from the reaction products to the colder particles may form a cold sheath around the particles which acts to isolate them as electrical current carriers. Furthermore, since the gas phase has lost energy (both thermal and kinetic) by heat transfer and drag acceleration of the particles, its electrical conductivity is reduced below that existing without a diluent, whether metal or nonconductor. One possible but rather unlikely means to eliminate this as a source of conductivity decrease is to have the particles react exothermally with the explosive on detonation. The magnetic particles, if fine enough, could react with an overoxidized explosive to maintain the high heat-release necessary for adequate conductivity. Experience with the aluminized commercial explosives shows this is not the case; detonation velocity and peak pressure are both reduced (21). Perhaps ultimately an inherent exothermic magnetic material could be developed that would not have a diluent effect like aluminum, which reacts only on the surface. Then, however, no conductivity enhancement would be possible through the mechanism of metallic inclusions.

b. Conductivity Increase by Metallic Addition

In the first paragraphs of this presentation on conductivity, it was concluded that at the present state-of-the-art it is impossible to calculate the electrical conductivity of a detonating high explosive on theoretical grounds. However, given a particular explosive and experimentally determined conductivity data, it is possible to calculate for simple cases what the conductivity increase should be when conducting inclusions are added. The only restrictive assumption is that the inclusions do not chemically react and thereby change the initial conductivity. Furthermore, it is assumed that no heat transfer occurs between explosive and diluent particles.

c. Cubical Array of Cubic Inclusions

To understand the important parameters affecting conductivity increase, assume the somewhat oversimplified structure in Figure 40(a).

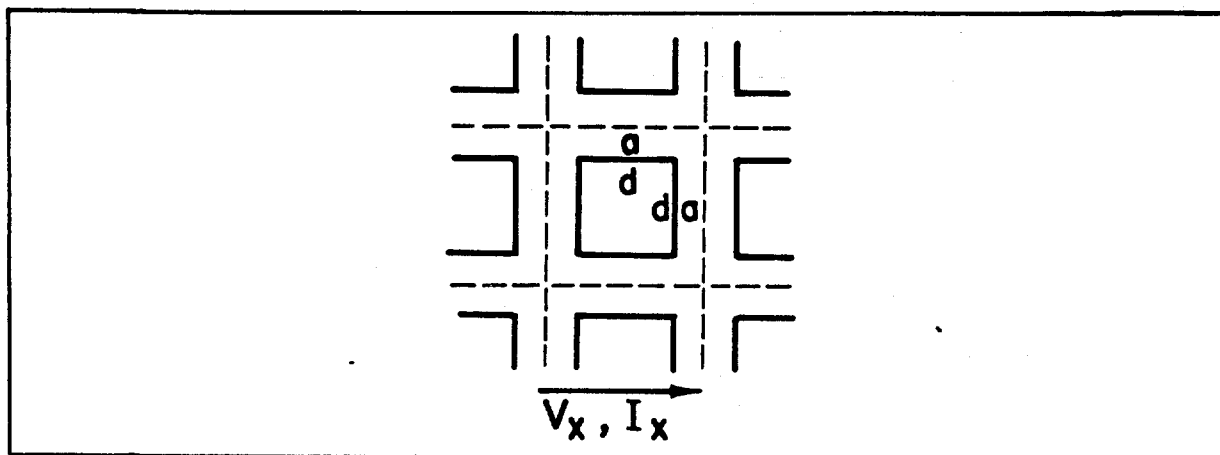


Figure 40(a). Cube model for conductivity enhancement - unit cell

It is a uniform conducting medium containing a simple cubic array of cubic inclusions. Making the assumption of one-dimensional current flow (along the x-axis) allows choosing the unit lattice shown by dotting. The total resistance to current flow will then be that due to the volume of inclusion of conductivity, σ_c , in series with the small volumes of σ_o , paralleled by the hollow cube of σ_o , as shown in Figure 40(b).

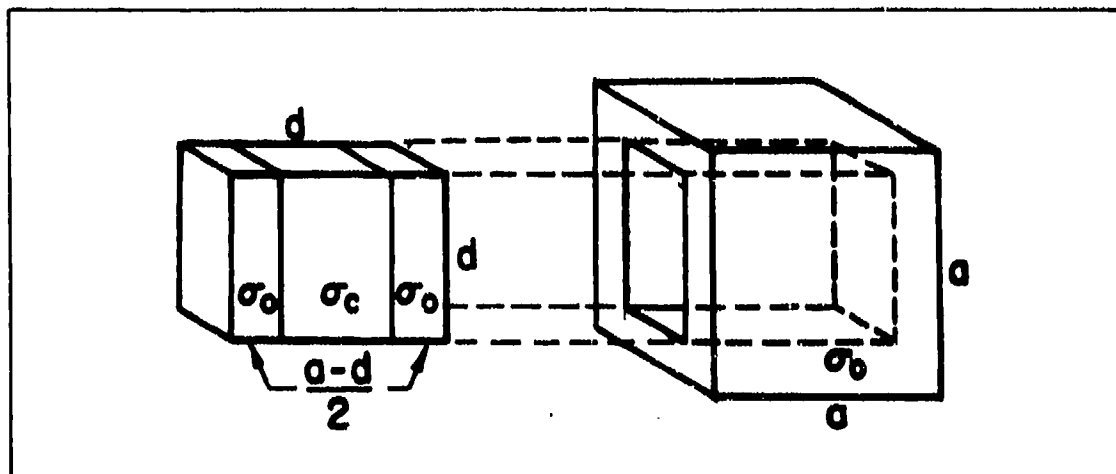


Figure 40(b). Cube model for conductivity enhancement - breakdown of unit cell

The electrical schematic for this is shown in Figure 40(c).

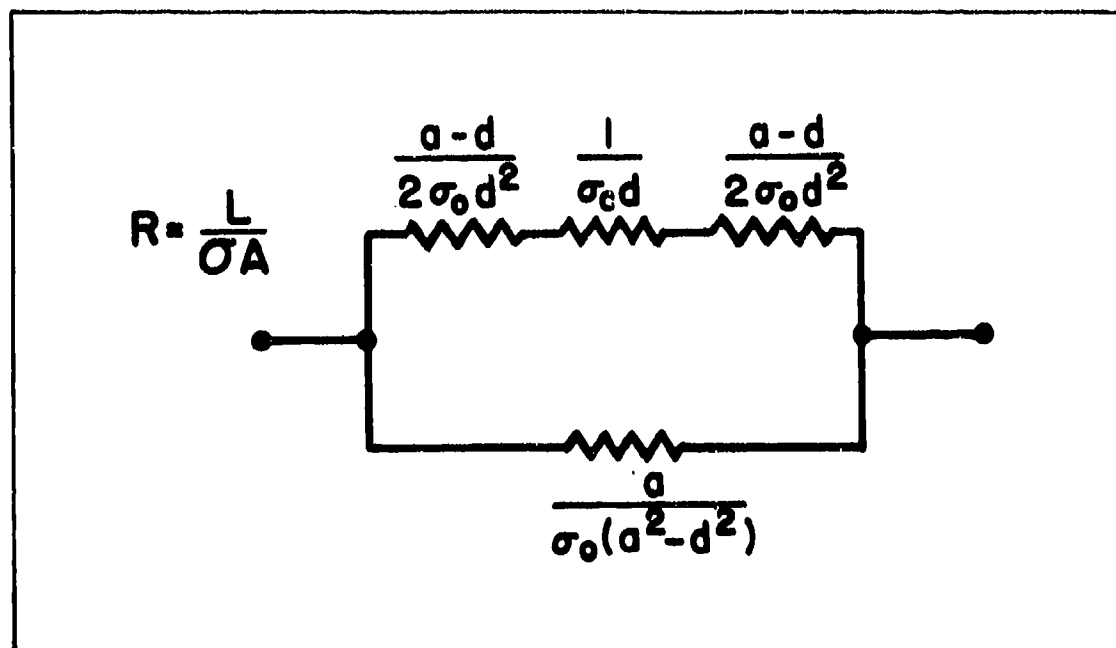


Figure 40(c). Cube model for conductivity enhancement - equivalent network

The total resistance, R_T , can then be written as:

$$\frac{1}{R_T} = \frac{\sigma_T a^2}{a} = \frac{1}{\frac{1}{\sigma_o d} + \frac{a-d}{\sigma_o d^2}} + \frac{1}{\sigma_o \frac{a}{a^2 - d^2}} \quad 25$$

since paralleled resistors combine reciprocally. The important ratio σ_T/σ_o is easily obtained from Equation 25:

$$\frac{\sigma_T}{\sigma_o} = \frac{d^4}{ad^2(a-d) + \frac{\sigma_o d^3}{\sigma_o}} + \frac{a^2 - d^2}{a^2} \quad 26$$

The ratio of σ_o/σ_o is small ($\sigma_o \sim 10^2$ mho/m and $\sigma_o \sim 10^7$ mho/m), so neglecting it is justified and results in:

$$\frac{\sigma_T}{\sigma_o} = \frac{1}{\frac{a}{d} \left[\frac{a}{d} - 1 \right]} + 1 - \frac{d^2}{a^2} \quad 27$$

The important variable is the volume fraction of inclusion in the total of the composite, or d^3/a^3 , denoted by P . In terms of P , Equation 27 becomes:

$$\frac{\sigma_T}{\sigma_o} = \frac{P^{1/3}}{\left[\frac{1}{P^{1/3}} - 1 \right]} + (1 - P^{2/3}) = \frac{1 - P^{1/3} + P}{1 - P^{1/3}} \quad 28$$

This relation is plotted as Curve 1 in Figure 41. Equation 28 can be put into more compact form by expanding the denominator:

$$\frac{\sigma_T}{\sigma_o} = 1 + \sum_{n=0}^{\infty} P \frac{n+3}{3} \quad 29$$

which converges for all $P < 1$, with an asymptote at $P = 1$ as expected. It is important to note this model allows an inclusion fraction, P , from zero to 1. When the cubes touch, the conductivity becomes that of the cube material. The final result contains no factor that accounts for a finite ratio of conductivities, σ_o/σ_o , as it was eliminated after Equation 26.

d. Simple Cubic Array of Spheres

A more realistic, classical case of conductivity increase has been studied by Ruleigh (29) and more recently by Meredith and Tobias (30), Keller (31), and Keller and Sachs (32). The assumption of one-dimensional flow is not necessary. Rayleigh started with the arrange-

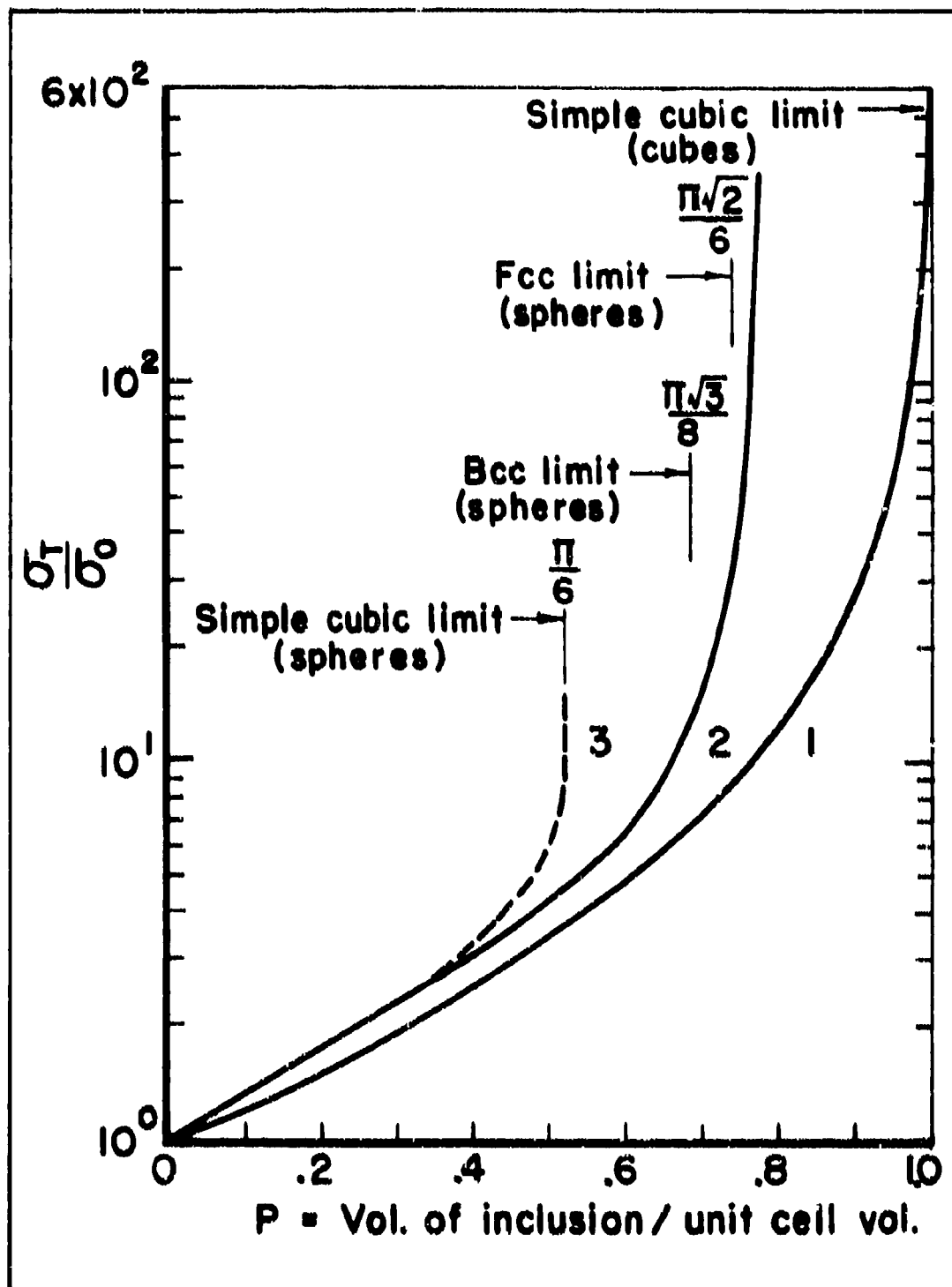


Figure 41. Conductivity ratio versus volume fraction of inclusion for simple cube model, Rayleigh's sphere model, and Keller's improvement near simple cubic limit

ment of Figure 42(a),

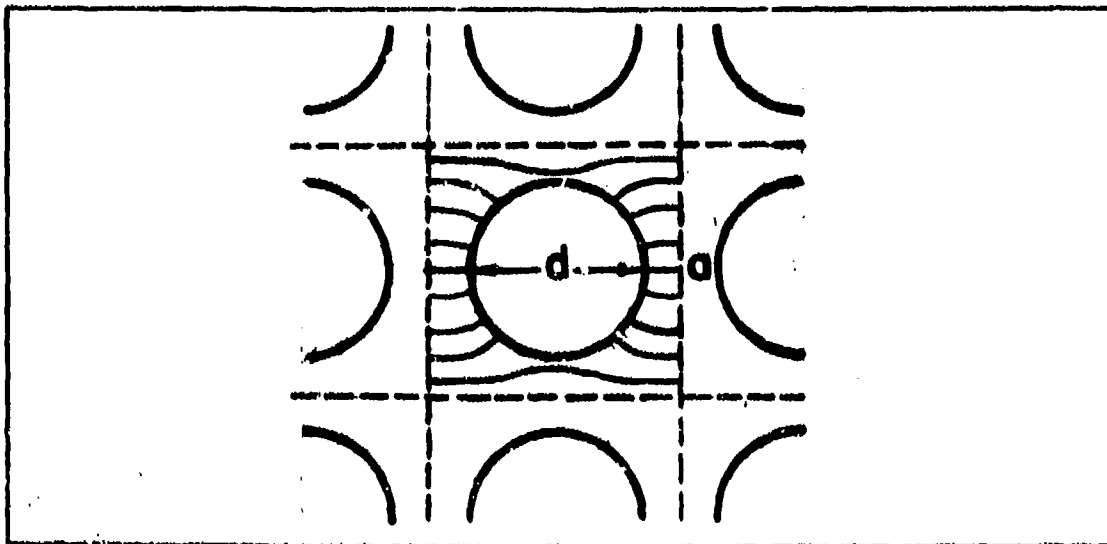


Figure 42(a). Simple spherical model for conductivity enhancement

where the unit cube is the same as in Figure 40(a). If an electrical potential is applied in the "x" direction, the current streamlines will be as pictured. The differential equation for the potential is:

$$\nabla^2 v = 0,$$

30

It is natural to use spherical coordinates with an origin at the center of the sphere. The boundary conditions are that the potential be continuous across the border of the sphere and that the electrical current likewise be continuous.

The potentials that result are given in terms of spherical surface harmonics. What complicates the analysis is that, by supposition, the potential at any point in the field is that given by all the spheres together. A series results which is terminated after superposing a solution for a basic sphere and its 248 closest neighbors to give an approximate expression for the conductivity ratio:

$$\frac{\sigma}{\sigma_0} = \frac{\left[\frac{2+\nu}{1-\nu} \right] - 2P - 0.525 \left[\frac{3-3\nu}{4+3\nu} \right] P^{10/3}}{\left[\frac{2+\nu}{1-\nu} \right] + P - 0.525 \left[\frac{3-3\nu}{4+3\nu} \right] P^{10/3}}$$

31

where P is the volume fraction of inclusion and ν is the ratio of conductivity, σ/σ_0 . For the case of interest, ν is effectively infinite, so Equation 31 reduces to:

$$\frac{\sigma_T}{\sigma_0} = \frac{1 + 2P - 0.525P^{10/3}}{1 - P - 0.525P^{10/3}}$$

32

This relation is plotted as Curve 2 in Figure 41. Rayleigh's solution is approximate and has been refined by others. The main objection to it is that for the simple cubic arrangement the maximum allowable value of P allowed is $\pi/6$. Rayleigh makes no mention of this limitation.

Keller has considered an exact solution of potential flow for simple cubic packing of spheres close to the limit of $\pi/6$. His result is shown as the dotted Curve 3 in Figure 41. Experimental results by Meredith and Tobias confirm Keller's analytical calculation.

Also shown for reference in Figure 41 are the values of P that occur if face-centered cubic and body-centered cubic packing are allowed. Curve 2 obviously should not be used for these cases.

The next portion presents a simple extension of Rayleigh's theory which makes it possible to get an approximate value of σ_T/σ_0 when P is greater than $\pi/6$, by allowing for more than one size of particles.

e. Multiple Size Conductivity Increase

The results of the preceding writeup pertain to a highly academic situation that could never represent any practical situation. First, any mixture would be nonuniform and without simple cubic packing. Second, any practical additive would have a size distribution instead of a single size. Spherical particles are technically feasible, so there is no shortcoming of the simple theory on this account.

To develop a method of accounting for conductivity increase when more than one size is present in the additive, consider first the simple case of an additive with three sizes present, as in Figure 42(b).

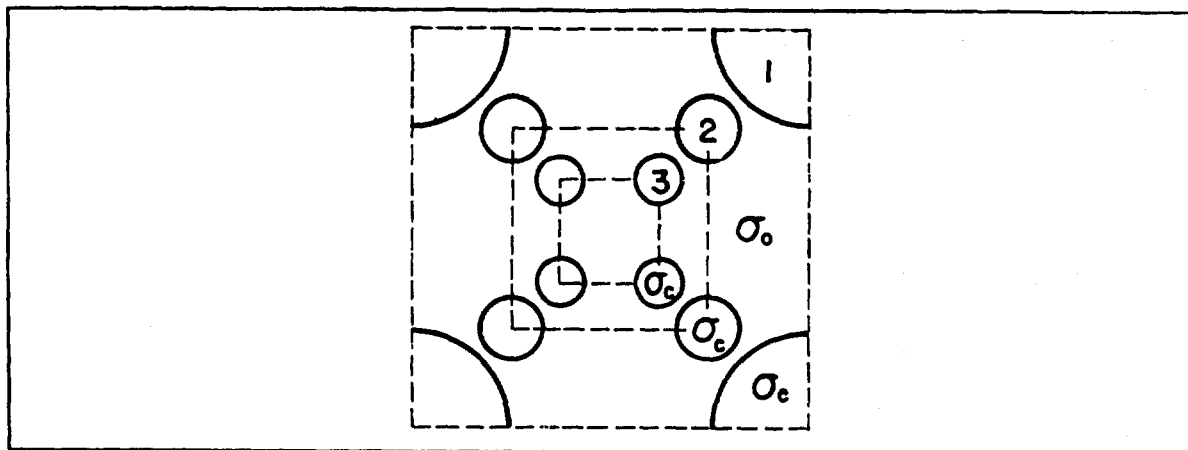


Figure 42(b). Multiple-size conductivity model

To show better the volumes of interest, the unit cube has been shifted by half the lattice spacing. Due to symmetry in all directions, this unit cube is just as satisfactory as the one in Figure 42(a), but the boundary conditions would be harder to specify. The theory to follow is not concerned with any electrical boundary conditions or superposition of potentials, but rests solely on the premise that each particle size contributes a conductivity increase so that the overall conductivity increase is the product of all conductivity ratios based on the volume fraction available to each species. For instance, in Figure 42(b), the smallest particle species, 3, increases the conductivity of the basic matrix of σ_0 to become a new matrix of:

$$\sigma_0' = \sigma_0 f(P_3). \quad 33$$

This becomes the σ_0 of a new matrix for unit cube 2 that has its conductivity increased by the presence of particle species 2, or:

$$\sigma_0'' = \sigma_0' f(P_2) \quad 34$$

and so forth. The overall conductivity increase for n particle sizes is then:

$$\frac{\sigma_T}{\sigma_0} = \frac{n}{\prod} f(P_n) \quad 35$$

where $f(P_n)$ is Curve 2 of Figure 41 for simple cubic packing and the P_n 's in this case are the species volume fractions that account for the space occupied by all other particles. To determine these volume fractions, start with the largest particles. The smallest particles could be chosen, but for practical reasons, only the largest is used. (It is relatively difficult to determine experimentally the distribution of the finer particles compared to the larger.)

The volume fraction for particle species 1 is:

$$P_1 = v_1 / v_T \quad 36$$

Where v_T is the total volume of the largest unit cube. The volume fraction for particle species 2 is then:

$$P_2 = v_2 / (v_T - v_1) \quad 37$$

Extending this process to n particle size results in:

$$P_n = \frac{v_n}{v_T - \sum_{r=1}^{n-1} v_r} \quad n > 1 \quad 38$$

Since the independent variable is the overall volume fraction, P_T ,

$$P_T = \frac{\sum_n v_n}{v_T} \quad 39$$

is used to eliminate v_T from Equation 38. Thus:

$$P_n = \frac{v_n}{\frac{\sum_n v_n}{P_T} - \sum_{r=1}^{n-1} v_r} \quad 40$$

which reduces immediately to:

$$P_n = \frac{P_T}{1 + (1 - P_T) \frac{\sum_{r=1}^{n-1} v_r}{v_n}}; \quad n \geq 1. \quad 41$$

For $n=1$, it is convenient to combine Equations 36 and 39 to get:

$$P_1 = \frac{v_1 P_T}{\sum_n v_n} \quad 42$$

In reducing the experimental data, the weight distribution for the particles is employed instead of volume fraction as it is measured directly.

When all additive particles have the same density,

$$\frac{\sum_{r=1}^{n-1} v_r}{v_n} = \frac{\sum_{r=1}^{n-1} w_r}{w_n} = \frac{\sum_{r=1}^{n-1} \gamma_r}{\gamma_n} \quad 43$$

where w is the weight of each size species, and γ is the weight fraction.

The important relations are collected using Equation 43.

$$P_1 = \frac{\gamma_1 P_T}{\sum_n \gamma_n} \quad 44$$

$$P_n = \frac{P_T}{1 + (1 - P_T) \frac{\sum_{r=1}^{n-1} \gamma_r}{\gamma_n}} \quad 45$$

$$\frac{\sigma_T}{\sigma_o} = \prod_n f(P_n) \quad 35$$

f. Description of Method

For computing theoretical values of σ_T/σ_o a value of P_T is chosen initially. The values for the various P_n 's are calculated for Equations 44 and 45 using the experimentally determined particle size distributions. For each value of P_n the appropriate $f(P_n)$ is found from Curve 2 of Figure 41, and Equation 35 is then used to calculate the overall conductivity ratio.

Figure 43 shows three curves drawn from such calculations for spherical copper powder samples. The dotted curve is based on the particle size percentage distribution furnished by the supplier, the Federal Mogul Co. In the calculation using the supplier's particle size distribution, it was assumed that all particles finer than 500 mesh were of one size, resulting in a total of six sizes. Actual measurements were made of the particle size distributions in both the copper powder and for a stainless-steel powder. These distributions are shown in Figure 44. These measurements resolved the finer sizes and indicate somewhat of a flat distribution near 10 percent. Therefore, the two solid curves on Figure 43 are drawn for 10 sizes of 10 percent and five sizes of 20 percent for comparison. A similar set of curves is shown in Figure 45 for the Type 316 stainless-steel powder, with the addition of a curve showing the expected results with particles of a single size.

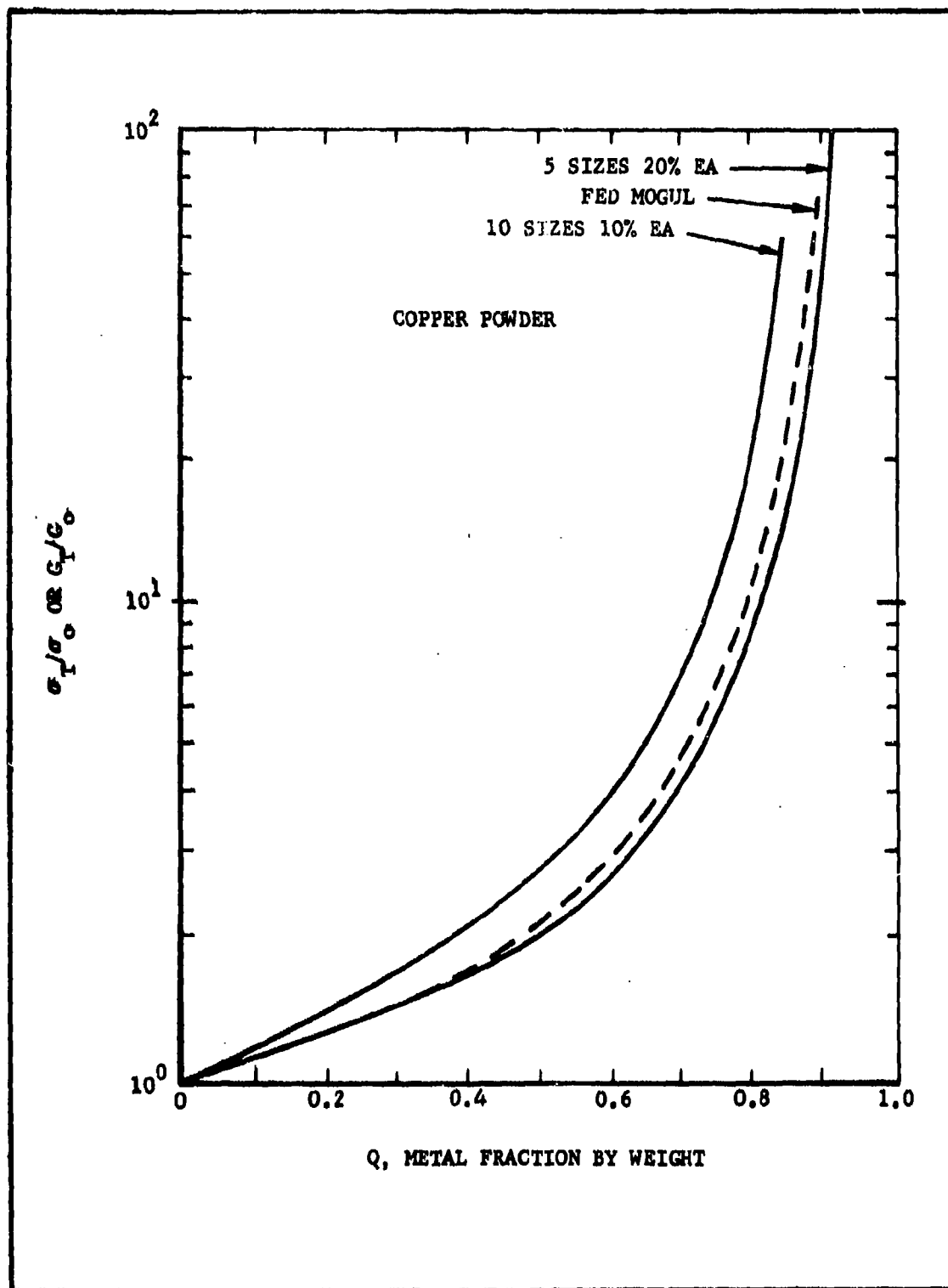


Figure 43. Theoretical conductance ratio G_T/G_0 as a function of the copper fraction by weight, Q

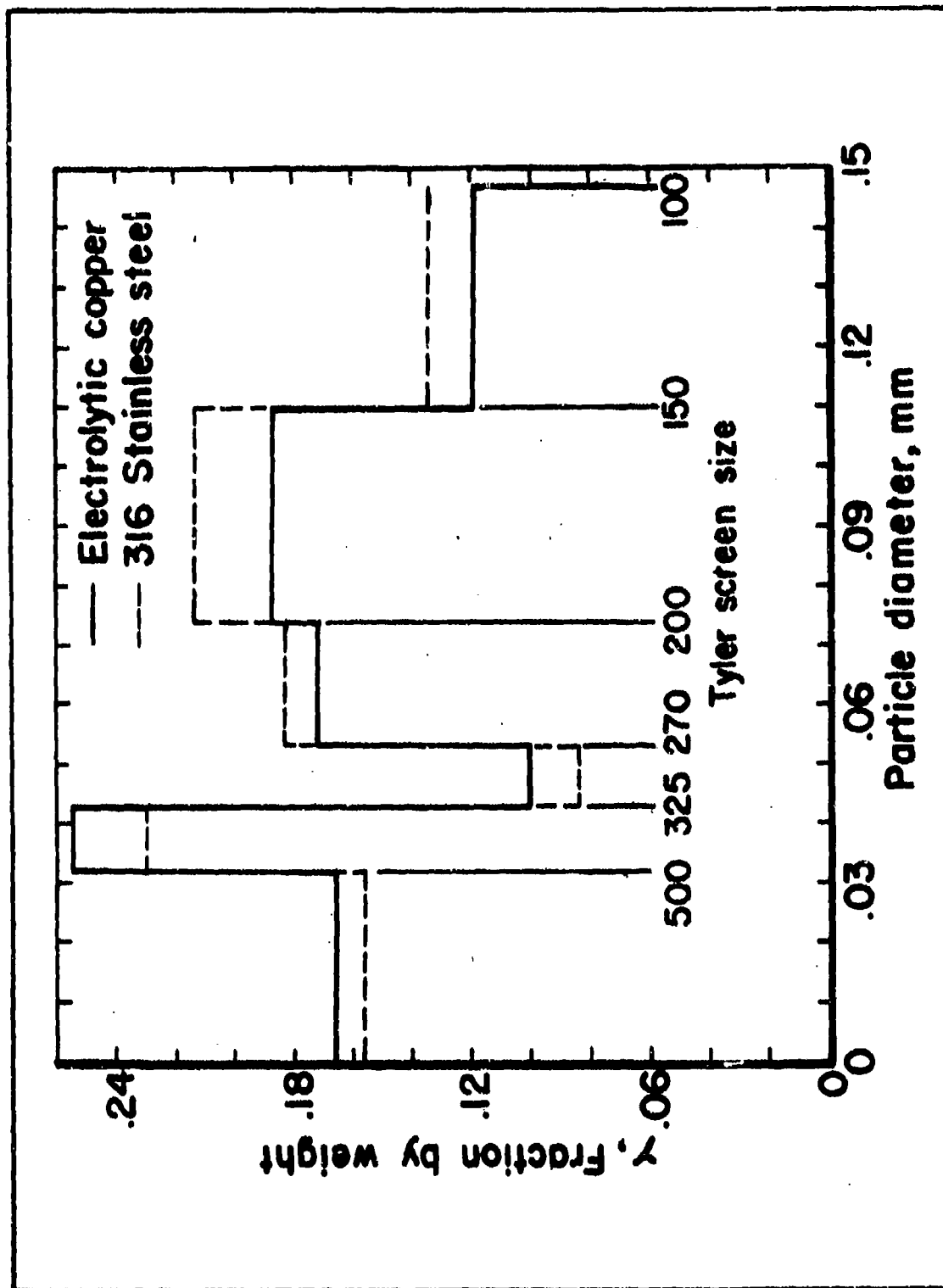


Figure 44. Particle size distributions

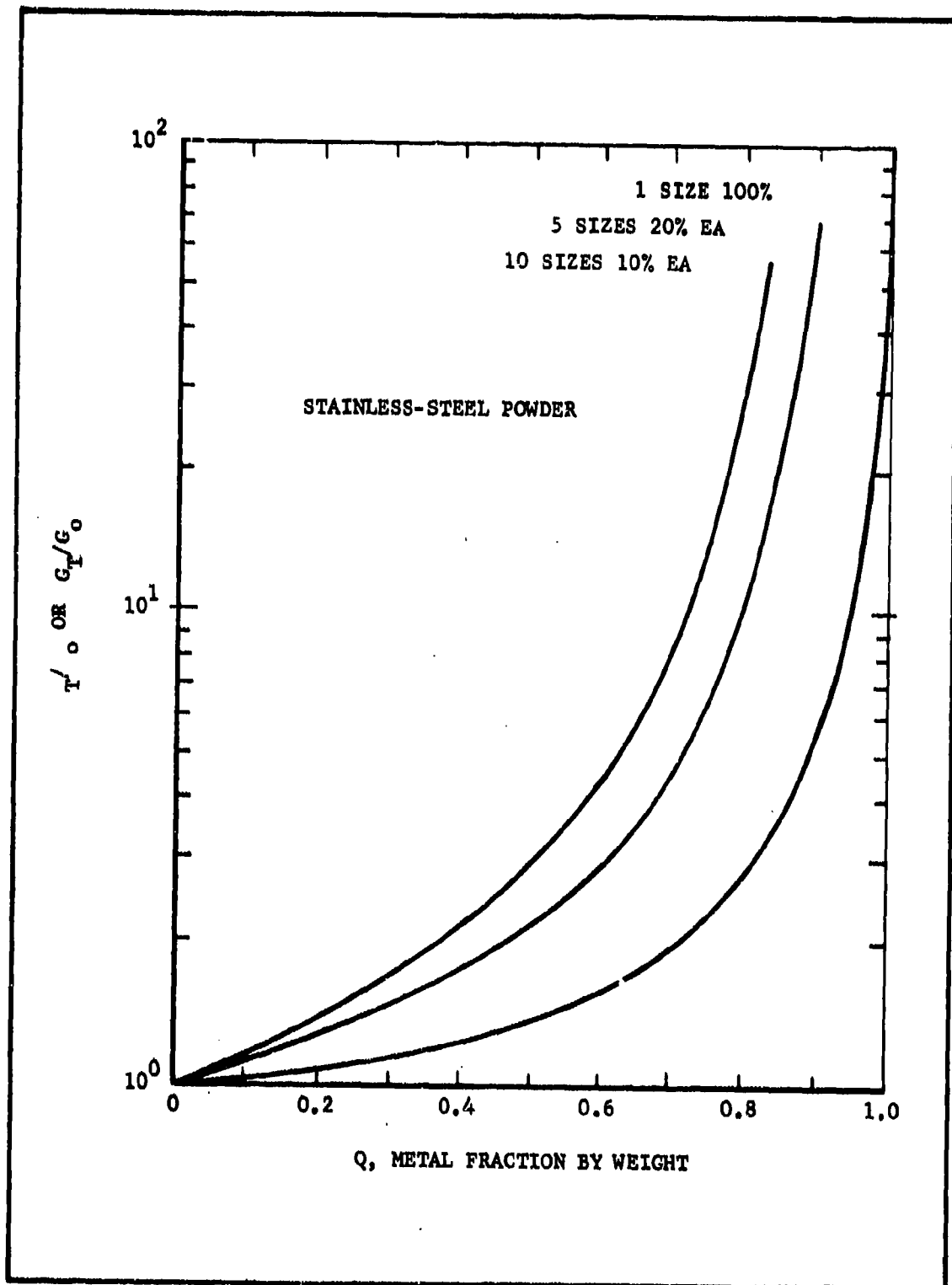


Figure 45. Theoretical conductance ratio G_T/G_0 as a function of the weight fraction of Type 316 stainless-steel powder, Q

C. CONDUCTANCE MEASUREMENTS

As discussed previously, electrical conductivity increase offers the only hope of producing the necessary high magnetic Reynolds number, R_m . Experiments by others have shown that generally detonation-zone conductivities are low, but the effects of high pressure or the presence of impurities can produce order of magnitude increases in this quantity. Therefore a series of experiments was performed to evaluate the possibility of increasing the conductivity by metallic inclusions or dopants. The experimental apparatus and techniques, together with the results of the experiments, are discussed in the following paragraphs.

1. Experimental Apparatus

a. Blast Tank Facility

To detonate safely a test charge of high explosive, many precautions are necessary. Because the amount of explosive used in any one shot is small, it was calculated that the experiments could be safely performed inside the laboratory. To contain fragments and the noxious gases of detonation, all firings took place in a wood-lined steel barrel, which has a removable cover for access to remove fragments and splinters and to patch any damage (frequent) to the tank. The tank and associated equipment are shown schematically in Figure 46, while Figure 47 shows the actual equipment. The test charge is installed in the tank through the small porthole in the top and suspended by the instrumentation cable approximately in the center of the tank. The wood lining successfully absorbs the fragments and blast impact, and needs replacing only after about 50 shots. The vacuum pump is used to reduce tank pressure, minimizing the blast potential on the walls; it also serves to purge the tank after firing. Propane is admitted before firing to suppress ionization in the air around the test charge, which could cause spurious signals on the measuring circuit.

When a new wood lining is installed, the moisture in the wood prevents obtaining sufficiently low pressure, so a cold trap of liquid air is used to condense out this moisture. After initial dehydration, no further cold trap action is needed. Pressure is measured with a standard U-tube mercury manometer, and for lower pressures, a 0 to 100 torr Wallace and Tiernan dial gage is used.

b. Firing Control and Safety Circuit

All detonations were initiated by electric blasting caps. To accomplish this safely and only at the proper time, the circuitry of Figure 48 was devised. The current requirement for the blasting cap initiation is adequately provided by the battery, B, in this case a 6-volt auto storage battery. In order that it is not fired until needed by inadvertent closing of firing switch, S_5 , a relay, RL_1 , is included in the basic series circuit of battery, cap, and S_5 . Before the relay will close, 110 volts ac must be supplied as shown; the main power switch, S_1 , must be

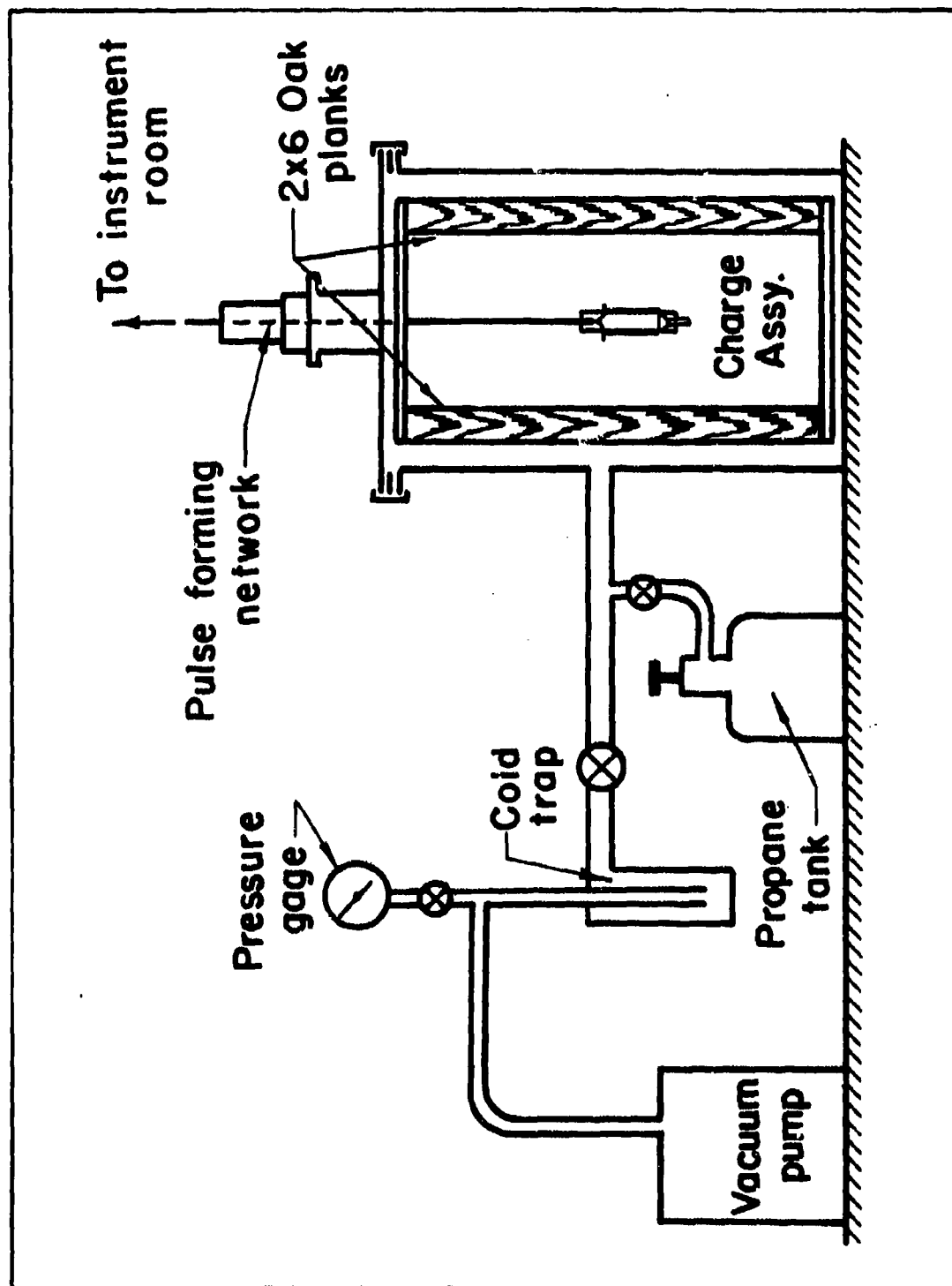


Figure 46. Schematic of blast facility



Figure 47. Photo of blast tank and associated equipment indicated in Figure 22

closed; the doors in the blast room must be locked, closing S_2 and S_3 ; and finally, S_4 is closed by turning a key which is always kept by the operator. The various pilot lights indicate when the related switches have been closed.

c. Explosive Test Charge Assembly

Measuring the conduction of direct current through the detonation zone requires a geometry of charge that allows for contact of the detonation zone with electrodes. The assembly must be of accurate dimensions to assure repeatability since charge geometry and degree of confinement both affect detonation-zone shape. Furthermore, the charge assembly is expended each shot, so a simply constructed device is desired. All these goals are served by the charges shown schematically in Figure 49. The detonation wave begins at the blasting cap and is shaped into a line wave by the trapezoidal section of sheet explosive containing "refracting holes". The wave continues to propagate to the right in the standard explosive before propagating through the test charge. Another

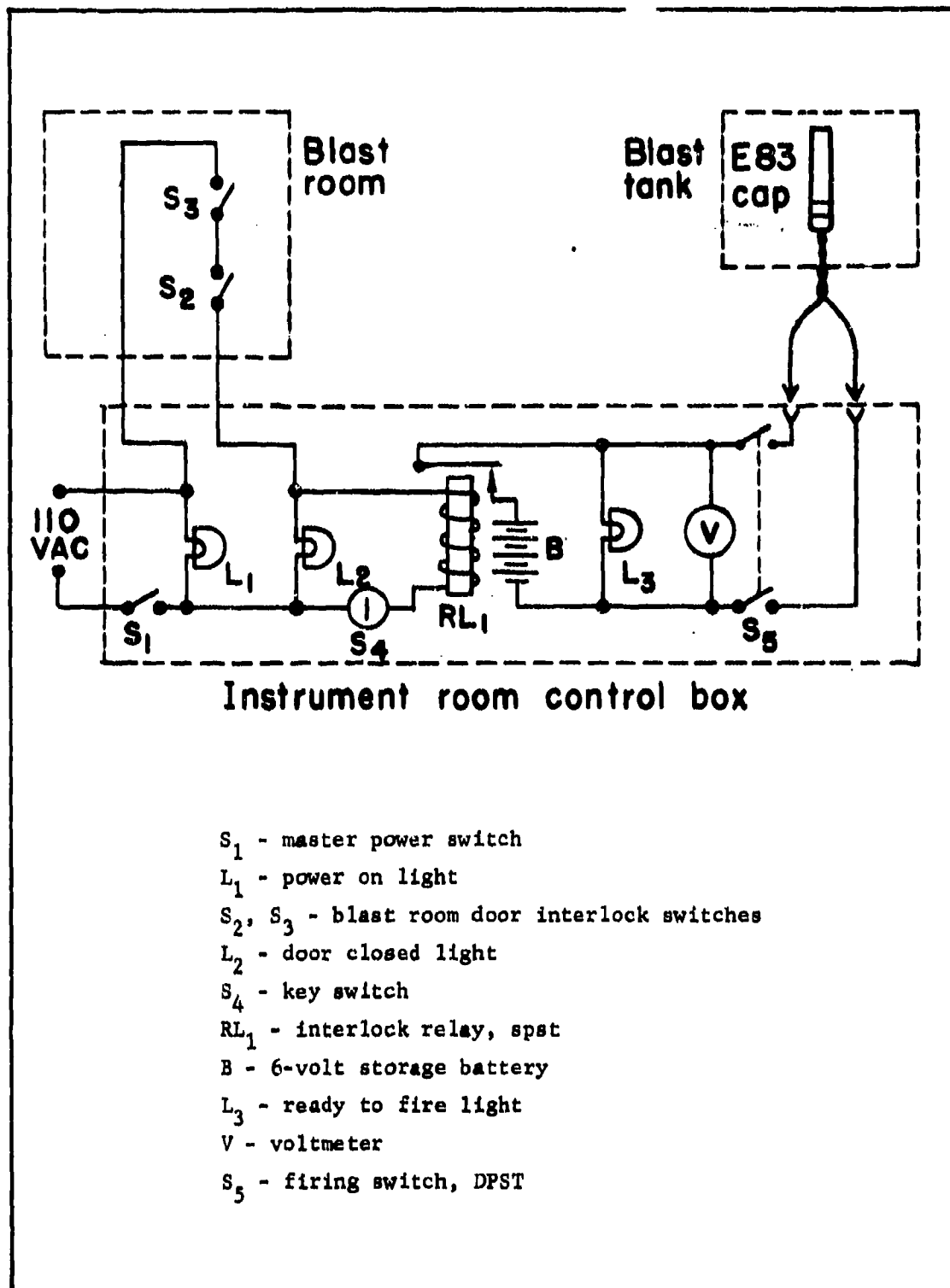


Figure 48. Conductance measurement firing control and safety circuit

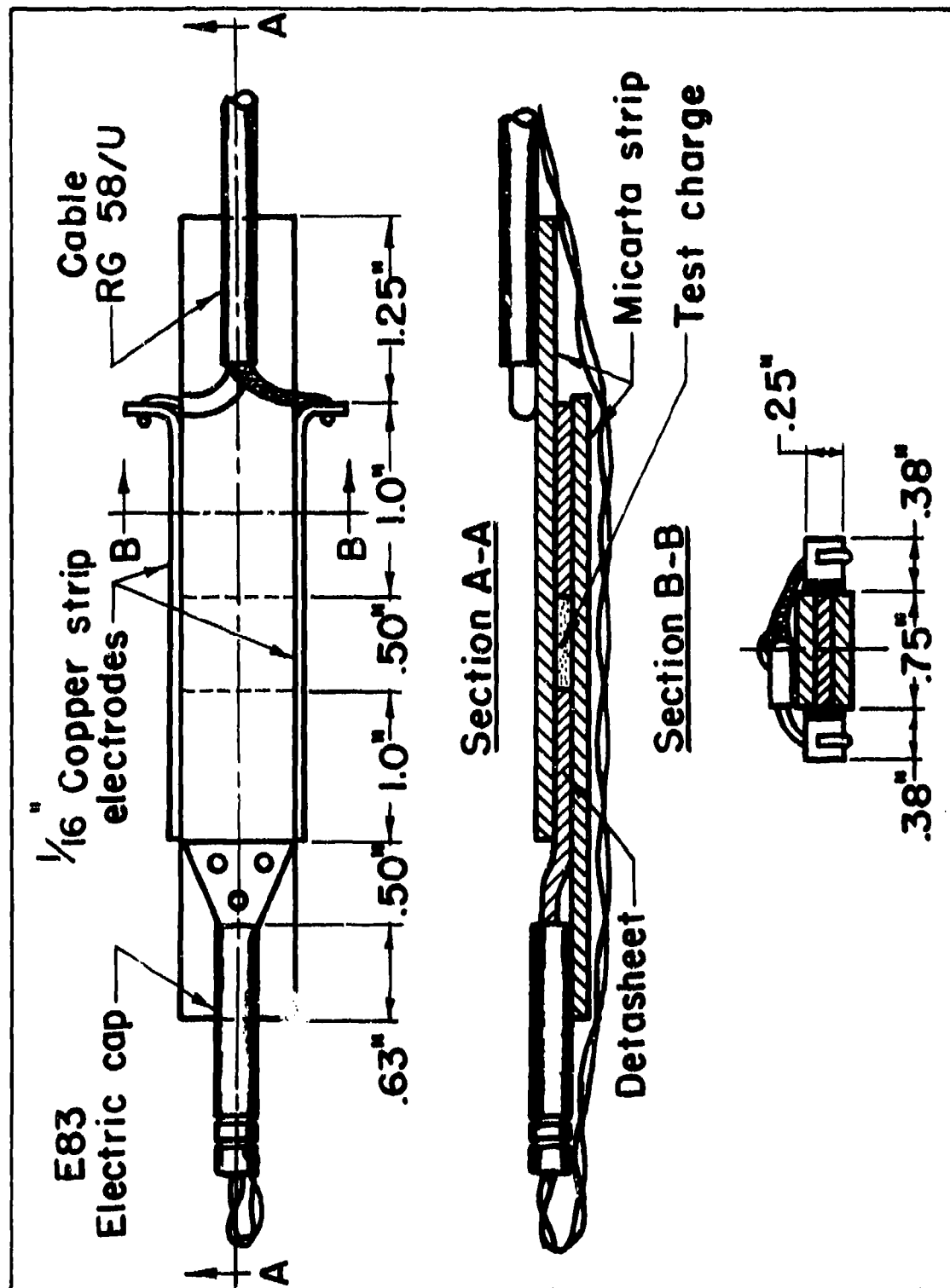


Figure 49. Schematic of test charge assembly.

section of standard charge follows the test charge (this is discussed later). The 1/8-in.-thick micarta strips serve to confine the explosive somewhat, provide a convenient mount for cap and cable, and in addition, provide accurate spacing for the 1/16-in. copper electrodes. The whole assembly is held together with plastic electrical tape. A cutaway photo is shown as Figure 50. The test charge has been darkened only for photographic contrast.

The basic explosive used in all experiments, both for the standard charge and for the test charge matrix, is commercial Detasheet A, which is basically PETN (pentaerythritol tetranitrate), manufactured by the DuPont Company. This is a stabilized plastic explosive in sheet form, the approximate characteristics of which are shown in Table II.

TABLE II
PROPERTIES OF DETASHEET A

Major Ingredient	85% PETN, Pentaerythritol Tetranitrate, $C_5H_8(NO_3)_4$
Energy release	60 kJ/gm
Density	1.50 gm/cm ³
Detonation velocity	7.2 km/sec
Thickness	0.105 in.
Electrical conductivity of detonation zone (PETN)	60 mho/m at 1.7 gm/cm ³ 30 mho/m at 1.5 gm/cm ³
Useful storage life	1 yr

The additive used to make the test charges was spherical powder of either electrolytic-grade copper or Type 316 stainless-steel alloy. (The sieve analysis for these powders is presented in Figure 44.) Spherical powder was used to better conform to the analytical curves and prevent possible friction points which might be a source of premature detonation while molding or cutting the test charge. Even though copper is nonmagnetic, it was used because it represents essentially infinite conductivity by comparison to the detonation products. Type 316 stainless-steel is not magnetic either but has a composition similar to the popular Alnico magnetic materials, the important similarity being the electrical conductivity which is thirty to forty times less than copper. For all computations, copper was assumed to have a density of 8.9×10^3 kg/m³ and an electrical conductivity of 5.85×10^7 mho/m. Type 316 stainless-steel has a density of 8.0×10^3 kg/m³ and an electrical conductivity of

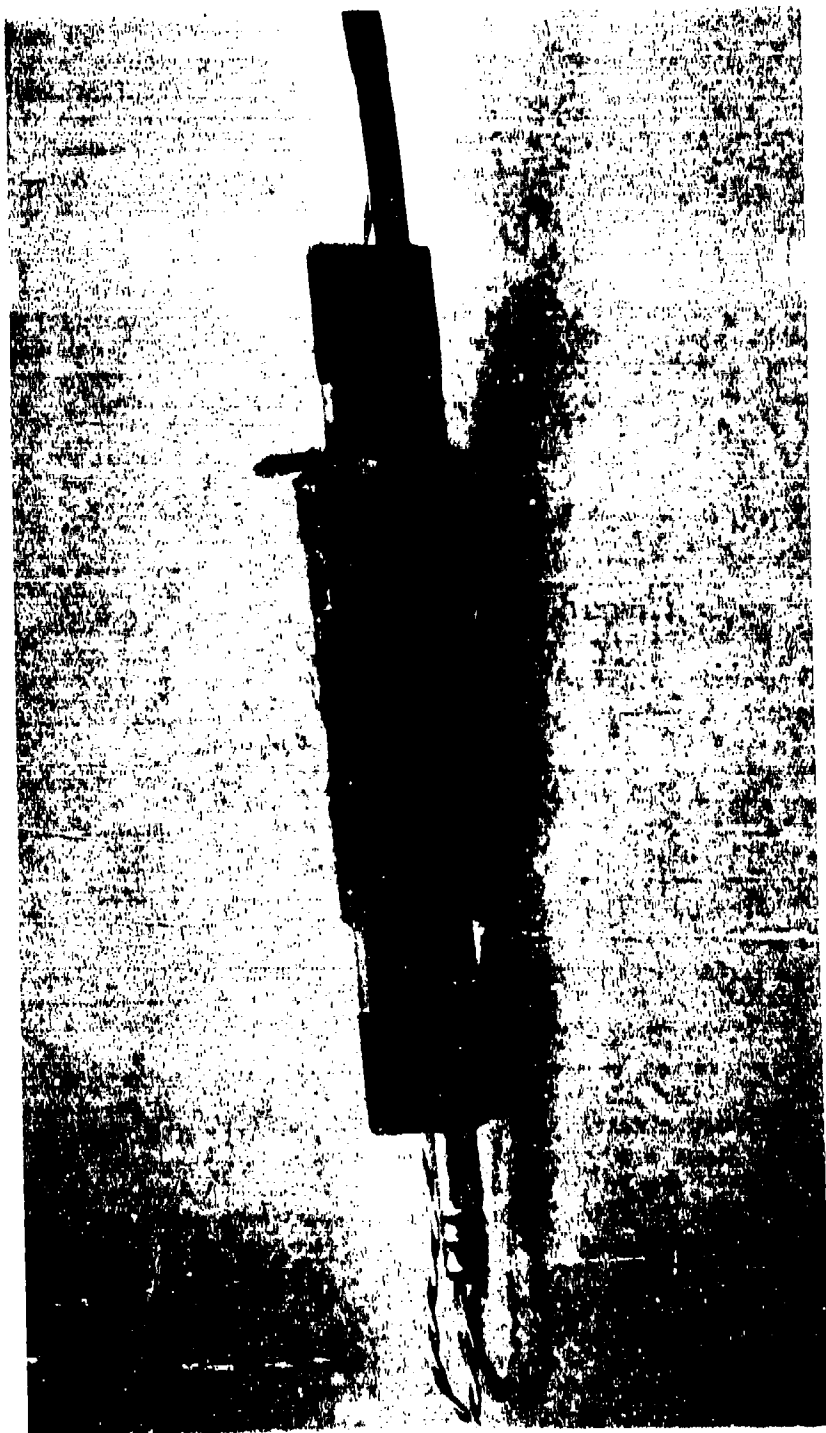


Figure 50. Cutaway view of charge assembly (test charge darkened for contrast)

1.35×10^6 mho/m. The ratio of conductivity between copper and stainless-steel is 43.3 at room temperature.

d. Conductance Measuring Circuit

To measure conductivity of a medium not only must voltages be applied and currents measured, but the geometric factor must also be known. It was beyond the scope of the present investigation to determine this geometry factor, so a relative conductance measurement was made. This is the reason for the plain Detasheet on both sides of the charge in Figures 49 and 50. Since the conductivity of PETN is known and that of Detasheet should not be much different (or it could be determined if necessary), the circuit was set up to measure the voltage and currents through both standard explosive and test charge. Figure 51 shows the important elements. This is a standard circuit and has been used successfully by many investigators, most recently by Jameson (24).

Basically, the plasma resistance is in series with a current measuring shunt, R_s , and a capacitor, C, which functions as a constant voltage source for the event time which is short compared to the time constant of the circuit, even if the plasma resistance were zero. The $R_s C$ time constant is 1 microsec and the event times are on the order of 10 microsec.

The network for measuring the pulse shape is located just outside the blast tank and is connected to the charge assembly with a short piece of coaxial cable. The voltage across R_s is conducted to the instrument room by a 52-ohm coaxial cable to the terminal resistance, R_T (52 ohm); the signal is applied to the vertical amplifiers of a Tektronix 555 oscilloscope. The capacitor, C, is initially charged by a storage battery located in the instrument room. Isolation resistors, R_I , are used to prevent ground loops in the circuit. A Hewlett-Packard Model 412A VTVM, having 1 percent of full-scale accuracy, is used to measure the initial voltage on the capacitor. Typical values of components and the technique of reducing data are described in paragraph 2.

2. Procedure

a. Fabrication of Test Charge

Ordinarily, an ingredient is not deliberately added to an explosive without checking compatibility, sensitivity, etc; and even then, only under controlled conditions with remote handling equipment. The additives used in the manufacture of Detasheet are desensitizing; past work with the material and other plastic explosives confirms the safety of adding inert ingredients to almost all plastic explosives.

The spherical metal powders were therefore added to the Detasheet by hand, and no more than 3 grams of explosive were mixed at one time. To disperse the metal thoroughly in the Detasheet, a taffy-pulling

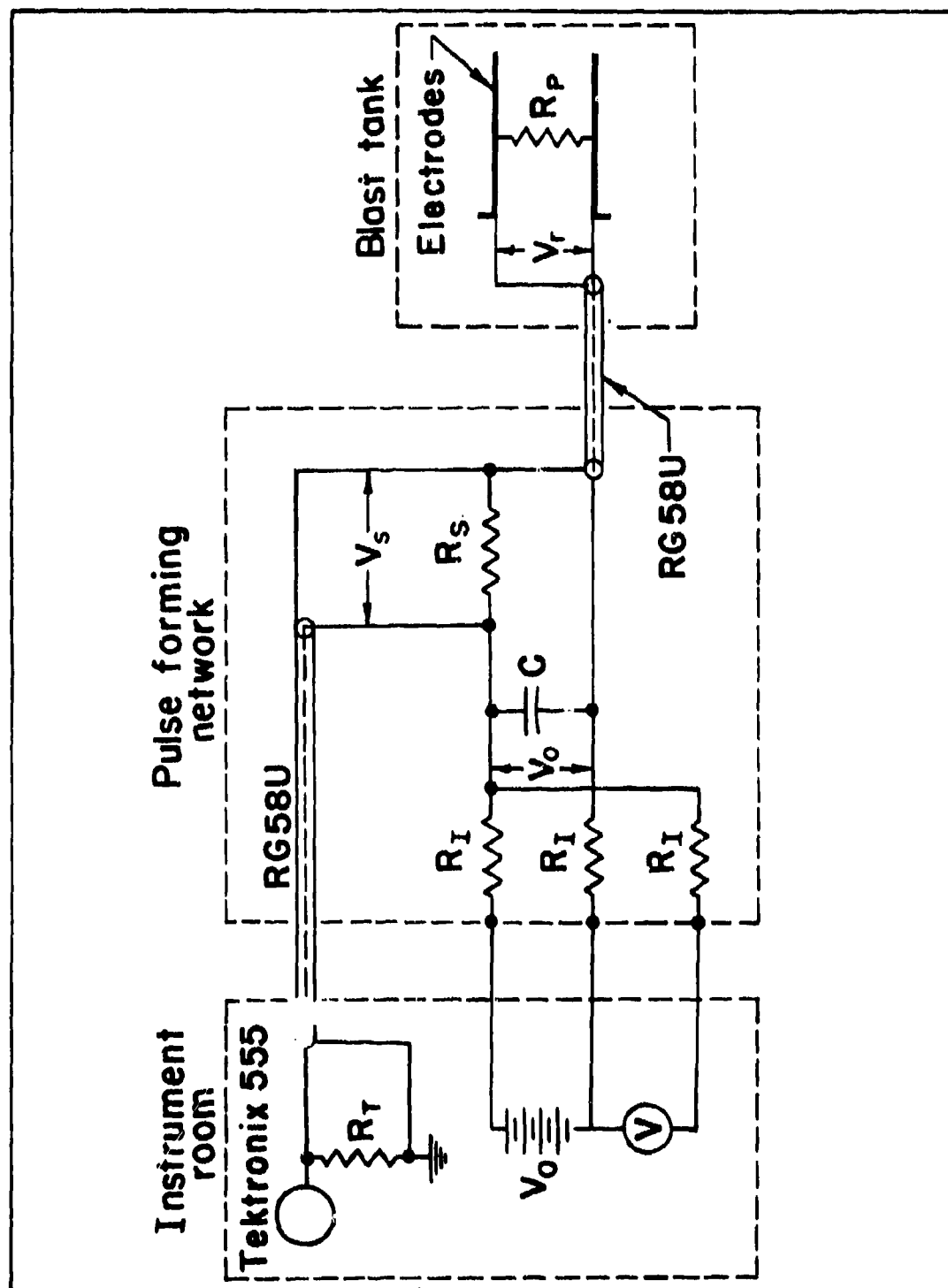


Figure 51. Instrumentation circuit

motion was found successful. To determine accurately the amount of metal in the final charge, the charge material was weighed before and after adding the metal on an analytical balance having a repeatability of 0.2 mg.

To form the charge into a sheet, the lump of charge material was pressed between two plates of 1/4-in. micarta, using an arbor press with a stop set to give the proper thickness (0.105 ± 0.005 in.) when the pressure was relieved. Approximately 10-percent springback was noted. The charge was then cut to size with a razor blade, as was the ordinary Detasheet. All dimensions were cut to a tolerance of ± 0.010 in. using a straight edge and a steel scale. The pieces of charge were fitted together on one side of micarta taking care to avoid air gaps between Detasheet and test charge. The other micarta side was laid on to form a sandwich on which the electrodes bordered. Tape was then applied, holding all pieces securely. The blasting cap was positioned with tape also. Soldering of the blasting cap leads to the feedthrough bushings in the porthole cover was always done with the twisted leads shorted together to prevent any induced currents from initiating the charge. As a further precaution, the leads were soldered after a charge was lowered into the tank.

b. Firing

After a charge was lowered into the tank and the porthole installed, the vacuum pump was started and allowed to run until the pressure reached about 10 torr. The pump was valved out of the system and propane admitted until the total tank pressure reached 150 torr. This was low enough to prevent the blast from damaging the tank and high enough to dilute the remaining air so ionized air shocks did not form, causing spurious electrical signals. Before firing the charge, the oscilloscope triggering level was checked, the voltage applied to the capacitor, C, and the blast room secured. A countdown was initiated so that the oscilloscope camera shutter was opened manually 1 sec before firing; it was closed immediately following the blast. The operator and the camera viewed the traces simultaneously to have at least qualitative information should the camera or film malfunction. The film used was Polaroid-type 107, having a 3000 ASA rating.

c. Data Deduction

The oscilloscope traces yielded information that allowed calculation of two vital parameters: (1) the conductance ratio between plain Detasheet and the test charge, and (2) the average time for detonation to propagate through the test charge, Δt . A typical oscilloscope trace is shown in Figure 52.

d. Relative Conductance Data Analysis

Both traces of Figure 52 are identical. The vertical distance measures the potential, V_s , across the current shunt, R_s (See

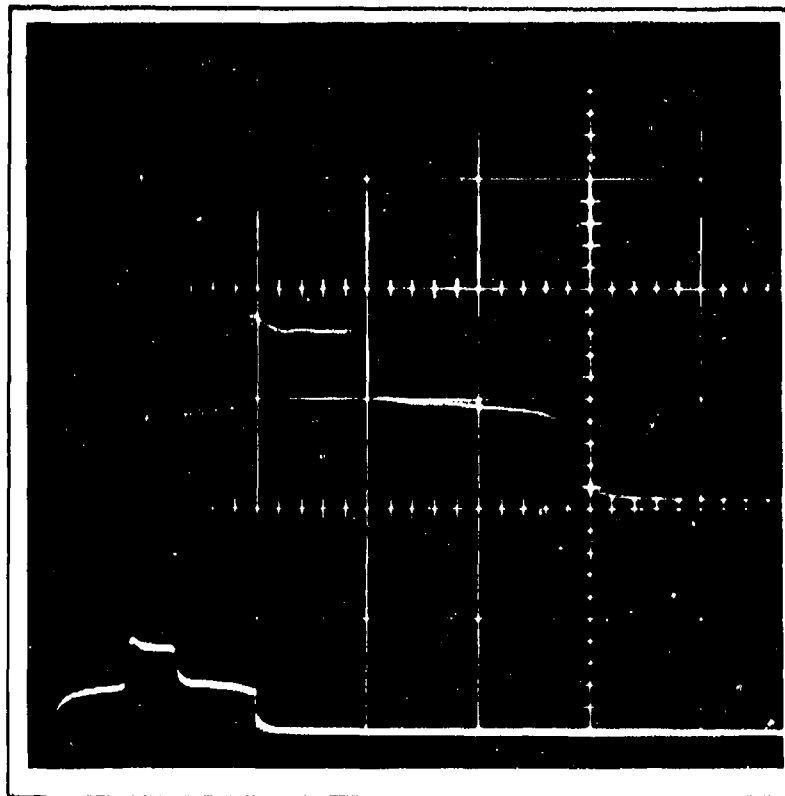


Figure 52. Typical test record, Shot 57, 20.8% copper by weight (upper trace, 5v/div vertical and 2 microsec/div horizontal; lower trace, 10v/div vertical and 5 microsec/div horizontal)

Figure 50). It is convenient to designate voltages, currents, and resistances with no superscript when the detonation wave is in pure Detasheet, and the same values with a prime superscript when the detonation wave is in the test charge. Thus on Figure 52 the first portion of the trace is V_s , the center portion V_s' , then V_s again. The reason for the different gain settings on the two traces of Figure 52 is clear when the shunt voltage of the test charge, V_s' , is considered. It increases substantially at higher metal fractions, Q . The top trace is kept at the same gain setting to record the Detasheet shunt voltage, V_s , while V_s' goes off scale. The lower trace gain is reduced to keep V_s' on scale.

Referring to Figure 52, it is noticed that the traces taper off on both ends, more noticeably on the upstream side. The upstream decrease can be explained in part by the fact that the explosive is initiated from a point and the detonation wave front is curved. It gradually

straightens up after about two to three lengths (3/4-in. diameter) of travel. Since resistance is proportional to the length of the plasma column, a curved column has a longer length and hence higher resistance than a straight column. Higher resistance is reflected in a lower height on the trace.

The other factor involved is related to the high creep rate or malleability of the sheet explosive compared to that of the test charge. Plastic electrical tape is used to hold all components of the charge together, and is necessarily wound on with tension. This causes a compression on the Detasheet and test charge. The softer Detasheet extrudes out the ends, reducing the thickness there, which decreases the area for electrical conduction. A decrease in area results in higher overall resistance, again lowering the trace. For this reason V_g is measured at its value just prior to the rise to V_g' .

The overshoot in V_g' was at first suspected to be a circuitry frequency-response phenomenon, but on simulating the charge with a square-wave generator, the circuitry was exonerated. It must be an effect of the charge, possibly a transient conductance increase due to overboosting from the plain Detasheet. V_g' was measured after it had settled to its steady value.

It should be borne in mind that a relative measurement of conductivity is desired, but only voltages and currents were recorded as the detonation plasma progressed from plain Detasheet to test charge and back to plain Detasheet. Since the geometry factor was not measured, the experimental data yielded more correctly a conductance ratio. It is expected that at low metal fractions the geometry of the detonation zone would remain practically the same as in pure Detasheet, but at higher metal fractions large changes could exist. It is speculated that the effective area of conduction increases in the test charge because the metal present acts, along with the walls, as additional explosive confinement which is known to produce a longer detonation zone. This effectively increases the conduction area in the present case. No way to evaluate these effects was available, so with this in mind, all conductance ratios determined will be considered as conductivity ratios. Other factors entered which tend to offset this effect. The most important was that the capacitor, C, had some equivalent series resistance, R_c . When extremely high currents are drawn $Q > 0.7$, the actual voltage, V_c , is reduced, which makes a calculated conductance lower than the actual. This was not corrected for, as the unknown geometry factor likely overshadows it in magnitude, although they tend to cancel one another.

To measure the relative conductance designated by G, recall Ohm's law:

$$I_p = G V_p = \frac{\sigma A_p}{e_p} V_p$$

46

where I_p and V_p refer to the current through and voltage across the plasma, respectively (See Figure 51). The desired conductivity ratio is then (assuming A_p' equals A_p and e_p' equals e_p):

$$\frac{\sigma'}{\sigma} = \frac{G'}{G} = \frac{I_p' V_p}{I_p V_p'} \quad 47$$

but I_p is given by V_s/R_s and I_p' by V_s'/R_s , and V_p and V_p' are $V_o - V_s$ and $V_o - V_s'$ respectively, so Equation 47 becomes:

$$\frac{G'}{G} = \frac{V_s'}{V_s} \cdot \frac{V_o - V_s}{V_o - V_s'} = \frac{V_s'}{V_s} \cdot \frac{1 - \frac{V_s}{V_o}}{1 - \frac{V_s'}{V_o}} \quad 48$$

This relation was used to reduce the trace data.

Now reverting back to the notation of paragraph B., it is evident that $\sigma' = \sigma_T$ and $\sigma = \sigma_o$. Thus:

$$\frac{\sigma'}{\sigma} = \frac{\sigma_T}{\sigma_o} = \frac{G_T}{G_o} \quad 49$$

The experimental results are a plot of G_T/G_o versus Q , the metal fraction for copper and Type 316 stainless-steel. A discussion of these results is presented in paragraph 3.

e. Velocity Measurement

The charge lengths are accurately (± 0.005 in.) measured during assembly. This allows calculation of the average detonation velocity since time is accurately marked on the traces by the rise and fall from V_s to V_s' to V_s . The time is measured at the halfwidth on the traces (halfway between V_s and V_s'). Sometimes it was measured at the rise from V_s to the fall from V_s' as the lines disappeared on the steep vertical portions of the trace. The average detonation velocity is then:

$$\bar{D} = c' / \Delta t. \quad 50$$

The reasons for the use of plain Detasheet on either side of the test charge are now apparent: (1) accurate timing marks are generated, and

(2) the last piece allows determination of whether the strength of the detonation wave in the test charge was strong enough to reinitiate the Detasheet.

3. Discussion of Conductance Measurement Data

The data obtained show scatter typical of electrical measurements in high explosives.

a. Accuracy of Results

Before discussing the actual results, it is necessary to warn the reader of one characteristic of electrical measurements in high explosives; namely, wide apparent variation in results under seemingly identical initial conditions. Jameson's experiments on conductivity, for instance, show such scatter in the data that the reliability of the reported conductivity of Pentolite or Composition B is within a ± 50 percent tolerance (33). Our own work with similar measuring techniques showed somewhat the same variation. Several factors affect the accuracy of the present experiments.

First, the explosive is specified to have a storage life of 1 yr at ambient temperatures. It is a well-established fact that age or storage at improper conditions lead to erratic properties on detonation of the explosive. In the present case, the explosives were over 1-yr-old and had been stored during one summer in a hot, humid atmosphere. One would expect pieces of one lot stored under identical conditions to have identical characteristics, however.

Second, the actual test charges were made using the explosive as a matrix with mixing done by hand. Several variables entered here. Air is entrained in the composite by the mixing process (taffy motion). Upon detonation, air pockets are compressed adiabatically to a high temperature and contribute to electrical conduction because of the thermal ionization in the pocket (33). This was another reason for evacuating the blast tank prior to firing--to allow trapped air to diffuse out. To check for air entrainment, a shot was made by pretending to mix in an imaginary additive by performing all operations (taffy pulling, etc) without actually adding a metal. The results indicate no air was trapped in this case. However, there was no way to check this at the high metal fraction, and there is some reason to suspect an effect, for the material becomes much more difficult to mix as the metal fraction increases. A cursory check under a 100-power microscope showed a very inhomogeneous structure; voids exist, at least on the surface. Density measurements were made on completed charges, confirming voids, and, even though the scatter was great, a general trend of lower explosive density (1.3 gm/cm^3) at high metal fraction was confirmed. Later experiments were designed to control final density within about 10 percent.

Another minor factor associated with the mixing process is that, although only plastic gloves were in contact with the explosive during mixing, handling the charge with bare hands after mixing was unavoidable.

b. Copper-Doped Charges

The first shots fired were those using a 1.4-cm-long charge. When the data were plotted (Figure 53) the very high conductance ratios were compared to the simple Curve 2 of Figure 41. It was this large discrepancy that led to the multiple-size conductivity theory. No other mechanism was able to account for such high conductance ratios, except perhaps chemical reaction.

While this topic is generally beyond the scope of the present investigation, a simple experiment was undertaken to clarify the effect. If chemical reactions do occur, only the very fine particles would have time to react because of their high surface area to volume ratio (19). To check this, one shot was made using copper particles that consisted of one relatively large size grouping, namely those passing a 115 screen and stopped by a 150 screen (average diameter 115 micron). No noticeable difference in conductance ratio was observed compared to the general trend with the same length charge. This point is marked with an asterisk on Figure 53. If chemical reactions due to small particles of copper increase conductance, then their absence in this shot would have substantially reduced the conductance ratio. No further attempt was made to verify this in copper.

The data in Figure 53 is compared to the multiple conductivity-increase theory; the two solid curves are for a metal with five and ten discrete sizes. A curve of 100 discrete sizes could have been drawn and found to agree fairly well with the data; however, this is misleading and has been omitted.

When velocity measurements were attempted on the 1.4-cm charges, much scatter was apparent. Longer, 3-cm charges were tried, and, in general, higher conductance ratios were obtained because at the higher metal fractions more time was needed to reach steady conditions. Far less scatter in the data is apparent for 3-cm charges, so the experimental curve in Figure 53 was drawn through these points.

At the higher values of Q , some charges showed such high conductance that it was difficult to measure. Although the current was measured accurately by V_p' , the plasma voltage, V_p' , was extremely low. Hence, only an upper limit could be calculated by summing the known voltages existing in the series circuit ($V_p' = V_o' - V'$); any stray voltage drop not accounted for would reduce the calculated value of V_p' . One such drop is the unknown equivalent to series resistance of the capacitor. By Equation 47, a high V_p' reduces the calculated value of G_T , and likewise the value of G_T/G_o since G_o is known accurately. Data marked with an

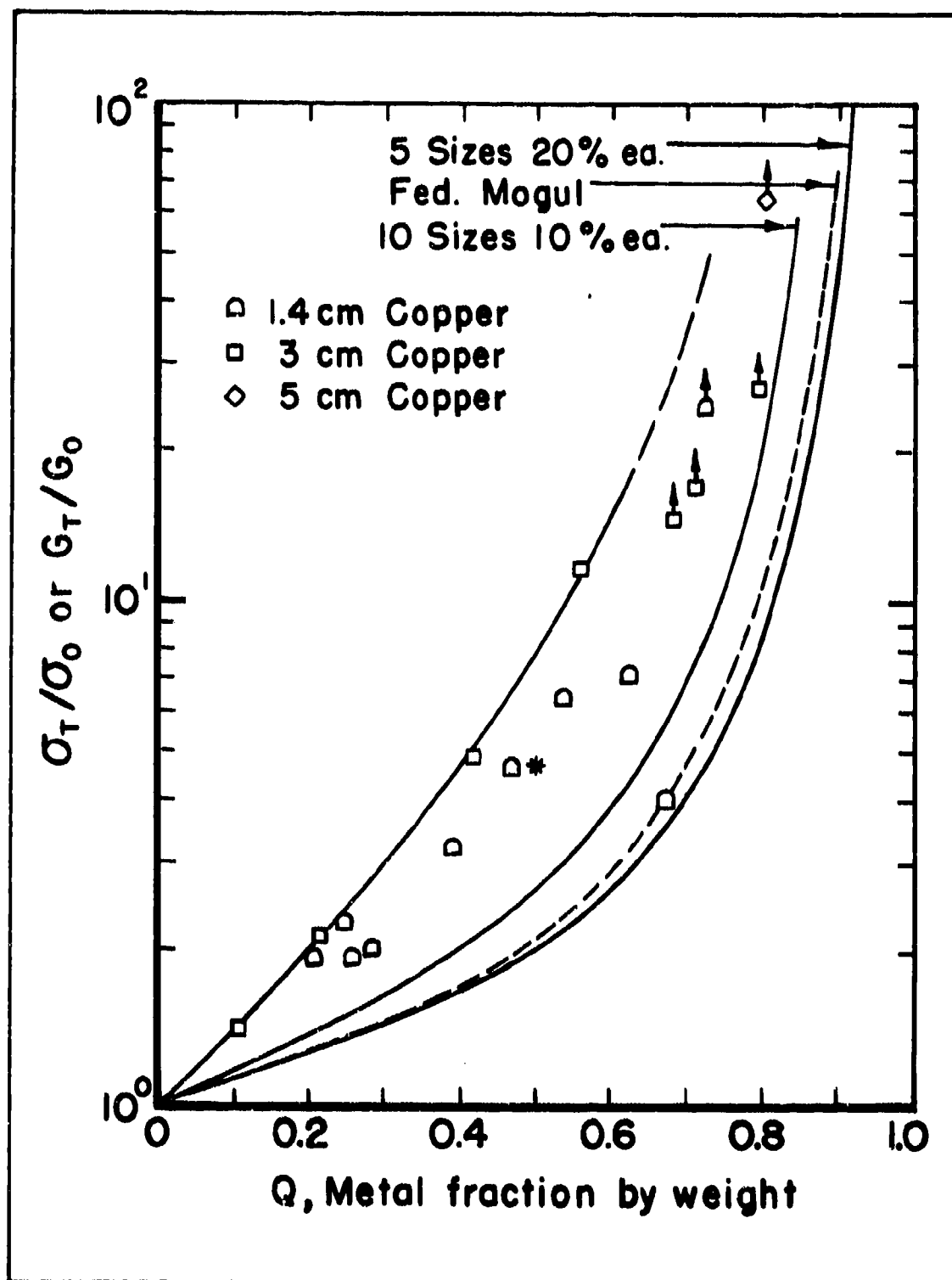


Figure 53. Conductance ratio G_T/G_0 versus Q, copper fraction by weight

upward-pointing arrow on Figure 53 have been calculated this way; the true conductance ratio lies above the indicated point. The highest point, at $Q = 0.802$, was made with a 5-cm charge length to ensure steady conditions. Again V_P was practically zero, and only a lower limit to the conductance ratio was established. The actual value of shot 64 is approximately a two order of magnitude increase.

c. Type 316 Stainless-Steel-Doped Charges

Figure 54 shows similar conductance data for the Type 316 stainless-steel-bearing charges. As with copper, the 1.4-cm charges showed a lower conductance trend at the higher metal fraction because not enough time was allowed for steady conditions to develop. The 3-cm charges showed very consistent results both in conductance ratio and velocity. The last point at $Q = 0.826$ indicated that a very definite plateau in conductance was being reached. With other charges containing greater than 80-percent metal, the detonation either failed to propagate or "low order" detonation occurred. This is typified by temperature, pressure, and velocity intermediate to that obtained during detonation or strong deflagration. The data became very erratic in this regime; therefore, most shots were made at lower metal fractions.

The experimental data falls so close to a theoretical curve that no experimental curve was deemed necessary. The correspondence is only coincidental, however. To check further the effect of size distribution on conductance and confirm if chemical reaction was a factor, a shot (marked by an asterisk) was fired with all metal particles less than 400 mesh (diameter less than 38 microns). No chemical reaction effects are indicated because instead of a conductance ratio increase, a definite drop was noted. Since there were fewer size groups left in the charge, this result could be anticipated on the basis of the multiple-size theory. The point falls somewhere between one size and five sizes. This is very analogous to the size distribution requirements for obtaining strong concrete from rock gravel, sand, and cement. Very definite proportions of the ingredients exist for optimum properties depending on the size distribution of rock, gravel, and sand, the usual rule being that the strongest concrete is obtained by using a nominal amount of cement. (The cement itself is very weak, especially in tension, and is only used to bind the stronger mineral fragments together.) For the conductivity problem, just enough explosive (cement) should be used to bridge the gaps between higher conductivity particles (rocks, etc).

d. Iron-Doped Charges

Spherical iron powder was also tried as a dopant. Even in the 3-cm-long charges the conductance when using spherical iron powder was inferior to stainless-steel at similar metal fractions. On an intuitive basis, commercial-grade sponge iron was then tried as a dopant with gratifying results. The measured conductance was similar to that with copper although pure iron is about a factor of 5 less than copper in

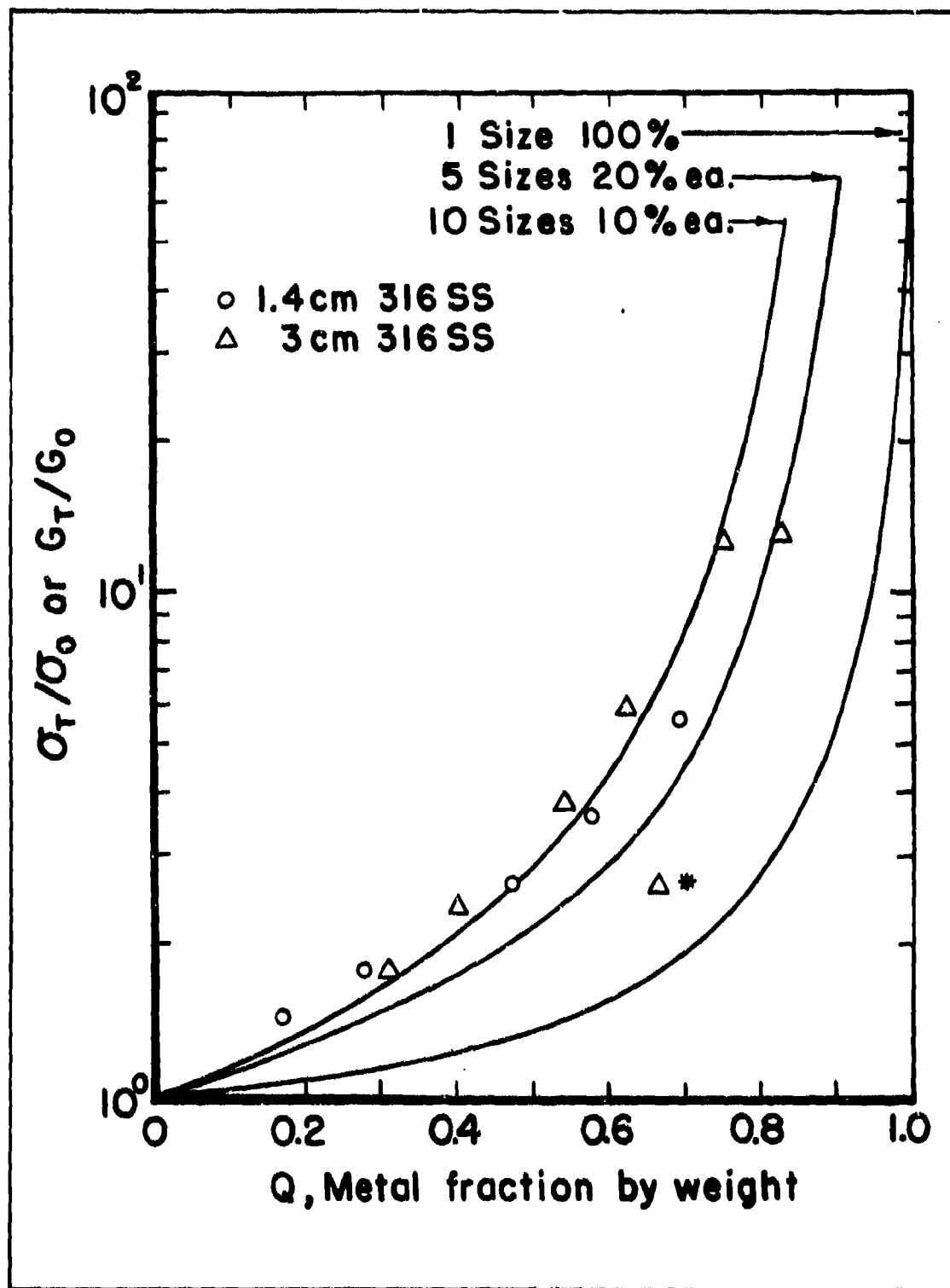


Figure 54. Conductance ratio G_T/G_0 versus Q , Type 316 stainless-steel fraction by weight

basic conductivity. To examine for differences between the two types of iron powders, several physical properties were examined. Upon screening, the sponge iron had a size distribution almost identical to the spherical copper and Type 316 stainless-steel powders. The spherical iron, however, was heavy in fine particles. To clarify the reason for the poor performance when using spherical iron, a mixture of spherical powder was made from the various screenings to duplicate the size distribution of the sponge iron. The results of this experiment are shown in Figure 55. Since the undetonated sponge iron charge conductance increases drastically when the iron content is greater than 50 percent by weight, only enough shots were fired to illustrate the difference between identical size distributions of sponge iron and spherical iron in Detasheet. The reference curves are from Figures 53 and 54. The upper curve follows the 3-cm copper data while the lower curve corresponds to experimental results with Type 316 stainless-steel. Notice that the sponge iron produces a conductance which is equal to or better than the copper dopant while spherical iron is similar to Type 316 stainless-steel or worse. Based on the relative conductivities of the various ingredients one would expect iron to fall somewhere between copper and Type 316 stainless-steel. It was thought from the duller appearance of the spherical iron that oxides had formed causing an electrical insulation layer. However, under microscope examination, both the sponge iron and spherical iron have equally bright, shiny surfaces indicating that this is not the case. More is said about iron powder in paragraph D.

e. Comparison of Copper and Stainless-Steel

It is definitely clear from the experimental data that the conductivity enhancement due to copper is significantly greater than that of stainless-steel. The simple theory was based on an infinite conductivity ratio, ν , because both copper and stainless-steel have essentially infinite conductivity compared to the conductivity of the detonation products. The difference may result from a change in \bar{a} (See Figure 35) due to the different metal densities involved. Obviously, the simple multiple-conductivity theory is inadequate. It does, however, show the trend in conductivity when there is a size distribution.

f. Velocity Measurements

The effect of the additive metal on the detonation velocity is summarized in Figure 56. All of the 1.4-cm data are considered unreliable because of insufficient charge length. For some reason even the 3-cm charges of copper showed erratic average velocities, but this can be correlated with the reignition of the downstream piece of Detasheet. For instance, a 3-cm charge containing 79-percent copper had an average detonation velocity of about 3 km/sec; the downstream Detasheet did not ignite. A charge with approximately 70 percent had an average velocity of 5 km/sec; the downstream piece did ignite. This is associated with "low order" detonation just mentioned.

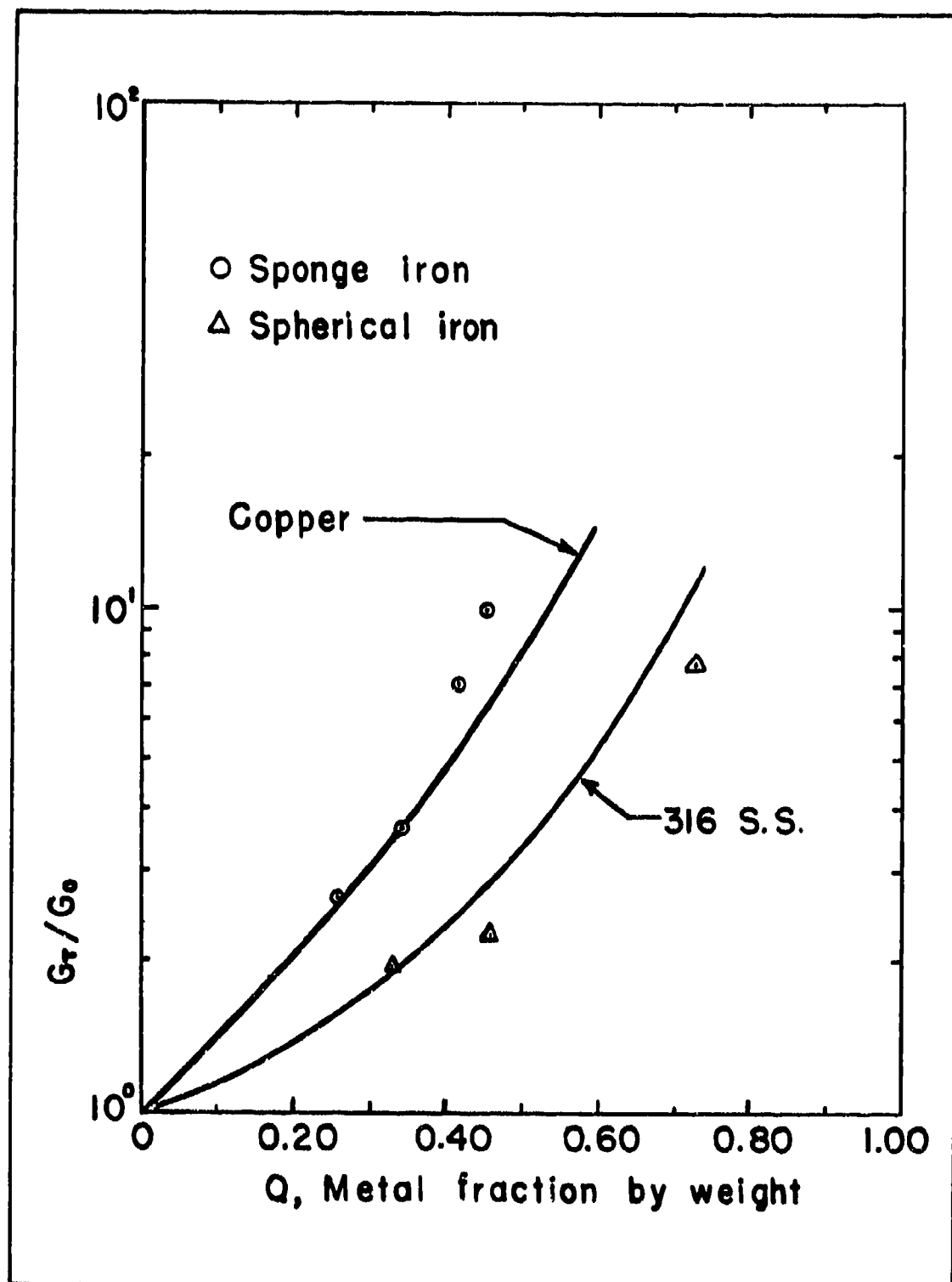


Figure 55. Conductance ratio for sponge iron and spherical iron in Detasheet versus Q (solid lines are averaged experimental values from nominal 3-cm charges of spherical copper and 316 stainless-steel, from Figures 53 and 54)

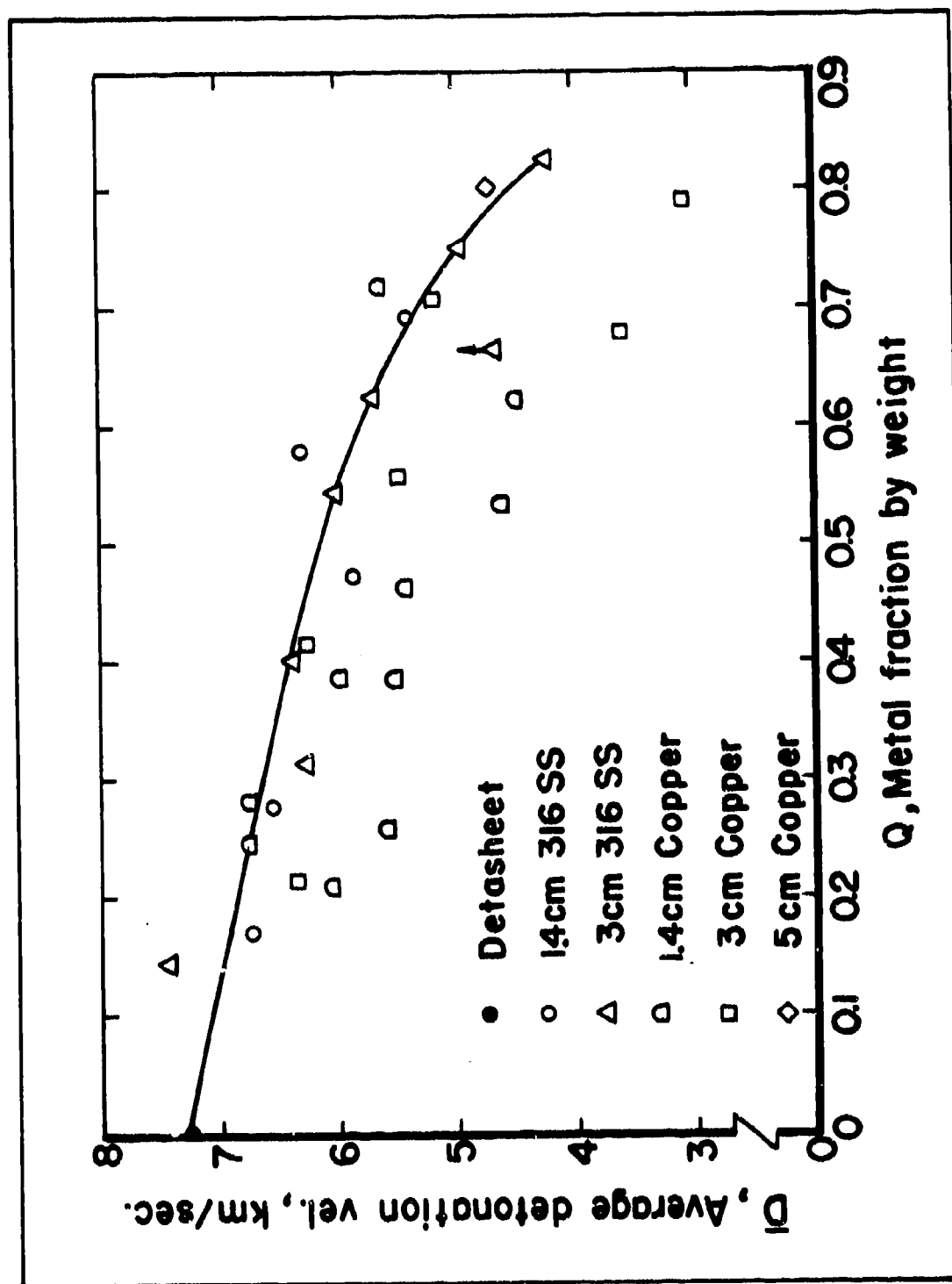


Figure 56. Average detonation velocity \bar{D} vs Q, metal fraction by weight for both copper and Type 316 stainless-steel

The 1.4-cm Type 316 stainless-steel charges likewise showed scatter due to insufficient length, but were generally above the copper values. The most consistent data resulted from the 3-cm stainless-steel charges. For this reason, the only curve drawn is through these points. These points also are generally above corresponding copper data. One possible reason for the difference between copper and stainless-steel aside from a slight density difference, is the fact that the thermal conductivity of stainless-steel is less than that of copper. As mentioned previously, work by Taylor indicated that the secondary mechanism for velocity slowdown was heat transfer to the colder metal particle. The present data are similar to Taylor's past work and are not unexpected. The major importance of this velocity data is in connection with R_m , which is the subject of the next paragraph.

g. Magnetic Reynolds Number

An intelligent estimate of the value of R_m to use in Equation 8 can now be made. All of the factors constituting R_m have been investigated. In paragraph B., μ was determined to be between one and ten times μ_0 , depending on the metal fraction, Q . A constant value of $8 \mu_0$ is sufficient for the present calculations. Conductivity and velocity information have been obtained experimentally as shown in Figures 53, 54, 55, and 56. Because of the uncertainty in the value of \bar{a} , the effective conduction zone width, it is seen why conductance ratio was measured. Conductance and conductivity are related by:

$$G = \frac{1}{R} = \frac{A}{\rho l} = \frac{A}{l} = \frac{\sigma \bar{a} b}{e} \quad 51$$

Since b and e are the same for Detasheet and the test charge, the conductances ratio can be written from Equation 51:

$$\frac{G_T}{G_0} = \frac{\sigma' \bar{a}'}{\sigma_0 \bar{a}_0} \quad 52$$

Again using primes for the test charge quantities, Equation 8 becomes:

$$R_m' = \mu' \sigma' \bar{a}' \bar{D}' \quad 53$$

which by Equation 52 can be written as:

$$R_m' = \mu' (\sigma_0 \bar{a}_0) \frac{G_T}{G_0} \bar{D}' \quad 54$$

The important point about Equation 52 is that with assumed or experimental values of σ_o , \bar{a}_o , and μ' , the magnetic Reynolds number may be estimated by multiplying the conductance data on Figures 53 and 54 by values of \bar{D} from Figure 56.

Assuming the not unreasonable values of

$$\mu' \approx 8\mu_o = 10^{-5} \text{ h/m}$$

$$\sigma_o \approx 10^3 \text{ mho/m (from the tabulation on page 71, Composition B)}$$

$$\bar{a}_o \approx 10^{-2} \text{ m}$$

allows Equation 54 to be written as:

$$R_m' \approx 10^{-4} \frac{G_T}{G_o} \bar{D}$$

55

Equation 55 has been plotted in Figure 57 for both copper and Type 316 stainless-steel. The most significant features are an increase in R_m to values greater than ten for stainless-steel (which is appropriate^m to anticipated magnetic materials) and a maximum in R_m at about 80-percent metal fraction. Note that the two curves have been shifted vertically to separate the data points for clarification. If the fact that μ is a function of Q had also been included in Equation 55, then increases in R_m for stainless-steel, from no metal present to the maximum value, would^m have been closer to a factor of 100. This is indeed a significant increase. However, the fact remains that regardless of the increase in R_m from the metal addition, high absolute values of R_m are necessary. These results indicate that an R_m of about ten is attainable, depending on the actual values of σ_o and \bar{a} that are attained in an optimum charge.

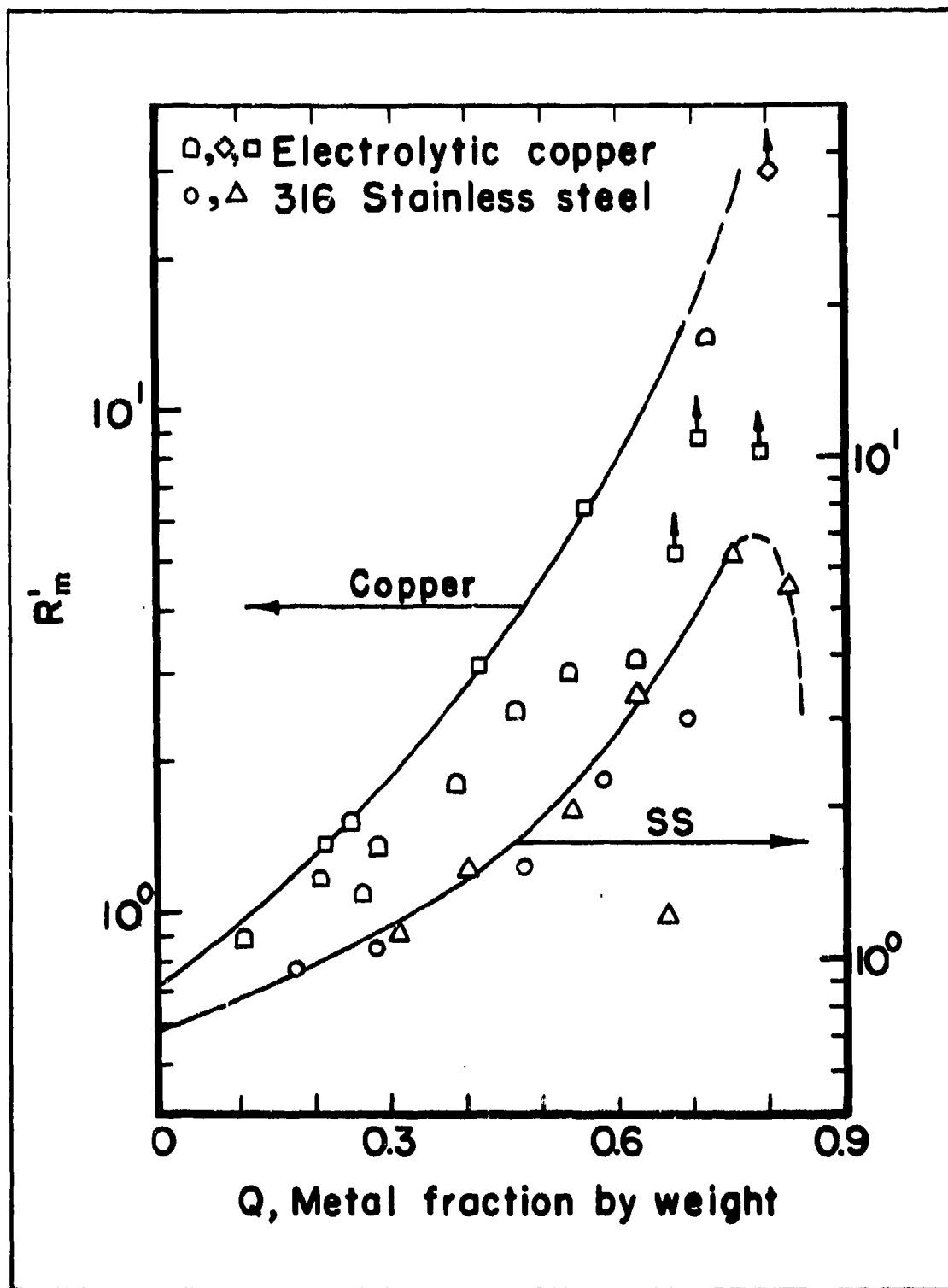


Figure 57. Rationalized magnetic Reynolds number versus Q, metal fraction by weight for copper and Type 316 stainless-steel

D. POWER GENERATION EXPERIMENTS

The conductance experiments described previously definitely verify the hypotheses that a metal additive can be used successfully to increase the conductance of the detonation zone. With this data as a guide, power generation experiments were undertaken. The magnetic field was simulated by a steady magnetic field. Because finely divided permanent magnet materials were not available, it was not feasible to fabricate a charge with a high permanent magnetization.

The power generation experiments were also prompted by several deficiencies of the conductance measurements. Besides conductance, an important power generation parameter is the effective velocity of the detonation products, αD , from Equation 11. This can only be determined by measuring open circuit voltages in actual power-generating configurations. When higher metal fractions were utilized, the conductance became so great that the simple dc conductance measuring system was incapable of accurate measurement because of unknown series voltage drops. Also, when the undetonated charge conductance increased, it was difficult to keep a charge on Capacitor C.

The experimental equipment is described in paragraph 1. (below), and the power generation characteristic curves are presented in paragraph 2. for the various compositions. The various power generation experimental data are compared by magnetic Reynolds number consideration in paragraph 3.

1. Experimental Apparatus

a. Magnet

The main piece of equipment used in these experiments was a large, H-frame, watercooled electromagnet of 75-kw rating (Pacific Electric Motors, Model 12 A-LI). The magnet was used without pole faces so the largest possible volume was available. This resulted in a working space of 20-in. diameter x 6-1/2-in. net gap. The field strength is limited to about 0.9 tesla in this configuration.

The magnet was calibrated with a rotating coil-type meter. For a particular shot the voltage across the current shunt is measured just prior to firing, and again immediately after the shot. Any variation (< 5 percent) during this interval allows the actual current shunt voltage to be deducted by interpolation.

b. Test Section

To detonate safely the charges in the magnet, a test chamber was constructed from a short length of nonmagnetic stainless-steel tubing (5-in. OD and 3/4-in. wall). End plates of micarta and aluminum were held on with through-bolts, spring loaded to absorb the shock of the blast.

The end plates served to mount the charge sting, feedthrough bushings for the instrumentation, and a vacuum fitting. No special precautions were taken to protect the magnet from blast damage. The test chamber successfully contained all fragments of the shot and the generated gas escaped harmlessly by blowing out the rubber cork feedthrough bushings in the end plates. Air in the chamber was pumped out and propane admitted to preclude ionization of the residual air in the test section.

The test chamber was suspended from a small I-beam rail providing easy access to both ends of the tube. When fully instrumented, it was easily rolled into the magnet gap. The physical arrangement of the magnet and test chamber is shown in Figure 58. The oscilloscope instrumentation is shown in the lower right-hand corner.



Figure 58. Phase II power generation equipment: magnet is behind metal cabinet and test section is hanging on I-beam with-drawn from magnet gap; oscilloscopes are in lower right-hand corner

c. Charge Assembly

Figure 59 shows the charge on the wooden sting. The blasting cap was housed in a wooden block to prevent the metal case shrapnel from moving through the magnetic field and inducing stray triggering voltages. Reliable triggering was obtained by using the two probes shown entering the trapezoidal piece of Detasheet explosive. When the detonation passes the probes they are effectively short-circuited. A 12-volt battery forms a series circuit with the probe switch and is applied to the triggering circuit of both oscilloscopes. The charge is fired by applying 6 volts dc to the blasting cap with the same control scheme as in Figure 48.

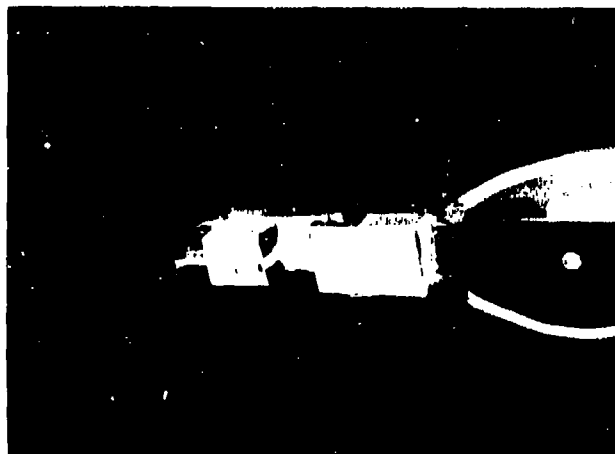


Figure 59. Test charge mounted on sting: blasting cap is on right end, then wave shaper and test charge; electrodes protrude from charge case for load and signal lead connection

The charge case is made of epoxy-glued micarta with metal electrodes. The explosive composite is compacted in layers from rear to front as viewed from the detonation direction and tamped with a wooden dowel between layers. The charge assembly dimensions are measured with a micrometer and recorded. The charge case is weighed to an accuracy of 1 mg before and after filling, so the total charge density can be calculated. Electrical tape is used to mount securely all components of the detonation train in their proper position.

d. Instrumentation

Figure 60 shows the charge configuration, electrical schematic, and a typical test record. As in the conductance measurements, coupling to the charge is effected by electrodes in contact with the explosive. The range of load resistances used was between open circuit, which is 102 ohms due to the cable terminating resistors, and about 5 milliohms. The loads were made of nichrome or constantan wire. The only variable measured is the voltage across the load. An analysis of the pulse length shows that the electrical skin effect in the load can be neglected since the basic frequency is about 50 kHz. Thus the dc resistance measured before firing is considered as the resistance during the event. The charge resistance is usually greater than 10^9 ohms. Joule heating of the load during the event is found to be of small order (for a typical shot the voltage across the load is 1 volt and the current is 400 amp for

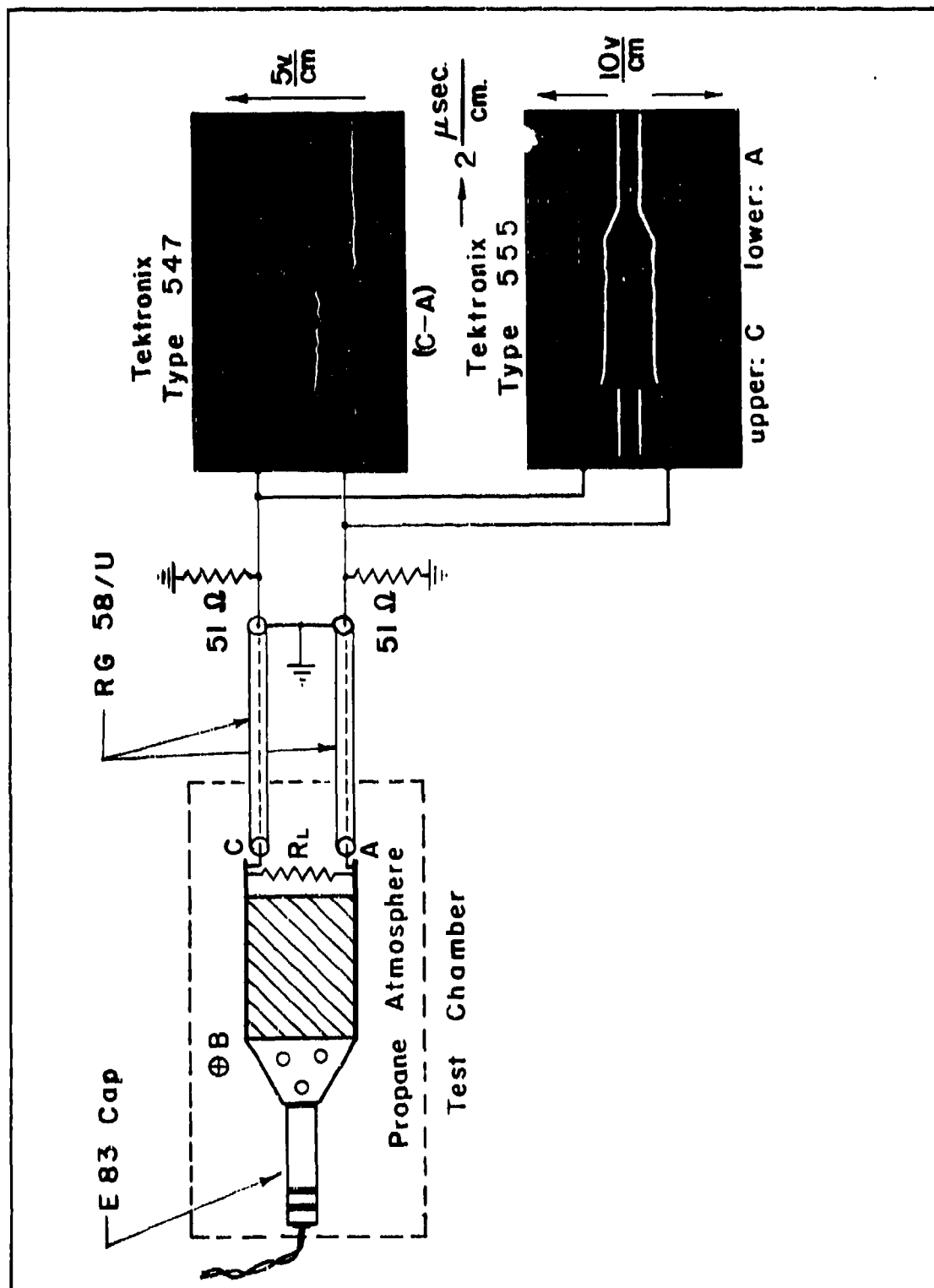


Figure 60. Charge configuration, electrical schematic, and typical test record

8 microsec, yielding 3.2×10^{-3} joules dissipated in the load). Hall effects and magnetoresistance can also be neglected. Thus the current can be calculated with confidence from the measured values of load voltage, V_L , and load resistance, R_L .

The load resistance was placed close to the end of the charge to eliminate voltage drops when high currents are drawn. Terminated RG58/U coaxial cables applied both the cathode and the anode voltages to the vertical amplifiers of the oscilloscopes. The 547 oscilloscope presented the cathode-anode difference, which is the net voltage across the load. The actual load consists of a paralleled combination of the load resistance, R_L , and the two 51-ohm cable terminating resistors in series which would be 102 ohms. The 555 oscilloscope traces measure the voltage of each electrode with respect to ground and in a sense yield redundant data to enable calculation of load voltage in case of malfunction of the other oscilloscope. Electrical shorts to ground would be indicated by the 555 trace.

All traces show a characteristic overshoot at the beginning of the event with a rapid relaxation to steady conditions. The slight oscillation in the amplitude of the voltage may be due to density changes in the charge as a result of tamping the composite by hand. Voltages used for comparative purposes are measured at the average, toward the end of the event. Detonation velocity is calculated by measuring the event time from the trace (beginning of rise to beginning of fall) combined with the known length of the charge.

2. Results of Power Generation Experiments

a. Spherical Copper in Detasheet (1/8-In.-Thick)

The first power generation experiments were conducted using spherical copper dopant in reconstituted Detasheet 1/8-in.-thick. The first series of shots yielded the data shown in Figure 61. The ordinate is the voltage across the load, V_L , obtained from the oscilloscope trace. The abscissa is the current calculated on the basis of V_L and the measured load resistance, R_L , before firing. The maximum open circuit voltage of about 5 volts indicates that effective velocity of the detonation products is about one-tenth the detonation velocity. We define the parameter, α , as the ratio of the effective velocity for voltage generation to the detonation velocity, D , by the relation $\alpha = V_{oc} / B D e$, where e is the electrode separation and B is the magnetic induction. From a conventional MHD generator the generated voltage would be uBe , so αD is equivalent to u .

Another feature is the large scatter in the data; the bars indicate the maximum (except initial overshoot) and minimum voltage appearing across the load resistance during the event. This variation is thought to be due to the fact that the charges are tamped by hand forming multiple layers of varying density in the detonation direction. Since the

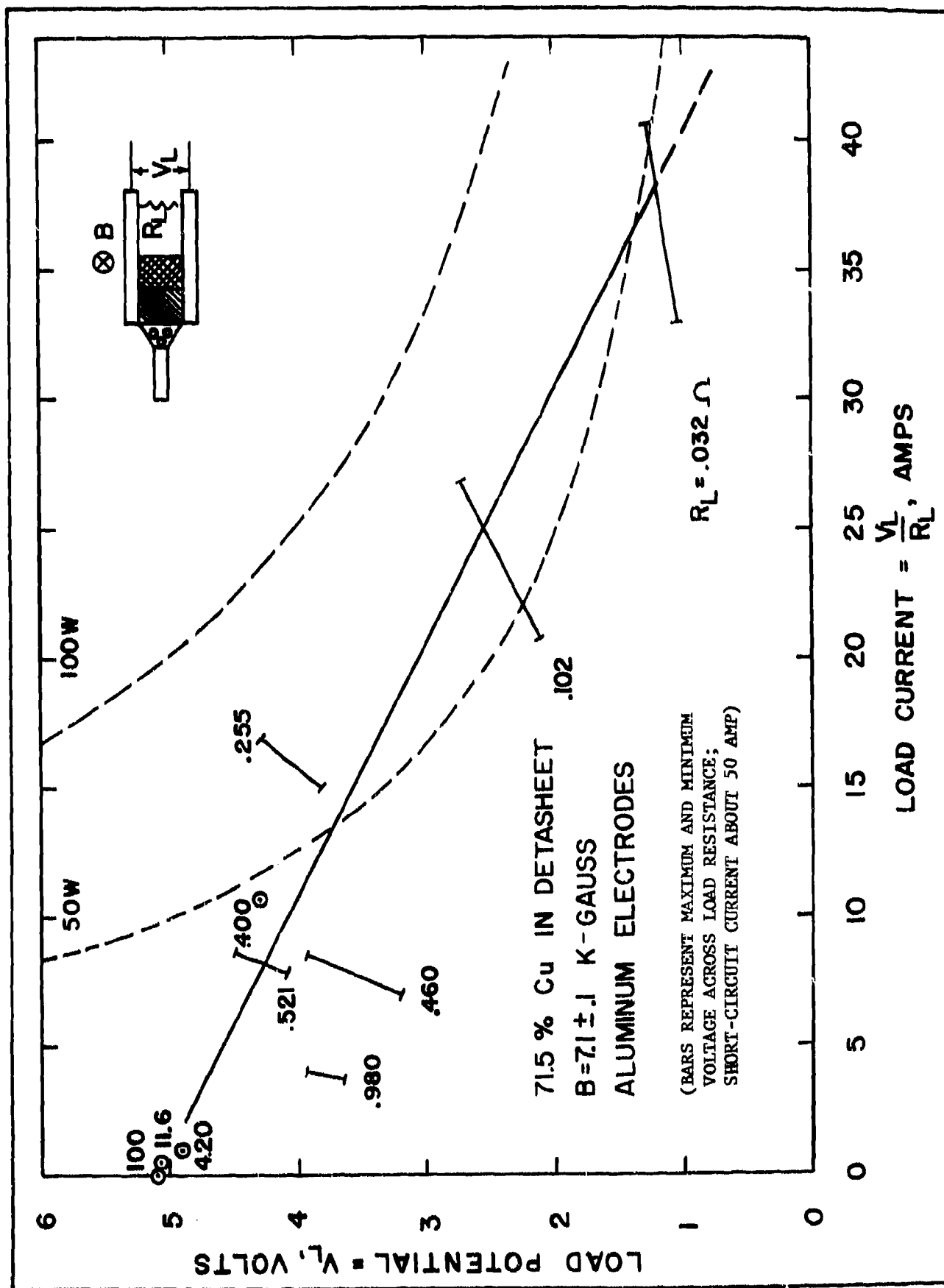


Figure 61. Generator characteristics curve, 71.5% copper in Detasheet,

open circuit voltage is fairly steady, the data suggests that the plasma conductance is more sensitive to density variation than is the detonation velocity ($V_{oc} = \alpha B \bar{D}e$). This is confirmed by the increased excursion as the currents approach short-circuit conditions. For this set of experiments, a short-circuit current of about 50 amps results. Maximum power generated was about 70 watts. When referred to the cross-sectional area, the power was $1.1 \times 10^6 \text{ w/m}^2$.

No attempt has been made to refine this data by taking into account variations in charge geometry, detonation velocity, magnetic field strength, or orientation with respect to magnetic direction, etc. The reason is that the detonation velocity varies widely, most likely due to the thinness of the charge at such a high metal fraction. A 1/4-in. charge was selected subsequent to experimentation. In this case the velocity data proved much more consistent. The series of experiments with the 1/8-in. Detasheet was of value in developing techniques and procedures.

In attempts to explain the scatter in the data of the previous figure it was found that detonation velocity was directly involved. Shots with a higher than expected output voltage had a higher detonation velocity, all other parameters constant. Since the product $B\bar{D}e$ has the units of volts, it is natural to normalize the data against this parameter. For purpose of analyses, the succeeding data are presented in the form of plots where the voltage has been normalized to $V_L/B\bar{D}e$ and the normalized current is given by $(V_L/B\bar{D}e)/R_L$. The slope of the nominally straight lines connecting the data points is the plasma resistance, R_L . The reciprocal of this is the plasma conductance, G . If the data is extrapolated back to open circuit conditions, the intercept is by definition α , or the ratio of effective actual particle velocity to detonation velocity ($v = \alpha \bar{D}$). The parameter k is usually used to indicate the degree of loading of a generator. It is defined as $k = V_L/V_{oc}$. Thus the ordinate of the generator curves is:

$$\frac{V_L}{B \bar{D} e} = \frac{V_L}{V_{oc}} \cdot \frac{V_{oc}}{B \bar{D} e} = k \alpha. \quad 56$$

The current axis (abscissa) is then the normalized value, $k \alpha$, divided by R_L .

b. Spherical 316 Stainless-Steel in Composition C-4

The next test series was conducted using Type 316 stainless-steel dopant in Composition C-4. The charges were made 1/4-in.-thick on the basis of the discussion presented previously. Stainless-steel was selected for these experiments because of its more consistent performance in the conductance measurements, especially the small scatter in detonation velocity decrease at high metal fractions. The results of these experiments are shown in Figure 62. Because of normalization, the data points

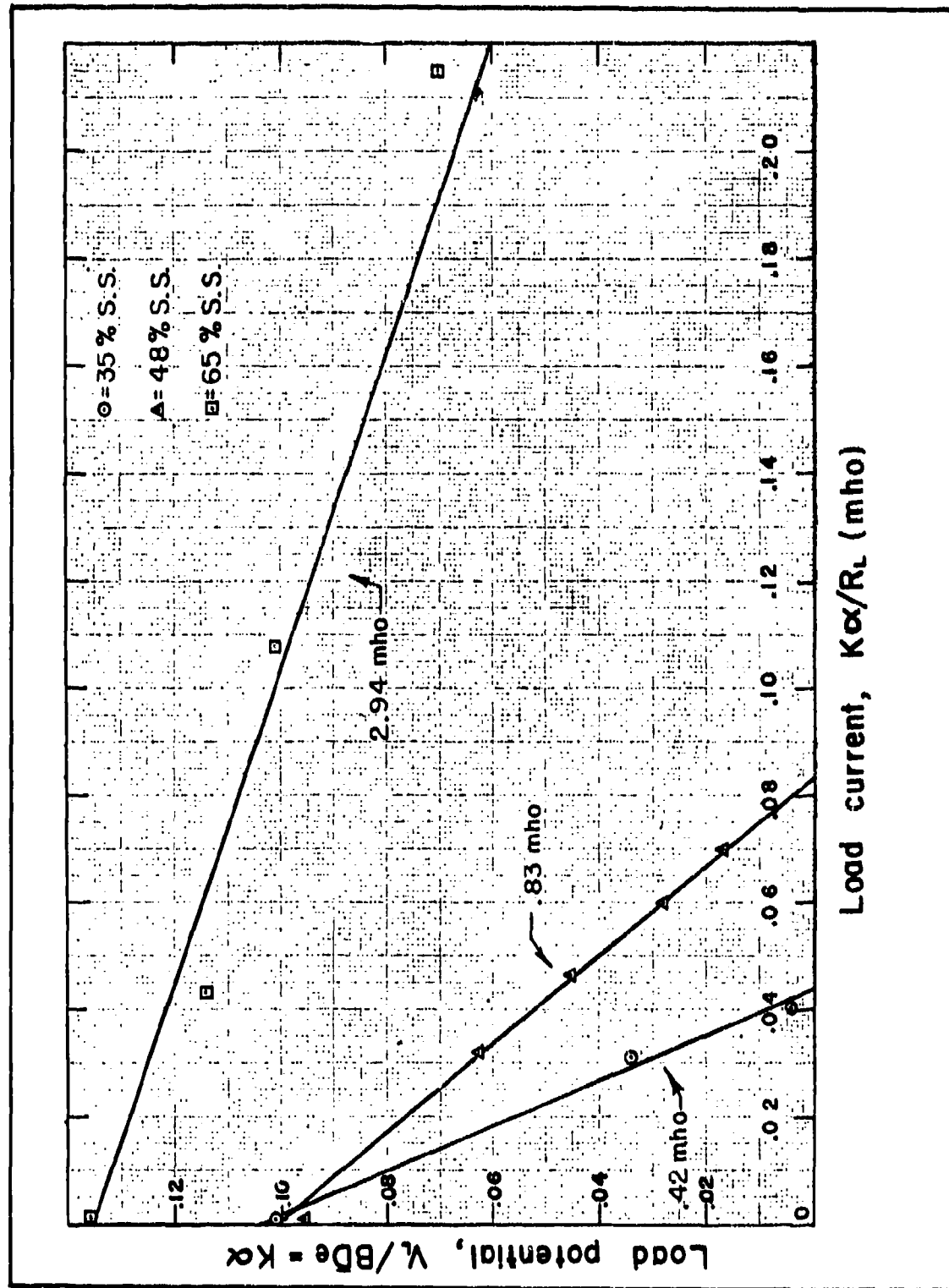


Figure 62. Summary of normalized generator characteristics for Type 316 stainless-steel in Composition C-4; reciprocal of load lines slope is the plasma conductance ($B \approx 0.5$ tesla; charge thickness is $1/4$ in.)

have smaller deviation than those shown in the previous figure. Notice that the scatter is greater at the highest metal fraction, again indicating that the charge width is too thin to consistently give steady, equilibrium detonation.

The normalized open circuit voltage indicates that $\alpha = 1/10$, but there is a slight increase at the higher metal fraction. The reason is unknown at this time, but it can possibly be explained in terms of the two-phase flow characteristics of detonations (interference drag between particles). This point will be clarified when the next series is discussed. To obtain an idea of generator action efficiency, the current value at $k \alpha / R_t = 0.2$ corresponds to about 10 amps. On this basis, the short-circuit current would be double this or 20 amps. In terms of $H = 1/b$, this is 20 amps/0.25 in. or 3×10^3 ampere turns/meter.

c. Sponge Iron in Composition C-4

The results of the series using Allen-Wood Steel Co. sponge iron in Composition C-4 are presented in Figure 63. The most notable difference between this figure and the previous stainless-steel summary is the factor of three increase in open circuit voltage; $\alpha \approx 1/3$ for all three curves. Also note that the current scale is a factor of ten greater in the present figure. For reference, the dotted line indicates the 65 percent Type 316 stainless-steel data from the previous figure. The maximum power delivered to a resistive load is one-half the open circuit voltage times one-half the short-circuit current, or one-half the area of a triangle formed by the axes and the load line. On this basis the maximum power output of the 65-percent iron-loaded Composition C-4 is approximately 100 times better than the 65-percent stainless-steel charges.

Using Equation 14, the power generated in these experiments can be determined. The power per unit area is

$$\frac{K}{b e} = \frac{\alpha^2 \bar{D}^2 B^2}{4} \sigma \bar{a} \quad 57$$

For the 65-percent Allen-Wood iron shots, $\alpha^2 = 0.1$ and $\sigma \bar{a} = G \approx 70$ mho, $\bar{D} \approx 4$ km/sec. $B = 1$ tesla, so

$$\frac{K}{b e} \approx 3.0 \times 10^7 \frac{\text{watts}}{\text{m}^2} = 3 \frac{\text{kw}}{\text{cm}^2} \quad 58$$

This is an even higher value than estimated in Equation 15. However, caution should be exercised in trying to apply this result to an actual device using a permanent magnet material. The main reason is that G will likely be much less and B will be much less than 1 tesla for the low volume fraction of metal present (~ 30 percent).

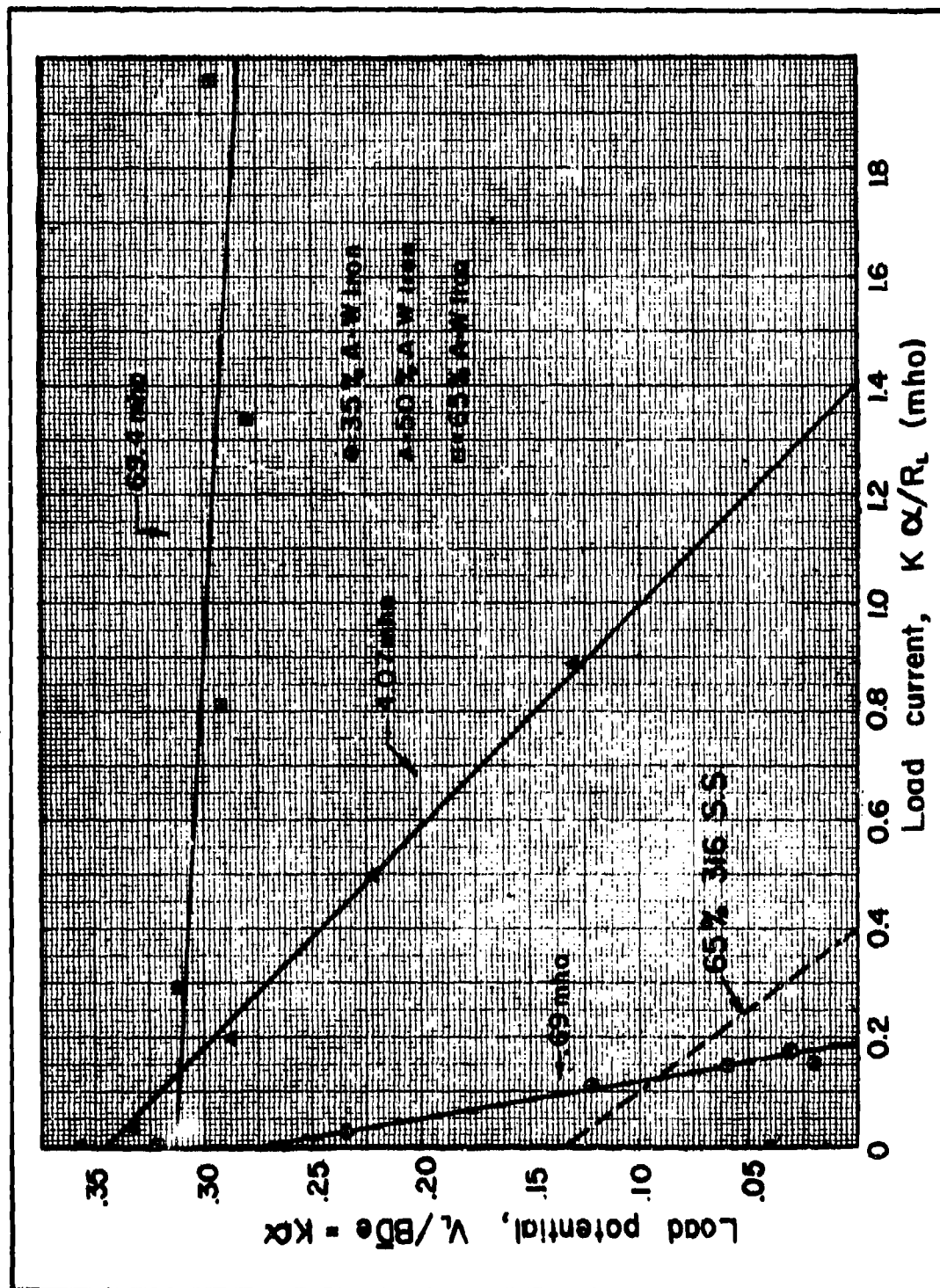


Figure 63. Summary of normalized generator characteristics for sponge iron in Composition C-4 ($B \approx 5$ -K gauss; charge thickness is $1/4$ in.)

In both the Type 316 stainless-steel experiments and the sponge iron experiment, Composition C-4 was used as the parent explosive. By plotting G versus Q for the two metals, one can extrapolate both curves back toward zero and determine the effective conductance of pure Composition C-4. It was not possible to confirm this value experimentally because of the excess amount of explosive required. This data closely resembled the conductance data of Figures 53 and 54; that is, a roughly parabolic shape on semilog paper. Thus, the conductance data can be represented as an equation in the form:

$$\ln G_T - \ln G_0 = \lambda (Q^2) \quad 59$$

or

$$G_T/G_0 = \exp \lambda (Q^2) \quad 60$$

The data for sponge iron was put on a curve-fitting routine for an IBM 360/40 computer and a value of 20 was derived for λ . Time did not permit evaluating λ for Type 316 stainless-steel, but it is expected to be around 5. Using this functional relationship it is possible to extrapolate back to $Q = 0$ and to determine G_0 for Composition C-4. On the basis of this backward extrapolation, it is seen that there is a three order of magnitude increase in conductance when Composition C-4 is doped with a 65 percent by weight metal fraction. If the charges were large enough to allow "ideal" one-dimensional detonation, an even higher metal fraction could be utilized before the detonation failed to propagate. In the size charge used here, propagation was not obtained at 73 percent by weight. It should be noted, however, that 65 percent by weight is approximately 30 percent by volume for iron in Composition C-4.

d. Velocity Effects, Spherical versus Angular

It can be definitely stated that the particle shape must be (at least in part) responsible for the higher open circuit voltages. Chemical reactions can also be invoked, but then why do such chemically diverse particles, copper and Type 316 stainless-steel, have the same open circuit potential? From simple aerodynamics, the drag coefficient for irregular shapes can be up to a factor of ten greater than for a sphere under similar flow Reynolds numbers. The iron particles were viewed under a metallurgical microscope and photographed to illustrate the irregular shape (Figure 64). An idea of the size distribution is also easily determined. This photograph was selected because it shows both the larger sized particles and the smallest. The superimposed scale is graduated in 0.0005-in. (12.7 micron) divisions.

If the iron particles are accelerated to a higher velocity, then the gas phase necessarily loses this additional amount of kinetic energy. This should appear as a further decrease in detonation velocity. Figure 65(a) shows the measured detonation velocity plotted against

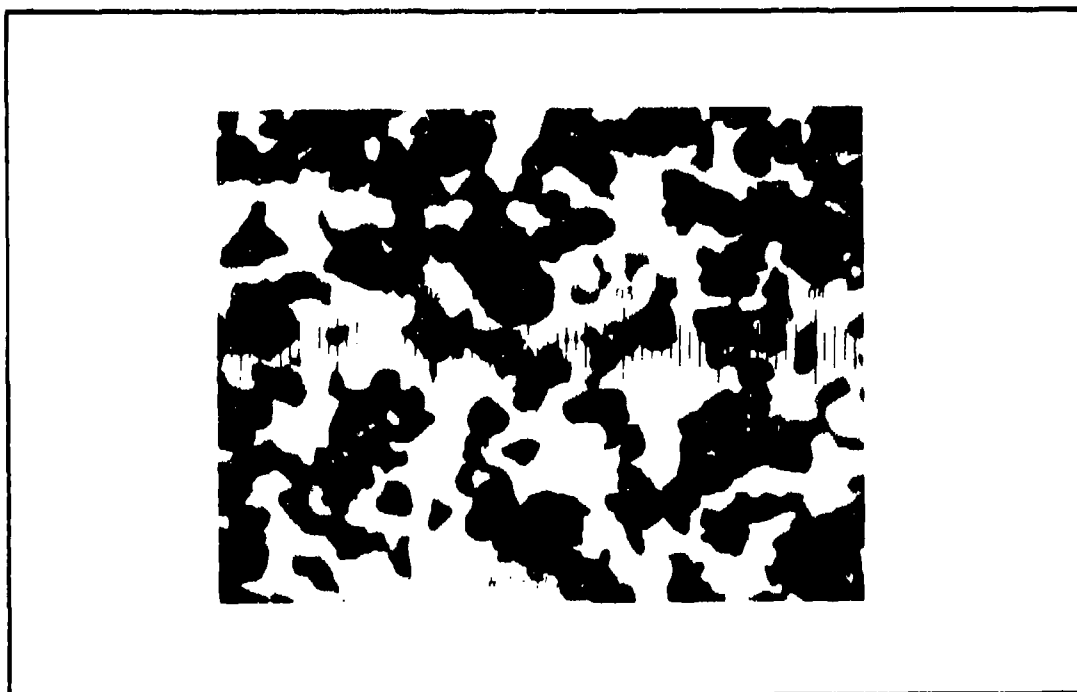


Figure 64. Photograph of the sponge iron additive showing definite angular shape and size distribution (distance between superimposed vertical lines is 0.0005 in.)

the total calculated charge density for both iron and Type 316 stainless-steel. The straight lines are drawn to eliminate the scatter so that Figure 65(b) can be plotted to show \bar{D} as a function of Q . From either figure it is clear that the iron particles with their higher drag coefficient have reduced the detonation velocity more than the same amount by weight of spherical particles. The density of iron and Type 316 stainless-steel are nearly the same, ruling out the effect of different inertial forces on the velocity decrease.

The only trouble encountered in the use of the iron powder is that above 65 percent by weight, the undetonated charge becomes more conductive. This is attributed to the irregular shape, allowing particles to touch, forming long metallic conducting paths in the composite. This definitely contributes to the scatter in data taken at high metal fractions. The use of cast charges would improve this situation.

e. Spherical Copper in Composition C-4

It has been possible to confirm further what has been concluded about spherical versus angular shape. One short series of shots has been made with 65-percent spherical copper in Composition C-4, resulting in Figure 66. As expected, the open circuit conditions indicate $\alpha = 1/10$. The conductance is the highest so far measured. Detonation velocity for these shots remained higher than those with Type 316 stainless-steel (also spherical)

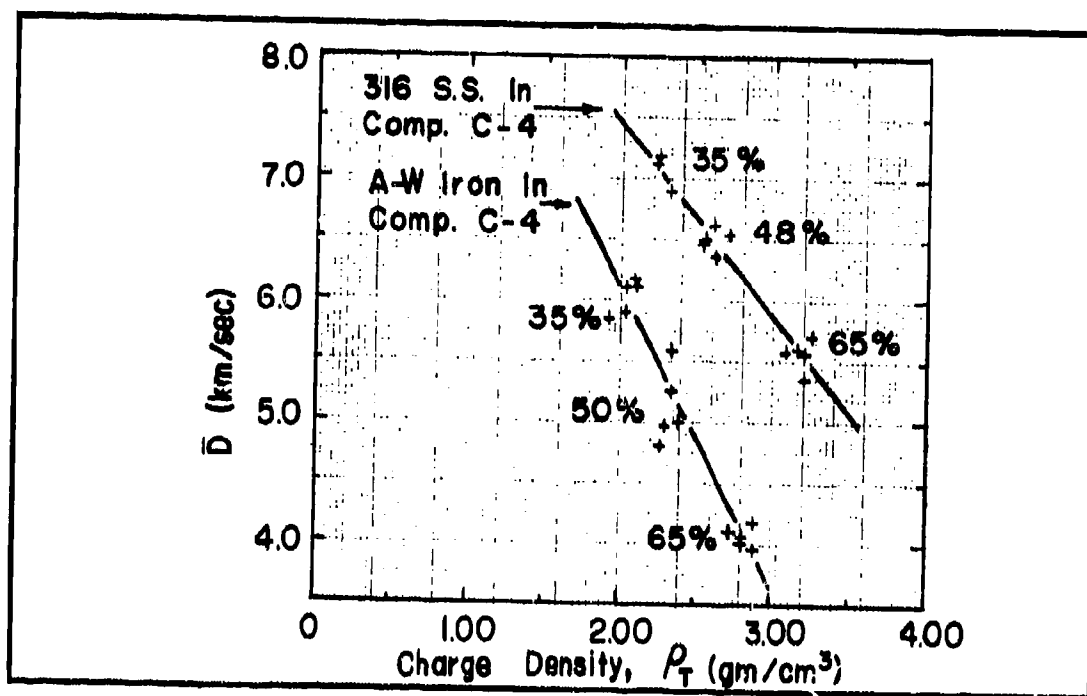


Figure 65(a). Measured average detonation velocity as a function of calculated total charge density for sponge (Allen-Wood) iron and spherical stainless-steel

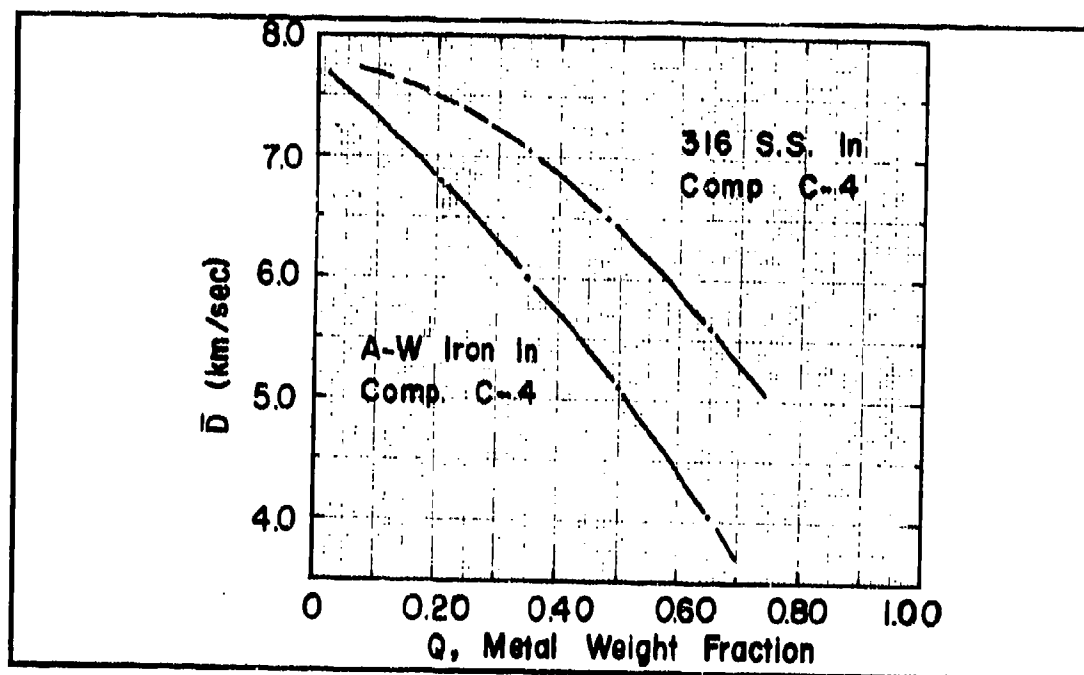


Figure 65(b). Data in Figure 65(a) reduced to show average detonation velocity as a function of Q, metal weight fraction

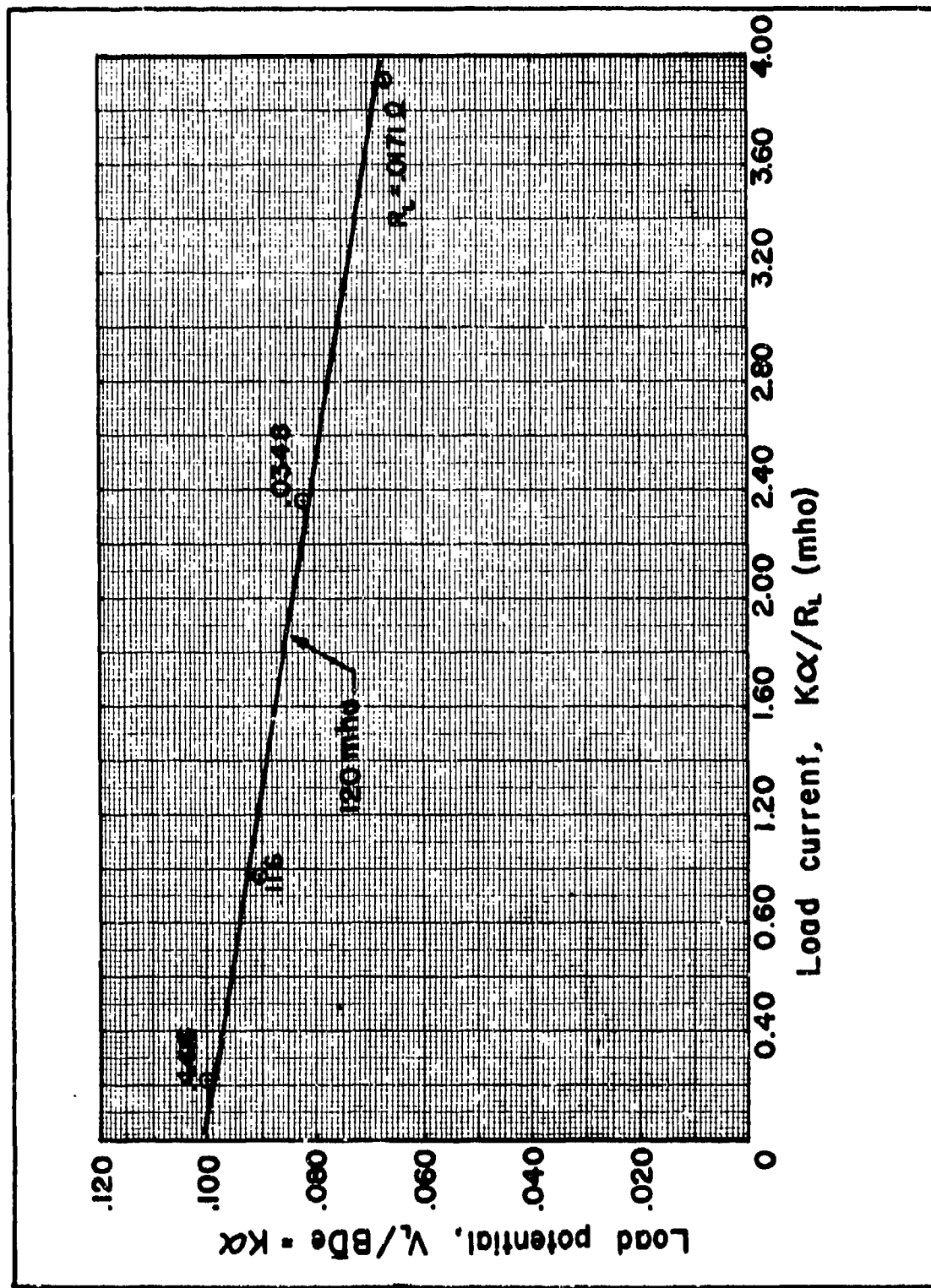


Figure 66. Normalized generator characteristics for 65% spherical copper in Composition C-4 (B field is about 8-K gauss; charge thickness, 1/4 in.)

but were plotted versus total charge density as in Figure 65 for Type 316 stainless-steel, large deviation was apparent even though greater efforts have been taken to ensure accurate measurement of both detonation velocity and density. It was found, however, that when the detonation velocity was plotted versus the load resistance a very definite correlation was noted. From a velocity of 5.98 km/sec at 0.11 Ω , \bar{D} decreased smoothly to 5.43 km/sec at 0.017 Ω , roughly a 10-percent drop.

3. Magnetic Reynolds Number

All of the previous data presented on the characteristic curves can be compared by using the magnetic Reynolds number as a criterion. It is desirable to normalize the data for variations in charge width (b) and height (e); this is easily done by considering basic equations for conductance,

$$G(Q) = \sigma(Q) \frac{b \bar{a}(Q)}{e} \quad 61$$

Since $R_m = \bar{a} \sigma \bar{D} \mu$, we can use the conductance value, G, to determine the $\sigma \bar{a}$ product. From above $\sigma \bar{a} = G(Q) \left(\frac{e}{b} \right)$.

Therefore

$$R_m = \mu(Q) G(Q) \left(\frac{e}{b} \right) \bar{D}(Q) . \quad 62$$

Time has not permitted a definite evaluation of μ as a function of Q for the iron or expected permanent magnet materials. However, it can never be less than μ_0 so this value will be used to simplify the calculations. We can calculate R_m as a function of Q using the functional variation of conductance, G(Q) (shown in Figures 53, 54, and 55), the detonation velocity, $\bar{D}(Q)$ (shown in Figure 65), and the geometrical factors, e and b, for the various experiments. For the conductance data using Detasheet, e = 0.019 m and b = 0.028 m, so $\left(\frac{e}{b} \right) = 6.82$. For the power generation experiments e = 0.0152 m and b = 0.063 m, so $\left(\frac{e}{b} \right) = 2.44$. Figure 67 is a plot of R_m which summarizes this data. The most important fact is that these curves are absolute Reynolds numbers based on μ_0 and not rationalized as was done in the preparation of Figure 57. It is considered notable that the data indicates R_m approaching unity. If an eventual material with a permeability of a few times μ_0 is employed, then R_m will definitely be greater than one. Factors worth consideration for improving these values are:

- (a) Different parent explosives, such as Composition B with higher initial σ
- (b) Larger charges so that ideal detonation is achieved giving larger \bar{D} values and less percentage electrode voltage losses

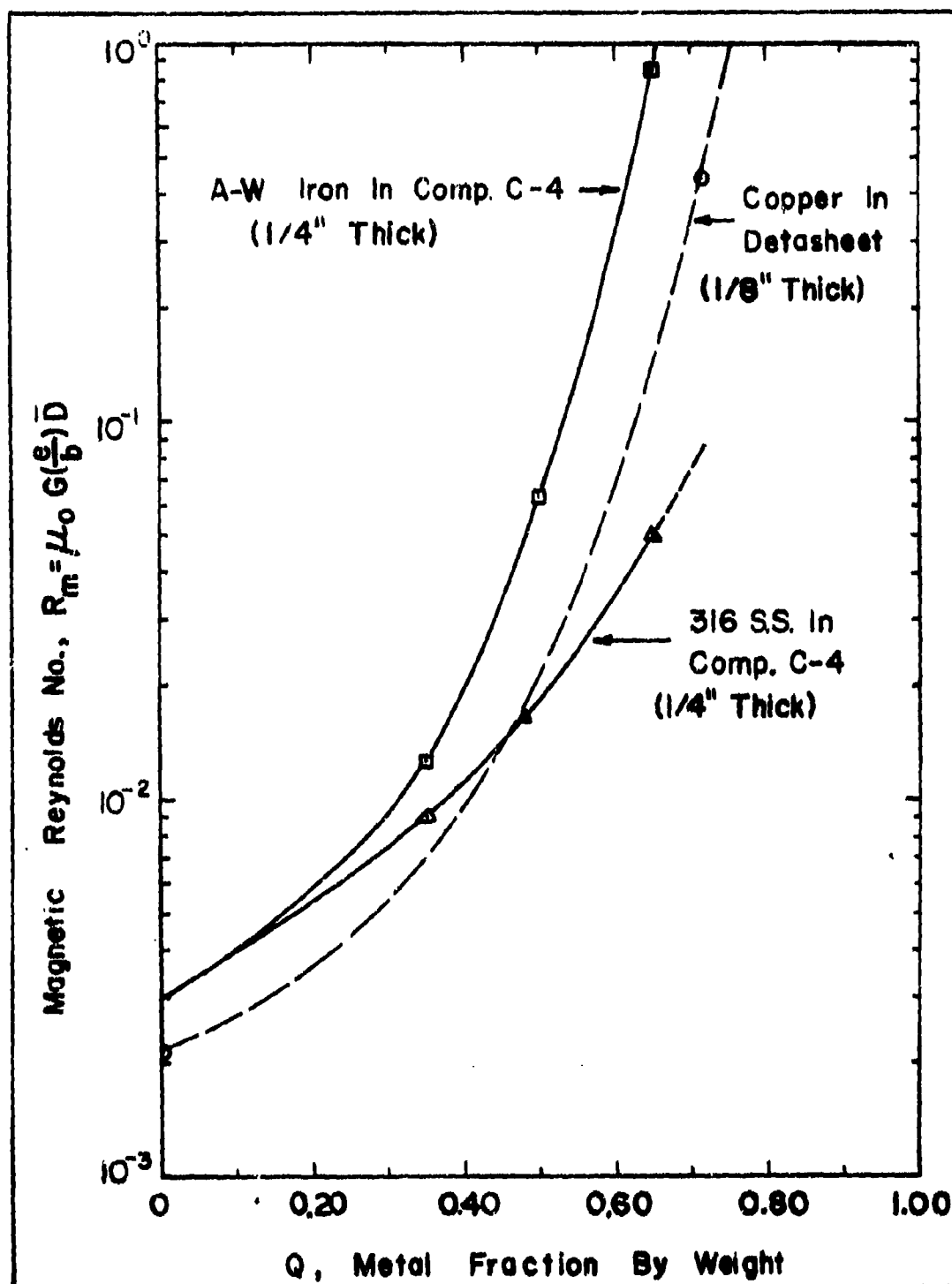


Figure 67. Summary of absolute magnetic Reynolds number, based on μ_0 , for various explosive-metal combinations as a function of the metal weight fraction

(c) Better fabrication technique, such as casting a molten explosive

The fact that R_m values near one have been attained make a more thorough theoretical treatment necessary. R_m based on $\mu_o \bar{D} \sigma \bar{a}$ is an order of magnitude figure of merit. A more accurate parameter can be evolved by considering the circuit as a whole (remembering that in Equation 8, $R_L = 0$). Defining the circuit magnetic Reynolds number, R_{mc} , as the magnetic field induced by the circuit current compared to the applied field, we have

$$\frac{B_{ind}}{B_{app}} = R_{mc} = \frac{\mu_o \bar{I}}{B} \quad 63$$

where the current I is given by

$$I = \frac{V_{oc}}{R_L + R_p} = \frac{\alpha B \bar{D} e}{R_L + R_p} \quad 64$$

Thus (63) becomes

$$R_{mc} = \mu \alpha \bar{D} e / b (R_L + R_p) \quad 65$$

The load factor k was defined as

$$k = V_L / V_{oc} = R_L / (R_L + R_p) \quad 66$$

$$\text{So, } 1 - k = R_p / (R_L + R_p) \quad 67$$

Thus

$$R_{mc} = \alpha \mu \bar{D} \left(\frac{e}{b} \right) \left(\frac{1 - k}{R_p} \right) = \mu G \bar{D} \left(\frac{e}{b} \right) \alpha (1 - k) \quad 68$$

using $G = 1/R_p$ giving finally,

$$R_{mc} = R_m \alpha (1 - k) \quad 68a$$

From this we see that to obtain large induced magnetic fields, a large α is desirable along with heavy loading, $k \rightarrow 0$. The value of R_m deduced from Figure 66 is about 2.7 (not shown on Figure 67); for

short-circuit conditions, $k = 0$, a circuit magnetic Reynolds number would be 0.27. The lowest load resistor used was 0.017Ω making $k = 0.67$. R_{mc} is then ~ 0.10 . The oscilloscope trace for this shot suggests an increase in load voltage toward the end of the event suggesting that the magnetic field was increasing with time.

E. CONCLUSIONS

The electrical conductance of the detonation zone in a condensed high explosive can be increased substantially by adding a metal powder to the explosive. For these experiments the increased conductance can be expressed by

$$\frac{G_T}{G_0} = e \lambda Q^2$$

69

where λ is a coefficient greater than 1 and depends on the electrical conductivity of the metal additive. For example, $\lambda = 20$ for sponge iron.

The effective velocity of the detonation products available for generation of electrical power ranges from one-tenth for spherical particles to one-third for very angular particles. This holds for both explosives used, Detasheet and Composition C-4. The variable most directly involved is the additive particle drag coefficient.

The detonation velocity decreases as the metal fraction present increases so that detonation failure occurs around 70 to 80 percent by weight for the compositions tried. The magnetic Reynolds number, which is the product of conductance and velocity, increases up to the velocity propagation limit. Magnetic Reynolds numbers around one have been attained in these experiments. Values substantially greater than this are possible if improvements are made in charge size, fabrication technique, and basic explosive conductivity. This technique for generating electrical power is feasible based on magnetic Reynolds number greater than unity.

It is possible to make an estimate of the design parameters for a device which would be capable of producing a 50-joule output in 20 micro-sec. If the magnetic Reynolds number is greater than or about equal to one, a device can be designed basing the size on the stored magnetic energy. Assuming $E_{mag} = 0.1$ joule/cc and $P = 0.50$, the volume of composite needed is

$$Vol = \frac{(E_T)}{(E_{mag}) P} = \frac{50 \text{ joules}}{0.1 \frac{\text{joule}}{\text{cm}^3} \times 0.5} \approx 10^{-3} \text{ m}^3$$

70

The event time controls the dimension in the direction of detonation

$$L = \bar{D} t_0 = 5 \times 10^3 \frac{\text{m}}{\text{sec}} \times 2 \times 10^{-5} \text{ sec} = 0.1 \text{ m} \quad 71$$

The device will be essentially a cube 0.1 m on a side. Of course, for higher values of magnetic Reynolds number, the volume is correspondingly less.

It is worthwhile noting that such a device has no moving parts and should be very inexpensive to produce. The composite needed for 10^{-3} m^3 is about 4 kg, based on $\rho = 4 \text{ gm/cm}^3$ (See Figure 65(a)), or roughly 10 lb. The composite should cost about \$1/lb with the whole manufactured device costing less than \$5/lb so that the total cost would be about \$50. Conventional ordnance techniques could be used to initiate the device using either single-point or multiple-point initiation. By changing the relative height and width of the explosive charge, the internal impedance could be varied by a factor of about 10^2 . With larger charges, this range of generator internal impedances could be correspondingly increased. Several different geometries for such devices have been previously described.

SECTION IV

MILLISECOND-DURATION PULSED MHD POWER GENERATION

A. INTRODUCTION

The objective of this phase of the program was to investigate the phenomena associated with fast-burning solid fuels for MHD generators and to produce power pulses of 10^3 - 10^4 joules over action times of 1 to 5 ms. Although both longer (1 sec) and shorter (100 microsec) systems have received attention in the past, operation in the millisecond time regime seemed to require additional study. New military weapon and surveillance systems dictate the power-time regime investigated. To facilitate the repetitive-pulse aspects of future requirements, it was proposed to use standard 20-mm automatic cartridges as the combustor assembly.

This presentation is separated into the following parts:

- (1) Fuel Characteristics
- (2) Theory and Method
- (3) Fuels Used in the Study
- (4) Experimental Equipment
- (5) Experimental Results
- (6) Data Analysis
- (7) System Design
- (8) Conclusions and Recommendations

B. FUEL CHARACTERISTICS

According to the principles of MHD power generation, it is necessary to have a highly electrically conductive fluid in motion in a magnetic field. Many sources of this fluid are available, but of particular interest for a lightweight generator are the combustion products of rocket fuels. These fuels produce large amounts of high-velocity, high-temperature gas for a minimum weight and volume. The addition of materials which produce a copious supply of free electrons make the seeded rocket fuel one of the most attractive energy sources for MHD power generation (4) (5).

Since rocket fuels can be tailored for many different applications, it is necessary to determine selection criteria to be used in the optimization process. For MHD applications the fuels are selected so that some function of electrical conductivity, electron collision frequency, and specific impulse rather than specific impulse alone, is a maximum. The

specific function of the three parameters used depends on the application for which the fuel is intended. For example, a fuel optimized for a Hall device would require a lower electron collision frequency than would a fuel developed for a Faraday generator. In the discussion that follows the fuel composition and the influence of the size of the fuel elements upon combustion are considered.

C. THEORY AND METHOD

To characterize MHD fuels sufficiently to evaluate their relative performance, it is necessary to determine the thermodynamic and electrical properties of the combustion products.

The thermodynamic properties of the combustion gases of rocket fuels are calculated with the aid of a digital computer using a "Free Energy Specific Impulse Program". Use of this program requires a set of chemical compounds to be considered as the fuel ingredients. The chemical compositions, heats of formation, and densities of these compounds are also required. It is necessary to examine the chemical formulae of these ingredients and generate a set of probable reaction products which would be formed in a combustion reaction involving the reactants. In practice, JANAF thermochemical data are used for the individual reaction products.

At an arbitrarily specified reaction pressure, the molar amounts of the chemical elements in the ingredient mixture are distributed among the products with an initial temperature estimate. The Gibbs free energy of the mixture is calculated using the thermodynamic data of the individual products. The exhaust product composition is adjusted until the Gibbs free energy is at a minimum, thus determining the equilibrium composition of the reaction product mixture. The enthalpy of the mixture is calculated and compared with the heat of formation of the combined ingredients. The temperature is recalculated so the mixture enthalpy and heat of formation are identical. At the recalculated temperature the mixture composition is again adjusted to minimize the Gibbs free energy. These two operations are repeated until convergence is obtained for the two criteria. This results in an equilibrium composition for the first pressure. This is normally called the chamber composition, and the temperature and pressure are the chamber conditions. Once these are known other properties, such as entropy heat capacity, molecular weight, and ratio of specific heats, can be calculated. With the chamber properties and conditions being known, the rocket nozzle exit conditions are calculated in a similar manner. Either an arbitrarily specified exit pressure or an expansion ratio is used. For the composition determination at equilibrium, the Gibbs free energy is again minimized, but the enthalpy criterion is replaced with the criterion that the exhaust expansion in the nozzle is isentropic. Hence, a temperature is determined for the product mixture so that its entropy equals the entropy in the chamber. Convergence is sought for the entropies to be equal and the Gibbs free energy to be a minimum. The temperature and composition thus obtained allow the exit condition properties of the exhaust to be calculated. With the chamber and exhaust

conditions obtained, the specific impulse of the fuel can be determined. The composition of the rocket exhaust products includes the amounts of electrons and ions due to thermal ionization at the gas temperature as well as the species arising from the thermochemical reactions involving the ingredients. From the temperature and composition, the electrical properties of the exhaust are calculated.

D. FUELS USED IN THE STUDY

In the course of the experimental study, three specific fuels were used: VGM, VJM, and VJP.¹ These fuels are aluminum double-base seeded with potassium salt. The fuel designated VGM is the one used in past work for 1-sec burn times and was used in this study as a baseline for evaluating the newer fuels. VGM used KClO_4 as a partial oxidizer and seed material. The two newer fuels, VJM and VJP, used KNO_3 for this purpose.

The use of standard rocket grain configurations is not applicable to pulses of less than 100-ms duration because of the characteristic burning rate of solid fuels. The burning rate is fixed by the pressure and is in the range of 6 cm/sec for the pressures of interest. For a 1-ms burst, therefore, the burning thickness or web would have to be 6×10^{-3} cm, which is not structurally feasible. Thus, the use of granulated fuels has been adopted for this time regime. Manual cutting was used for the granules in these experiments; hence, the degree of granulation was limited. The size of the granules used was a cube of about 3 mm on a side. The total amount of fuel used in the chamber was experimentally determined as that required to give a pressure of 5000 psia ($3.42 \times 10^7 \text{ n}^t/\text{m}^2$) for the given nozzle size.

An ideal grain size can be found by using the burning rate and the time for which the pulse is to last. If we consider a burn time of 1 ms and the burn rate of 6 cm/sec, the ideal granule would be a hollow cylindrical grain with a web of 1.2×10^{-2} cm. The hollow cylinder is used to give a neutral burning grain² and the thickness is determined by the fact that the web burns from both sides. An inside diameter of 0.10 cm is possible, which would give an outside diameter of 0.125 cm.

E. EXPERIMENTAL EQUIPMENT

The equipment needed to conduct the study included a magnet, a combustion chamber, MHD channels, and data handling equipment. The magnet was designed for use in continuous-flow MHD experiments and is not necessarily optimized for a pulsed system. The magnet, which is shown in Figure 68,

¹The designation of fuels by letters follows the practice of the rocket industry and is intended only for cataloguing. The letters themselves are not indicative of properties, ingredients, etc.

²A hollow cylinder burns from both the inside and outside surfaces and both areas are a function of the radius, so as one area increases the other decreases. Neutrality is required since the chamber pressure of a solid fuel is dependent on the ratio of nozzle area to grain surface area.



Figure 68. Magnet

has water-cooled, saddle-shaped copper windings. An iron shroud is provided to increase the magnetic induction for a given power input. The cross section area or window in the magnet is 0.2×0.22 m with the 0.2-m dimension being in the magnetic field direction. The magnetic field is constant over a 0.6-m length. A curve of magnetic field versus field current is shown in Figure 69. The magnet is powered by an external battery bank. The field strength used for most runs was 2.4 tesla.

Two combustion chambers were used in this series of experiments. The first, shown in Figures 70 and 71, used a standard 1-lb-charge combustion chamber (designated OPC in later discussions), into which was inserted a phenolic sleeve. This sleeve holds the granulated fuel as well as the igniter assembly. The fuel and igniter assembly is covered with a 6-mil polyolefin disc backed up with an aluminum wire screen. The forward end contains ignition wire lead post, pressure taps, and an over-pressure blowout disc. The second system (Figure 72), utilizes a 20-mm cannon shell loaded with 35 grams of fuel. For the purposes of these experiments, a chamber was cast around the 20-mm shell and then the casting was inserted into the chamber described above. A short expansion zone is provided between the shell and the nozzle. Both nozzles have the same diameter (3.01 cm).

Two basic channel designs were used. The first (Figure 73), was designed to be operated in the segmented mode. Certain design approximations were made. They were dictated by the availability of materials and ease of construction. For example, the divergence angle of the channel was held at a constant $2\frac{1}{2}$ degrees, even though a varying divergence angle would be required for optimum performance. The electrodes were made of $\frac{1}{2}$ -in. (1.27 cm) bar stock with spacings of $\frac{1}{2}$ -in. while the calculations used 1 cm for both dimensions. The channel was 60-cm long with 22 pairs of electrodes. Table III gives various calculated parameters for the three fuels in similar generators.

The second channel (Figure 74) utilized the steel shell developed for previous MHD work, with an insert placed inside to achieve a tapered channel. Solid-copper electrodes, spaced at 12.7 cm, were used and the insulating walls diverged at a rate predicted to achieve a constant gas velocity. The calculations on which this channel was based utilized a two-phase exhaust gas. The transition section in both cases was cast of an epoxy-based filler.

The primary data recording system utilized oscilloscopes, although data was also recorded on a magnetic tape FM recorder. The current from the generator was measured through the use of toroids whose output voltage was proportional to $\frac{di}{dt}$. This signal was then electrically integrated in an R.C. network containing a feedback loop to eliminate the R.C. decay. A schematic of this system is shown in Figure 75. The $\frac{di}{dt}$ trace was also manually integrated in several cases as a check against the electronic integration. A typical load is shown in Figure 76. These loads are constructed in a low-inductance configuration with resistance values of 0.004, 0.040, 0.100, and 0.400Ω .

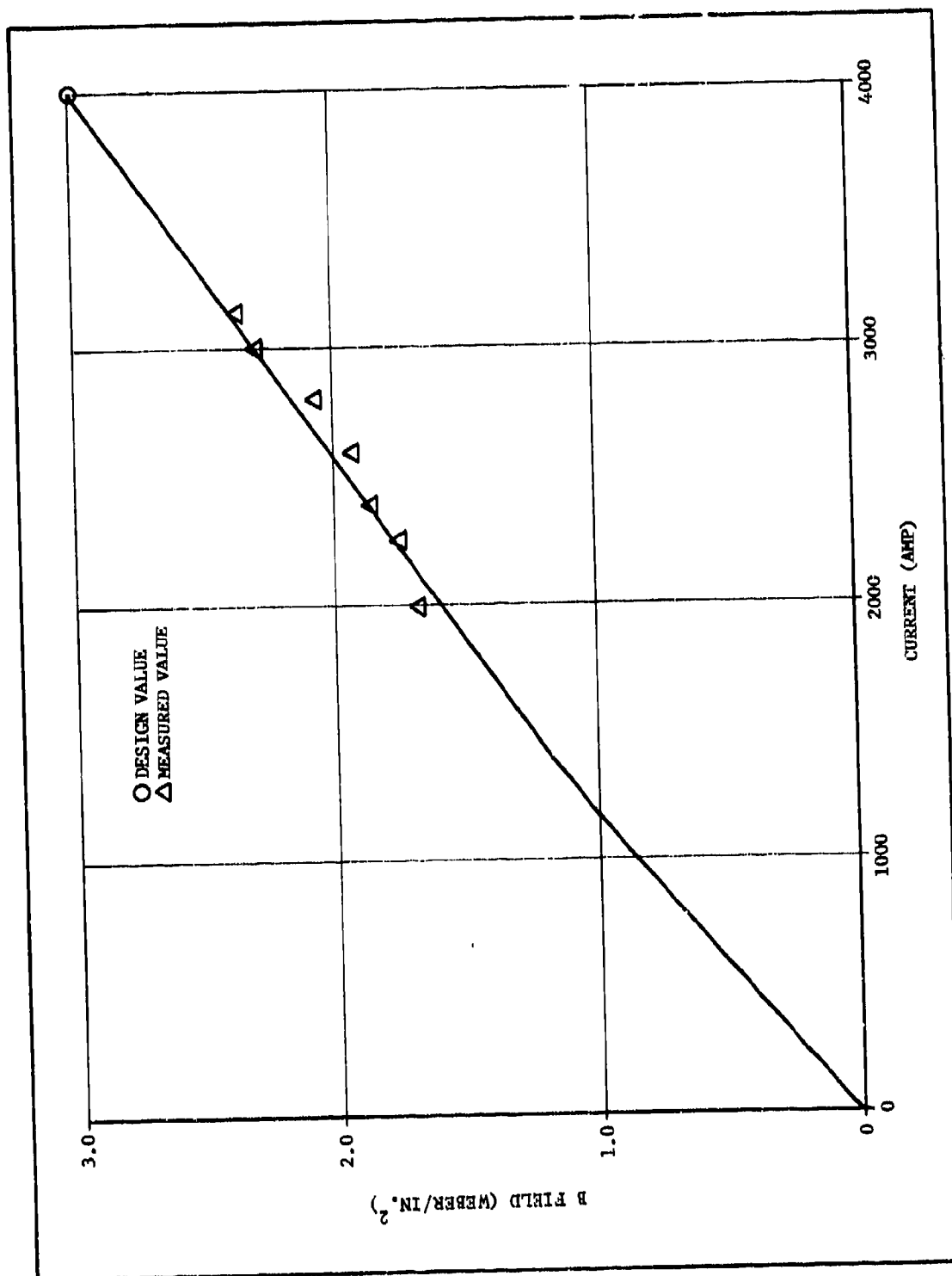


Figure 69. Magnet calibration curve



Figure /1. One-pound-charge combustion chamber

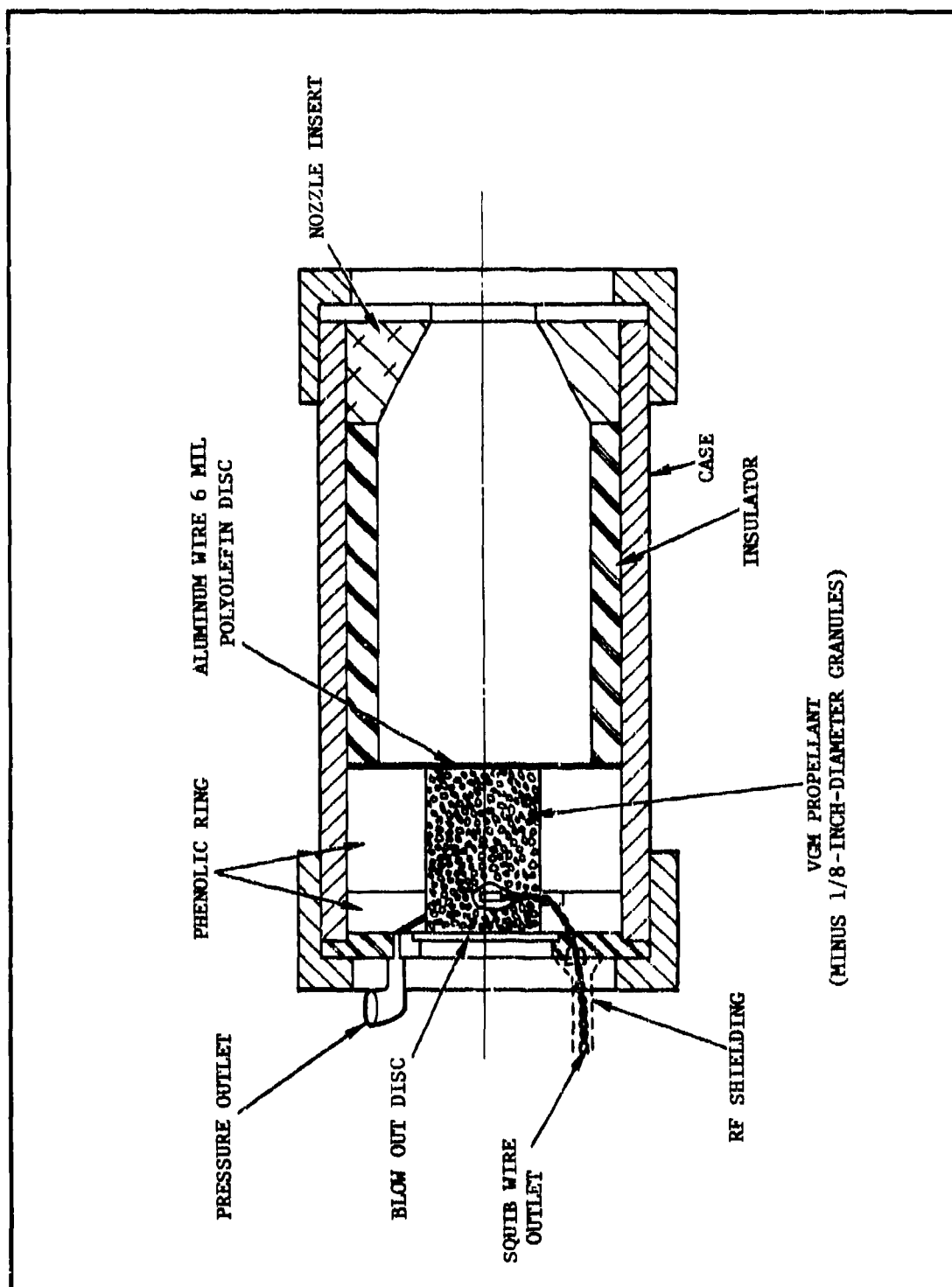


Figure 70. Pulse motor cross section (2/3 scale)

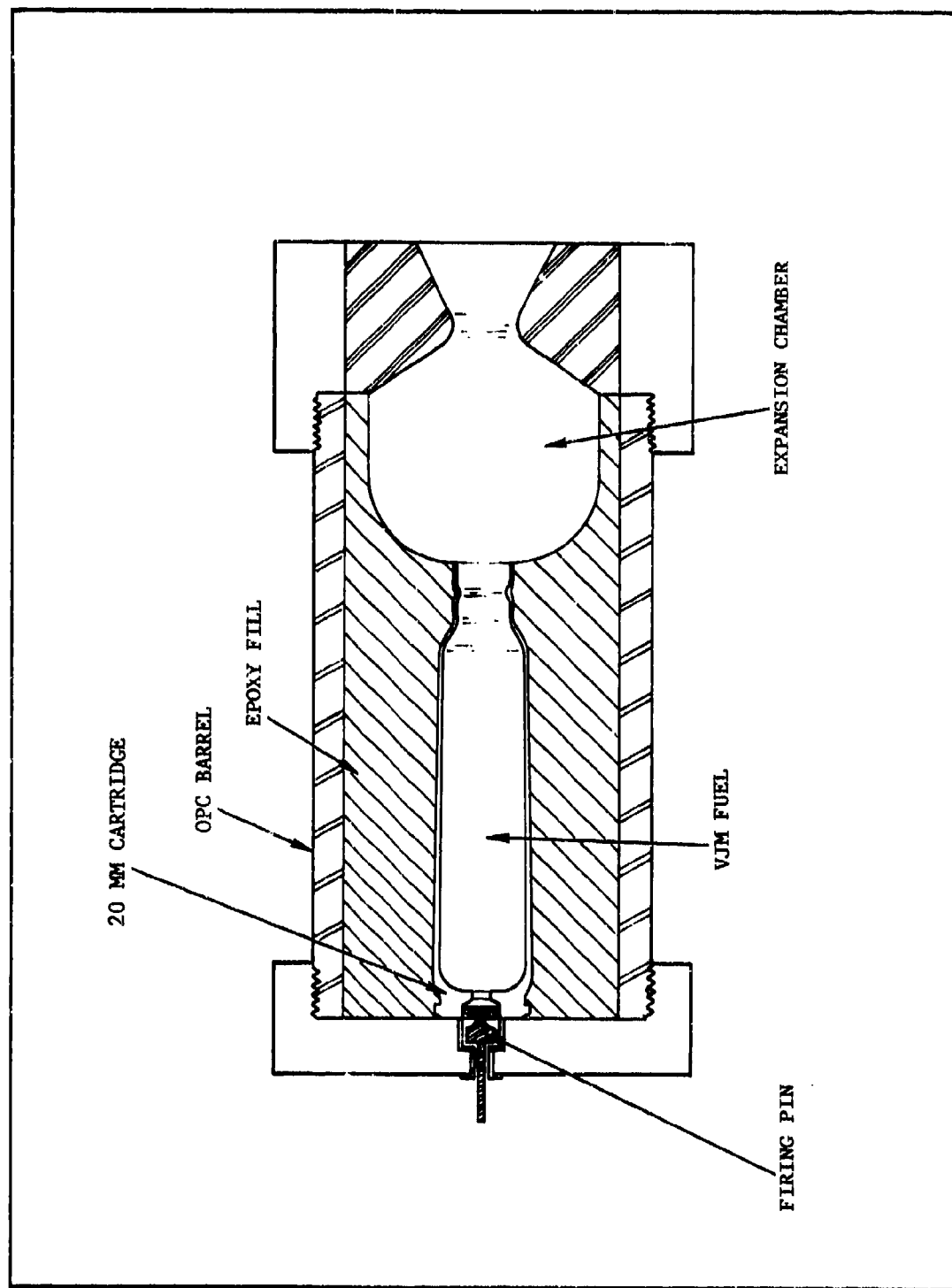


Figure 72. 20-mm combustor system



Figure 73. Segmented-mode channel design

TABLE III
CALCULATED PARAMETERS OF THREE MID FUELS IN CONSTANT MACH NUMBER CHANNEL
FOR VARIATION OF AREA RATIO (MAGNETIC FIELD STRENGTH (B) EQUALS 2.8 TESLA)

Electrode No.	Area Ratio	Mach No.	Velocity (m/sec)	Pressure (nt/m ²)	Gas Temp (°K)	$\frac{\sigma_0 v^2}{1+(\omega\tau)^2} \frac{\text{mho/m}}{\text{sec}^2}$	$\frac{\sigma_0}{1+(\omega\tau)^2} \frac{\text{mho/m}}{\text{mho/m}}$	σ_0 mho/m	$\frac{\omega\tau}{B}$
<u>VGM</u>									
1	10.45	2.08	2238	11.1×10^4	2656	15.5×10^7	30.9	34.8	0.130
2	11.25		2236	10.3	2646	14.9	29.8	34.3	0.142
3	12.00		2234	9.6	2640	14.3	28.7	33.9	0.155
4	12.72		2232	9.1	2635	14.3	28.7	33.9	0.155
5	13.42		2229	8.6	2630	13.7	27.5	33.5	0.169
6	14.00		2228	8.2	2625	13.7	27.5	33.5	0.170
7	14.78		2226	7.8	2621	13.0	26.3	33.1	0.186
<u>VJM</u>									
1	11.40	2.06	2334	10.1×10^4	2529	60.5×10^7	111	160	0.241
2	13.56		2321	8.4	2502	51.9	96.3	158	0.290
3	16.33		2307	6.9	2473	42.8	80.5	155	0.351
4	20.21		2292	5.6	2439	33.9	64.6	153	0.426
5	25.76		2274	4.3	2400	25.8	50.0	151	0.517
6	34.89		2250	3.2	2351	16.1	31.8	147	0.694
7	53.96		2217	2.0	2282	8.6	16.3	143	1.01
<u>VJP</u>									
1	11.61	2.24	2429	9.3×10^4	2374	63.2×10^7	107	173	0.285
2	14.11		2414	7.6	2345	57.3	98.2	171	0.313
3	17.55		2397	6.1	2312	41.6	72.3	167	0.417
4	22.85		2376	4.6	2272	31.9	56.39	165	0.503
5	31.63		2350	3.3	2222	20.0	36.3	161	0.673
6	50.17		2314	2.1	2154	0.98	18.6	155	0.983
7	126.1		2248	0.79	2032	0.18	3.49	143	2.29

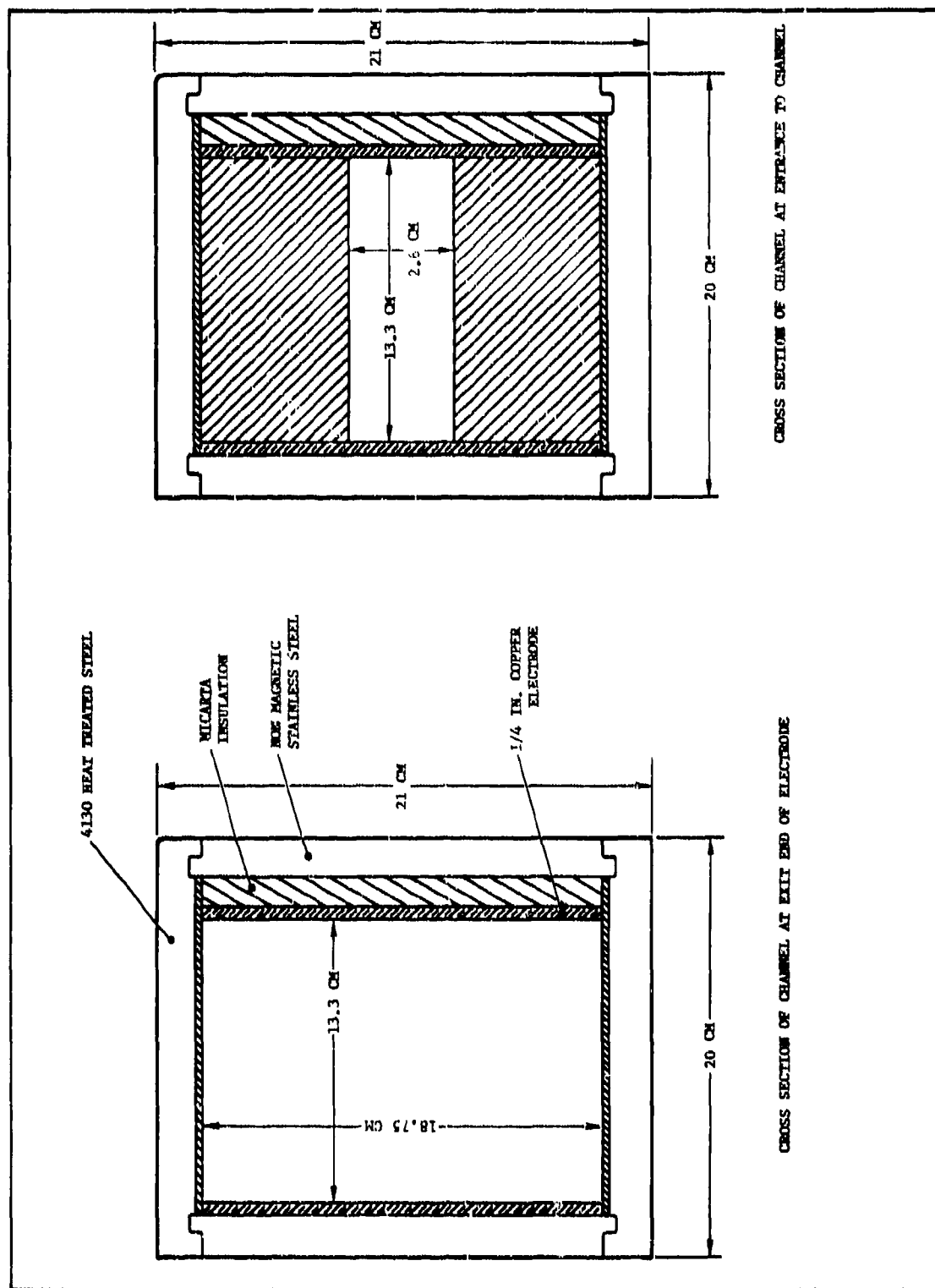


Figure 74. Cross sections of channel at exit end of electrode and at entrance to channel

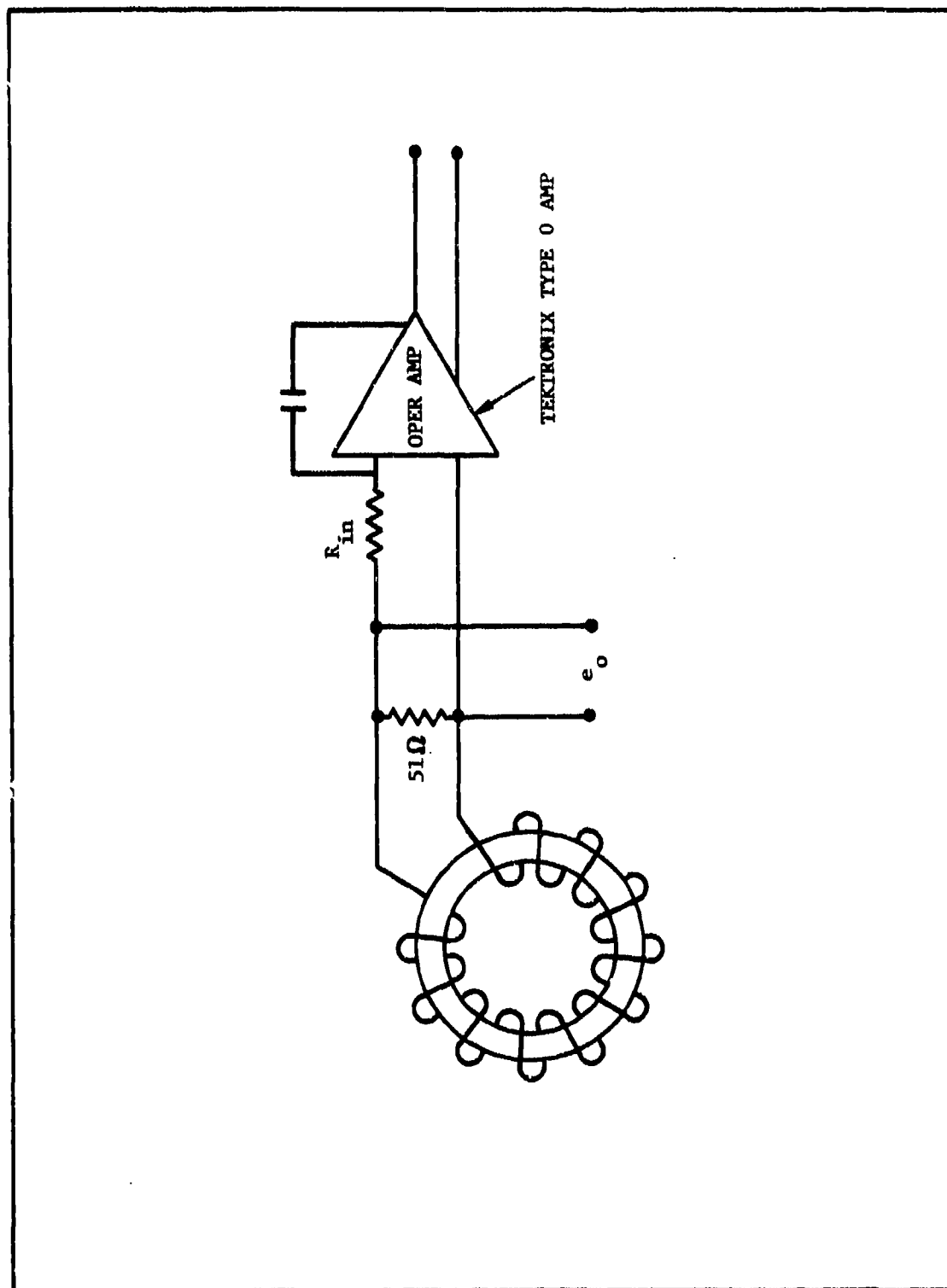


Figure 75. Toroid and integrator schematic

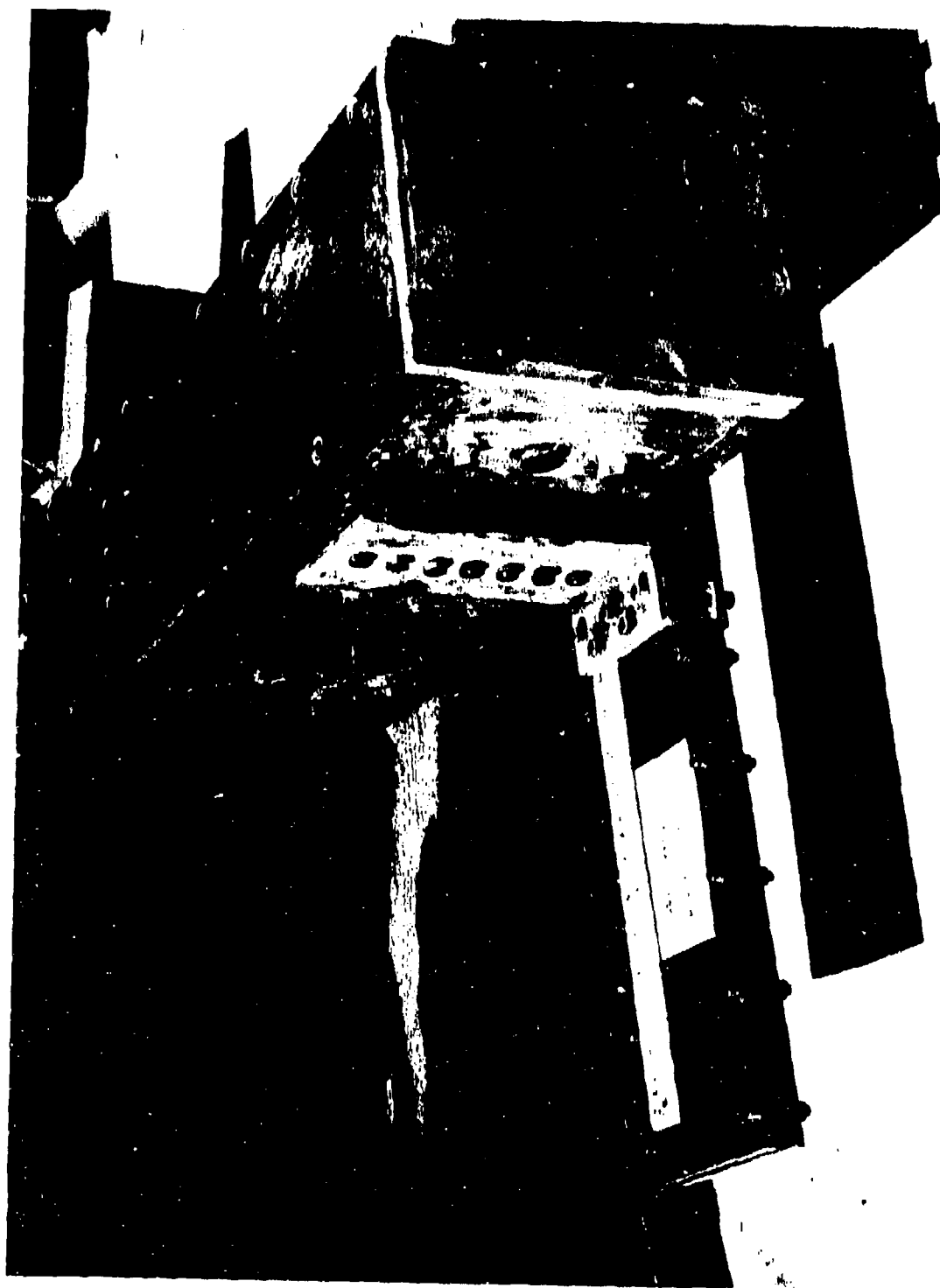


Figure 76. Typical load

F. EXPERIMENTAL RESULTS

The experimental results are presented in the following order (discussion of the results appears in paragraph G.):

20-mm Feasibility Tests

Pressure-Time History

Segmented-Electrode Channel

Continuous-Electrode Channel

The 20-mm feasibility test was designed to show that the standard igniter would ignite MHD fuel in granulated form. The data shows that the MHD fuel will be ignited in a 20-mm case. The feasibility test also had as its goal to demonstrate that successful pressure-time histories could be obtained. A sequence of tests was arranged to define the proper load and orifice characteristics. The fourth test showed that 30 grams of fuel fired through a 3.01-cm orifice was satisfactory and resulted in a peak pressure of just under 400 psi (2.74×10^7 n^t/m²). Pulse duration was about 2 ms. It was found that 35 grams of 3-mm granules could be contained in the case. Since new 20-mm cases were not readily available, it was decided to proceed with the testing program using a standard OPC rocket case containing 50 grams of fuel. The nozzle size was the same as used with the cartridge, and it was felt that the data accumulated on these tests could be transcribed to the 20-mm tests.

Examination of the pressure traces suggested that the combustor physical characteristics rather than the fuel burn time are dictating the pressure-time plot. The curve strongly resembled a pressure vessel decaying through an orifice. The pressure decay curve during all runs appeared to have about the same time constant independent of peak pressure as shown in Table IV. That is, if all traces were normalized so that the peak pressure was unity, the traces would be very similar. It will be shown that this behavior is significant.

The segmented channel was tested under open circuit conditions for its first test. The voltage averaged 500 volts for a period of 1 ms and then dropped to 300 volts for 5 ms. The pressure peaked at 600 psi (4.11×10^7 n^t/m²). Two unsuccessful tests were then made to measure short-circuit current on this channel; the traces were very noisy due to inductive ringing. The ringing seemed to be caused by the long leads required in the segmented configuration. The channel was then operated in a continuous electrode mode to measure the open circuit voltage. A voltage of 440 volts was recorded.

The remainder of the test program used the second channel.

TABLE IV

EXPERIMENTAL DATA WITH OPC COMBUSTOR

Test No.	Load (ohm)	Voltage	Current (amp)	Power (kw)	Peak Pressure (psi)	Time Const. (ms)	Comments
366	SC*	--	2770	--	5600	1.0	--
+373	SC	--	2770	--	4500	0.5	VCM fuel, old linear channel
+374	SC	--	4250	--	6000	0.9	VCM fuel, old linear channel
+375	0.036	75	2310	173	--	0.6	--
382	SC	--	2000	--	6000	1.0	--
383	OC**	430	--	--	3400	1.0	--
384	0.036	79	2200	174	3100	1.5	--
385	0.386	200	515	103	4500	1.1	--
386	0.386	184	481	88.5	4500	0.9	Electrodes coated with CsNO ₃
394	0.036	32	982	31.4	5875	--	Carbon electrodes
396	0.036	22	570	12.5	5500	1.0	Carbon electrodes
398	0.036	41	1170	48	5700	1.0	Carbon electrodes
399	OC	400	--	--	3200	1.4	Carbon electrode cathode ground
400	0.036	70	2100	147	4500	1.0	Copper electrode cathode ground
403	0.105	170	1630	277	5100	1.0	--
404	--	55	2300	127	5400	0.9	--
405	OC	420	--	--	4200	1.0	--
407	0.200	172	860	148	4200	0.8	--

*Short circuit

**Open circuit

A series of tests was then made using both the 20-mm shells and the OPC combustor. It was found that the peak values of voltage and current were compatible for both systems although the decay was faster for the 20-mm combustor. Results of the tests and their related parameters are given in Table V.

Tests 394, 396, 398, and 399 were made with graphite electrodes replacing the copper. This was done to determine the relative electron emission characteristics of copper, carbon, and CuO. As can be seen from Table IV, the output for the tests with carbon electrodes was well below the values obtained with copper. This indicates that the field emission characteristic of copper is the prime method of transplating electrons across the boundary layer.

Two electrode lengths were utilized in the series of tests. They were 40 cm and 60 cm. The data for the two lengths is shown with voltage versus current in Figures 77 and 78. Although few points are shown with the 40-cm channel, they fit well with those of the 60-cm data.

G. DATA ANALYSIS

The principal problem is to find the cause of the gross difference between the measured and predicted power. Using steady-state equations, a power of 3×10^6 watts was predicted with an open circuit voltage of 700 volts. The calculated conductivity was 150 mho/m with an effective conductivity (Faraday) in the transverse direction of 73 mho/m. The actual open circuit voltage was 440 volts, producing a peak power of 2.70×10^5 watts. The effective conductivity is 35 mho/m or about half of that predicted. It is evident that many loss mechanisms are operating in this time region which are not present in the steady-state channels. As a first step the combustion history will be deduced from the pressure traces to determine the level of combustion inefficiency.

One can examine the discharge of a pressure vessel decaying through a nozzle using the parameters of solid-rocket fuel combustion products. The pressure at anytime, t , is given by (3):

$$p = P_0 e^{-\frac{C_D A_t}{VB} t} \quad 72$$

where

C_D = discharge coefficient

A_t = throat area

V = volume of combustion chamber

β = $\frac{\text{density}}{\text{pressure}}$

$\tau = \frac{V\beta}{C_D A_t}$

73

TABLE V
EXPERIMENTAL DATA WITH 20-MM COMBUSTOR

Test No.	Load ¹ (ohm)	Voltage	Current (amp)	Power (kw)	Peak Pressure (psi)	Comments
303	OC ²	500	--	--	3500	Segmented
324	OC	450	--	--	3000	Segmented
329	OC	425	--	--	3700	Continuous
330	OC	400	--	--	--	--
345	OC	450	--	--	3500	Channel No. 2
347	0.036	107	2970	318	2500	No current recorded, value from voltage and resistance
363	0.036	71	1960	139	4000	--
364	0.036	50	1500	75	3200	--
365	SC ³	--	2775	--	3000	--

¹Inductive shunt used with load caused error in voltage and current values.
Subsequent firings incorporated toroid measuring techniques, thus eliminating this error
²Open circuit
³Short circuit

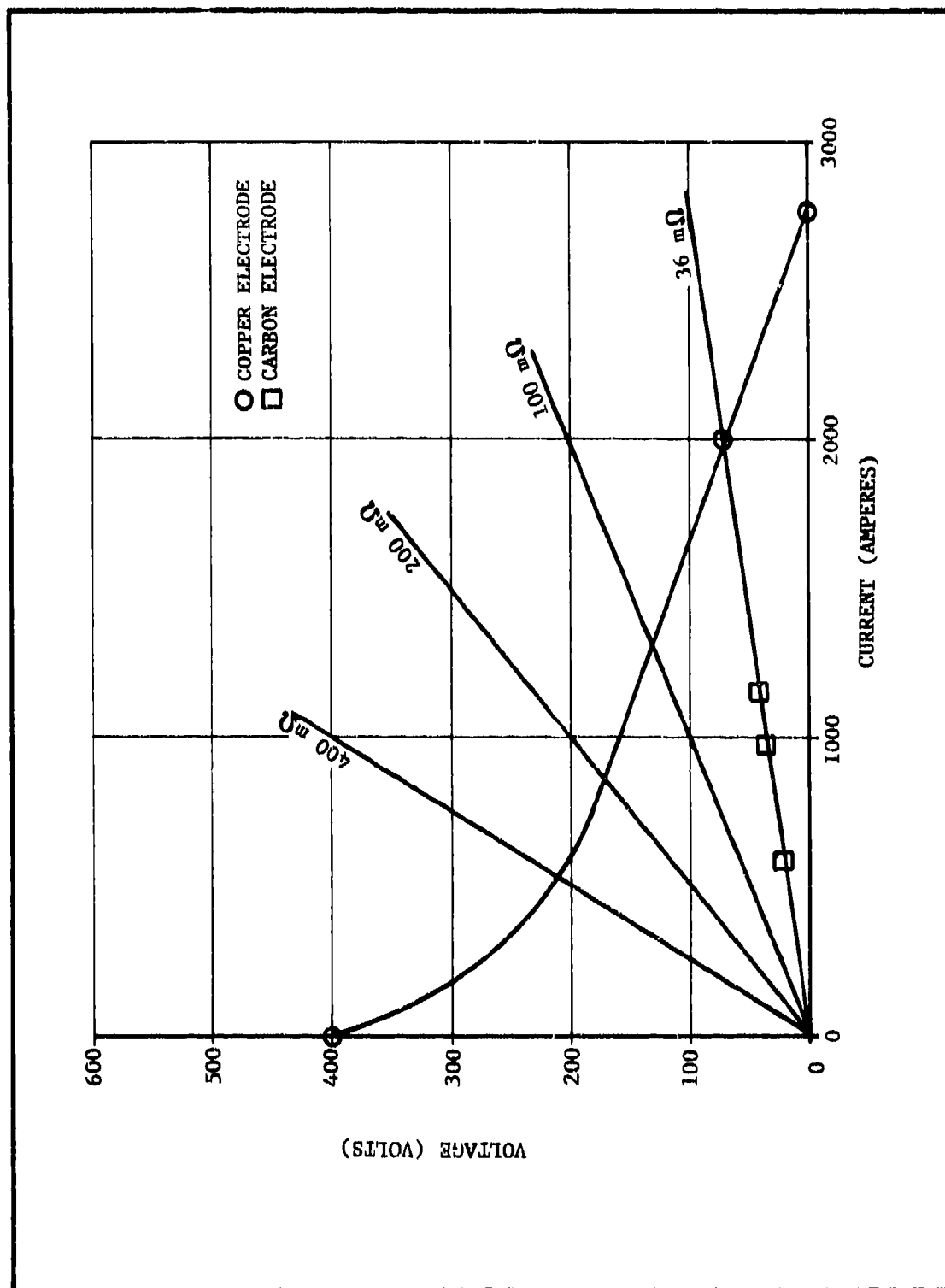


Figure 77. Plot of voltage versus current for 40-cm channel

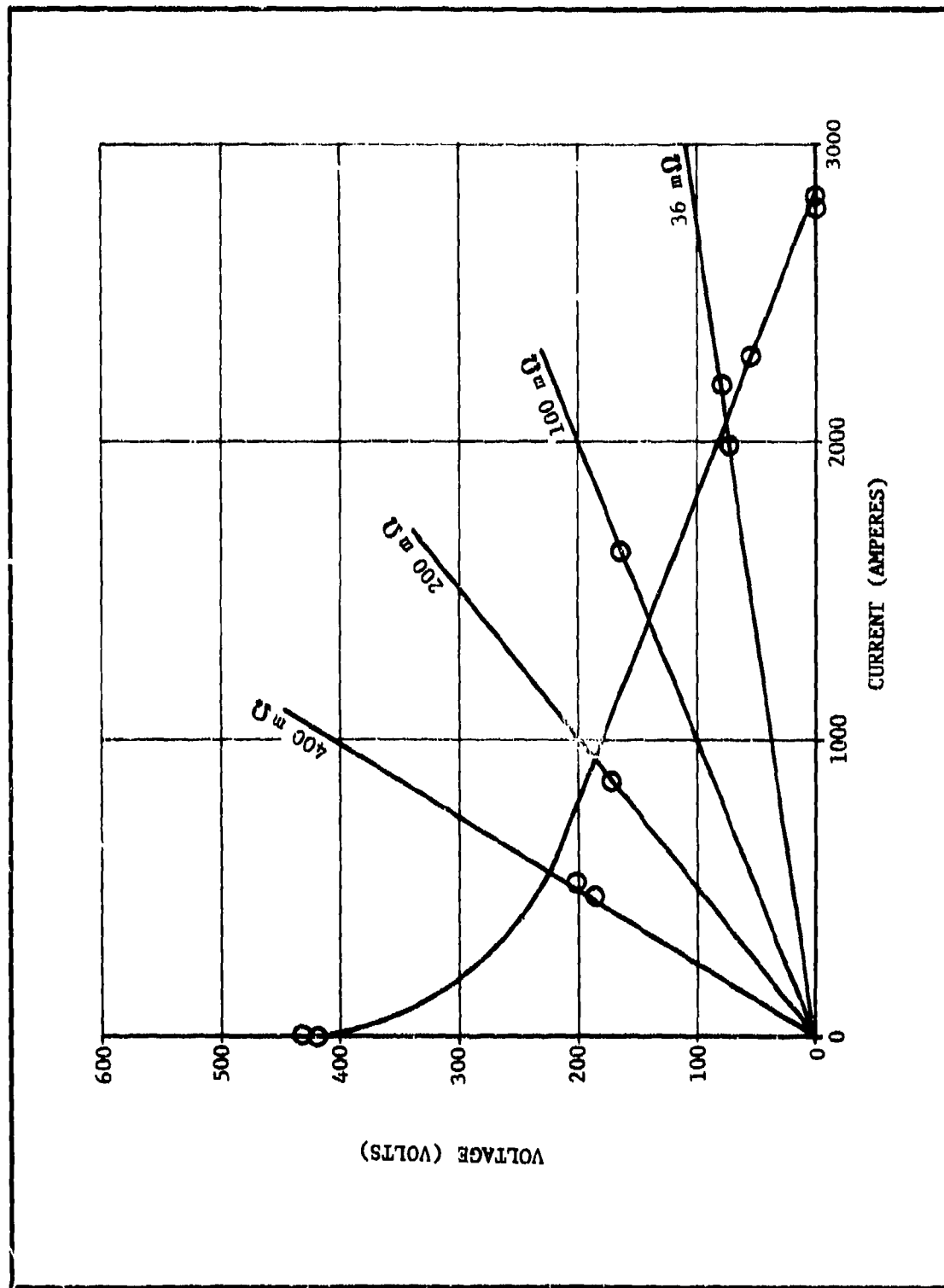


Figure 78. Plot of voltage versus current for 60-cm channel

is the time constant, using typical examples (34), it has a value

$$\tau = \frac{(310 \text{ cm}^3) (4.0 \times 10^{-8}) \frac{\text{sec}^2}{\text{cm}^2}}{(2.8 \times 10^{-3}) \frac{\text{sec}}{\text{cm}} (7.1 \text{ cm}^2)} = 6.2 \times 10^{-4} \text{ sec}$$

Equation 3 then becomes

$$P = P_0 e^{-1560t}$$

At $t = 0.5 \text{ ms}$, $P = 0.46 P_0$, and at $t = 1.0 \text{ ms}$, $P = 0.21 P_0$.

The discharge curve with this time constant is shown in Figure 79, which also shows the normalized data.

The next step is to determine whether or not all the fuel is burned during the rise time. From Figure 80, which gives the burning rate of VJM as a function of pressure, and Figure 81, which gives the ratio of fuel surface area to nozzle area, the burning rate of fuel at any given pressure can be calculated. The mass flow rate versus pressure is shown in Figure 82 for the nozzle diameter used (3.01 cm). The mass flow rate is given by:

$$\dot{m} = \rho A_g r \quad 74$$

but since $A_g = K A_t$, the mass flow rate becomes:

$$\dot{m} = \rho K A_t r \quad 75$$

where

\dot{m} = mass flow rate

ρ = fuel density = 2 gm/cm^3

A_g = fuel surface area

A_t = nozzle throat area = 7.3 cm^2

r = fuel regression

Since the majority of the tests were made at 4000 psi ($2.74 \times 10^7 \text{ n}^t/\text{m}^2$), the mass flow rate of 14.4 gm/ms will be considered. Assuming that 1 ms elapses between ignition and the peak pressure point, the average mass flow rate to that point is 7.5 gm/ms or about 15 percent of the actual

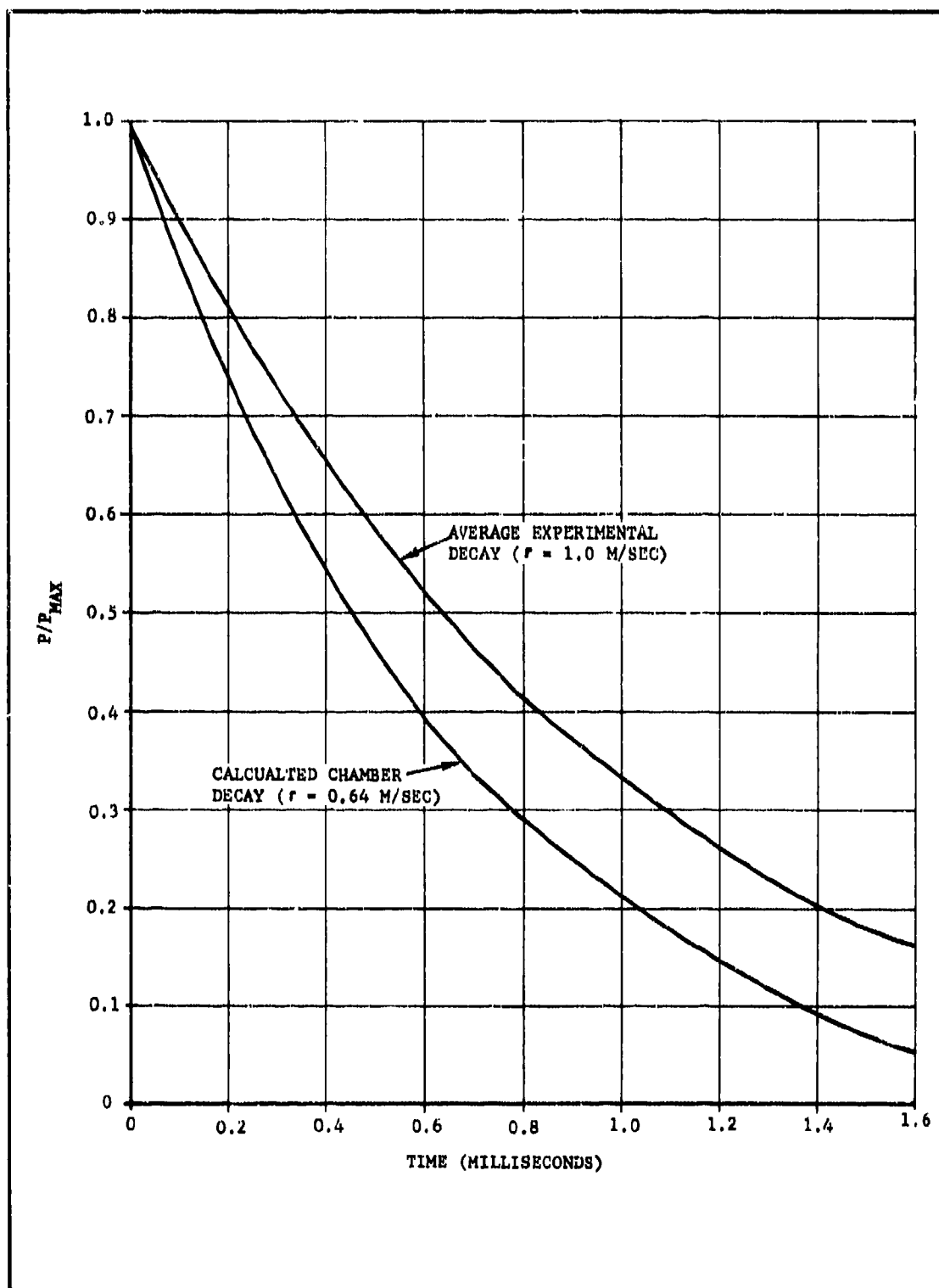


Figure 79. Discharge curve

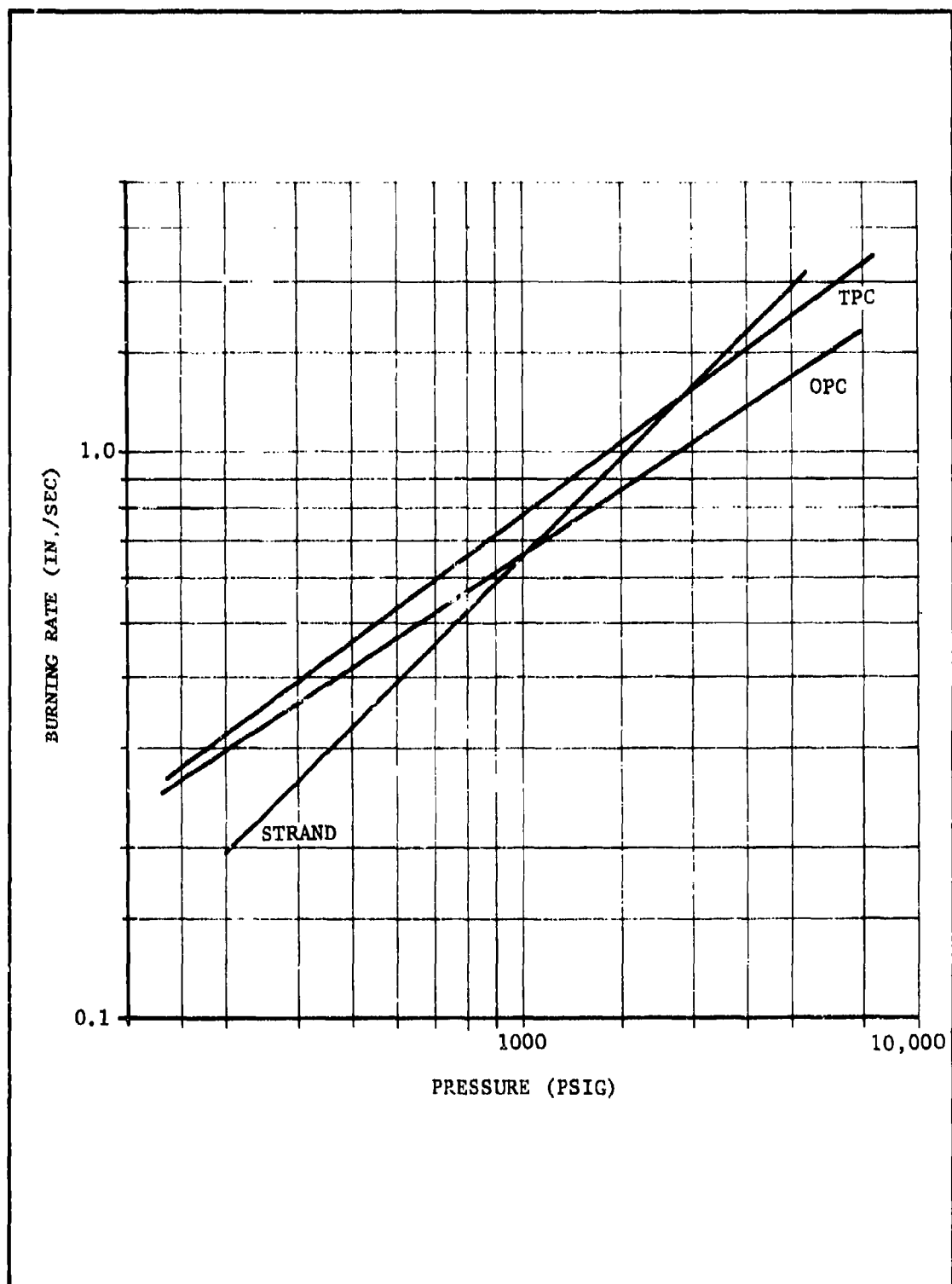


Figure 80. Burning rate versus pressure - VJM fuel

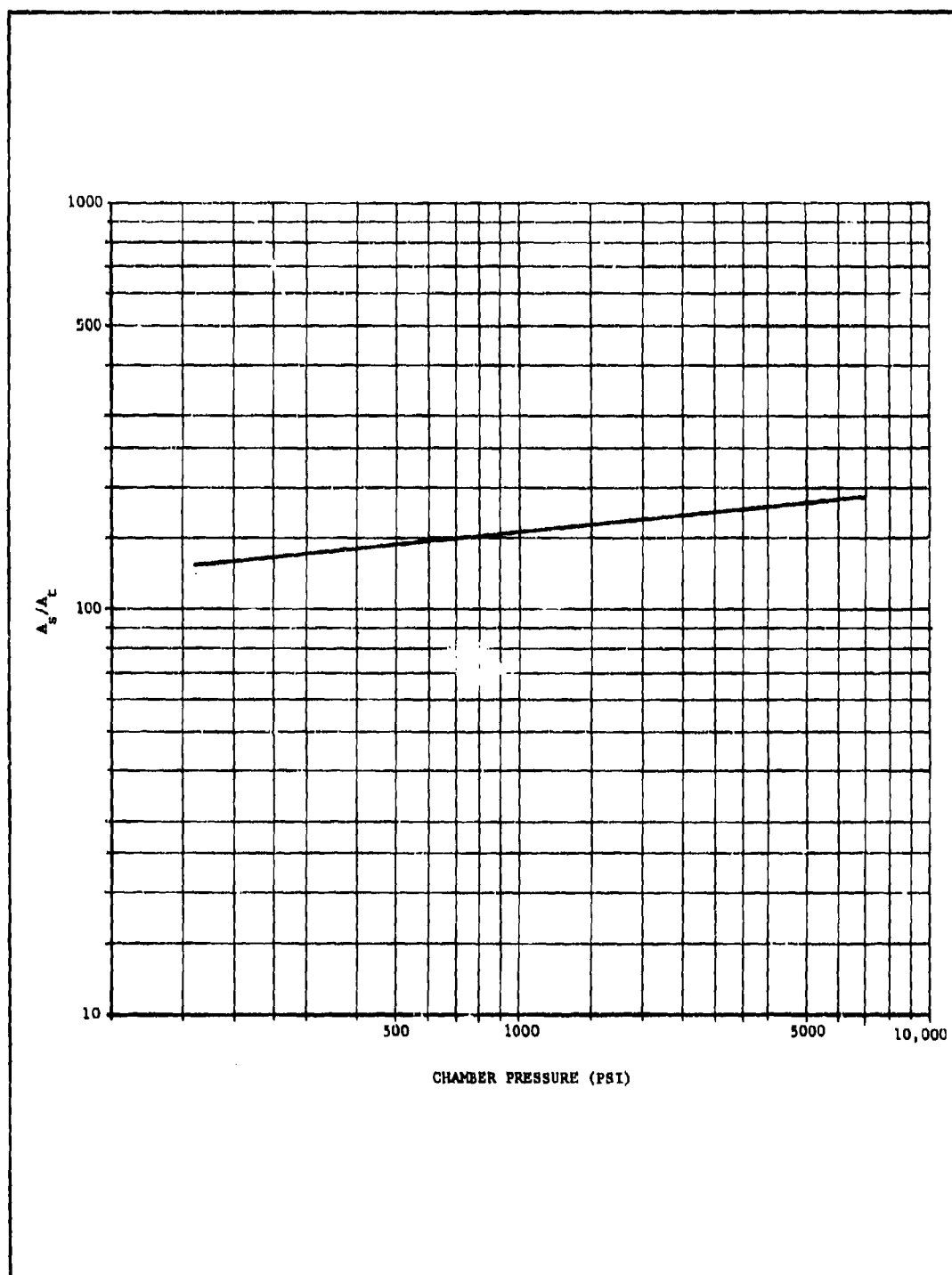


Figure 81. Ratio of fuel surface area to nozzle area

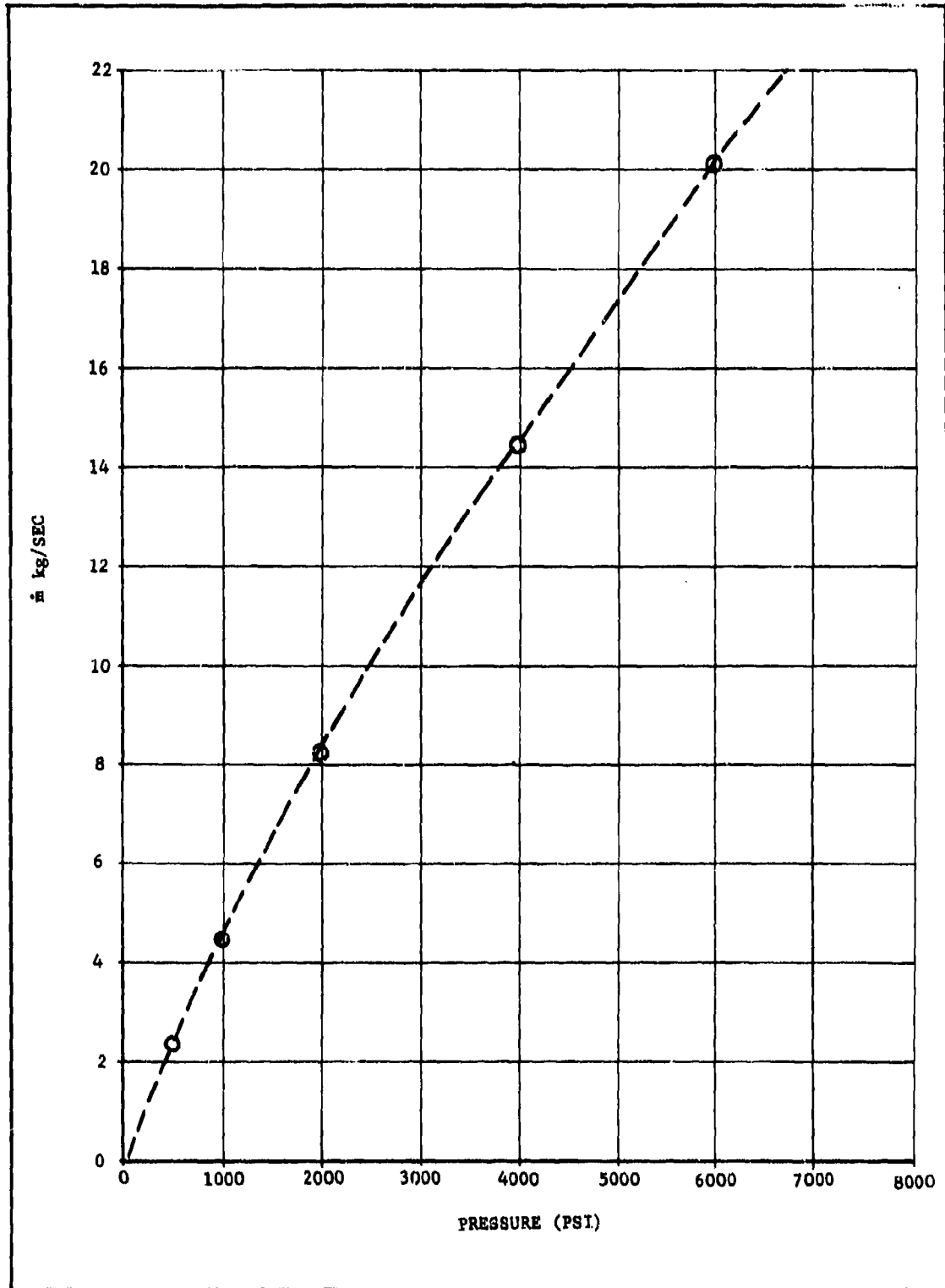


Figure 82. Instantaneous mass flow rate with VJM fuel,
throat diameter = 3.05 cm gm/ms

fuel in the chamber. This indicates that more than one-half of the fuel is being expelled unburned. It is inferred that the amount of fuel burning dictates the peak pressure but from there on the pressure-time decay curve is controlled by the physical parameters of the combustion chamber. The gases which evolve from the burned material must accelerate the unburned mass, which represents a further loss in the system. An elementary calculation suggests that this loss is about 40 percent of the loss due to incomplete combustion. So the maximum possible power is about 30 percent of that desired.

Consideration of the load line can begin with the open circuit voltage. The data shows that the parameter is considerably lower than predicted. Dicks (35) indicates that the electrode drop on a cold copper electrode is of the order of 100 volts. This would account for a drop from the value of 700 volts, which was predicted, to a value of 500 volts. The remaining difference (40 to 50 volts) is easily accounted for by the nonuniform velocity profile.

All channels appear to be limited to a current density of approximately 5 amp/cm^2 on short circuit. The question to be answered is which of two alternative explanations cause the current limiting. These alternatives are based upon either the existence of a shock in the channel, or the electrode temperature. A shock would give a drop in potential at constant current on this V-I plot, to a load line corresponding to about 0.35 times the unshocked open circuit voltage. Under these circumstances, the short-circuit current would be about 1000 amp, or about one-third the measured short-circuit current. Hence, it is likely that the current limitation is due to electrode temperature as indicated by Cobine (36). The slope of the load line of Figure 78 indicates an effective conductivity of 35 mho/meter. An effective conductivity of 73 mho/meter is predicted for an area ratio of 20 (Table III, with B reduced to 2.4 tesla), which is the average in the channel. The difference may be due to incomplete combustion or due to the high resistance of the cold boundary layer.

The optimum power point indicated by Figure 78 would generate 204 kw at 120 volts. Firing No. 403, which fell above the line, produced 267 kw at 170 volts. The voltage, current, and chamber pressure plots for this test are shown in Figure 83. The characteristics of the curve are typical of all other tests. The total energy of 261 joules is less than the 1000 joules, which was anticipated, but is compatible with the calculation of the amount of fuel that was burned and the power loss due to acceleration of unburned fuel.

H. SYSTEM DESIGN

This portion covers a preliminary design estimate for an MHD generator producing 10^3 and 10^4 joules of energy for a period of 10^{-3} sec. Two pulse repetition rates are considered: 1/sec and 10/sec. Since the device could be used for powering a flash lamp, some consideration must be given to high voltage output. In the system considered, a feed mechanism would

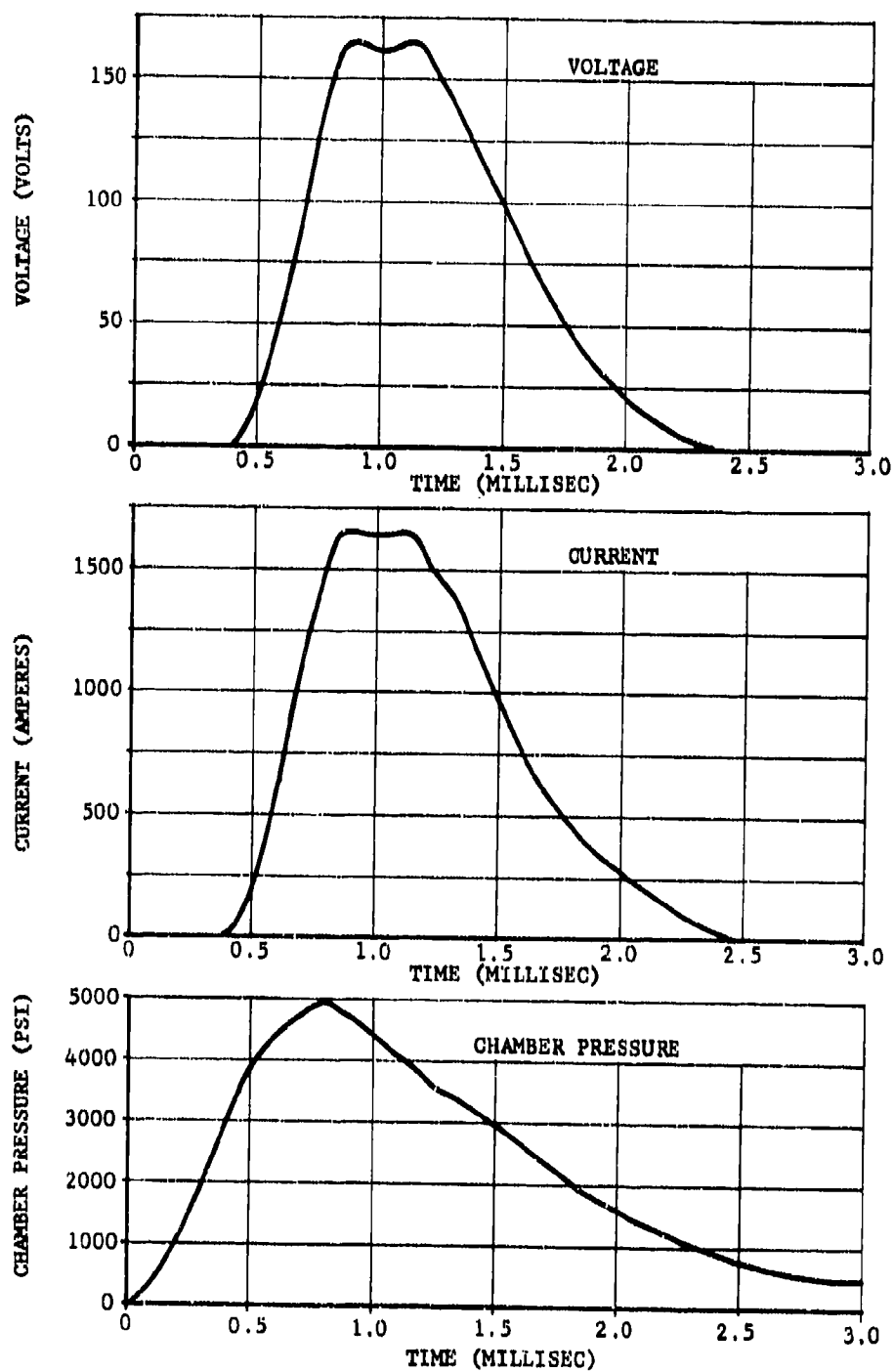


Figure 83. Voltage, current, and chamber pressure plots; test 403

provide 1 ms of combustion for each pulse desired.

The scheme envisioned for producing repetitive pulses with a solid-fuel MHD generator uses a prepacked automatic weapon cartridge as the fuel source. This method of packing allows repetition rates up to 100/sec using a Catling gun breech assembly. Standard 20-mm breeches would allow 10/sec. The 20-mm shell is being used in current experimentation and will hold 35 grams of fuel at a 50-percent packing density. The fuel granule size is selected for proper burn time and chamber pressure.

Since it is difficult to self-excite a magnet in the period of 1 ms, a constant-field magnet will probably be required. A practical magnet for use in a flight-weight system would be superconducting, since a standard electromagnet would consume more power than the pulse generator average power. A continuous electromagnet is therefore not practical. Use of a superconducting magnet is further dictated by the fact that in the relatively small channels a field level of 7 to 10 tesla would be required to produce 1000 volts at operating conditions. This appears to be a voltage requirement of most application areas studied.

Using a power density of 8×10^8 watt/m³, which appears to be achievable, a volume of 1.2×10^{-3} would be required for the 10^3 joule and 1.2×10^{-2} m³ for the 10^4 joule system. The dimension would be approximately 3.5-cm across at the entrance, 9-cm across at the exit, and 31-cm long for the 10^3 joule case. The 10^4 joule system would be 7.5 cm at the entrance, 19.5 cm at the exit, and 65-cm long. These two channels are shown in Figures 84 and 85.

The weight of the channel, using an average wall material density of 2 gm/cm³ with a thickness of 2 cm, is 6.2 kg for the small channel and 25 kg for the large channel.

The fuel mass required per pulse is based upon experimental data and, assuming that the electrode and combustion problems can be solved, is 22 grams for the small and 90 grams for the large. The small channel would use a 20-mm cartridge while a 25-mm cartridge would be used for the larger size. These standard cartridges are suggested for logistic reasons, but a weight saving could be realized if a special shell were used. The weight of fuel and cartridge for the small channel could be 140 grams/pulse while the large channel would require 270 grams/pulse. If the cartridge cases were fabricated of aluminum rather than steel, the weights would reduce to 60 grams and 156 grams respectively. The total fuel and cartridge weights are shown as a function of repetition rate in Figure 86 for an operating time of 300 sec. One of the problems which should be considered in the design of a repetitively pulsed system is the question of heat transfer to the channel walls and cooling requirements. The heat transfer parameters for seeded solid-rocket propellant combustion products in an MHD channel have been estimated in previous studies (4). For the pressures, velocities, and wall temperatures being considered here, an appropriate heat transfer rate or thermal flux would be about 1 kw/cm². Since the pulse length would be short compared to the thermal time constant of the

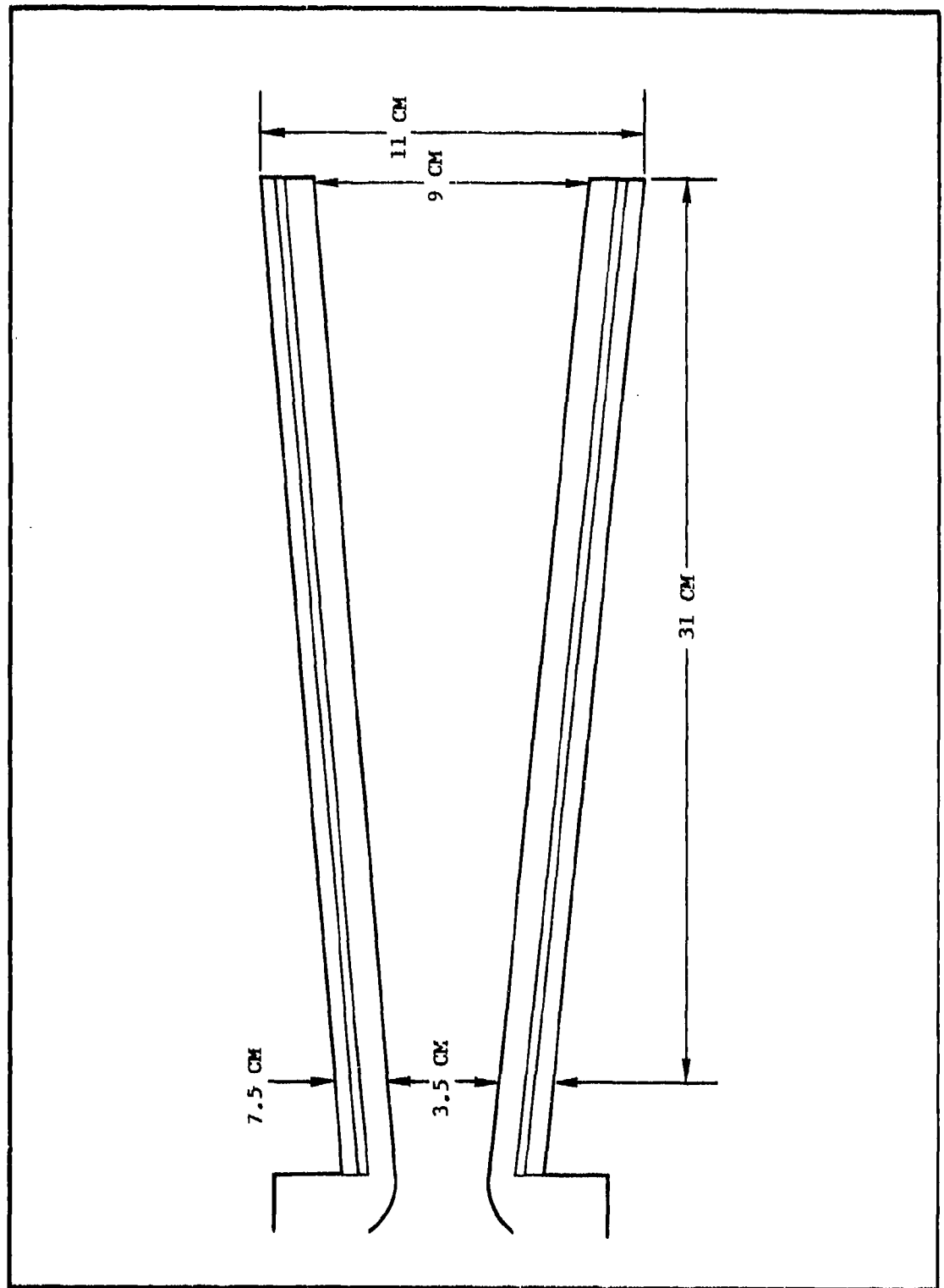


Figure 84. 10^3 joule channel with aspect ratio of unity

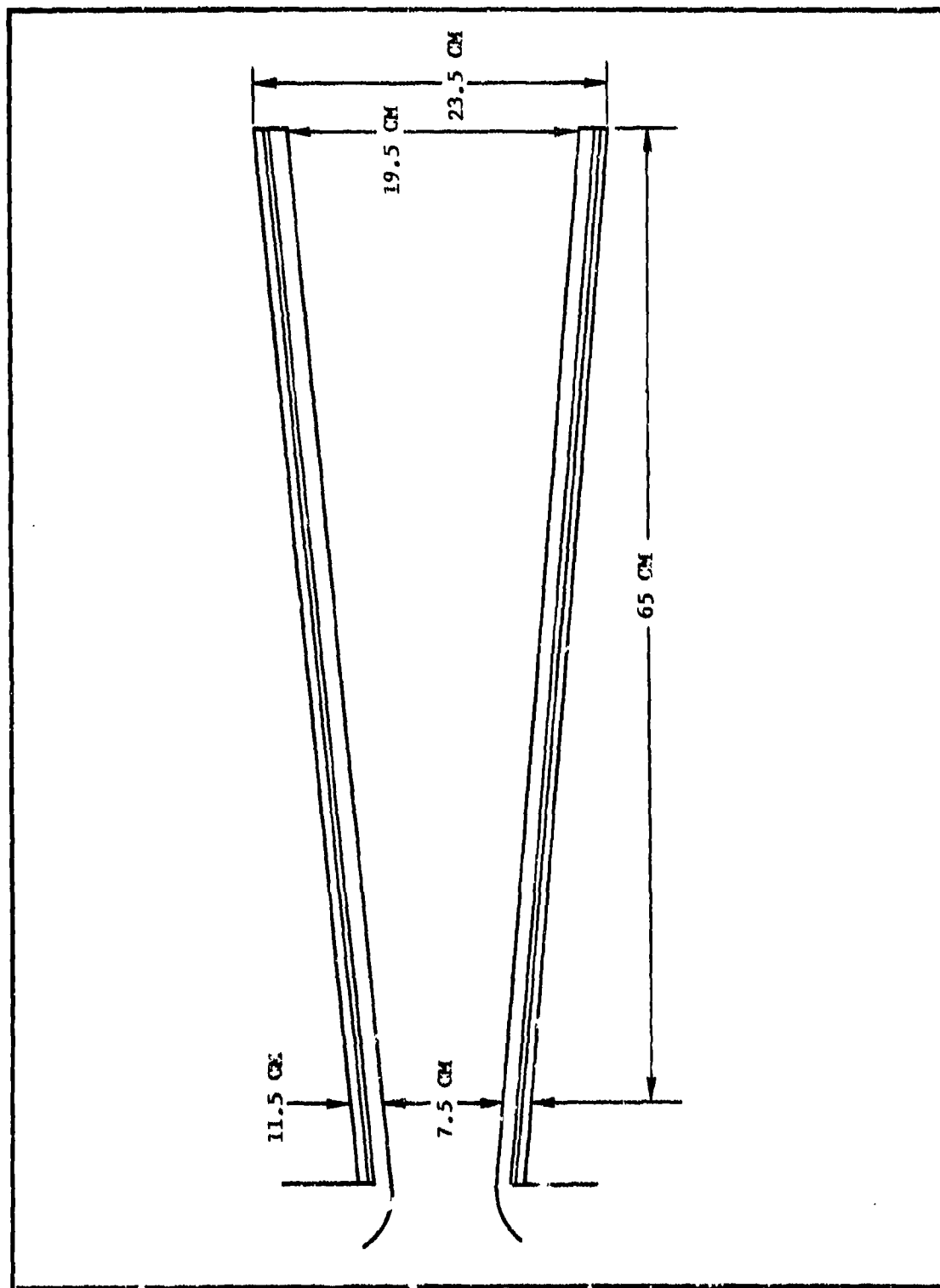


Figure 85. 10^4 joule channel with aspect ratio of unity

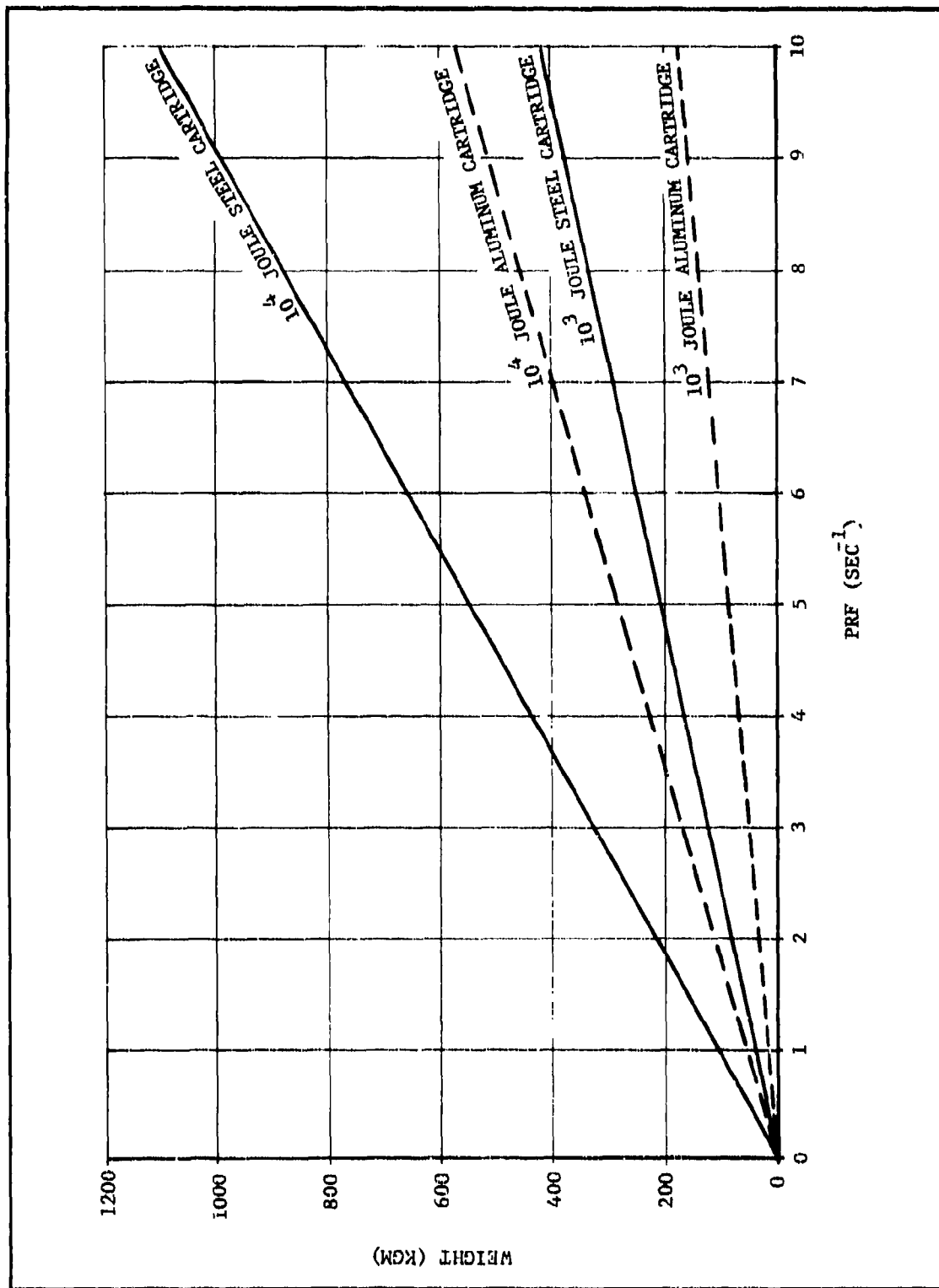


Figure 86. Weights of fuel and cartridge for 10³ joule and 10⁴ joule

channel walls, the heat transfer rate must be averaged over the period between pulses. With a thermal pulse length of 2 ms and a repetition rate of 10/sec, the effective heat flux would be about 20 w/cm^2 or $48 \frac{\text{Kcal}}{\text{m}^2 \text{ sec}}$.

With a wall area of 0.2 m^2 , the thermal throughput required to maintain the walls at an equilibrium temperature would be about $10 \frac{\text{Kcal}}{\text{sec}}$. Assuming that water is to be used as a coolant and allowed to load off into the ambient atmosphere, which may be of reduced pressure because of altitude, the removal of this amount of heat would require $1.6 \times 10^{-2} \text{ kg/sec}$ of water. For a 300-sec operating period 4.8 kg of H_2O would be required. Values for the other systems can be derived from channel wall area and pulse repetition requirements.

The total weight of the system will have a fixed weight comprised of the magnet, channel, and breech mechanism and a weight due to fuel, cartridge, and coolant which are dependent on the pulse repetition rate. Estimations of the magnet weight, including dewar and liquid helium, are 75 kg for the small channel and 250 kg for the large channel. The breech mechanism weights are 10 kg and 25 kg for the two channels. Component weights for the two energy levels at pulse rates of 1 and 10 per sec are as follows:

System	Channel Weight (kg)	Magnet Weight (kg)	Fuel and Cart Wt (kg)	Breech Weight (kg)	Coolant Weight (kg)	Total Weight (kg)
10^3 joule-1/sec	7.0	75	18	10	1.0	111
10^3 joule-10/sec	7.0	75	180	10	4.8	277
10^4 joule-1/sec	25.0	250	48	25	1.4	349
10^4 joule-10/sec	25.0	250	480	25	13.5	793

I. CONCLUSIONS AND RECOMMENDATIONS

The two major problems found in this system are that of achieving complete combustion in the time duration specified and in reducing the current limitation in the electrode. Two methods are available for solving the first problem: using extruded grains which are thin enough to burn in the time available or plugging the nozzle until the initial pressure reaches a high enough value. The extruded grains would be cylinders similar to the form used in sporting powders. A mass flow versus time plot for typical solid and hollow cylinders is shown in Figure 87. In addition, the pressure should be raised to a higher value which will increase the burning rate. Higher pressures are readily achievable in a breech mechanism since design pressures of 20,000 psi are commonly used. The data currently available can be extrapolated to show that burning rates of the magnitude desired can be obtained at practical pressures. Extrapolation of the data for VJM fuel is shown in Figure 80. It is felt, however, that at least up to 20,000 psi ($1.37 \times 10^8 \text{ n/m}^2$) the data can be expected to be linear.

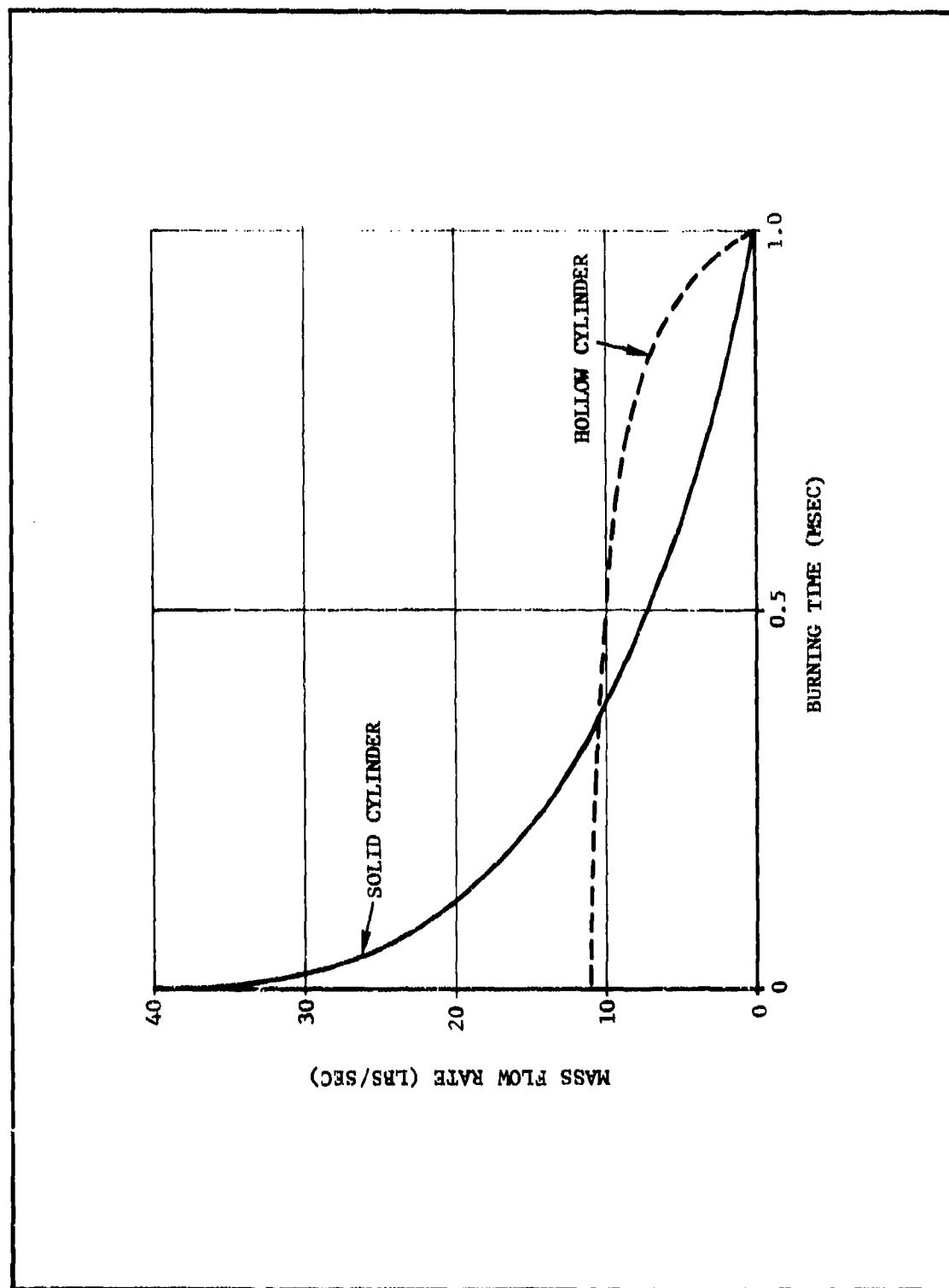


Figure 87. Plot of mass flow rate versus burning time for hollow and solid cylinders

In further support of this assumption, the burning rates of several double-base sporting powders are shown in Figure 88. Experimental data is readily available for these propellants up to 20,000 psi and no anomalies occur up to this pressure.

To build up the chamber pressure more rapidly the end of the cartridge could be stopped with a frangible disc which is set to rupture at a given pressure. A short expansion chamber would be required before the gas is nozzleed since the frangible disc would create flow disturbances in the area just downstream from it.

The second problem, electrode current limitation, is a factor which is very dependent on electrode temperature. In applications with repetition rates greater than 1/sec, this should not be a problem after the initial rounds, since the electrodes will heat up. For repetition rates less than this, some form of preheating may be required. An alternate procedure involves roughening the electrode surface. This is beneficial not only because the high points could heat up sooner and increase thermal emission, but also the roughened electrode will have a greater surface area, which implies a greater current density. As a further bonus, the roughened electrodes will emit due to the field emission process because the local rough spots can have high potential near their peaks (36).

It is recommended that further experiments be conducted to, (1) Demonstrate that complete combustion and increased electrode current flux can be achieved in practice, and (2) provide the experimental verification of a repetitive-millisecond-pulsed generator system.

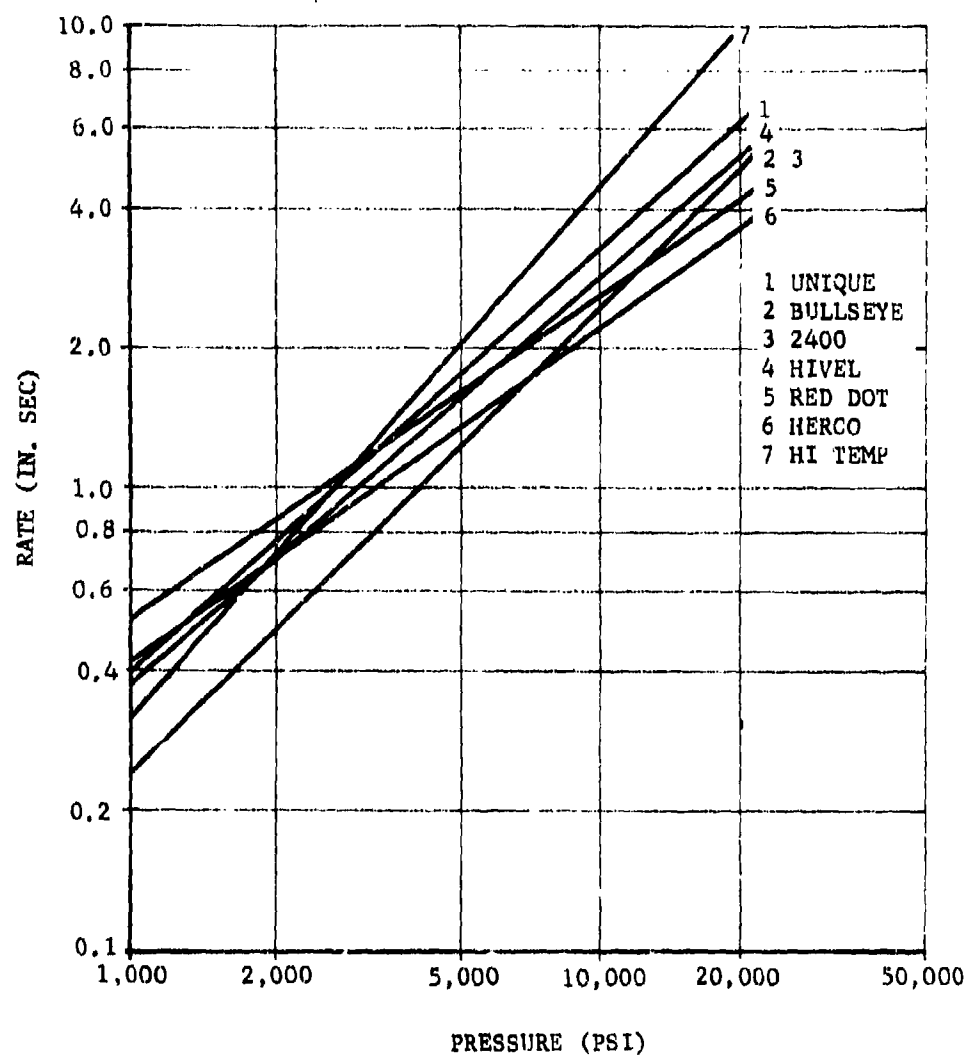


Figure 88. Experimental burning rates of several double-base type sporting powders up to 20,000 psi

LIST OF REFERENCES

- (1) Jones, M. S., Explosive Magnetohydrodynamics, AFAPL-TR-65-61, AD 470 711, April 1965
- (2) Jones, M. S., Blackman, V. H., Brumfield, R. C., Evans, E. W., and McKinnon, C. N., Research on the Physics of Pulsed MHD Generators, AD 426 448, December 1963
- (3) Jones, M. S. and McKinnon, C. N., "Explosive Driven Linear MHD Generators", Proceedings of the Conference on Megagauss Magnetic Field Generation by Explosives and Related Experiments, Frascati, Italy, 21-23 September 1965
- (4) Solid and Hybrid Fuel MHD Generator Study - Final Report, Part I (Contract AF 33(615)-3224), MHD Research, Incorporated and Hercules, Incorporated, June 1966, SECRET
- (5) Bangerter, C. D., "Operation of Solid Fuel MHD Generators", Eighth Symposium on Engineering Aspects of Magnetohydrodynamics, March 1967, Stanford, California
- (6) Spitzer, L., Physics of Fully Ionized Gases, Interscience Incorporated, 1956, New York
- (7) Cummings, D. B. and Morley, M. J., "Electrical Pulses from Helical and Coaxial Explosive Generators", Proceedings of the Conference on Megagauss Magnetic Field Generation by Explosives and Related Experiments, Frascati, Italy, 21-23 September 1965
- (8) Mecker, M. E., Experimental Study of High-Voltage, One-Shot Ferromagnetic Explosive-Electric Transducers, Sandia Corporation Technical Memorandum 229-57, 1951
- (9) Kulterman, R. W., Neilson, F. W., and Benedick, W. B., Pulse Generator Based on High Shock Demagnetization of Ferromagnetic Material, Sandia Corporation Reprint SCR-16, June 1958
- (10) Besançon, J. E., et al., "Transducteurs Ferromagnétiques", Proceedings of the Conference on Megagauss Magnetic Field Generation by Explosives and Related Experiments, Frascati, Italy, 21-23 September 1965
- (11) Besançon, J. E. and Vedel, D. J., "Transducteurs Ferroelectriques", Proceedings of the Conference on Megagauss Magnetic Field Generation by Explosives and Related Experiments, Frascati, Italy, 21-23 September 1965
- (12) Zeldovich, Ia B. and Kompaneets, A. S., Theory of Detonation, Academic Press, 1960, New York, Chapter 4

162

Preceding page blank

LIST OF REFERENCES (Cont)

- (13) Hildebrand, F. B., Advanced Calculus for Engineers, Prentice Hall, 1949, New York, p. 7ff
- (14) Payne, W. T. and Zadoff, L. N., "Electromagnetic Diffusion into a Moving Conductor", AIAA Journal, 3, July 1965, pp. 1294-7
- (15) Underhill, Earl (editor), Permanent Magnet Handbook, Crucible Steel Company of America, 1956
- (16) Polydoroff, W. J., High Frequency Magnetic Materials, J. Wiley and Sons, 1960, New York, Chapter 1
- (17) Howe, G. W., Wireless Engineering, 10, 1933, p. 1
- (18) Becker, J. J., Recent Developments in Magnetic Metals and Alloys, General Electric Report No. 62-RL-3098M, August 1962
- (19) Dekker, A. J., Solid State Physics, Prentice Hall, 1962, New Jersey, Chapter 11
- (20) Mayor, J. E., "The Theory of Ionic Solutions", J. Chem. Phys., 18, 1950, pp. 1426-36
- (21) Cook, M. A., The Science of High Explosives, Reinhold Publishing Company, 1959, New York
- (22) Cook, M. A. and McEwan, U. S., "Cohesion in Plasma", J. Applied Physics, 29, 1958, pp. 1612-3
- (23) Robinson, J., "Measurement and Interpretation of Plasma Properties to 100 Kilobars of Pressure", NASA Report CR-446, April 1966
- (24) Jameson, R. L., et al., "Electrical Measurements in Detonating Pentolite and Composition B", J. Applied Physics, 35, March 1964, p. 714
- (25) Brish, A. A., Tarasov, M. S., and Tsukerman, V. A., "Electric Conductivity of the Explosion Products of Condensed Explosives", Soviet Physics JETP, 37, June 1960, pp 1095-1100
- (26) Hayes, B., "On Electrical Conductivity in Detonation Products", Navy Symposium on Detonation, Los Alamos Scientific Laboratory, 1965
- (27) Mader, C. L., "Detonation Properties of Condensed Explosives Computed Using the BFW Equation of State", Los Alamos Scientific Laboratory Report LA-2100, 1963
- (28) Taylor, J., Detonation in Condensed Explosives, Clarendon Press, Oxford, 1952, Chapter 8

LIST OF REFERENCES (Cont)

- (29) Lord Rayleigh, Philosophical Magazine, 34, Fifth Series, 1892, p. 481ff
- (30) Meredith, R. E. and Tobias, C. W., "Resistance to Potential Flow through a Cubical Array of Spheres", J. Applied Physics, 31, July 1960, pp. 1270-3
- (31) Keller, J. B., "Conductivity of a Medium Containing a Dense Array of Perfectly Conducting Spheres or Cylinders or Nonconducting Cylinders", J. Applied Physics, 34, April 1963, pp. 991-3
- (32) Keller, H. B. and Sachs, D., "Calculations of the Conductivity of a Medium Containing Cylindrical Inclusions", J. Applied Physics, 35, March 1964, pp. 537-8
- (33) Paterson, S., "The Structure of the Reaction Zone in a Detonating Explosive", Fifth Symposium on Combustion, Reinhold Publishing Corporation, 1955, New York, pp. 672-684
- (34) An Introduction to the Theory and Practice of Military Rocket Engineering, George Washington University, 1944, Washington, D. C., pp. 54-55
- (35) Dicks, J. B., et al., "Characteristics of a Family of Diagonal Conducting Wall MHD Generators", Eighth Symposium on Engineering Aspects of Magnetohydrodynamics, March 1967, Stanford, California, p. 50
- (36) Cobine, J. D., Gaseous Conductors, Dover, 1958, New York, p. 107

UNCLASSIFIED

Security Classification

DOCUMENT CONTROL DATA - R&D

(Security classification of title, body of abstract and indexing annotation must be entered when the overall report is classified)

1. ORIGINATING ACTIVITY (Corporate author) MHD Research, Inc PO Box 1815 Newport Beach, California 92663		2a. REPORT SECURITY CLASSIFICATION UNCLASSIFIED	
		2b. GROUP	
3. REPORT TITLE EXPLOSIVE MAGNETOHYDRODYNAMICS			
4. DESCRIPTIVE NOTES (Type of report and inclusive dates) Final Technical Report			
5. AUTHOR(S) (Last name, first name, initial) Jones, Malcolm S.; Bangerter, Clinton D.; Peterson, Albert H.; & McKinnon, Charles H.			
6. REPORT DATE August 1967		7a. TOTAL NO. OF PAGES 185	7b. NO. OF REFS 36
8a. CONTRACT OR GRANT NO. AF33(615)-3233 ✓ b. PROJECT NO. 5350 c. Task No 535004 d. BPSN 6(63 5350 62405214)		9a. ORIGINATOR'S REPORT NUMBER(S) MHD Report 700 9b. OTHER REPORT NO(S) (Any other numbers that may be assigned this report) AFAPL-TR-67-64	
10. AVAILABILITY/LIMITATION NOTICES Foreign announcement and dissemination of this report by DDC is not authorized.			
11. SUPPLEMENTARY NOTES		12. SPONSORING MILITARY ACTIVITY Air Force Aero Propulsion Laboratory Wright-Patterson AFB, Ohio 45433	
13. ABSTRACT The objective of this program was to investigate the feasibility of using explosive-driven MHD generators to produce pulses of various time durations and to investigate the feasibility of producing alternating currents. Four principal approaches were investigated: <i>times 10 to the 7th power</i> a. Power densities of 5×10^{20} w/m ² <i>measured</i> were achieved in Comp C4 explosive with copper and iron powder dopants. Detonation zone conductance was increased by three orders of magnitude, with magnetic Reynolds numbers approaching unity. b. Sixty kilohertz alternating current was generated using segmented electrodes to commutate the current in an explosive-driven MHD channel and the output was transformer coupled to various loads. c. One millisecond pulses with maximum power outputs of 277 Kw were achieved with 50 grams of seeded propellant. These fuels were successfully ignited using standard 20-mm electrically fired cartridges. d. A series of pulses were generated in the explosive-driven MHD channel using a multiple charge transport mechanism. Channel pumping downtimes were found to limit this technique to the 10 to 20 pulse per second pulse repetition frequency.			

DD FORM 1 JAN 64 1473

UNCLASSIFIED
Security Classification

14 KEY WORDS	LINK A		LINK B		LINK C	
	ROLE	WT	ROLE	WT	ROLE	WT
1. Magnetohydrodynamics						
2. Explosive Magnetohydrodynamics						
3. MID						
4. Explosive MID						
5. Alternating Current Pulses						
6. Repetitive Pulses						
7. Magnetically Loaded Explosives						

INSTRUCTIONS

1. ORIGINATING ACTIVITY: Enter the name and address of the contractor, subcontractor, grantee, Department of Defense activity or other organization (*corporate author*) issuing the report.

2a. REPORT SECURITY CLASSIFICATION: Enter the overall security classification of the report. Indicate whether "Restricted Data" is included. Marking is to be in accordance with appropriate security regulations.

2b. GROUP: Automatic downgrading is specified in DoD Directive 5200.10 and Armed Forces Industrial Manual. Enter the group number. Also, when applicable, show that optional markings have been used for Group 3 and Group 4 as authorized.

3. REPORT TITLE: Enter the complete report title in all capital letters. Titles in all cases should be unclassified. If a meaningful title cannot be selected without classification, show title classification in all capitals in parenthesis immediately following the title.

4. DESCRIPTIVE NOTES: If appropriate, enter the type of report, e.g., interim, progress, summary, annual, or final. Give the inclusive dates when a specific reporting period is covered.

5. AUTHOR(S): Enter the name(s) of author(s) as shown on or in the report. Enter last name, first name, middle initial. If military, show rank and branch of service. The name of the principal author is an absolute minimum requirement.

6. REPORT DATE: Enter the date of the report as day, month, year; or month, year. If more than one date appears on the report, use date of publication.

7a. TOTAL NUMBER OF PAGES: The total page count should follow normal pagination procedures, i.e., enter the number of pages containing information.

7b. NUMBER OF REFERENCES: Enter the total number of references cited in the report.

8a. CONTRACT OR GRANT NUMBER: If appropriate, enter the applicable number of the contract or grant under which the report was written.

8b, 8c, & 8d. PROJECT NUMBER: Enter the appropriate military department identification, such as project number, subproject number, system numbers, task number, etc.

9a. ORIGINATOR'S REPORT NUMBER(S): Enter the official report number by which the document will be identified and controlled by the originating activity. This number must be unique to this report.

9b. OTHER REPORT NUMBER(S): If the report has been assigned any other report numbers (*either by the originator or by the sponsor*), also enter this number(s).

10. AVAILABILITY/LIMITATION NOTICES: Enter any limitations on further dissemination of the report other than those

imposed by security classification, using standard statements such as:

- (1) "Qualified requesters may obtain copies of this report from DDC."
- (2) "Foreign announcement and dissemination of this report by DDC is not authorized."
- (3) "U. S. Government agencies may obtain copies of this report directly from DDC. Other qualified DDC users shall request through _____."
- (4) "U. S. military agencies may obtain copies of this report directly from DDC. Other qualified users shall request through _____."
- (5) "All distribution of this report is controlled. Qualified DDC users shall request through _____."

If the report has been furnished to the Office of Technical Services, Department of Commerce, for sale to the public, indicate this fact and enter the price, if known.

11. SUPPLEMENTARY NOTES: Use for additional explanatory notes.

12. SPONSORING MILITARY ACTIVITY: Enter the name of the departmental project office or laboratory sponsoring (*paying for*) the research and development. Include address.

13. ABSTRACT: Enter an abstract giving a brief and factual summary of the document indicative of the report, even though it may also appear elsewhere in the body of the technical report. If additional space is required, a continuation sheet shall be attached.

It is highly desirable that the abstract of classified reports be unclassified. Each paragraph of the abstract shall end with an indication of the military security classification of the information in the paragraph, represented as (TS), (S), (C), or (U).

There is no limitation on the length of the abstract. However, the suggested length is from 150 to 225 words.

14. KEY WORDS: Key words are technically meaningful terms or short phrases that characterize a report and may be used as index entries for cataloging the report. Key words must be selected so that no security classification is required. Identifiers, such as equipment model designation, trade name, military project code name, geographic location, may be used as key words but will be followed by an indication of technical context. The assignment of links, rules, and weights is optional.